Modelling HIF-1α Dynamics within Single Cells and Neurospheres

Thesis submitted in accordance with the requirements of the University of Liverpool for the degree of Doctor in Philosophy by

Joseph Leedale

August 2013

Abstract

HIF-1 (Hypoxia Inducible Factor-1) is an oxygen-regulated transcription factor that mediates the intracellular response to hypoxia in human cells, targeting specific genes that promote cell survival by inducing processes such as angiogenesis and glycolysis. The HIF-1 signalling pathway has been of considerable interest due to its role in mammalian development and in particular several pathologies such as ischemia and cancer. Low cellular oxygen levels are found in cancer due to the rapid proliferation of tumour cells distant to blood vessels (forming a hypoxic core) and the typically irregular vasculature is unable to properly perfuse the tumour.

In the Centre for Cell Imaging at the University of Liverpool, time lapsed imaging in an oxygen-controlled environment has captured the transient dynamics of the oxygen regulated subunit of HIF-1, HIF-1α, and revealed heterogeneity between individual cells. The essential characteristics of this data are modelled with a system of differential equations describing the feedback inhibition between HIF-1α and the pathway's effective oxygen sensors. This novel model was formulated by employing a minimalist approach initially, allowing us to use the rich variety of single-cell data to determine the structure of the feedback loop between two key pathway components. Once the central regulatory motif was identified, the model was expanded to include more complexity, including experimental measurements for model parameter values and additional system components.

Oxygen plays an especially important role in the early stages of tumour formation. Measurements of oxygen within cells have been recorded in cultured spheres of neuroblastoma cells at different atmospheric conditions. This data is representative of the early development stages of an avascular tumour and a spatial oxygen-diffusion model was coupled with the single-cell HIF-1α model to describe the dynamics of HIF-1α across a developing tumour. This coupled model is used to study HIF-1α dynamics in the context of various oxygen-dependent cellular functions such as cell-cycle progression and apoptosis by integrating with modifications of published mathematical models.

Acknowledgements

I would like to thank my supervisors Violaine Sée, Kieran Sharkey and especially Rachel Bearon without whom the completion of this thesis would not have been possible. Thank you Rachel for your advice and guidance throughout. You have taught me a lot and I will always be grateful for your patience and generosity. Thanks also to my brilliant collaborators in biology, James Bagnall and Anne Herrmann.

I would also like to acknowledge the many friends that I have made in the maths department during my PhD who have helped me along the way. Discussions about research, but mostly the mutual support and talking about anything but research made my time in the department that much more enjoyable. Special thanks to Ashley Brereton, Nigel Harrison, Andrew Monaghan, Graham Reeve, Kirk Waite, Jenna Birch, Stewart Haslinger, Heather Riley, Manou Rasolonjanahary, Demetris Avraam and to everyone else who I played football with, went to the pub with, tutored with and who generally made me smile. I wish you all the best of luck in whatever paths you may take.

I would like to thank my family and Carrie for their continued love and encouragement. Thank you for always being there to support me unconditionally. Thank you Carrie for listening, advising, comforting and motivating. Your words have often inspired me when I needed them most. Your constant support is something for which I can never thank you enough. I only hope to provide the same continued source of encouragement and understanding.

Finally, I would like to acknowledge the University of Liverpool for providing the opportunity for me to write this thesis and for funding this most rewarding experience.

Contents

Chapter 1

Introduction

1.1 Background

Systems biology is a field of scientific inquiry whose roots can be traced back hundreds if not thousands of years depending on its definition, of which there are many. However, in more recent times the term 'systems biology' has become much more prevalent owing to its renewed importance and effectiveness following the advance of technology. As suggested by the name, systems biology is based on a more integrative or holistic philosophy when compared to the more reductionist approaches of classical biology. Despite the slight variations in literature definitions there are general principles of systems biology that appear to be universally agreed upon. A basic concept of systems biology is to study a particular biological process that can be divided into integral components, but whose properties cannot be fully explained solely from the knowledge of these components (Konopka 2007). These properties are sometimes referred to as 'emergent' properties. The 'system' represents the wholeness that is the studied phenomenon, defined by the interactions of its components (parts). Thus, it is the nature of these links between system components that is the focus of systems biology and the functional states of the networks that arise from the assembly of all such links (Palsson 2006). Systems biology is often concerned with the study of complex interactions and networks in cell biology that can be modelled using some simplifying principles to enable better understanding of system behaviour. This paradigm shift towards system-level understanding was prompted by the increasing rate of experimental technological advances that allow a more quantitative analysis of cell biology using microscopy and bioinformatics. However, the accumulation of genomic data outgrows the rate of improvement in computer power to process so much information. Therefore, in order to enhance understanding of the critical links between genome and cellular function, the use of mathematical models has become ever more predominant in the field. The emerging, central role of mathematical modelling and computer simulations distinguishes systems biology from other fields of holistic thinking such as integrative biology (Edwards and Thiele 2013, Rigoutsos and Stephanopoulos 2007). Consequently, systems biology is a field of study that focuses particularly on an interdisciplinary approach and the collaboration between theoreticians and experimentalists. The following is an example of a concise definition of the term 'systems biology' which reflects my own interpretation and experience:

> [Systems biology is] an iterative process of computational model building and experimental model revision with the aim of understanding or simulating complex biological systems. (Edwards and Thiele 2013)

An important part of systems biology is the mathematical modelling of biological systems. The emphasis of mathematical models in systems biology is to provide a more intuitive understanding of the collective dynamics and emergent properties of the system of interest, rather than just an extremely accurate reproduction of experimental data for individual components. This holistic

emphasis is well-suited to modern cell biology where there are vast amounts of data but also a great degree of noise in individual experiments. Due to the immense complexity of cellular systems, it is difficult to measure precise experimental results for a specific function that don't show much variation (a rare feat in biology when compared to physics for example (Roose, Chapman and Maini 2007)). The approach of systems-level understanding acknowledges the importance of understanding genes and proteins for example, but the focus is rather on understanding the structure and dynamics of the system (Kitano 2002). As a result of this, reliable models are often relatively simple but qualitatively reproduce general features of a system and even make accurate predictions. This is in contrast with what might appear to be a more complex and realistic model for which the inevitable increase in fitted or unreliably estimated parameters can result in poorer predictions. An overly complex model may describe the experiment of interest very well but not be a good representation of the system of interest. Reductionist biological models can become very complex very quickly as they are built from the bottom-up to maximise information. However, as a consequence of this they are very difficult to analyse mathematically and thus fail to provide understanding and intuition. There is a delicate balance of reliability to be found between a complex realistic model and a well-parameterised yet simplistic model (Roose, Chapman and Maini 2007).

A classic case of the application of mathematics within systems biology involves the investigation of the building blocks of life known as cells. Cells are the smallest units of life and are efficient and organised in maintaining the vitality of the cell and host body and have a vast range of cellular functions largely carried out by the activity of molecular subunits called proteins. Each protein has a specific function and so protein dynamics are widely studied in an attempt to further understand how the cell works. The cell continuously monitors its environment by sensing various signals in order to determine what proteins need to be produced and how many. Transcription factors are specialised proteins that, when activated by an environmental signal, can bind to a specific stretch of DNA and regulate the transcription of specific proteins known as target genes. Transcription of the target gene in the nucleus produces mRNA which is then translated in the cytoplasm into the desired protein. The modified rate of transcription caused by transcription factor activity affects the relative quantities of cellular proteins and subsequently the cell activity. In this way, the activities of transcription factors can be considered to be an internal representation of the environment (Alon 2006). Understanding the mechanisms of transcription factor regulation is an interesting research area in its own right but also a widely studied area due to the associated medical implications. The clinical significance of transcription factors arises due to their major role in the cellular response to specific stimuli that represent a disturbance of the homeostasis. As a result, impairment of the function of a transcription factor via mutation can have severe consequences on the condition of the cell leading to diseases such as cancer and diabetes (Latchman 1996, Al-Quobaili and Montenarh 2008) as the cell cannot respond

to signals appropriately. Correspondingly, transcription factors are natural therapeutic targets for the use of drugs that aim to manipulate the signalling pathway of interest.

The general procedure of theoretical study for protein behaviour following various stimuli is based on mathematical reasoning derived from the biological interpretation of experimental results. This reasoning forms the basis of a mathematical model, where phenomena observed in experiments are incorporated into a bigger picture of chemical reactions in a network that includes the deemed key molecular species. The way these species, or system components, interact within the network is often explained by using systems of differential equations; a way of describing the evolution of the dynamics of a variable (a component representing the amount or concentration of a protein or mRNA molecule for example). To investigate the dynamics of a transcription factor, one must first understand what the major means of regulation are (e.g. external environmental signals, gene targets, facilitating enzymes, competing factors). This biological information can help provide a visualisation of a system of interacting components containing cause-and-effect results typically involving chains of interactions (biochemical cascades) and feedback loops important for regulation as information is constantly being updated. This visualisation is often presented in the form of a schematic diagram using a loose convention of boxes and arrows where different arrowheads denote activation or repression and the arrows between boxes symbolise the relationship between system components (see Figure 1-1). This network can be thought of as a signalling pathway where the signal is usually represented by an external influencing factor that mediates the state of the internal system components.

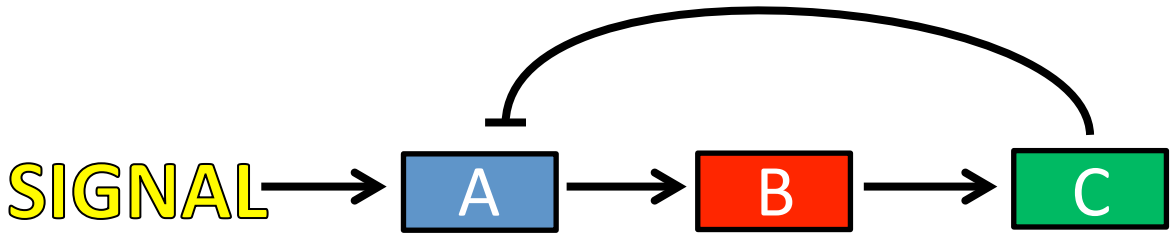

Figure 1-1: An example of a typical schematic diagram of a signalling pathway. Boxes *A*, *B* and *C* represent different system components in the pathway and orthodox arrowheads represent activation/upregulation and 'flat' arrowheads represent repression/downregulation. In this system the signal activates the expression of component *A* which in turn activates *B* which activates *C*. Component *C* represses component *A* forming a negative feedback loop.

Once a hypothetical understanding of the interaction between components of interest in a system has been determined, the form of these interactions must be studied. This is where mathematical modelling has become most important; to attempt to explain how system components interact to produce observed dynamics. Insights gained from good mathematical models can lead to a greater understanding of the signalling pathway of interest. This understanding can arise in the form of

parameter value estimates relating to chemical reaction rates, for example, that are unable to be measured experimentally. This understanding can also be enhanced by making predictions, effectively simulating experiments at a much faster rate and cheaper cost with the representative model. A greater intuition of the involved system gained from a good model can also provide insight into what gaps there are in the current understanding of the pathway, i.e. hypotheses of missing components or new properties of components can be made by analysing the mathematical model and these hypotheses can then hopefully be tested experimentally. This is a good representation of the circular nature of systems biology and the inherent collaboration involved of theoreticians and experimentalists in this field. Biological phenomena reported in experiments prompt the formulation of mathematical models and analysis, while the enhanced understanding and intuition provided by models can prompt the direction for new experiments in turn.

1.2 Research Motivation

Oxygen is essential for aerobically respiring cells, being used in the mitochondria for the generation of energy in the form of ATP (adenosine triphosphate). Consequently, cells require a constant supply of oxygen to ensure survival, first and foremost, and facilitate all other metabolic reactions. However, this requirement for oxygen has to be balanced against oxidative damage to components of the cell itself (lipids, nucleic acids, proteins) and as a result cellular oxygen concentrations must be tightly regulated (Semenza, HIF-1 and human disease: one highly involved factor 2000). Hypoxia represents a disturbance of this oxygen homeostasis, where there is an insufficient supply of oxygen to the cell, a key factor in a number of pathologies. Cells of all metazoan species have a highly conserved signalling pathway that attempts to address the oxygen debt and minimise hypoxic damage through the use of specific transcription factors. The signalling pathway that will be the focus of the research presented in this thesis is the pathway involved in the cellular response to oxygen stress.

1.2.1 The HIF-1α Signalling Pathway

HIF-1 (Hypoxia Inducible Factor-1) is the name given to the oxygen regulated transcription factor that controls the intracellular hypoxic response. HIF-1 was originally identified as a regulator of erythropoietin (EPO), a growth factor that stimulates the production of red blood cells (Smith, Robbins and Ratcliffe 2008). However, it is now known that HIF-1 is a conserved transcription factor in all animal species, regardless of specialised oxygen transfer systems, and functions as the master regulator of oxygen homeostasis (Semenza, Hydroxylation of HIF-1: oxygen sensing at the molecular level 2004). The activity of HIF-1 is crucial in facilitating the adaptation and survival of cells and HIF-1 is found ubiquitously in human tissues (Ke and Costa 2006). HIF-1 is a transcription factor that

targets a series of adaptation genes under hypoxic conditions for transactivation (an increase in gene expression). These genes induce the response to hypoxia in the cell through diverse functions such as angiogenesis, glycolysis, cell proliferation and iron metabolism and these responses are mediated by HIF-1 (Lee, et al. 2004). The activities of the HIF-1 transcription factor have been of considerable interest due to the role of HIF-1in mammalian development and in particular several pathologies such as ischemia and cancer, where oxygen pressure is reduced due to the rapid proliferation of tumour cells distant to blood vessels (hypoxic core) and the irregular vasculature which is unable to properly perfuse the tumour (Semenza, HIF-1 and human disease: one highly involved factor 2000).

The regulation of HIF-1 is determined by the activities of interacting components of the HIF-1α signalling pathway (see Figure 1-2). HIF-1 is a heterodimer, comprised of an oxygen regulated HIF-1α subunit and a constitutive (unregulated) HIF-1β subunit (also known as the aryl hydrocarbon receptor nuclear translocator, or ARNT). Dimerisation between the two subunits is necessary for DNA binding. To model the pathway, we are concerned with how oxygen regulates the levels of HIF-1α concentration. In the presence of sufficient oxygen, a state known as normoxia, prolyl hydroxylases (PHDs) catalyse the hydroxylation of HIF-1α. This reaction with PHD promotes the interaction of the von Hippel-Landau protein (pVHL) with the hydroxylated HIF-1α subunit. This binding acts as a targeting mechanism for an E3 ubiquitin ligase complex therefore promoting proteasomal degradation. PHDs need molecular oxygen to hydroxylate HIF-1α, and so HIF-1 can increase in number and transcriptional activity in hypoxia where nearly all available oxygen is used by the mitochondria. There is a feedback loop in this dynamical system as HIF-1 also induces the transcription of the inhibitor, and main cellular oxygen sensor, PHD (Metzen, et al. 2005, Semenza, HIF-1 and mechanisms of hypoxia sensing 2001, Schmierer, Novák and Schofield 2010, Epstein, et al. 2001).

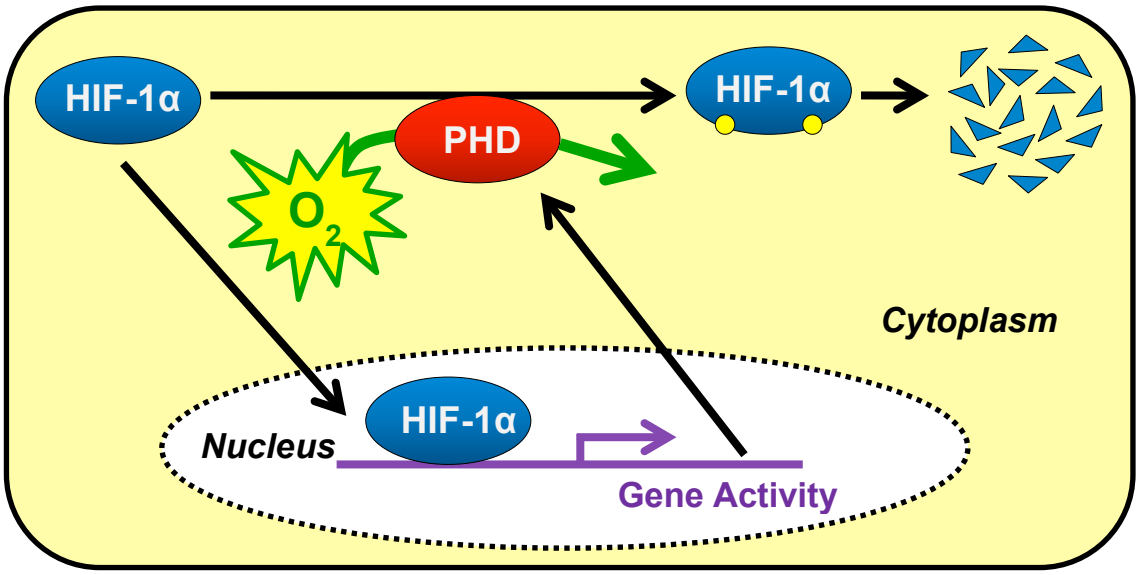

Figure 1-2: A diagrammatic representation of the negative feedback loop between HIF-1α and PHD. PHD uses molecular oxygen to hydroxylate HIF-1α causing it to be targeted for degradation. The rate of this chemical reaction depends upon oxygen availability (the signal in the pathway) and therefore directly affects the amount of HIF-1α in the system. The PHD gene is also one of many of the direct transcriptional target genes of HIF-1, completing a regulatory motif in the pathway.

Some mathematical modelling of the HIF-1α signalling pathway had already been carried out prior to the beginning of this project and many more models have been published since (Kohn, et al. 2004, Qutub and Popel 2006, Dayan, et al. 2009, Schmierer, Novák and Schofield 2010, Bruning, et al. 2011). However, all these models are based on the dynamics of HIF-1α at the population level or the steady state HIF-1 values at different oxygen concentrations. In contrast our proposed model of HIF-1α dynamics is based on the unique insight provided by single-cell dynamics and we are particularly interested in the transient temporal dynamics that result from negative feedback within the signalling pathway. Crucially these alternative models did not use experimental data for parameterisation such that they could be representative of single-cell dynamics. These models often incorporated more components of the HIF-1 signalling pathway, such as pVHL and FIH (Factor inhibiting HIF, another oxygen sensor that impairs the transcriptional activity of HIF-1 via the hydroxylation of HIF-1α), than we will concern ourselves with for simplicity. Biological data obtained at the Centre for Cell Imaging in Liverpool allows us to directly compare our models with single-cell activity (see Chapter 2 section 2.1 and (Bagnall, et al. 2013) for more details). NB: Any time an experiment or measurement is referred to as 'ours' in this thesis I am referring to experimental data obtained in the Liverpool laboratory of my secondary supervisor Dr Violaine Sée.

The Kohn model was based on a Molecular Interaction Map, a network diagram (similar in principal to the schematic diagram notation of Figure 1-1) representing HIF-1 regulation with 23 different molecular species and 32 rate constants. These parameter values were determined qualitatively to demonstrate switch-like behaviour of HIF-1 in different oxygen conditions and the affinity of HIF-1α

for PHDs rather than HIF-1β was deemed necessary for this. The Qutub & Popel model includes more complex environmental conditions by including ascorbate, iron, and 2-oxoglutarate in the kinetic equations (all factors which can modulate the hydroxylation rate of HIF-1α). This model is concerned with temporal dynamics but is limited to coarse, population-level experimental data for refinement. The Dayan model is an adaptation of the earlier Kohn model that focuses specifically on the transcriptional activity of HIF-1α, neglecting the HIF-1β component from Kohn. This activity modification is modelled by the distinction of two separate transactivation domains on HIF-1α that are hydroxylated by two oxygen sensors (PHD and FIH). Similar to the Kohn model, emphasis was placed on steady state values of this model to investigate HIF-1 mediated gene regulation under different grades of hypoxic stress. The Schmierer model also focuses on FIH regulation in the pathway and in particular the competition for FIH-binding between HIF-1α and ankyrin-repeat domain (ARD) proteins. This model neglects the HIF-PHD feedback mechanism. The Bruning model represents a simpler model, similar to our own, with few pathway components and also describes the feedback loop between HIF-1α and PHD. In addition to this, a secondary negative feedback loop is incorporated through the introduction of microRNA-155 and the explicit modelling of HIF-1α mRNA dynamics. This model simulates hypoxia by altering the hydroxylation rate of the generic PHD feedback. Unfortunately, this model is also limited in terms of experimental data for validation and subsequently satisfactory parameterisation. Model parameters were optimised by fitting model outputs to coarse, population-level data for each component simultaneously.

Mathematical models of signalling pathways are typically composed of differential equations and this is how we shall formulate our initial model of the HIF-1α signalling pathway in Chapter 2. These equations are useful for describing an approximation of the dynamics of the components of the system being studied, e.g. proteins involved in pathway interactions. For intracellular temporal protein dynamics, where there is assumed to be a relatively large amount of each protein and the spatial aspect of the pathway interactions are deemed insignificant, continuous ordinary differential equations (ODEs) can be used with the independent variable representing time. Reaction kinetics in biology are often modelled effectively using the 'Law of Mass Action' which states that the rate of a reaction is proportional to the product of the concentration of the reactants (Murray 2001). This law is often applied as an initial estimate to describe mathematically how two chemicals interact, especially when they are both in abundance. Using this law one can describe chemical reactions in the cell such as enzyme kinetics using differential equations involving reactants and rate constants. From here, classical mathematical methods of dynamical systems in continuous models can be applied to study the resulting properties of the system of differential equations. These include properties such as the equilibria and stability of the reactants/protein concentrations to deviations from steady states. However, we will be primarily concerned with the initial transient dynamics of our system after a change in parameter rather than just the long term protein dynamics. This perturbation will initially be

implemented by a parameter switch representing a change in the oxygen signal, but later we will consider a continuous function of oxygen to allow for more complex oxygen dynamics.

1.2.2 Tumoural Hypoxia

Hypoxia is a key feature in numerous pathologies, due to the critical role oxygen plays in the healthy function of living things. One of the most apparent pathologies hypoxia features heavily in, and one of the most widely studied, is cancer. More specifically, hypoxia is a prevalent theme in the growth stages of solid cancerous tumours. This is due to the rapid growth characteristic of mutated cancer cells causing an abnormal distribution of cells and nutrient-supplying blood vessels.

One of the most important nutrients that blood delivers to cells is oxygen, essential for the survival and proliferation of organic life. As cancer cells typically proliferate more rapidly than normal cells, a clump or tumour is soon formed that is unable to be adequately supplied by the surrounding vasculature. A hypoxic core is formed in the centre of the tumour due to the distance between the oxygen supply and this core of cells. This process is symptomatic of an early-stage tumour, otherwise known as an avascular tumour as the tumour has not yet induced the production of its own blood vessel network. Avascular tumours are studied experimentally by culturing cancer cells as three-dimensional multi-cellular spheres. These spheres share similar growth kinetics with avascular tumours. The avascular phase of the life cycle of a cancerous tumour covers the initial mutations of normal cells through to a diffusion-limited steady state where the tumour's growth is limited by a balance between nutrient consumption and nutrient supply via diffusion. This is what is seen in laboratories with multi-cellular spheres typically reaching a steady state sphere size of a few millimetres in diameter (Folkman and Hochberg 1973). The steady state is characterised by a three-layered system. The inner core of the sphere, where nutrient deprivation (e.g. hypoxia) is the most severe, becomes necrotic. The outer rim of the sphere, comprising a layer just a few cells thick, contains proliferative cells. In between these two extremes lies the quiescent region, an intermediate layer where cells are neither proliferative nor necrotic but can be recruited to either extreme (Chaplain 1996).

For a tumour to become malignant the second phase of the cancer life cycle must be entered known as the vascular phase of tumour growth. This phase results in the tumour no longer being constrained in its growth and achieving potential for tissue invasion and metastasis. A tumour enters the vascular growth stage by developing its own vascularisation through the activation of many processes governed initially by the transcription factor HIF-1. For example angiogenesis, the process of new blood vessel formation from pre-existing vasculature, is stimulated by the Vascular Endothelial Growth Factor (VEGF), a transcriptional gene target of HIF-1. The critical process of angiogenesis allows better perfusion of the solid tumour mass so that growth is no longer diffusion-limited by the

pre-existing network of blood vessels. Metastasis is the process whereby cancer cells invade the local tissue and are capable of spreading throughout the body via the bloodstream or lymph system and setting up secondary sites of tumour growth. This stage is the most critical when it comes to prognosis and usually dramatically reduces the patient's chances of survival.

Chapter 4 of the thesis introduces the multiscale modelling aspect of my research. This research direction is a natural progression from our work on the oxygen-based signalling pathway in single cells. The movement towards considering the effects of oxygen dynamics (and hypoxia in particular) in a multi-cellular environment was motivated by a desire to investigate the full extent of the influence of transient HIF-1α dynamics observed at the single-cell level. Further inspiration was provided by experimental data recording the emergence of hypoxic gradients in cellular spheres cultured in a range of hypoxic states. Key to the motivation of this research is trying to understand how hypoxia, and HIF-1α dynamics in particular, can affect the development of these multi-cellular spheres. In Chapter 4, we are interested in the short timescale HIF-1α dynamics and early stages of tumour development where the oxygen supply is limited by diffusion as the tumour grows. There have been many multiscale models developed to describe the dynamics of avascular tumour growth as cancer is inherently a multiscale problem. These scales vary from the macroscopic scale (cell migration, angiogenesis, diffusion of nutrients and chemicals) to the mesoscopic scale (cell-cell adhesion, inter-cellular communication via cytokines) to the microscopic scale (intracellular signalling pathways) (Martins, Ferreira Jr. and Vilela 2007). As a result there are also multiple timescales to be modelled. We are interested in dynamics at the macroscopic scale, specifically the diffusion and consumption of nutrients (oxygen), but only on the relatively short timescale of transcription factor dynamics and thus we do not attempt to model growth. We will then couple to the microscopic scale of intracellular HIF-1α dynamics.

1.2.3 Downstream Gene Targets

The central role of the HIF-1 transcription factor in the hypoxic response has implications in almost all cellular functions. Oxygen is a vitally important resource for life providing the key ingredient for efficient energy production via aerobic respiration. As such, the smooth running of all life processes within cells can be thought of as being fuelled by an optimal range of oxygen supply. We refer to this range as normoxia and it is desirable to maintain this oxygen homeostasis for the ultimate goals of the cell: survival and proliferation. It follows that disturbance of this homeostasis requires a swift response to maintain the cell's viability. This response is primarily mediated by HIF-1 which transcriptionally induces a series of genes for adaptation. More than 100 target genes have been identified that are transcriptionally regulated by HIF-1 and these genes are associated with a wide variety of functions (see Figure 1-3). These functions are primarily concerned with adaptation to the

new hypoxic environment in the short term (increased glycolysis, cell-cycle arrest) and addressing the oxygen deficit in the long-term (angiogenesis, erythropoiesis). The overexpression of HIF-1 has been found in various cancers and is a key factor in the development of avascular tumours due to the hypoxic state of these tissues. Some of these target gene functions are of particular relevance in tumour progression such as tumour angiogenesis, tumour anaerobic energy metabolism and metastasis. The diverse role of HIF-1 in many different cellular functions (Figure 1-3) emphasises the value in understanding the dynamic activity of this transcription factor and its downstream consequences.

The dynamics of transcription factors are particularly important with regards to downstream gene expression whether through delayed feedback, oscillations or localisation. How the temporal profile of transcription factor concentration varies can propagate from an initial simple signal to enhance complexity in the control of the response (Nelson, et al. 2004). This aspect of our research is a present focus throughout the thesis generally, but Chapter 5 focuses on some specific downstream responses. There are many examples of models that highlight the important role of temporal transcription factor dynamics in gene expression such as the NF-κB signalling pathway (Ashall, et al. 2009) and the p53 system (Geva-Zatorsky, et al. 2006). These models of network dynamics and feedback loops can provide inspiration for the regulatory motifs to be found in other signalling pathways such as that of HIF-1α. Although biological systems are extremely complex, with each biochemical reaction having evolved over time amongst thousands of other reactions in complex networks, cellular functions are mostly robust and there are general simplifying design principles and motifs to be found (Alon 2006). Introducing downstream gene targets and functions to a model of the HIF-1α transcription factor network provides a method of probing model applications and integrating the complexities of hypoxic cell signalling.

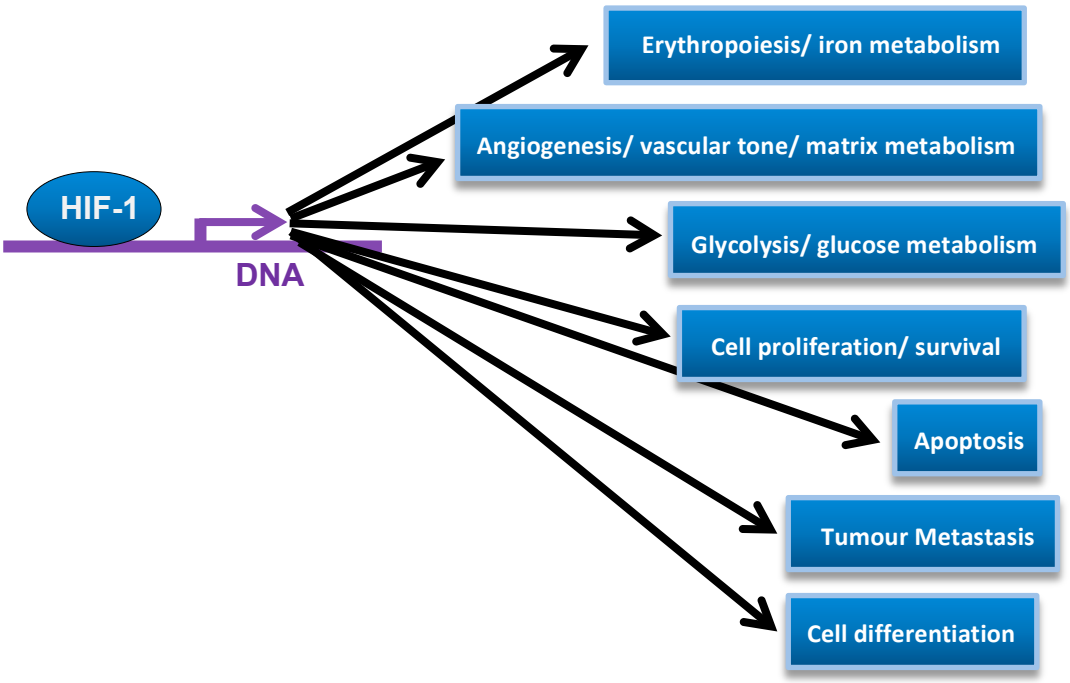

Figure 1-3: HIF-1 is the critical transcription factor involved in cellular sensing and adapting to changes in oxygen levels. These adaptations come in the form of a variety of functions that are regulated as a result of the altered transcription rate of HIF-1 target genes. The cellular functions represented here are based on the review articles of Ke & Costa (Hypoxia-inducible factor-1 (HIF-1) 2006) and Liu, et al. (Targeted genes and interacting proteins of hypoxia inducible factor-1 2012).

1.3 Thesis Outline

In Chapter 2 of the thesis there is a full description of how we combined existing biological knowledge of the HIF-1α signalling pathway with obtained experimental data and mathematical tools to develop a completely new model. There is a basic explanation of the experiments conducted that motivated the project and the novelty and importance of the data is highlighted. Following this, there is a summary of the early processes of model development where several alternative minimalistic models are compared. The rest of the chapter is focused on how the earliest, simple model is refined by parameter optimisation and data fitting in order to find a reliable feedback structure to proceed with.

Chapter 3 continues with further development of the model formulated in Chapter 2, as an initial 2-component ODE model representing the negative feedback loop between HIF-1α and PHD is expanded to a 4-component model to include three different isoforms of PHD (PHD1, PHD2 and PHD3). In Chapter 2 they are combined to form a generic PHD feedback. This Chapter 3 expansion allows for the inclusion of more experimental measurements and system perturbations during model simulations which can be validated by experiments. The chapter includes a detailed account of the

parameterisation of the expanded 4-component model including information on parameter values found using our own experiments, literature results and our own optimisation methods. Finally the model is compared with experiments and also used to make predictions for potentially difficult experiments involving varying the temporal dynamics of oxygen.

In summary, Chapters 2 and 3 cover the development of a mathematical model of the HIF-1α signalling pathway using a system of ODEs, experimental measurements and fitted parameters. This model is based on a network motif that can capture the heterogeneous, transient single-cell dynamics by describing the feedback loop between HIF-1α and PHD. The model agrees with experiments that perturb the signalling pathway.

Chapter 4 describes the development of a simple model of tumoural oxygen dynamics. The model includes the effects of oxygen consumption and separate oxygen diffusion rates inside and outside a model tumour. Experimental data is used to refine this model before it is coupled to the HIF-1α signalling pathway model developed in Chapters 2&3. Rapid oxygen switches at tumour-sphere boundaries lead to biologically interesting results with respect to the spatial variation of single-cell HIF-1α dynamics. Further applications and predictions of the coupled model are investigated by analysing PHD dynamics, varying external oxygen conditions and varying tumour size.

Chapter 5 is an investigation into further applications of the HIF-1α signalling pathway model. This chapter attempts to clarify the downstream significance of the type of HIF-1α dynamics found experimentally in single cells and throughout respiring spheres after rapid oxygen switches. This investigation is carried out by identifying cellular functions that are affected by hypoxia in some way, and determining the role of HIF-1α. Once this has been identified we couple our model to existing published models of the cellular function of interest and study the effects of the characteristic transient HIF-1α dynamics. The two cellular processes that are specifically focused on in this chapter are the cell cycle and apoptosis pathways, both of which are sensitive to hypoxic conditions.

Finally, Chapter 6 is in the form of a discussion and summary of results from our studies.

Chapter 2

Modelling the Dynamics of the HIF-1α Signalling Pathway: Model Formulation and Development

2.1 Biological Motivation

Mathematical modelling of the hypoxia-inducible factor-1 (HIF-1) signalling pathway previous to the beginning of my research was limited by the dynamic experimental data available. Experimental results in the field of HIF-1 signalling have shown temporal dynamics of HIF-1 when exposed to hypoxia in the form of bulk cell analyses such as the western blot assay (Bruning, et al. 2011, Stiehl, et al. 2006). Data arising from this type of experiment highlights the transient nature of HIF-1 dynamics when hypoxia is introduced into the signalling pathway but it can only represent the cell-population level and has a very low time resolution. Other examples of quantitative HIF-1 data found in the relevant literature include the measurements of total HIF-1 protein found in a range of oxygen environments (Jiang, et al. 1996, Dayan, et al. 2009). Again this represents population data and also refers only to the steady states at each oxygen tension.

The modelling in this thesis was largely motivated by the novelty of the imaging data recorded by Dr Violaine Sée's laboratory at the Centre for Cell Imaging in the Institute of Integrative Biology, University of Liverpool. The imaging data was able to capture the transient dynamics of the oxygen-regulated subunit of HIF-1, HIF-1α, in single cells after hypoxic induction. This data was recorded using live-cell time-lapse confocal microscopy providing quantitative, high temporal resolution data of fluorescently tagged HIF-1α (see Figure 2-1). The full details of these experiments including measurements and protocols have been written up in the form of a paper, "*Tight control of Hypoxia Inducible Factor (HIF)-alpha transient dynamics is essential for cell survival in hypoxia* ", submitted for publication in 2013 (Bagnall, et al. 2013).

In order to use time-lapse images as a measure of HIF-1α dynamics, a HIF-1α fluorescent fusion reporter was expressed in cultured mammalian cells. Using this reporter, the cells would fluoresce whenever HIF-1α was present and become dim whenever HIF-1α was absent providing a visual means of dynamic measurement. In order to make comparisons with the mathematical model, we assume that the fluorescent intensity is directly proportional to the amount of HIF-1α. In this way a dynamic illustration of the hypoxic accumulation of HIF-1α could be observed by measuring the relative brightness of the cells with more fluorescence signal corresponding to more HIF-1α.

Cells were visualised for fluorescence after transiently introducing a plasmid expression vector coding for HIF-1α genetically fused to EGFP (enhanced green fluorescent protein). EGFP is a protein originally derived from a naturally occurring protein in jellyfish that displays bright green fluorescence following excitation with ultra violet light. The transfection plasmid contains a HIF-1α gene fused with an EGFP gene providing a region of DNA that, when transcribed, produces both HIF-1α and EGFP as a single protein. This fusion or tagging of EGFP to HIF-1α is achieved by splicing the gene encoding for EGFP into the region of DNA that codes for HIF-1α so that the same regulatory

sequence controls transcription of both genes. The presence of green fluorescence in the transfected cells indicates the expression of the HIF-1α-EGFP fusion protein providing a visual representation for HIF-1α dynamics that can be measured in arbitrary units of fluorescence (AU). These units are arbitrary due to the individual optimisation of the images using the confocal microscope leading to separate experiments not being directly comparable. Furthermore an inevitable consequence of transient transfection is that different cells will contain different amounts of plasmid leading to different expression levels and therefore data from different cells are not directly comparable. More details of dealing with the use of arbitrary fluorescence units, including some scaling analysis, can be found in section 2.3.4 particularly subsection 2.3.4.1. Generally, transient transfection results in overexpression of the gene of interest and so an exaggerated representation of the dynamics may be recorded by experiments. This must be kept in mind when making comparisons with *in vivo* dynamics. The cells used in these experiments were HeLa cells. The HeLa cell line is an immortal cell line originally derived from cervical cancer cells, widely used in confocal microscopy due to its useful properties such as ease of transfection and low migration.

Images of the transfected cells were recorded using time-lapse confocal microscopy on a microscope equipped with an incubator that can control oxygen levels, carbon dioxide levels and temperature. Images were recorded at 5 minute intervals for 1 hour in normoxia (20% O_2) before the cells were subjected to a switch to hypoxia (1% O_2) for 20 hours. The kinetics of the transient accumulation of HIF-1α varied across the population of cells (see Figure 2-1).

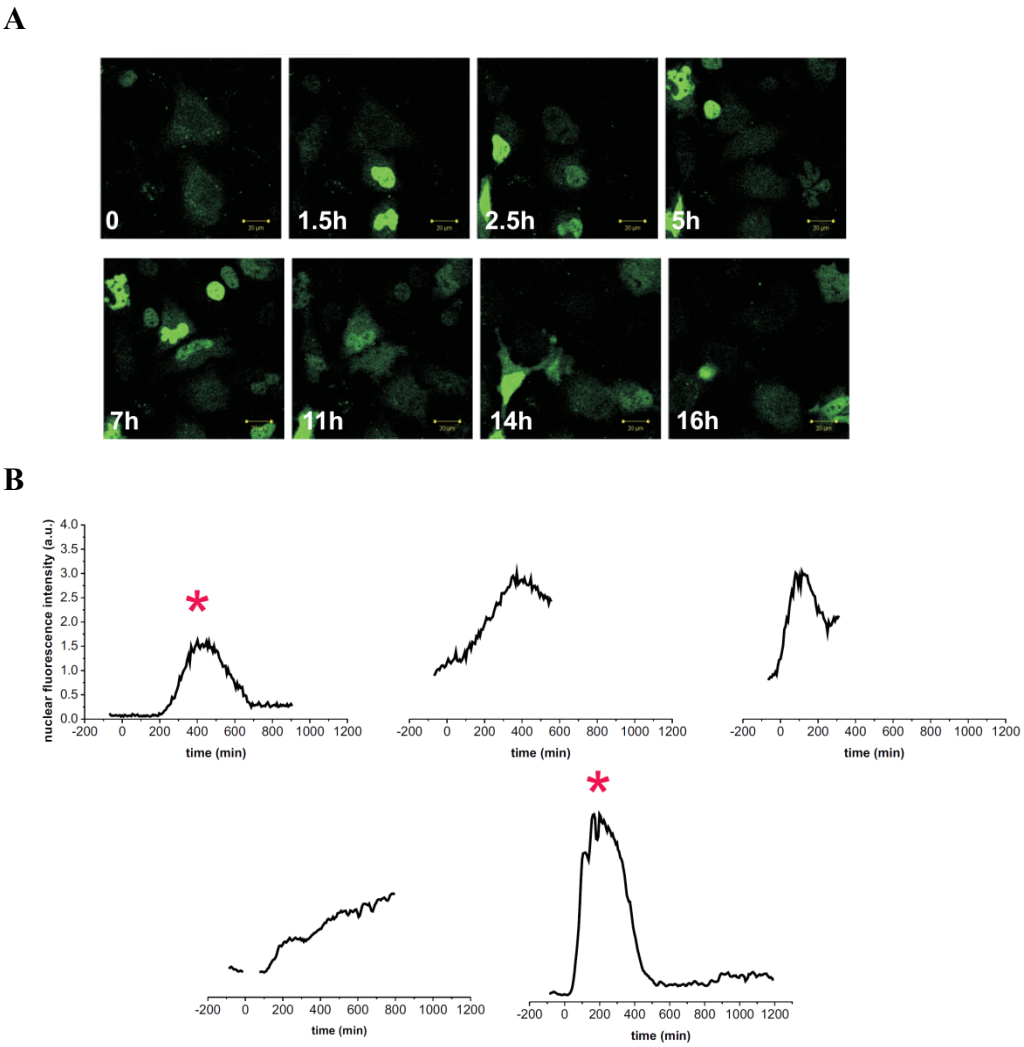

Figure 2-1: (A): Selected representative images of HeLa cells transiently transfected with HIF-1α-EGFP. Cells were imaged using time-lapse confocal microscopy every 5 minutes in 20% O_2 for 1 hour and then switched to 1% O_2 for 20 hours. (B): Fluorescence levels for HIF-1α are plotted against time for 5 representative cells. Some traces are shorter than the entire time course due to either cell death or migration out of the imaging field. Bell-shape curves were scored by eye and are labelled with a red star. This data was originally provided by Dr Sée's lab (Bagnall, et al. 2013).

A weakness of the transient transfection method is that in the majority of cases the DNA introduced into the cell is not properly integrated into the original nuclear genome. Consequently, the desired transfected genetic material is only transiently expressed as the foreign DNA is not replicated properly during mitosis (cell division). In order for transfection to have the desired effect for multiple cell divisions, a stable transfection is required. This method of stable transfection is achieved by using selective pressure on a population of transfected cells ensuring that only cells that have integrated the foreign DNA into their genome will survive and proliferate. This method is more difficult to implement as a large population of transfected cells is required due to the small probability of cells successfully incorporating the imported genetic material into their DNA. Also, a marker gene must be co-transfected into the cells in order to establish a selectable advantage in the minority of the

population's daughter cells that inherit the transfected material. This advantage would be a form of resistance to the said selective pressure to be applied.

As we are only concerned with the short-term hypoxic response of HIF-1α dynamics in individual cells, transient transfection should be a sufficient means of measurement. However, the results of Sée's imaging experiments revealed a considerable degree of heterogeneity with respect to the time-of-activation. 'Time-of-activation' here being a loose term used to denote a visually significant degree of change from the normoxic equilibrium levels of HIF-1α-EGFP fluorescence when compared with the underlying noise. In 50% of dividing cells, there was no discernible HIF-1α-EGFP activity in hypoxia until the cell had divided, upon which the daughter cells exhibited the transient accumulation dynamics believed to be characteristic of the HIF-1α signalling pathway (see Figure 2-2). This feature could be attributed to the method of transient transfection if the transfection occurred at a certain point in the cell cycle, i.e. at the time of nuclear breakdown and cell division (Pellegrin, et al. 2002). By calibrating the time of mitosis in these circumstances to $t = 0$ it was possible to artificially synchronise the heterogeneous data with the cell cycle. These synchronised data would be later used during the mathematical modelling process (see Figure 2-6).

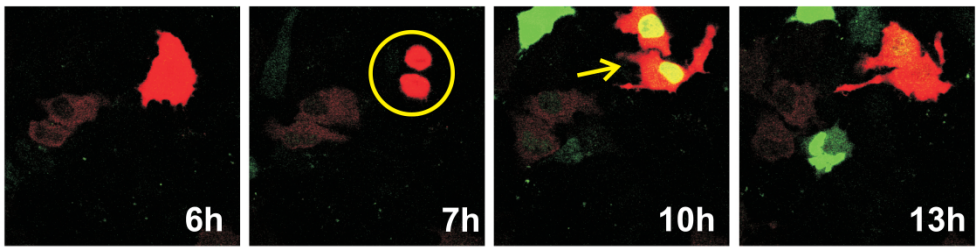

Figure 2-2: HeLa cells were transiently co-transfected with HIF-1α-EGFP (green) and a control plasmid (red) and subjected to a hypoxic switch to measure HIF-1α dynamics by time-lapse confocal microscopy. This figure shows HIF-1α nuclear accumulation (arrow, panel 3 – 10h) occurring after cell division (circle, panel 2 – 7h). This was observed in 50% of the responding cells. This data was originally provided by Dr Sée's lab (Bagnall, et al. 2013).

The transient nature of HIF-1α dynamics, as well as the relatively homogenous time-of-activation, was further validated in a HeLa cell line stably expressing the oxygen degradation domain (ODD) of HIF-1α fused to EGFP (termed ODD-EGFP). The oxygen degradation domain (ODD) is a region of the HIF-1α protein that controls the hydroxylation mediated degradation of HIF-1α via the ubiquitin-proteasome pathway. This time the cells displayed synchronised, transient ODD dynamics, yet the degradation was slower than for HIF-1α-EGFP. The explanation for this comes from the ODD being only a portion of the full-length HIF-1α protein and therefore not sharing all its properties. ODD-EGFP is suppressed in normoxia in the same manner as HIF-1α, by HIF-1 targets that form a negative feedback loop via hydroxylation mediated degradation (see Chapter 1 section 1.2.1), and therefore accumulates when oxygen is removed. However, it cannot bind with the constitutive subunit of HIF-1, HIF-1β, to form HIF-1 and transcriptionally activate HIF-1 target genes. The slower rate of

degradation observed is due to a saturation of the system whereby the amount of ODDs that can be hydroxylated is increased (ODD-EGFP plus endogenous HIF-1α) but the amount of feedback proteins that use oxygen to mediate HIF-1α (and ODD-EGFP) degradation remains dependent on HIF-1 only.

We also characterised the transient dynamics of HIF-1 activity. The HIF-1-dependent transcriptional activity in live cells was assessed by imaging the light produced by a Hypoxia Response Element luciferase reporter gene (see Figure 2-3). The Hypoxia Response Element (HRE) is present in the promoter region of genes that are transcriptional targets of HIF-1 and luciferase is a commonly used light emitting reporter of transcriptional activity. C51 cells (from the murine colon cancer cell line, C51) stably expressing a HRE-luciferase and HeLa cells transiently transfected with HRE-luciferase were examined. In both conditions, a transient luciferase signal was found indicating transient transcriptional activity. These transient transcription dynamics correspond with what is happening in the pathway at the HIF-1α protein level and imply that the expression of HIF-1 gene targets is directly linked to the amount of HIF-1 in the system.

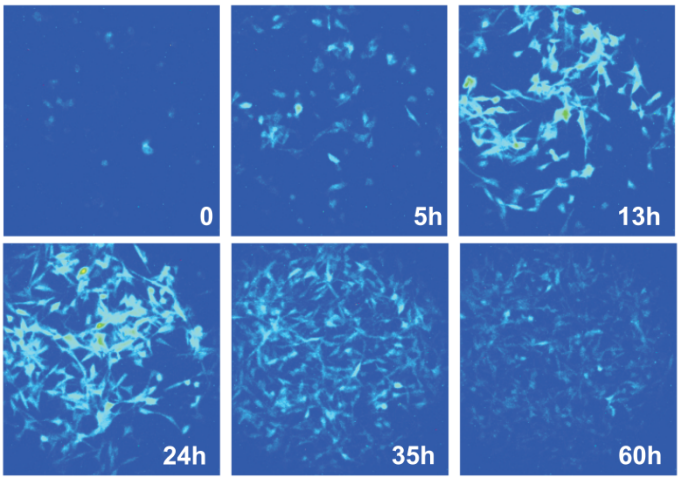

Figure 2-3: Luminescence images of C51 cells stably transfected with HRE-luciferase in 1% O_2. This data was originally provided by Dr Sée's lab (Bagnall, et al. 2013).

The dynamic response of the HIF-1α protein to re-oxygenation was also measured via the same methods; only the cells were incubated in hypoxia before a normoxic switch was introduced. The advantage of recording information on single-cell protein dynamics is that it allows one to study any heterogeneities that might exist within a cell population. Such cell-to-cell variation may be lost in the population-level dynamics as asynchronous events are effectively averaged out. This heterogeneity on the single-cell scale is not entirely unexpected as out-of-phase biological oscillations at this level can represent an enhanced stability for tissue level responses to system perturbations (Paszek, et al. 2010). The information provided by these experiments elucidated the transient response of HIF-1α to oxygen variation and the heterogeneous response of individual cells. It was these dynamics that motivated the formation of a new mathematical model based on a negative feedback motif that exists in the HIF-1α signalling pathway.

2.2 Mathematical Modelling

2.2.1 Initial Model

Our modelling of the HIF-1 signalling pathway was based on the negative feedback loop that exists between the oxygen regulated sub-unit of HIF-1, HIF-1α, and the pathway's main oxygen sensors, prolyl-hydroxylases 1-3 (PHDs). This was based on existing biological knowledge outlined in Chapter 1 and the dynamics observed in our experimental data.

Firstly, we tried to describe mathematically the feedback interaction between HIF-1α and a generic PHD in its simplest form to produce the hypoxic response observed in the data. We have the following 2-component negative feedback system used to model the interaction between HIF-1α and PHD. HIF-1α (x) induces the transcription of PHD (y) at rate k. PHD uses molecular oxygen to hydroxylate HIF-1α at rate h resulting in HIF-1α degradation. Both proteins have basal synthesis (S_i) and degradation (d_i) rates. This relationship can be described by the following coupled system of ordinary differential equations (ODEs):

$$\begin{aligned} \frac{dx}{dt} &= S_x - hxy - d_x x \\ \frac{dy}{dt} &= S_y + kx - d_y y \end{aligned} \tag{2.1}$$

An increase in HIF-1α (x) causes an increase in PHD (y) represented by the kx term. Negative feedback occurs as an increase in PHD decreases the level of HIF-1α because PHD hydroxylates HIF-1α leading to the degradation of HIF-1α represented by the hxy term. The sensitivity to oxygen in this model can be represented through the parameter h, the rate at which PHD hydroxylates HIF-1α. A change in the value of h will represent a change in oxygen concentration; e.g. from normoxic to hypoxic conditions. Such a switch will be expected to produce the transient dynamics observed experimentally. Specifically, the parameter h can be considered to be an increasing function of oxygen concentration. In normoxia, where there is greater oxygen availability, h will have a relatively higher value as more hydroxylation occurs. In hypoxia there is less oxygen available so h should take a lower value. An increase in HIF-1α (x) occurs as a result of reduced hydroxylation. Consequently more PHD (y) is produced. The increase in PHD can compensate for the reduction in oxygen availability to regulate HIF-1α (Henze, et al. 2010). All variables and parameters are positive by definition.

We will analyse this system further to investigate its characteristics and, therefore its usefulness as a model. By using dimensional analysis, we can reduce the number of parameters in the system needed for any further dynamical investigation (e.g. stability analysis).

Here we choose to non-dimensionalise time (t) and protein amounts (x, y) based upon the degradation rate of PHD (d_y) and basal production rates (S_x, S_y) such that the production rates are unity.

Let

$$t^* = d_y t, \qquad x^* = \frac{d_y}{S_x} x, \qquad y^* = \frac{d_y}{S_y} y,$$

and define the following non-dimensional quantities

$$h^* = \frac{S_y}{d_y^2} h, \qquad d_x^* = \frac{1}{d_y} d_x, \qquad k^* = \frac{S_x}{S_y d_y} k.$$

The equations of system (2.1) can now be written in non-dimensional form (dropping the $*$ for notational simplicity):

$$\begin{aligned} \frac{dx}{dt} &= 1 - hxy - d_x x \\ \frac{dy}{dt} &= 1 + kx - y \end{aligned} \tag{2.2}$$

This system has the same characteristic behaviour and properties as system (2.1) but is easier to analyse due to the reduced number of parameters. We perform a standard linear stability analysis (see for example (Britton 2003)) to determine the local stability of any system equilibria.

Equilibrium occurs at the steady state (x^{EQ}, y^{EQ}) when there are no changes in the quantities of either protein with respect to time. By setting the right hand sides of the equations in system (2.2) to zero, we obtain the unique (by feasibility) equilibrium equations

$$\begin{aligned} x^{EQ} &= \frac{-(h + d_x) + \sqrt{(h + d_x)^2 + 4hk}}{2hk} \\ y^{EQ} &= 1 + kx^{EQ}. \end{aligned}$$

To determine the local stability of the unique equilibrium point, we calculate the Jacobian matrix at equilibrium:

$$\mathbf{J} = \begin{pmatrix} -hy^{EQ} - d_x & -hx^{EQ} \\ k & -1 \end{pmatrix}.$$

From this matrix we can compute the eigenvalues

$$\lambda_{1,2} = \frac{-(A+1) \pm \sqrt{(A+1)^2 - 4(A + hx^{EQ}k)}}{2}.$$

where we let $A = h(1 + kx^{EQ}) + d_x$.

It is useful to visualise the local stability of a steady state by phase portrait. This representation shows how the values of the system quantities change near to equilibria. Sample trajectories on a vector field represent the time evolution of the system variables and trajectories move towards stable equilibria and away from unstable equilibria. To determine the stability of the steady state and how phase trajectories move in the plane will depend on the nature of the eigenvalues. If the real parts of the eigenvalues are negative then the equilibrium point is a stable steady state and if the real parts are positive the equilibrium is unstable.

All parameters in system (2.2) are positive; the equilibrium values are positive; and so is A. Thus $4(A + hx^{EQ}k)$ is positive and so

$$(A+1) > \mathrm{Re}\left(\sqrt{(A+1)^2 - 4(A + hx^{EQ}k)}\right).$$

This means that the eigenvalues will have negative real parts, and therefore the unique equilibrium point is stable.

To decide how the trajectories move in the phase portrait we will need to know whether the eigenvalues are real or complex. When the eigenvalues are complex the trajectories move towards or away from the equilibrium point in a spiral motion. Real eigenvalues correspond to the equilibrium being what is known as a node (stable or unstable dependent on sign) where trajectories move towards/away from the point without oscillating about the equilibrium (see Figure 2-4).

We can simplify the eigenvalues further:

$$\lambda_{1,2} = \frac{-(A+1) \pm \sqrt{(A-1)^2 - 4hx^{EQ}k}}{2}$$

The eigenvalues are real if $(A-1)^2 - 4hx^{EQ}k > 0$.

Since

$$(A-1)^2 = h^2(y^{EQ})^2 + 2hy^{EQ}(d_x - 1) + (d_x - 1)^2,$$

and

$$4hx^{EQ}k = 4hy^{EQ} - 4h,$$

we can write our inequality condition as

$$h^2(y^{EQ})^2 + 2hy^{EQ}(d_x - 3) + (d_x - 1)^2 + 4h > 0. \tag{2.3}$$

We can see from equation (2.3) that some parameter values would guarantee real eigenvalues. Setting $d_x > 3$ for example, would ensure that the left hand side of equation (2.3) is positive, the criteria required for real eigenvalues and thus a stable node steady state.

The converse condition for complex eigenvalues, where we want the left hand side of equation (2.3) to be negative, is not as easy to see. However, if we set $h \ll 1$ and $d_x \ll 1$ such that higher order powers are deemed negligible ($h^2, d_x^2, hd_x \approx 0$), we can re-write (2.3) as

$$\begin{aligned} &2h(2 - 3y^{EQ}) - 2d_x + 1 < 0, \\ &\Rightarrow 1 - 2(h + 3hkx^{EQ} + d_x) < 0, \\ &\qquad\qquad \Rightarrow \frac{1}{2} < h + 3hkx^{EQ} + d_x, \end{aligned}$$

where we have changed the sign of the inequality to highlight that our condition is now for complex eigenvalues. Recall that

$$x^{EQ} = \frac{-(h + d_x) + \sqrt{(h + d_x)^2 + 4hk}}{2hk},$$

and so for small values of h and d_x we have

$$x^{EQ} \approx \frac{-(h + d_x) + 2\sqrt{hk}}{2hk},$$

and our inequality becomes

$$\frac{1}{2}(1 + h + d_x) < 3\sqrt{hk}$$

A large enough value of k (e.g. $k = 1/h$) would be sufficient to satisfy this inequality given the relatively small values of h and d_x assumed. This inequality defines complex eigenvalues with negative real part and thus a stable spiral steady state.

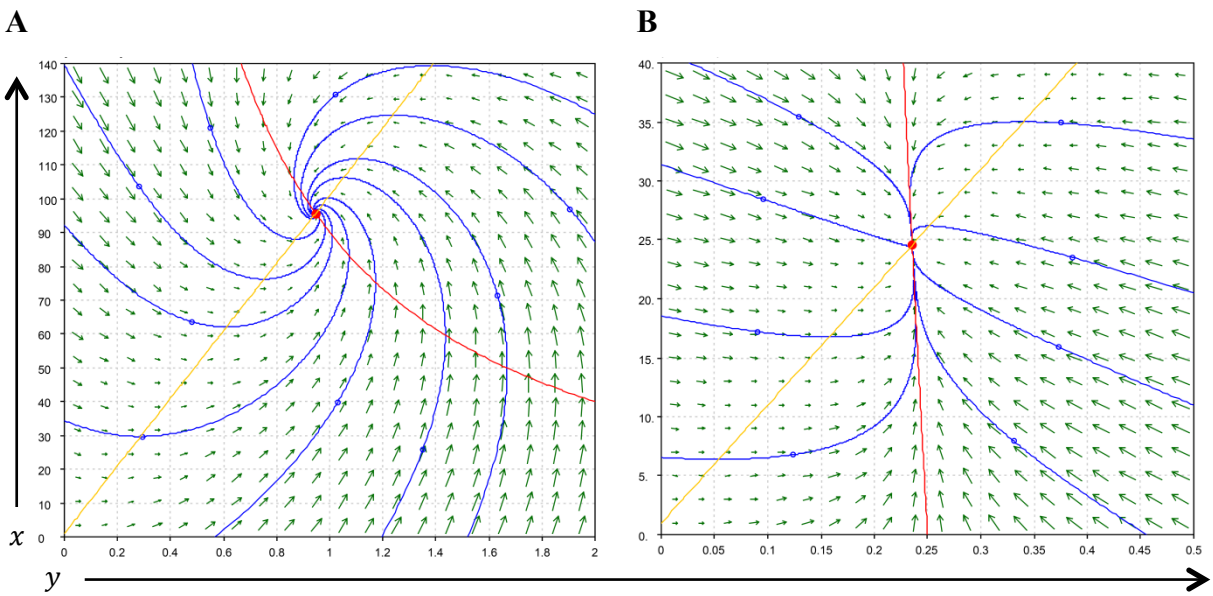

Figure 2-4: Phase portraits of system (2.2) with sample trajectories: A stable spiral steady state with $h = 0.01$, $k = 100$, $d_x = 0.1$ (A) and a stable node steady state with $h = 0.01$, $k = 100$, $d_x = 4$ (B). The red dots are the unique equilibrium points; the red and orange lines are the x and y nullclines respectively; and the blue curves are some sample trajectories. Green arrows indicate the direction of the vector field. The stable spiral (A) has eigenvalues $-1.0283 \pm 0.97248i$. The stable node (B) has eigenvalues -1.0743 and -4.1713. Phase portraits were produced using the Java version of MATLAB program *pplane* developed by John C. Polking (dfield and pplane 2002).

The phase portraits in Figure 2-4 show the two nullclines of system (2.2) and where they intersect at the unique, stable equilibrium. We have the x-nullcline, $y = (1 - d_x x)/hx$, and the y-nullcline, $y = 1 + kx$. Since we only have one parameter in our model that is sensitive to oxygen and therefore represents our oxygen state, h, only the x-nullcline is affected by oxygen status. In Figure 2-5 we can see what happens as we simulate oxygen reduction in the form of a hypoxic switch, reducing the hydroxylation rate h. This has the effect of shifting the x-nullcline hyperbola in the positive x direction while the linear y-nullcline remains the same. Consequently a new hypoxic equilibrium is found with an increase in both x and y.

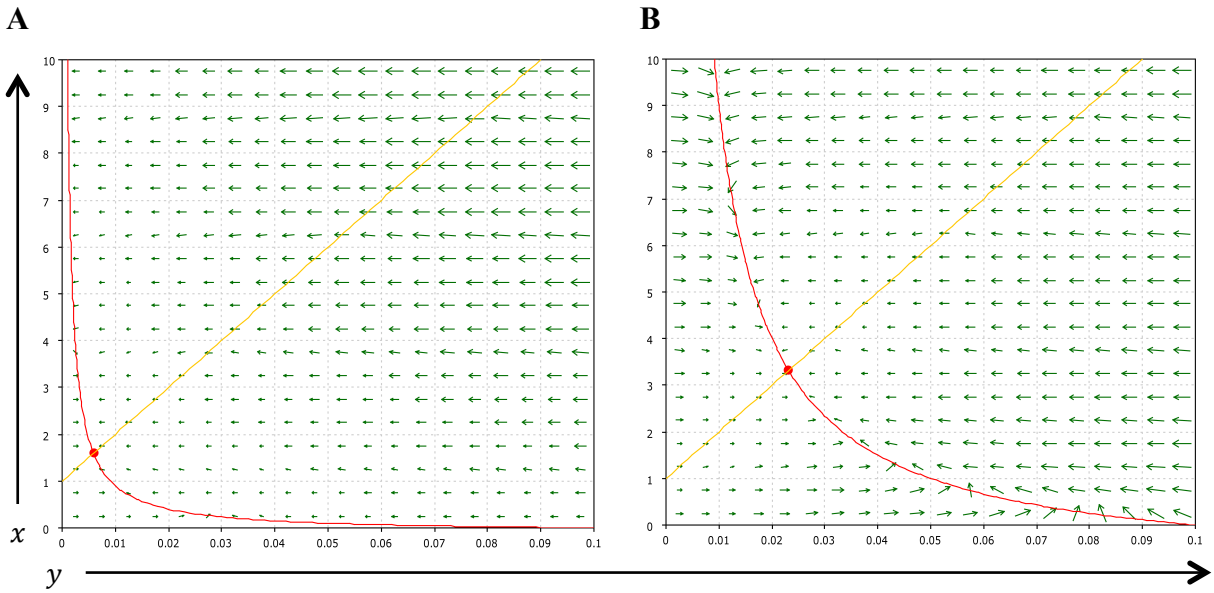

Figure 2-5: Phase portraits of system (2.2) for different values of parameter h representing normoxia (A) and hypoxia (B). Parameters: (A) $h = 100, d = 10, k = 100$; (B) $h = 10, d = 10, k = 100$. Colour coding as in Figure 2-4. Phase portraits were produced using the Java version of MATLAB program *pplane* developed by John C. Polking (dfield and pplane 2002).

2.2.1.1 Preliminary Simulations

Following stability analysis of our initial HIF-1α ODE model we begin to compare some experimental data of HIF-1α dynamics in hypoxia (see Figure 2-6) with some example solutions of system (2.2) after a hypoxic switch. This will give us a better, though not conclusive, idea of the type of qualitative solutions our model can produce providing us with some intuition about the suitability of our model in its current form, (2.1).

Figure 2-6 is representative of some of the more complex single-cell HIF-1α dynamics following a rapid switch to hypoxia. The accumulation of HIF-1α is transient with a very large peak relative to the HIF-1α levels prior to stimulation and HIF-1α levels after a long exposure to hypoxia. In order to generate some qualitative sample plots from our model, we solved the ODE system (2.2) for a range of parameters. To compare with experimental data we set values for parameters which are fixed for each cell for the duration of the experiment (k and d_x) and two values for the hydroxylation rate (h_N in normoxia, and h_H in hypoxia). Prior to stimulation (when $h = h_N$) we prescribed the values for HIF-1α (x) and PHD (y) to be at the unique stable equilibrium of the model. These values represent the normoxic equilibrium (x_N^{EQ}, y_N^{EQ}).

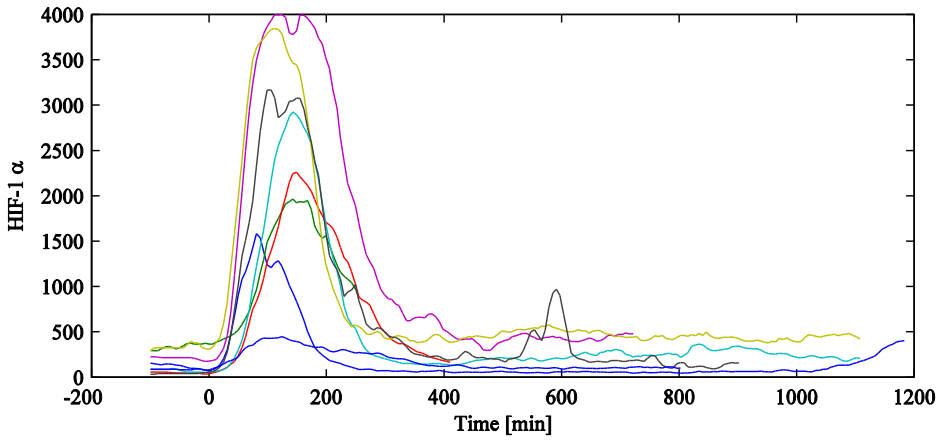

Figure 2-6: Single-cell data showing the transient peaks in levels of HIF-1α after stimulation (drop in oxygen levels). The initiation of hypoxic stimulation is represented here at 0 minutes. Each profile represents HIF-1α dynamics from a different cell.

A sample of plots for the solutions of system (2.2) with various parameter values can be seen in Figure 2-7. In the plots, negative values of time denote normoxia and $t = 0$ is the time of the hypoxic switch where h is reduced from h_N to h_H. Our only conditions were that all parameters should be positive, that $h_N > h_H$, and that our initial values for x and y corresponded to the unique equilibrium of system (2.2). In Figure 2-7 we have presented the results of a range of simulations that were performed using different combinations of high and low values for non-dimensional parameters k and d_x and different severities of hypoxic switching (either a 2-fold reduction in h or a 10-fold reduction in h).

The aim of generating plots such as those in Figure 2-7 was to provide motivation for the direction of further model development. Based on our preliminary analysis, it proved difficult to simulate a sharp accumulation in HIF-1α with the current model without a significant change in equilibrium levels before and after stimulation. There also seems to be an asymmetry in these model output peaks with a much sharper increase in HIF-1α compared to the subsequent slower decrease. These features contradict the observed data where we often see fairly symmetrical peaks or bell-shaped dynamics with relatively similar equilibrium levels before and after the reduction in oxygen. It is these complex dynamics that we need to be able to capture with our mathematical model and so we consider modifications of system (2.1) for this purpose.

A

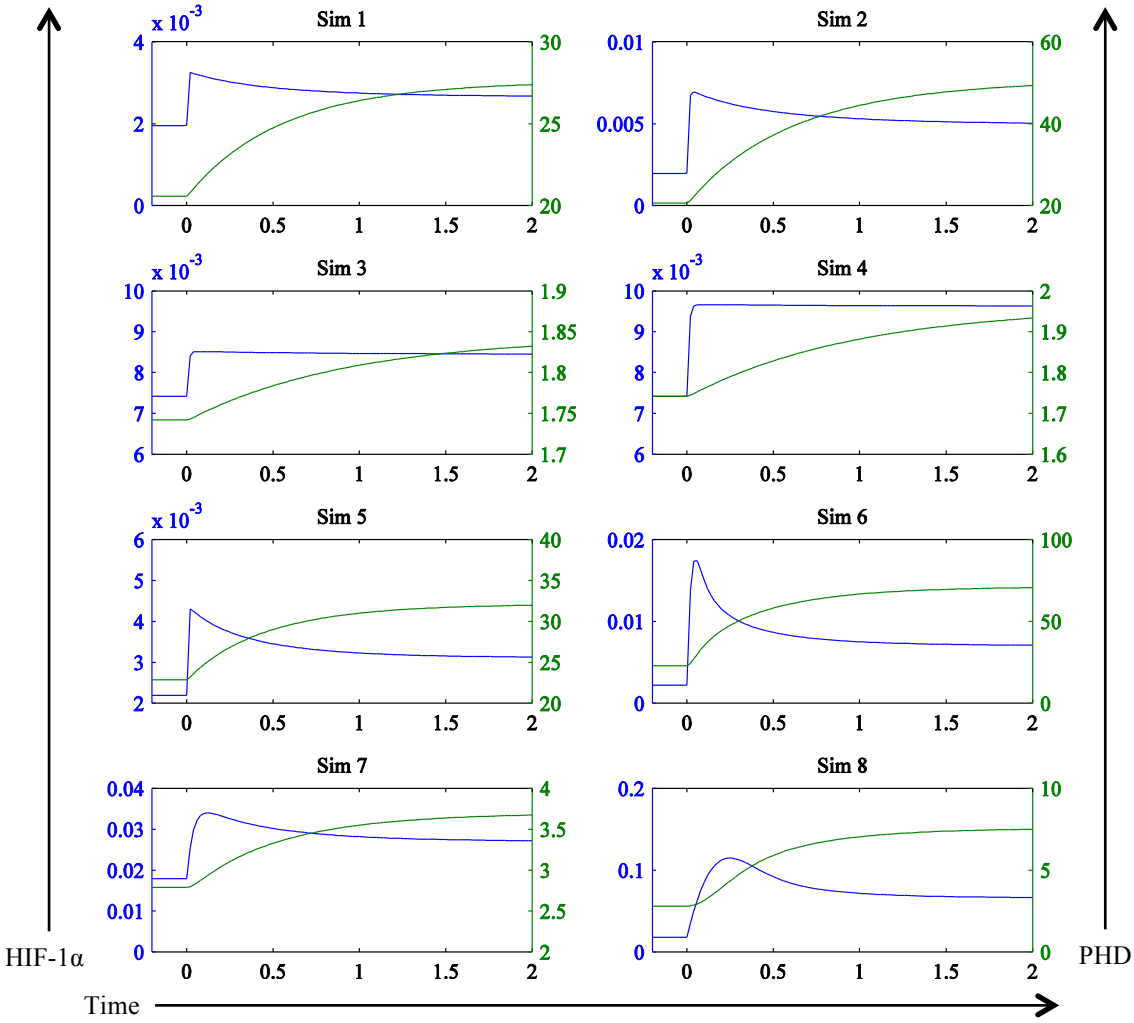

B

Figure 2-7A KEY	Mild switch ($h_H = h_N/2$)	Severe switch ($h_H = h_N/10$)
High d_x	**Sim 1** High k	**Sim 2** High k
	Sim 3 Low k	**Sim 4** Low k
Low d_x	**Sim 5** High k	**Sim 6** High k
	Sim 7 Low k	**Sim 8** Low k

Figure 2-7: The ODE system (2.2) was solved and plotted in (A) using an example selection of parameters to investigate the qualitative output of the model. System component values prior to $t = 0$ correspond to the normoxic equilibrium. We reduced h at $t = 0$ from h_N to h_H. HIF-1α dynamics are represented by blue curves and PHD dynamics are represented by green curves. The table in (B) provides a key to the plots in (A) revealing the nature of the parameter values used in each simulation, 'Sim i'. The parameters used were: $h_N = 20$, High $k = 1{\times}10^4$, Low $k = 1{\times}10^2$, High $d_x = 1{\times}10^2$ and Low $d_x = 1{\times}10^{-1}$.

2.2.2 Alternative Models

We have an initial 2-component model (2.1) of the HIF-1α cell signalling pathway that includes a negative feedback loop between HIF-1α and PHD. However this model does not appear capable of reproducing the qualitative dynamics of HIF-1α observed in single cells when exposed to a rapid switch to hypoxia. The shortcomings of model (2.1) led us to seek an improved description of single-cell HIF-1α dynamics. Alternative models were formulated by incorporating effects such as a delay in the synthesis of PHD and saturation of the PHD feedback.

The inclusion of delay in the model seemed plausible as it could potentially make the model more biologically realistic. This is due to the fact that the time taken for processes such as transcription and translation could now be taken into consideration, specifically in the induction of PHD by HIF-1α. Theoretically, with a delay in the accumulation of PHD there would be a delay in the accumulation of the negative feedback effect so that our transient increase in HIF-1α is higher, and takes longer to achieve its peak, and the feedback (when it does take effect) can bring HIF-1α levels back down. In this way, a delay in the accumulation of PHD is suggested to give us the required peak in HIF-1α before stabilisation where we aim to have relatively similar equilibrium levels before and after stimulation when compared to the large peak amplitude.

A saturating effect on the hydroxylation of HIF-1α by PHD would also be a biologically reasonable assumption as this reaction is limited by an individual PHD protein's maximum hydroxylation rate per unit time. This effect could similarly provide the necessary model framework to generate the characteristic HIF-1α dynamics of relatively high peaks with similar low levels of pre/post-peak equilibria. To investigate the effects of delay and saturation and hopefully integrate the features of the data, further models were designed with extra components, Michaelis-Menten kinetics and delay differential equations. These models are comparable to some of those proposed by Geva-Zatorsky et al. for the p53-Mdm2 feedback loop in the paper, 'Oscillations and variability in the p53 system' (Geva-Zatorsky, et al. 2006). Specifically we consider three alternative models described by the following sets of equations:

$$\begin{aligned} \frac{dx}{dt} &= S_x - hxy - d_x x \\ \frac{dm}{dt} &= S_m + \alpha x - d_m m \\ \frac{dy}{dt} &= \beta m - d_y y \end{aligned} \tag{2.4}$$

$$\begin{aligned}\frac{dx}{dt} &= S_x - hy\left(\frac{x}{x+\gamma}\right) - d_x x \\ \frac{dm}{dt} &= S_m + \alpha x - d_m m \\ \frac{dy}{dt} &= \beta m - d_y y\end{aligned} \tag{2.5}$$

$$\begin{aligned}\frac{dx}{dt} &= S_x - hxy - d_x x \\ \frac{dy}{dt} &= S_y + kx(t-\tau) - d_y y\end{aligned} \tag{2.6}$$

In (2.4) and (2.5), the temporal evolution of PHD mRNA, m, and its effect within the dynamical system have been explicitly described causing a delay in the accumulation of PHD. This is because PHD mRNA is a precursor to PHD which delivers the information required to synthesise a PHD protein (translation) from the nucleus to the ribosomes in the cytoplasm. Also, in (2.5), a non-linear function, $x/(x+\gamma)$, has been incorporated into the hydroxylation term to model a saturating effect of HIF-1α on HIF-1α degradation via hydroxylation. For low values of HIF-1α, (x) the hydroxylation term $-hyx/(x+\gamma)$ is linearly dependent on HIF-1α, but for large values of HIF-1α the hydroxylation term saturates such that it is independent of HIF-1α. This saturation effect can be altered by varying the threshold representing half the maximal expression of the function, γ. For greater values of γ, a greater value of x is required to achieve saturation. In (2.6), an explicit time delay has been added to the HIF-1α-induced PHD transcription term in the form of a delay differential equation (DDE), allowing for the time needed for PHD to be transcribed and translated. Specifically, the induced production of PHD at time t is taken to be proportional to the amount of HIF-1α at time $t-\tau$. For a full description of all variables and parameters in alternative models (2.4), (2.5), (2.6) see Table 2-1.

Variables	Parameters
x – HIF-1α	S_x – basal HIF-1α synthesis rate
m – PHD mRNA	S_m – basal PHD mRNA synthesis rate
y – PHD	S_y – basal PHD synthesis rate
	d_x – basal HIF-1α degradation rate
	d_m – basal PHD mRNA degradation rate
	d_y – basal PHD degradation rate
	h – hydroxylation rate of HIF-1α by PHD
	α – PHD mRNA production rate induced by HIF-1α
	β – PHD translation rate
	γ – HIF-1α hydroxylation threshold (Michaelis constant)
	k – PHD production rate induced by HIF-1α
	τ – delay in HIF-1α-induced PHD production

Table 2-1: A table describing all variables and parameters of the mathematical models described in (2.4), (2.5), and (2.6).

2.2.2.1 Non-dimensionalisation & Stability Analysis

We can non-dimensionalise models (2.4), (2.5) and (2.6) as follows:

Dimensionless Quantities	Models
$t^* = d_y t, \quad x^* = \frac{d_y}{S_x} x,$ $m^* = \frac{d_y}{S_m} m, \quad y^* = \frac{d_y}{S_m} y,$ $h^* = \frac{S_m}{d_y^2} h, \quad d_x^* = \frac{1}{d_y} d_x,$ $\alpha^* = \frac{S_x}{S_m d_y} \alpha, \quad d_m^* = \frac{1}{d_y} d_m,$ $\beta^* = \frac{1}{d_y} \beta.$	$\frac{dx}{dt} = 1 - hxy - d_x x$ $\frac{dm}{dt} = 1 + \alpha x - d_m m$ (2.7) $\frac{dy}{dt} = \beta m - y$

$t^* = d_y t, \quad x^* = \frac{d_y}{S_x} x,$ $m^* = \frac{d_y}{S_m} m, \quad y^* = \frac{d_y}{S_m} y,$ $h^* = \frac{S_m}{d_y S_x} h, \quad \gamma^* = \frac{d_y}{S_x} \gamma,$ $d_x^* = \frac{1}{d_y} d_x, \quad \alpha^* = \frac{S_x}{S_m d_y} \alpha,$ $d_m^* = \frac{1}{d_y} d_m, \quad \beta^* = \frac{1}{d_y} \beta.$	$\frac{dx}{dt} = 1 - hy\left(\frac{x}{x+\gamma}\right) - d_x x$ $\frac{dm}{dt} = 1 + \alpha x - d_m m$ $\frac{dy}{dt} = \beta m - y$	(2.8)
$t^* = d_y t, \quad \tau^* = d_y \tau,$ $x^* = \frac{d_y}{S_x} x, \quad y^* = \frac{d_y}{S_y} y,$ $h^* = \frac{S_y}{d_y^2} h, \quad d_x^* = \frac{1}{d_y} d_x,$ $k^* = \frac{S_x}{S_y d_y} k.$	$\frac{dx}{dt} = 1 - hxy - d_x x$ $\frac{dy}{dt} = 1 + kx(t-\tau) - y$	(2.9)

2.2.2.1.1 Stability of a HIF-PHD Model Including PHD mRNA

The system of equations (2.7) has a unique feasible equilibrium solution:

$$x^{EQ} = \frac{-(\beta h + d_x d_m) + \sqrt{(\beta h + d_x d_m)^2 + 4\alpha\beta h d_m}}{2\alpha\beta h}$$
$$m^{EQ} = \frac{1 + \alpha x^{EQ}}{d_m}$$
$$y^{EQ} = \beta m^{EQ}$$

We can compare this system with our original stable system (2.2) by thinking of the original model as a version of (2.7) where the PHD mRNA has reached equilibrium fast relative to the processes throughout the rest of the system (quasi-steady state), so that it can be discarded as a differential equation. This can be seen clearly by looking at the original dimensional forms (from (2.4)):

$$\text{At} \quad m = m^{EQ} = \frac{S_m + \alpha x}{d_m},$$

$$\frac{dy}{dt} = \frac{\beta S_m}{d_m} + \frac{\beta\alpha}{d_m}x - d_y y,$$

$$\tilde{S}_y = \frac{\beta S_m}{d_m}, \qquad \tilde{k} = \frac{\beta\alpha}{d_m},$$

where $\tilde{S}_y$ and $\tilde{k}$ refer to the S_y and k of the original 2-component system (2.1). In other words, the effective PHD production rate in the original system is equal to the steady-state mRNA level times the number of proteins translated from each mRNA. This quasi-steady state assumption in (2.1) is often reasonable, as mRNA is often degraded at a much faster rate than its protein product (Alon 2006), which in turn usually means that the mRNA response time is much quicker.

For linear stability analysis we calculate the Jacobian matrix for the unique steady state of (2.7),

$$\boldsymbol{J} = \begin{pmatrix} -hy^{EQ} - d_x & 0 & -hx^{EQ} \\ \alpha & -d_m & 0 \\ 0 & \beta & -1 \end{pmatrix}.$$

To analyse the stability of a multi-species system, we can use the Routh-Hurwitz criteria for stability, i.e. the criteria required for all eigenvalues to have negative real parts (description adapted from Edelstein-Keshet (Mathematical Models in Biology 2005)).

Routh-Hurwitz Criteria

Given the characteristic equation,

$$\lambda^n + a_1\lambda^{n-1} + a_2\lambda^{n-2} + \cdots + a_n = 0,$$

we define the following Routh-Hurwitz Criteria for $n = 2, 3, 4$:

$$\begin{aligned} &n = 2: \quad a_1 > 0, \quad a_2 > 0. \\ &n = 3: \quad a_1 > 0, \quad a_3 > 0, \quad a_1 a_2 > a_3. \\ &n = 4: \quad a_1 > 0, \quad a_3 > 0, \quad a_4 > 0, \quad a_1 a_2 a_3 > a_3^2 + a_1^2 a_4. \end{aligned} \tag{2.10}$$

From our Jacobian matrix, $\boldsymbol{J}$, we find the corresponding characteristic equation:

$$\begin{vmatrix} -hy^{EQ} - d_x - \lambda & 0 & -hx^{EQ} \\ \alpha & -d_m - \lambda & 0 \\ 0 & \beta & -1 - \lambda \end{vmatrix} = 0$$

$$\Leftrightarrow \lambda^3 + (hy^{EQ} + d_m + d_x + 1)\lambda^2 + \big(d_m + hy^{EQ}(d_m + 1) + d_x(d_m + 1)\big)\lambda + hy^{EQ}d_m + d_x d_m + \beta\alpha hx^{EQ} = 0$$

Following criteria (2.10) with $n = 3$ we define

$$a_1 = hy^{EQ} + d_m + d_x + 1,$$
$$a_2 = d_m + hy^{EQ}(d_m + 1) + d_x(d_m + 1),$$
$$a_3 = hy^{EQ}d_m + d_x d_m + \beta\alpha h x^{EQ}.$$

Clearly $a_1 > 0$ is satisfied and $a_3 > 0$ is satisfied but we also need $a_1 a_2 > a_3$ for stability. For this we want to prove that $a_1 a_2 - a_3 > 0$.

We can now reduce this problem, by removing some of the parameters involved in the comparison, via suitable substitutions. Note

$$y^{EQ} = \beta m^{EQ} = \frac{\beta + \beta\alpha x^{EQ}}{d_m},$$
$$\Rightarrow \beta\alpha h x^{EQ} = h(d_m y^{EQ} - \beta).$$

Therefore we can remove parameters α and x^{EQ} from consideration and re-write a_3:

$$a_3 = 2hy^{EQ}d_m + d_x d_m - \beta h.$$

So,

$$a_1 a_2 - a_3 = \left(\underline{hy^{EQ}} + d_m + d_x + \underline{1}\right)\left(\underline{hy^{EQ}(d_m} + 1) + \underline{d_x d_m} + \underline{d_m} + d_x\right)$$
$$- \left(\underline{\underline{2hy^{EQ}d_m + d_x d_m}} - \beta h\right).$$

Terms underlined cancel leaving

$$a_1 a_2 - a_3 = hy^{EQ}(hy^{EQ}(d_m + 1) + d_x d_m + d_x) + (d_m + d_x)a_2 + hy^{EQ} + (d_m + d_x) + \beta h,$$

which is clearly greater than 0 since all terms on the right hand side are positive by definition. Therefore the unique steady state is stable.

2.2.2.1.2 Stability of a HIF-PHD Model Including PHD mRNA and Hydroxylation Saturation

The system of equations (2.8) has a unique equilibrium solution:

$$x^{EQ} = \frac{-h\beta - d_m(d_x\gamma - 1) + \sqrt{\left(h\beta + d_m(d_x\gamma - 1)\right)^2 + 4(h\alpha\beta + d_x d_m)\gamma d_m}}{2(h\alpha\beta + d_x d_m)},$$

$$m^{EQ} = \frac{1 + \alpha x^{EQ}}{d_m},$$
$$y^{EQ} = \beta m^{EQ}.$$

To determine the stability of the system, let us now consider the Jacobian matrix

$$\left(\begin{matrix} -\frac{hy}{x+\gamma} + \frac{hxy}{(x+\gamma)^2} - d_x & 0 & -h\left(\frac{x}{x+\gamma}\right) \\ \alpha & -d_m & 0 \\ 0 & \beta & -1 \end{matrix} \right) \Bigg|_{(x^{EQ}, m^{EQ}, y^{EQ})},$$

and hence the characteristic equation

$$\begin{vmatrix} -\left(\frac{h\gamma\beta(1+\alpha x^{EQ})}{d_m(x^{EQ}+\gamma)^2} + d_x\right) - \lambda & 0 & -h\left(\frac{x^{EQ}}{x^{EQ}+\gamma}\right) \\ \alpha & -d_m - \lambda & 0 \\ 0 & \beta & -1-\lambda \end{vmatrix}$$

$$= \begin{vmatrix} -P-\lambda & 0 & -Q \\ \alpha & -d_m-\lambda & 0 \\ 0 & \beta & -1-\lambda \end{vmatrix} = 0,$$

where we have introduced the parameters P and Q for ease of notation.

This yields the characteristic equation

$$\lambda^3 + (P + d_m + 1)\lambda^2 + (P(\,d_m + 1) + d_m)\lambda + Pd_m + \,Q\alpha\beta = 0.$$

Using the Routh-Hurwitz criteria (2.10), $a_1 > 0$ is satisfied, $a_3 > 0$ is satisfied and we need to determine whether $a_1 a_2 > a_3$. This cannot be determined for the general case, and we shall now give examples showing the model having an unstable or stable equilibrium depending on the parameter values.

We gather insight of the stability of system (2.8) by comparing it with the very similar system, (2.7), which we have shown to be locally stable at its unique steady state. The two systems differ only in the hydroxylation term of the ODE describing the rate of change of HIF-1α. System (2.7) uses mass action dynamics, hxy, while system (2.8) uses Michaelis-Menten kinetics, $hy(x/(x+\gamma))$. To make both systems comparable is equivalent to letting $\gamma \gg x$ and making an appropriate rescaling of the parameter h in (2.8) so we can assume that in this case we have a stable equilibrium. To show that it is possible to choose parameter values such that the unique equilibrium of system (2.8) can be unstable we look at the limiting case where $\gamma = 0$.

Suppose $\gamma = 0$. Then (2.8) becomes

$$\frac{dx}{dt} = 1 - hy - d_x x$$
$$\frac{dm}{dt} = 1 + \alpha x - d_m m$$
$$\frac{dy}{dt} = \beta m - y$$

with unique equilibrium point

$$x^{EQ} = \frac{d_m - h\beta}{h\beta\alpha + d_m d_x}, \qquad m^{EQ} = \frac{1 + \alpha x^{EQ}}{d_m}, \qquad y^{EQ} = \beta m^{EQ}.$$

For feasibility we require that $d_m > h\beta$. To analyse the linear stability we calculate the Jacobian

$$\boldsymbol{J} = \begin{pmatrix} -d_x & 0 & -h \\ \alpha & -d_m & 0 \\ 0 & \beta & -1 \end{pmatrix},$$

which yields the characteristic equation:

$$(d_x + \lambda)(d_m + \lambda)(1 + \lambda) + h\alpha\beta = 0.$$

By using the Routh-Hurwitz criteria we determine that we need the following inequality to hold for stability:

$$d_x^2(d_m + 1) + d_x(d_m + 1)^2 + d_m(d_m + 1) - h\alpha\beta > 0 \tag{2.11}$$

From (2.11) we can see that for a large enough value of α, the induction rate of PHD mRNA, we can force the converse case, that is $a_1 a_2 - a_3 < 0$ and thus show instability of the unique equilibrium. Note that, unlike with h and β, any increase in α has no effect on our feasibility condition. This analysis then suggests that for a small enough value of γ and large enough value of α in system (2.8) we might be able to find unstable dynamics at the unique equilibrium.

To test the hypothesis that system (2.8) can be either stable or unstable dependent on parameter values we simulated two cases: one where $\gamma \gg x$ to represent stability akin to (2.7); and one where $\gamma \ll 1$ and $\alpha \gg 1$ to represent instability analogous to the case where $\gamma = 0$. The results of these simulations in Figure 2-8 show that it is indeed the case that the equilibrium point can be stable or unstable.

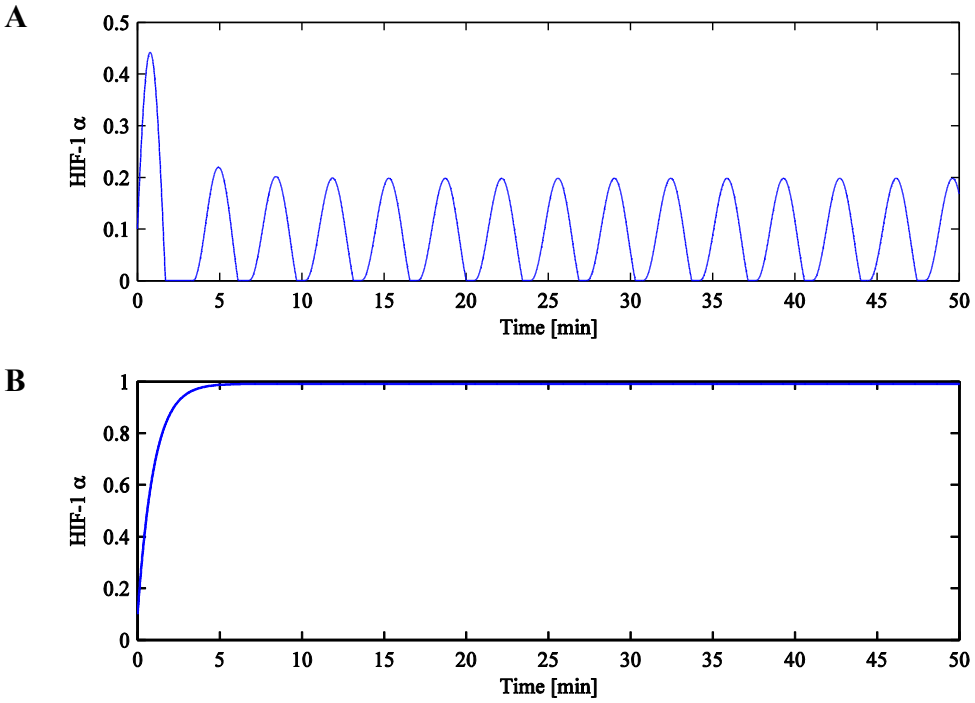

Figure 2-8: Simulations of system (2.8) showing the possibility of both an unstable equilibrium (A) and a stable equilibrium (B). Parameter values used: (A), $h = 1, d_x = 1, d_m = 1, \alpha = 1\times10^{3}, \beta = 1\times10^{-2}, \gamma = 1\times10^{-5}$; (B), $h = 1, d_x = 1, d_m = 1, \alpha = 1\times10^{3}, \beta = 1\times10^{-2}, \gamma = 1\times10^{3}$. The initial conditions in both cases were $x = m = y = 1\times10^{-1}$.

We can also analyse the case where PHD mRNA reaches equilibrium fast relative to the much slower process of the change in levels of proteins PHD and HIF-1α. This postulation leads to a reduced system. As the latter two equations in system (2.8) are the same as in (2.7), we once again have

$$\tilde{S_y} = \frac{\beta S_m}{d_m}, \qquad \tilde{k} = \frac{\beta\alpha}{d_m},$$

in the dimensional form. The new non-dimensional system (with m at equilibrium) can be written as

$$\frac{dx}{dt} = 1 - hy\left(\frac{x}{x+\gamma}\right) - d_x x$$
$$\frac{dy}{dt} = 1 + kx - y$$

with a unique equilibrium

$$x^{EQ} = \frac{-(h + d_x\gamma - 1) + \sqrt{(h + d_x\gamma - 1)^2 + 4\gamma(d_x + hk)}}{2(d_x + hk)},$$
$$y^{EQ} = 1 + ky^{EQ}.$$

By calculating the Jacobian matrix (below) of this system we can analyse its stability.

$$\begin{pmatrix} -\dfrac{hy^{EQ}\gamma + d_x(x^{EQ}+\gamma)^2}{(x^{EQ}+\gamma)^2} & -\dfrac{hx^{EQ}}{x^{EQ}+\gamma} \\ k & -1 \end{pmatrix}$$

From this we can see that trace of the Jacobian matrix is negative and the determinant is positive. Therefore any eigenvalues from a related characteristic equation would have negative real parts and therefore this system is stable.

2.2.2.1.3 Stability of a HIF-PHD Model Including Explicit Delay in PHD Induction

The system of equations (2.9) has a unique equilibrium solution:

$$x^{EQ} = \frac{-(h+d_x) + \sqrt{(h+d_x)^2 + 4hk}}{2hk},$$
$$y^{EQ} = 1 + kx^{EQ}.$$

This is the same steady state as in our original model due to the absence of a delay effect when at equilibrium. We now outline the method for determining linear stability in a system of delay differential equations.

Let $dx/dt = f(x, x_\tau, y, y_\tau)$ and $dy/dt = g(x, x_\tau, y, y_\tau)$, where $x = x(t)$ and $x_\tau = x(t-\tau)$, and similarly for y. Near to our fixed point we have $x = x^{EQ} + \epsilon_x$ and $y = y^{EQ} + \epsilon_y$ (and similarly $x_\tau = x^{EQ} + \epsilon_{x,\tau}$ and $y_\tau = y^{EQ} + \epsilon_{y,\tau}$). Also, let $\mathbf{EQ} = \{x^{EQ}, x_\tau^{EQ}, y^{EQ}, y_\tau^{EQ}\} = \{x^{EQ}, x^{EQ}, y^{EQ}, y^{EQ}\}$.

Thus, near to the unique equilibrium, we have

$$\frac{dx}{dt} = \frac{d\epsilon_x}{dt} = f(\mathbf{EQ}) + \epsilon_x f_x(\mathbf{EQ}) + \epsilon_{x,\tau} f_{x_\tau}(\mathbf{EQ}) + \epsilon_y f_y(\mathbf{EQ}) + \epsilon_{y,\tau} f_{y_\tau}(\mathbf{EQ}) + \cdots$$
$$\frac{dy}{dt} = \frac{d\epsilon_y}{dt} = g(\mathbf{EQ}) + \epsilon_x g_x(\mathbf{EQ}) + \epsilon_{x,\tau} g_{x_\tau}(\mathbf{EQ}) + \epsilon_y g_y(\mathbf{EQ}) + \epsilon_{y,\tau} g_{y_\tau}(\mathbf{EQ}) + \cdots$$

From this system we write the matrix equation

$$\frac{d\boldsymbol{\epsilon}}{dt} = \mathbf{A}\boldsymbol{\epsilon}(t) + \mathbf{B}\boldsymbol{\epsilon}(t-\tau),$$

with matrices $\mathbf{A} = \begin{pmatrix} f_x & f_y \\ g_x & g_y \end{pmatrix}\Big|_{\mathbf{EQ}}$ and $\mathbf{B} = \begin{pmatrix} f_{x_\tau} & f_{y_\tau} \\ g_{x_\tau} & g_{y_\tau} \end{pmatrix}\Big|_{\mathbf{EQ}}$.

Hence we look for a solution of the form $\boldsymbol{\epsilon}(t) = \mathbf{v}e^{\lambda t}$. That is,

$$\lambda\mathbf{v} = \left(\mathbf{A} + \mathbf{B}e^{-\lambda\tau}\right)\mathbf{v} = \mathbf{C}\mathbf{v},$$

where

$$\mathbf{C} = \begin{pmatrix} -hy^{EQ} - d_x & -hx^{EQ} \\ ke^{-\lambda\tau} & -1 \end{pmatrix}$$

with characteristic equation:

$$\lambda^2 + (1 + h(1 + kx^{EQ}) + d_x)\lambda + hkx^{EQ}e^{-\lambda\tau} + hkx^{EQ} + h + d_x = 0. \tag{2.12}$$

This transcendental equation cannot be solved analytically, and the Routh-Hurwitz criteria are not applicable. However, to determine whether the equilibrium is stable, we only need to determine whether the real parts of both eigenvalues are negative. We can re-write (2.12) as

$$\lambda^2 + a\lambda + be^{-\lambda\tau} + c = 0,$$

where $a, b, c > 0$. In the case when λ is real $\lambda^2 + be^{-\lambda\tau} + c > 0$ and therefore we must have

$$a\lambda < 0 \Rightarrow \lambda < 0$$

for equation (2.12) to be satisfied. Hence, for real eigenvalues, λ is negative and the steady state is stable.

So we look at the complex case, $\lambda = u + iv, v \neq 0$, and the resulting real and imaginary parts of (2.12). For more detail on a similar version of the following analysis, see Murray (Mathematical Biology: I. An Introduction (Interdisciplinary Applied Mathematics) (Pt. 1) 2001). For the complex case we have

$$(u + iv)^2 + (1 + h(1 + kx^{EQ}) + d_x)(u + iv) + hkx^{EQ}e^{-(u+iv)\tau} + hkx^{EQ} + h + d_x = 0.$$

We are interested in the value of τ when the value of $\mathrm{Re}\{\lambda\} = u$ first crosses from $u < 0$ to $u > 0$. So in order to see when u is first equal to 0 as τ increases, we set $u = 0$ and look for $\tau = \tau_c$, the bifurcation value.

Therefore, when $u = 0$,

$$-v^2 + hkx^{EQ}\cos(v\tau) + hkx^{EQ} + h + d_x + i\left((1 + h(1 + kx^{EQ}) + d_x)v - hkx^{EQ}\sin(v\tau)\right) = 0.$$

$$\Rightarrow \sin(v\tau) = \frac{(1 + h(1 + kx^{EQ}) + d_x)v}{hkx^{EQ}} = c_1 v,$$

$$\cos(v\tau) = \frac{v^2 - hkx^{EQ} - h - d_x}{hkx^{EQ}} = c_2 v^2 - c_3,$$

where c_i are constants. Therefore we can write

$$\sin^2(v\tau) + \cos^2(v\tau) = 1 = (c_1 v)^2 + (c_2 v^2 - c_3)^2, \tag{2.13}$$

giving us a polynomial of degree 4 which we could solve for v numerically with given parameter values. Given v, we can then find τ from above,

$$\tau = \frac{\arcsin(c_1 v)}{v},$$

and τ_c is the first $\tau > 0$ of this periodic solution, leading to instability in the steady state.

However, (2.13) may not yield any real solutions for v, which we have said is real by definition. So we look for a condition(s) such that (2.13) can be solved for real values of v. Now, note that we actually have $c_1 = c_2 + c_3$, and so we can write (2.13) as

$$c_2^2 v^4 + (c_2^2 + c_3^2)v^2 + c_3^2 = 1.$$

For v to have real solutions, we need the minimum of the function $q(v) = c_2^2 v^4 + (c_2^2 + c_3^2)v^2 + c_3^2$ to be less than or equal to 1. This minimum occurs at $v = 0$, as all coefficients in $q(v)$ are positive, and $q(0) = c_3^2$. Therefore we need $c_3^2 \leq 1$ for real solutions. Now,

$$c_3 = \frac{hkx^{EQ} + h + d_x}{hkx^{EQ}} = 1 + \frac{h + d_x}{hkx^{EQ}} > 1.$$

Thus, there are no real solutions for $q(v)$ and we cannot then have complex eigenvalues $\lambda = u + iv$. Therefore, eigenvalues will always be real and negative and the steady state is a stable node.

2.2.2.2 Preliminary Fitting & Discussion

We attempted to fit the alternative models to the experimental data to see which version of the HIF-1α-PHD feedback mechanism was most suitable for reproducing experimentally observed dynamics (see Figure 2-9). The alternative models are modified versions of our original mathematical description of the HIF-1α-PHD feedback mechanism in model (2.1). Using model (2.1), we were unable to obtain characteristic single-cell HIF-1α dynamics such as large-amplitude transient peaks in HIF-1α without a significant change in equilibrium levels between normoxic and hypoxic conditions. The alternative models comprised of the following modifications to model (2.1): explicit PHD mRNA inclusion (2.4); explicit PHD mRNA inclusion with saturating hydroxylation of HIF-1α (2.5); and a DDE model with a delay in the HIF-1α-induced production of PHD (2.6). For models (2.1), (2.4) and

(2.6) standard linear stability analysis shows that there is a unique equilibrium which is stable and thus the HIF-1α level will change to a new equilibrium following a transition to hypoxic conditions. The unique equilibrium point of model (2.5) can be stable or unstable allowing for sustained oscillatory behaviour. Note that for the purposes of data-fitting we will revert to using the dimensional forms of the models.

For this preliminary investigation, initial parameter estimates were arbitrarily chosen and applied to each model. Then parameter values were optimised such that the model solution for the HIF-1α variable fit time-series data for a specific cell as well as possible. The chosen cell represented a case of some of the more complex HIF-1α dynamics observed in experiments, the bell-shaped dynamics, in order to really test each model's capability of simulating HIF-1α behaviour during hypoxic induction. These bell-shaped dynamics displayed a rapid, transient increase in HIF-1α following hypoxic induction before stabilisation at a hypoxic steady state akin to the level of the normoxic steady state pre-stimulation. This optimisation was performed using the numerical computing software programme, MATLAB (for more technical optimisation details see section 2.3 and the Appendix, section 7.1). This process was carried out several times but was not an exhaustive analysis. A more systematic method for parameter optimisation is used once the model architecture has been finalised and this routine is presented in section 2.3.

The saturating response in model (2.5) allowed for better fits to the bell-shaped single-cell data than model (2.4). In particular, the inclusion of the saturating Michaelis-Menten hydroxylation function in model (2.5) appeared to improve the model's ability to generate large-amplitude transient peaks upon hypoxic transition as well as a low-level resolution of HIF-1α. In fitting both models (2.4) and (2.5) we obtained high degradation rates of mRNA. This suggests that the mRNA dynamics in these optimised models operate on a fast timescale when compared with the slower processes of the rest of the system. Furthermore, this implies that the explicit inclusion of a PHD mRNA component is not necessary to produce bell-shaped dynamics.

Approximate fits using DDE model (2.6) resulted in large values of parameter τ which represent long delays in the HIF-1α-induced production of PHD. These delays encapsulate a host of processes including the binding of HIF-1 to the PHD promoter region of DNA, PHD mRNA transcription in the nucleus and translation of PHD mRNA into PHD protein in the cytoplasm. However, these delays were considered large when compared to the protein dynamics in the system and the inferences of the other models suggesting a rapid response time of PHD mRNA and a quick negative feedback effect. Typically transcription factor binding and mRNA dynamics operate on a much faster timescale than that of the relatively slow timescale of changes in protein levels (seconds and minutes compared with many minutes to hours (Alon 2006)). This separation of timescales agrees with the ODE models that predicted high degradation rates of mRNA and thus fast response times. That is, the ODE model

fitting results suggest that mRNA levels reach steady state at a much faster rate than protein levels. Under this assumption, transcription factor binding and mRNA transcription rates should be fast compared to protein dynamics and contribute little to the delay parameter, τ, in model (2.6). This leaves only the rate of translation from PHD mRNA to PHD protein as the main contributor to τ. The process of translation typically only lasts 30 minutes (including mRNA nuclear export) in mammalian cells (Alon 2006) but τ was estimated to be of the order of protein dynamics, i.e. hours. These delay times in the DDE model also resulted in subsequent damped oscillations which were not seen in the data. For these reasons, together with the relative success of the model including hydroxylation saturation (2.5), we did not pursue explicit delay models further.

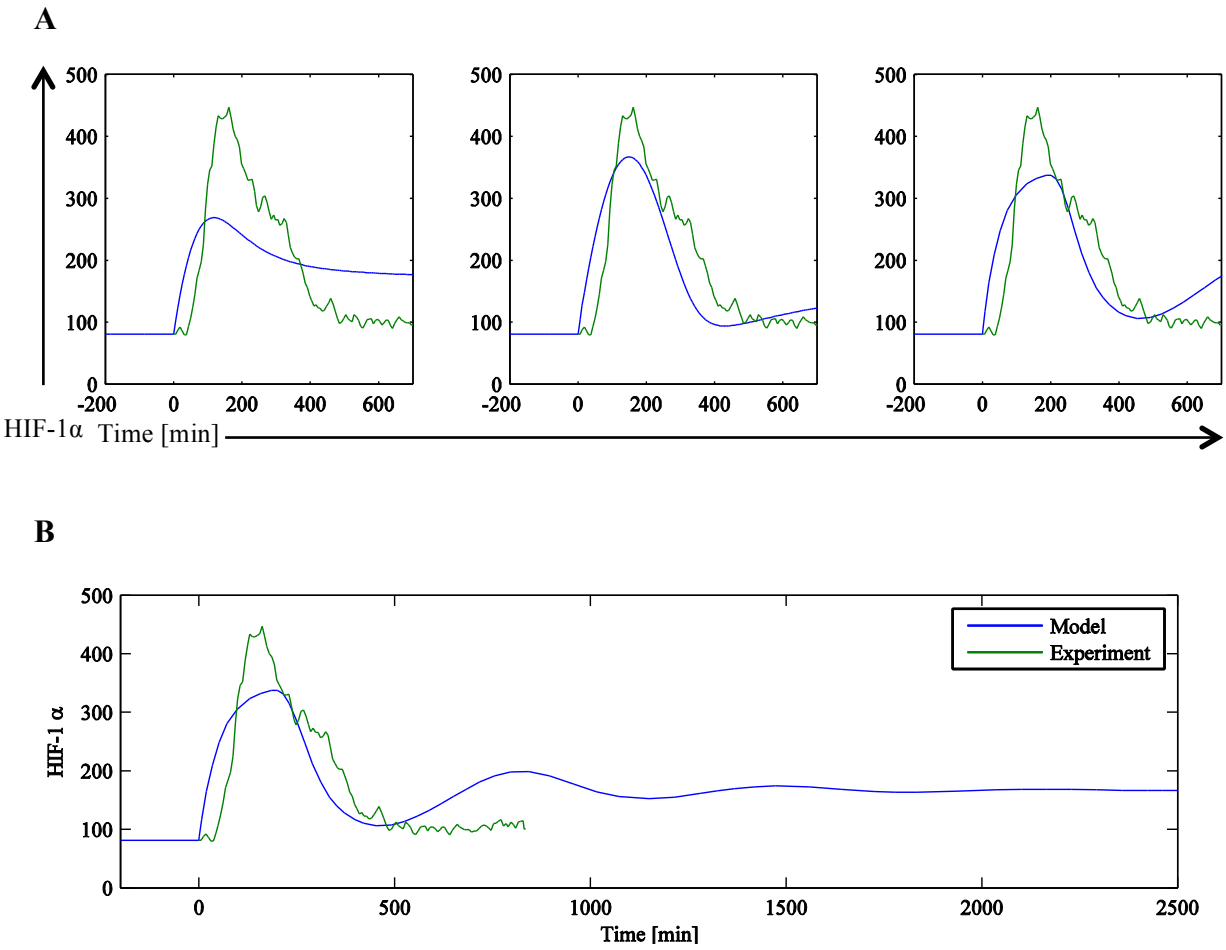

Figure 2-9: (A): Typical data-fitting plots for models (2.4), (2.5), (2.6) going from left to right respectively. The green line here represents experimental data from a single cell and $t = 0$ corresponds to the time of the hypoxic switch. Blue lines refer to the numerical solution for HIF-1α (x). The model parameters were optimised in each case such that the difference between the model output and experimental data was minimised. (B): Long delays in the DDE model tended to result in damped oscillations in HIF-1α.

2.2.3 The Minimal 2-component Feedback Model

Based on the preliminary results presented in the previous section, a new minimal model was constructed to describe the negative feedback mechanism between HIF-1α and PHD with the simplest network motif such that all the essential HIF-1α dynamics observed experimentally were represented.

The introduction of an intermediate component between HIF-1α and PHD, PHD mRNA, was discarded as preliminary fits of models including this component tended to favour fast mRNA dynamics with very high basal degradation rates. Therefore the new minimal model incorporated a quasi-steady state assumption and the mRNA dynamics were not described explicitly for these timescales. The alternate models all included parameter values denoting basal synthesis of PHD, S_y, and basal degradation of HIF-1α, d_x. The preliminary fitting for all models consistently suggested that these processes made negligible contributions to the dynamics as these parameters were reduced to trivially small values. A prototype to the minimal model kept these parameters but the same conclusions were drawn from preliminary fits and so indeed they were removed before any subsequent systematic parameter searches. By using simple mass action (i.e. models (2.1) and (2.4)), we were unable to get good fits of the single-cell bell-shape data; in particular we were unable to obtain a large-amplitude transient peak in HIF-1α without a significant change in equilibrium levels between normoxic and hypoxic conditions. We therefore included a saturating response to hydroxylation (as in model (2.5)) as this model feature seemed to be vital in capturing the more complex HIF-1α dynamics observed. This non-linear function represents a saturation of the hydroxylation reaction due to high levels of HIF-1α (x) and is effectively linear for very low values of x but saturates at 1 as x increases. Thus we include the parameter, γ, a Michaelis constant which can be thought of as representing the HIF-1α hydroxylation threshold. Using these observations the following model (2.14) consisting of a 2-component system of first order non-linear ordinary differential equations was developed for the purposes of more rigorous testing.

$$\begin{aligned} \frac{dx}{dt} &= S - hy\left(\frac{x}{x+\gamma}\right) \\ \frac{dy}{dt} &= kx - dy \end{aligned} \tag{2.14}$$

In the minimal 2-component feedback model (2.14), HIF-1α (x) induces the transcription of PHD (y) at rate k and HIF-1α is degraded via PHD-dependent hydroxylation at a maximal rate h. Saturation of the hydroxylation reaction is described by Michaelis-Menten kinetics. To prevent elimination of HIF-1α (x) and unbounded growth of PHD (y) we further suppose HIF-1α (x) is produced through basal synthesis at rate S and PHD (y) is degraded at rate d. The sensitivity to oxygen in this model is represented by the parameter h, the hydroxylation rate at which PHD induces the degradation of HIF-1α. A change in the value of this parameter represents a change in the oxygen environment of the

system and for now we consider just two possible states: normoxia (20% O_2, $h = h_N$) and hypoxia (1% O_2, $h = h_H$).

2.2.3.1 Analysis of the Minimal Model

By performing stability analysis similar to sections 2.2.1 and 2.2.2 one can show that the unique equilibrium solution to this system is also stable.

Firstly, we non-dimensionalise system (2.14) by re-scaling time with respect to the PHD degradation parameter and protein amounts with respect to the ratio of basal HIF-1α synthesis and PHD degradation as follows:

$$t^* = dt, \qquad x^* = \frac{d}{S}x, \qquad y^* = \frac{d}{S}y.$$

Now we can write

$$\begin{aligned}\frac{dx^*}{dt^*} &= \frac{d}{S}\frac{1}{d}\frac{dx}{dt} = 1 - \frac{h}{S}\frac{S}{d}y^*\left(\frac{x^*}{x^* + \frac{d}{S}\gamma}\right)\\ &= 1 - h^*y^*\left(\frac{x^*}{x^* + \gamma^*}\right),\\ \frac{dy^*}{dt^*} &= \frac{d}{S}\frac{1}{d}\frac{dy}{dt} = \frac{k}{d}x^* - \frac{d}{S}\frac{S}{d}y^* = k^*x - y^*,\end{aligned}$$

where we have the following non-dimensional quantities:

$$\gamma^* = \frac{d}{S}\gamma, \qquad h_i^* = \frac{1}{d}h_i, \qquad k^* = \frac{1}{d}k$$

We drop the $*$ for notational simplicity and acquire the following system:

$$\begin{aligned}\frac{dx}{dt} &= 1 - hy\left(\frac{x}{x + \gamma}\right)\\ \frac{dy}{dt} &= kx - y\end{aligned} \tag{2.15}$$

System (2.15) is at equilibrium for the following values:

$$\begin{aligned}x^{EQ} &= \frac{1 + \sqrt{1 + 4hk}}{2hk}\\ y^{EQ} &= kx^{EQ}.\end{aligned}$$

In order to determine the local stability at this unique system steady state we calculate the Jacobian matrix:

$$\boldsymbol{J} = \begin{pmatrix} \dfrac{-hy^{EQ}\gamma}{(x^{EQ}+\gamma)^2} & \dfrac{-hx^{EQ}}{x^{EQ}+\gamma} \\ k & -1 \end{pmatrix}.$$

From the Jacobian we can see that the trace of the matrix is negative and the determinant is positive. Therefore our eigenvalues have negative real parts and the equilibrium point is stable.

When we reduce h this is equivalent to simulating the hypoxic state and our unique system equilibrium value is increased for both HIF-1α and PHD as seen in Figure 2-10.

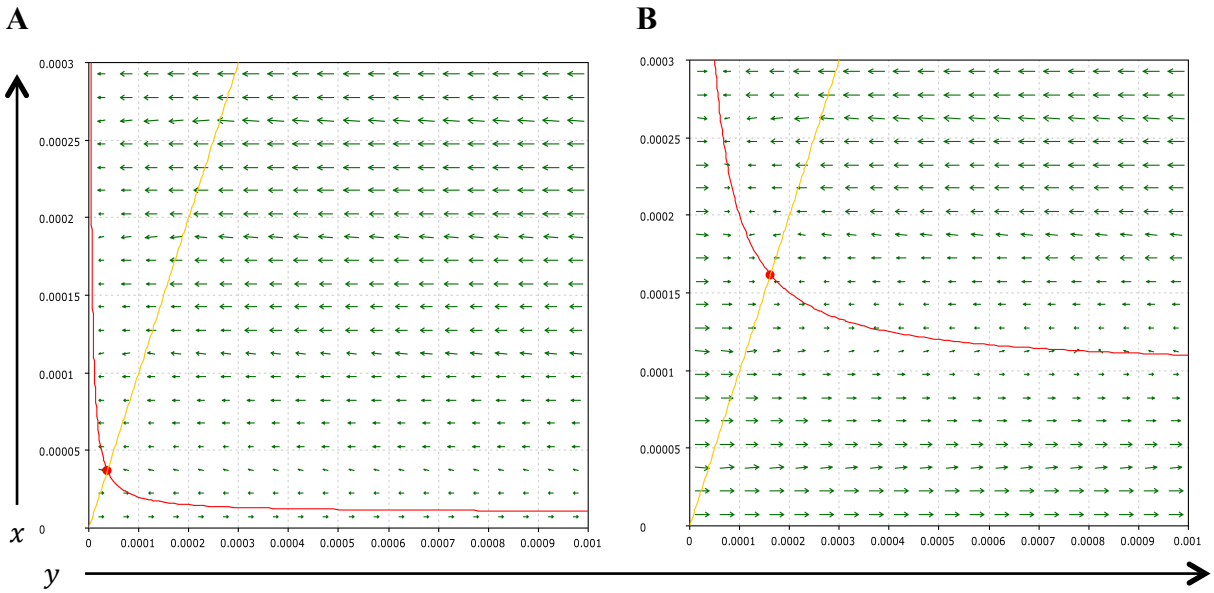

Figure 2-10: Phase portraits of system (2.15) for different values of parameter h representing normoxia (A) and hypoxia (B). Parameters: (A) $h = 1\times10^{5}, \gamma = 1\times10^{-4}, k = 1$; (B) $h = 1\times10^{4}, \gamma = 1\times10^{-4}, k = 1$. Colour coding as in Figure 2-4. Phase portraits were produced using the Java version of MATLAB program *pplane* developed by John C. Polking (dfield and pplane 2002).

By plotting phase portrait trajectories we can begin to see the differences in transient HIF-1α dynamics when comparing our initial model (2.1) and our revised, minimal model (2.14). In Figure 2-11 we have plotted phase portraits for both models with sample trajectories. These trajectories represent the transient system dynamics following a drop in oxygen from the prior equilibrium point. We can see that this corresponds to trajectory starting-points on the PHD nullcline. Different sample trajectories represent different severities of hypoxic switch. The figure shows a large overshoot for HIF-1α dynamics in model (2.14) but not model (2.1) which corresponds to our previous intuitions and preliminary results in Figure 2-7 and Figure 2-9 and justifies our introduction of hydroxylation saturation.

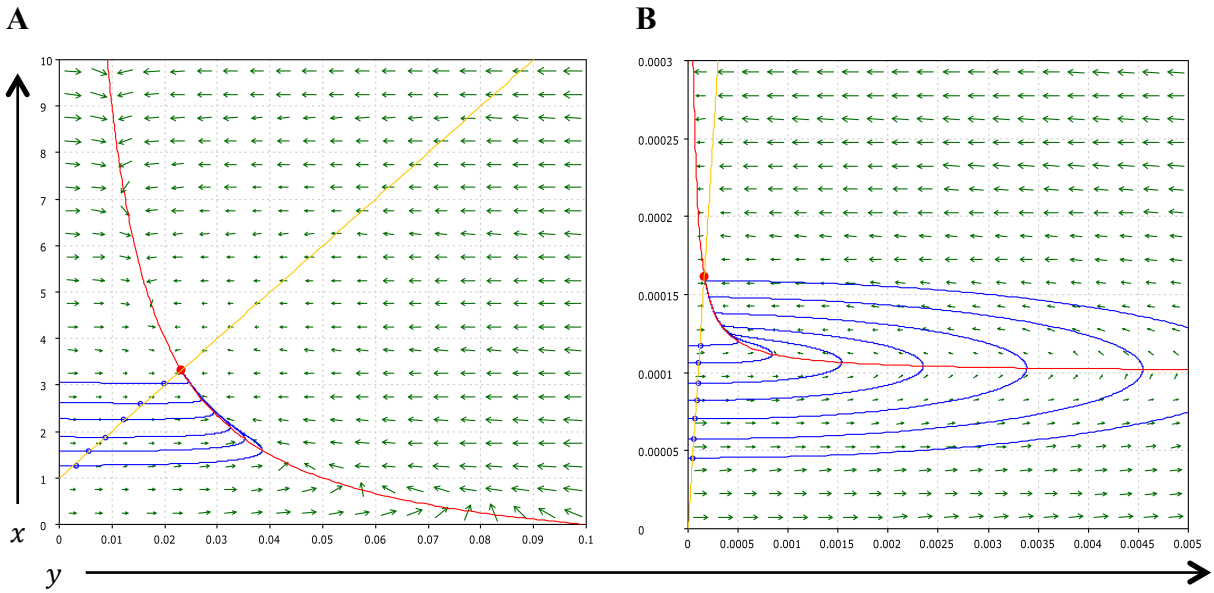

Figure 2-11: Phase portraits of system (2.2) (A) and system (2.15) (B) with sample trajectories. The trajectories in both cases represent a reduction in h and a shift to a subsequent hypoxic equilibrium. The introduction of a saturating hydroxylation term in system (2.15) appears to be more susceptible to transient HIF-1α overshoot behaviour. Parameters: (A) $h = 10, d = 10, k = 100$; (B) $h = 1\times 10^{4}, \gamma = 1\times10^{-4}, k = 1$. Colour coding as in Figure 2-4. Phase portraits were produced using the Java version of MATLAB program *pplane* developed by John C. Polking (dfield and pplane 2002).

2.3 Data Fitting & Parameter Optimisation

In order to test the model's ability to reproduce the measured HIF-1α dynamics we attempted to fit the x variable in (2.14) to HIF-1α experimental imaging data (fluorescent signal) for the time-series given by the experiment. The model variable was fit by varying parameters in the model.

The model parameters were optimised to minimise the difference between experimental data and model output of HIF-1α found by solving the ODEs using MATLAB. The experiments comprised of two oxygen regimes: de-oxygenation (where cells experienced a transition to hypoxia); and re-oxygenation (where the cells were incubated in hypoxia before oxygen levels were restored to a normoxic state). Altogether, the model was fitted to 81 pieces of cell data from 4 experiments: *Experiment 1* (de-oxygenation - 17 cells); *Experiment 2* (de-oxygenation - 22 cells); *Experiment 3* (re-oxygenation - 19 cells); *Experiment 4* (re-oxygenation - 23 cells). A model of the simplicity of (2.14) being able to reproduce the same dynamics seen in the data would go some way to suggesting that the core regulation motif was a sound basis on which to represent the negative feedback loop in the HIF-1α signalling pathway.

To measure the fit of the model an error function, χ, was defined (2.16). The value of this function indicates the relative accuracy of the fit between an ODE solution for x and the experimental data. A

minimisation algorithm was used in order to minimise this error. This error function was determined through a least squares approach and defined as the sum of squared residuals,

$$\chi = \sum_{i=1}^{n} (M_i - E_i)^2 \tag{2.16}$$

where E_i represents the i-th experimental data point and M_i represents the corresponding i-th model output point for HIF-1α ($x(t)$ from (2.14) for t corresponding to the time-point of the experimental data). The resolution of the data is indicated by n, the number of time-points.

To solve system (2.14) numerically in MATLAB we needed to select the following: values for the four constant rate parameters (S, k, γ and d); values for h in hypoxia (h_H) and in normoxia (h_N); and values for the initial conditions $x(0)$ and $y(0)$. The aim was to discover which values of these parameters gave the best fit to the experimental data.

The optimisation method we used to minimise the sum in (2.16) made use of a built-in algorithm in MATLAB, called *fminsearch*. This function uses the Nelder-Mead simplex algorithm, a direct search method used for multidimensional unconstrained minimisation that requires only function evaluations, not derivatives (Nelder and Mead 1965, Lagarias, et al. 1998). A limitation of this method is that like many other optimisation techniques, convergence can become stuck on local minima. For more information on this minimisation method, see section 7.1 in the Appendix.

Multi-dimensional parameter space can be very complex to search. The method of parameter optimisation can be made easier through the reduction of parameters to vary (or dimensions to search in) and a better choice of initial estimates (or starting position) to pass into the search algorithm. These modifications can enhance the chances of converging on the global minima and reduce the computational burden, increasing optimisation speed.

The simple feedback model (2.14) has six regulation parameters eligible for optimisation (recall we assume two different rates for h depending on the oxygen state) and initial conditions for x and y so we have eight values to optimise in total. This number can be reduced to four with reasonable assumptions and efficient scaling. We are not immediately concerned with the exact values or scale of PHD as we do not have the relevant data to simultaneously fit PHD and HIF-1α. We are however interested in how PHD interacts dynamically with HIF-1α. Consequently we can rescale y with h_N for example, the hydroxylation rate of HIF-1α in normoxia, by defining a new variable $h_N y = y^*$. In this way we can reduce the number of free parameters we need to optimise.

The system in normoxia now becomes

$$\frac{dx}{dt} = S - y^*\left(\frac{x}{x+\gamma}\right)$$
$$\frac{dy^*}{dt} = k^*x - dy^*$$

where $k^* = h_N k$.

Accordingly the system in hypoxia becomes

$$\frac{dx}{dt} = S - \left(\frac{h_H}{h_N}\right)y^*\left(\frac{x}{x+\gamma}\right)$$
$$\frac{dy^*}{dt} = k^*x - dy^*$$

We drop the $*$ for notational simplicity and obtain the following system again,

$$\frac{dx}{dt} = S - hy\left(\frac{x}{x+\gamma}\right)$$
$$\frac{dy}{dt} = kx - dy \qquad (2.17)$$

but we now have $h = 1$ in normoxia and $h = h_H/h_N$ in hypoxia. We have rescaled the system such that y and k now represent the original y and k parameters multiplied by h_N. This scaling has removed from consideration one of the parameters that needed to be optimised. Furthermore, we fix the hydroxylation ratio by taking h_H/h_N = 0.14 which is based on measured literature values from (Tuckerman, et al. 2004) for the hydroxylation rate of the PHD2 isoform (widely considered to be the 'critical oxygen sensor' e.g. (Berra, et al. 2003)). The number of values to optimise in the system is thus reduced to four model parameters (S, γ, k and d) and the two initial conditions $x(0)$ and $y(0)$.

For the remaining values to be chosen it is desirable to start in an appropriate (i.e. feasible and probable) part of the multi-dimensional parameter space to try and avoid convergence on unwanted local minima. This approach generally resulted in better fits that also converged to a minimum much faster than completely random initial estimates for the parameters. This was especially the case for more qualitatively interesting/complex dynamics such as the quasi-symmetric 'bell-shaped' HIF-1α profiles seemingly characteristic of the transient response in this signalling pathway. Indeed, it was this considerable subset of relatively complex dynamics in particular that inspired the inclusion of Michaelis-Menten kinetics in the model since a pure law-of-mass-action model seemed unable to represent these essential features successfully. The appropriate region of parameter space in which to begin the search was determined with a careful choice of initial parameter estimates.

2.3.1 Initial Parameter Estimates

2.3.1.1 Initial Conditions and Basal HIF-1α Synthesis

When fitting the data we assume that for $t < 0$, before a switch in oxygen conditions is applied, the state of the system is at equilibrium, (x^{EQ}, y^{EQ}).

$$x^{EQ} = \frac{dS + \sqrt{(dS)^2 + 4hkdS\gamma}}{2hk} \tag{2.18}$$

$$y^{EQ} = \frac{kx^{EQ}}{d} \tag{2.19}$$

Under this assumption we can then take the first experimental data-point as an initial estimate for the value of HIF-1α at $t = 0$ and hence the value of HIF-1α at the system's unique equilibrium (2.18). Using this initial estimate for x^{EQ} we can also derive an initial estimate for the value of PHD at $t = 0$, y^{EQ} using equation (2.19). We can also use the steady state assumption,

$$\frac{dx}{dt} = S - hy\left(\frac{x^{EQ}}{x^{EQ} + \gamma}\right) = 0,$$

to choose an initial estimate for another parameter, for example the basal synthesis rate of HIF-1α, S. That is, for initial parameter estimates in the optimisation algorithm, $x(0)$ was made equal to the experimental data point at $t = 0$, and $y(0)$ and S were re-defined as functions of the remaining parameters by assuming equilibrium at $t = 0$:

$$y(0) = \frac{kx(0)}{d},$$

$$S = h\frac{kx(0)}{d}\left(\frac{x(0)}{x(0) + \gamma}\right).$$

2.3.1.2 PHD Degradation

Experimentally measured half-lives of PHDs were used to calculate an initial estimate for d, the basal degradation rate of PHD. The half-life of the pathway's main oxygen sensor, PHD2, has been measured at 785 minutes by means of imaging experiments using cycloheximide to block protein synthesis (Bagnall, et al. 2013). More details about these experiments can be found in Chapter 3, section 3.3.1. The rate of change of PHD is described by the dynamic equation

$$\frac{dy}{dt} = kx - dy. \tag{2.20}$$

At equilibrium,

$$y^{EQ} = \frac{kx^{EQ}}{d}.$$

If we begin at the steady state and take away production terms from (2.20) (i.e. set $k = 0$) then we have the following exponential decay:

$$\frac{dy}{dt} = -dy,$$

$$\Rightarrow y = y^{EQ}e^{-dt}$$

So to find the degradation rate d, we need to now equate this exponential decay from equilibrium to the value halfway between equilibrium and 0.

$$y^{EQ}e^{-dt} = \frac{y^{EQ}}{2},$$

$$\Rightarrow d = \frac{\ln(2)}{t} = 8.83\times10^{-4}\text{min}^{-1}\ (3.\text{s.f})$$

2.3.1.3 PHD Induction Rate and the HIF-1α Michaelis Constant

For the two remaining parameters being optimised, k and γ, initial ranges were used rather than points. The Michaelis constant γ should be comparable to the amount of protein for which saturation is observed to justify its inclusion in the model. For this reason it was assumed to be of the same order as x as we consider the non-linear hydroxylation term in the model to be significant in capturing the full range of HIF-1α dynamics. Therefore, the initial estimate range for γ was based around the initial x value (the first data point) varying an order of magnitude either way. Let this value be γ^*. This degree of variation was implemented since it should also be noted that x reaches significantly higher levels during hypoxic induction compared to normoxic equilibrium.

During preliminary optimisation, the value for k showed less variation than the other parameters falling between 2.24×10^{-4} and 5.49×10^{-4} for 6 cells (a small subset of bell-shaped/peak data). This appeared to be due to the extreme sensitivity of the parameter and the emergence of its role (during parameter variation analysis, see Figure 2-12) as a key parameter in the model for determining peak duration. An average value was taken from these relatively conserved k values and the range for our current optimisation method was based upon this value allowing for variation of up to an order of magnitude either way. Let this average value be k^*.

The parameter variation results in Figure 2-12 indicate different properties of the model parameters. For example, varying the S parameter, representing HIF-1α synthesis, yields a linear response in peak

amplitude within the applied range. Other parameters show non-linear responses in peak amplitude to this form of variation. For example, linearly increasing parameters γ and d (Michaelis constant and basal PHD degradation) appears to have a saturating effect on the change in peak amplitude. Other potential dynamic properties of interest are peak duration and steady state levels. Reducing the k value, representing HIF-1α-induced PHD production, to 25% of the original value has by far the greatest effect on maximum peak amplitude when compared to analogous perturbations of the other model parameters. It also has a much greater effect on peak duration extension which appears to have a non-linear relationship with linear k variation within this range. These results highlight the sensitivity of the model to k variation in particular with respect to the hypoxic dynamics of HIF-1α. All simulations assume normoxic equilibrium before hypoxia is induced at $t = 0$ by reducing parameter h from 1 to 0.14.

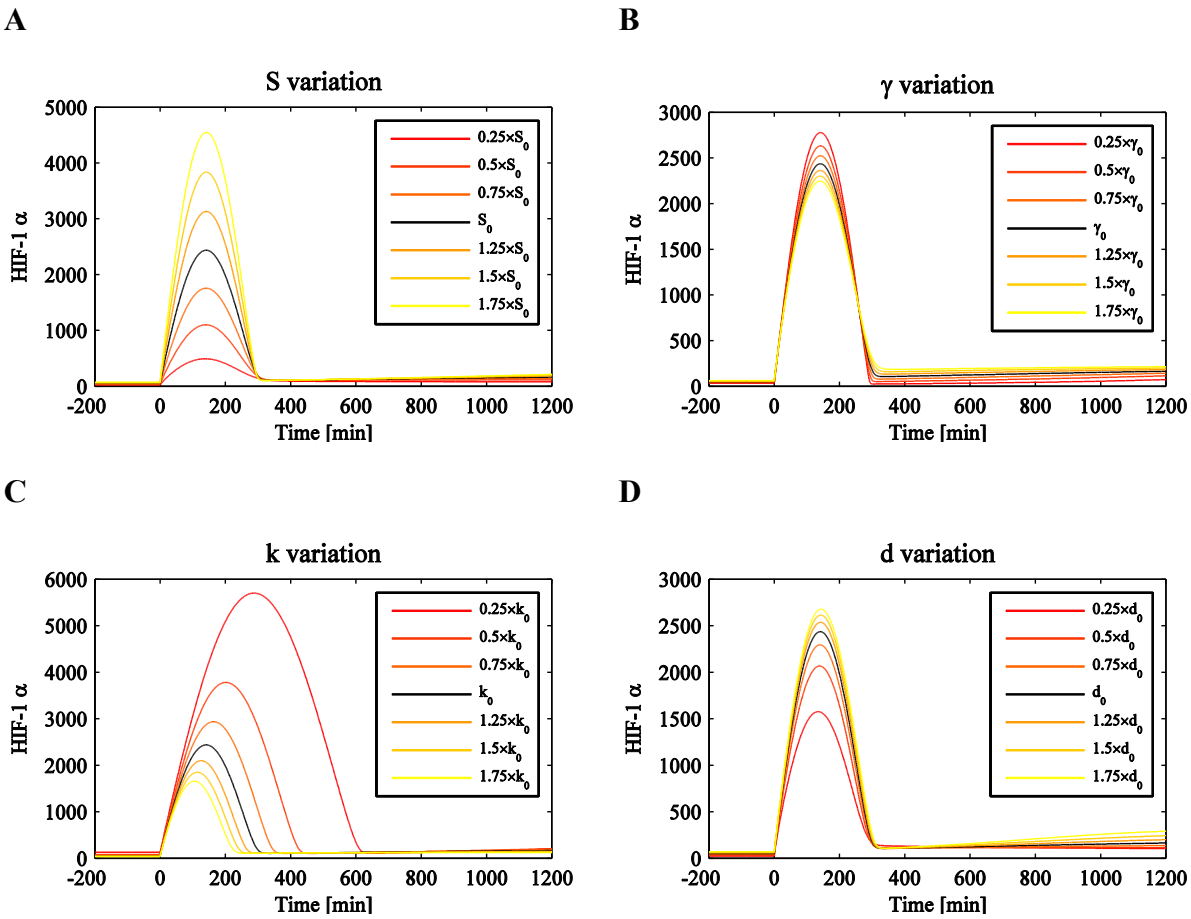

Figure 2-12: Four plots showing individual parameter variation from the same original parameter set (black curve, 0 subscripts) for model parameters S (A), γ (B), k (C) and d (D). In each of the four plots one parameter has been chosen to deviate away from an original parameter set (producing black curve HIF-1α dynamics). This parameter deviation was applied as a proportion of the original parameter value as denoted in the figure legend. For example, a curve with legend title $0.5*S_0$ represents HIF-1α dynamics for the parameter set identical to the original (black curve) except that the original S value, S_0, has been halved. Parameter values: $S_0 = 3.88\times10^{1}$ AU min^{-1}, $\gamma_0 = 7.13\times10^{1}$ AU, $k_0 = 8.99\times10^{-4}$ min^{-2}, $d_0 = 4.71\times10^{-4}$ min^{-1}.

2.3.2 Sampling

For each optimisation procedure a Latin Hypercube Sampling approach was used to generate initial γ and k values from their assumed ranges. These samples were then used along with the other pre-determined initial parameter estimates as the input for the minimisation algorithm, *fminsearch*. In practice, as we are now only sampling from the ranges of two parameters, a Latin Square is produced (ensuring that there is only one sample taken per row and column) and so a well spread distribution is guaranteed (see Figure 2-13). The optimisation for each experimental cell was repeated with 50 different initial estimate samples. For each of these 50 optimised sets of parameters, the error function χ is calculated and the smallest χ is elected to represent the best fit to the data. A flow chart outlines the parameter optimisation process in Figure 2-14. Once the *fminsearch* algorithm had converged on an optimised parameter set we repeated the process using these new parameters. This procedure was iterated until the χ value from the current parameter set was less than 1% smaller than the previous χ. A maximum of 100,000 iterations within each run of the *fminsearch* algorithm was permitted but never exceeded.

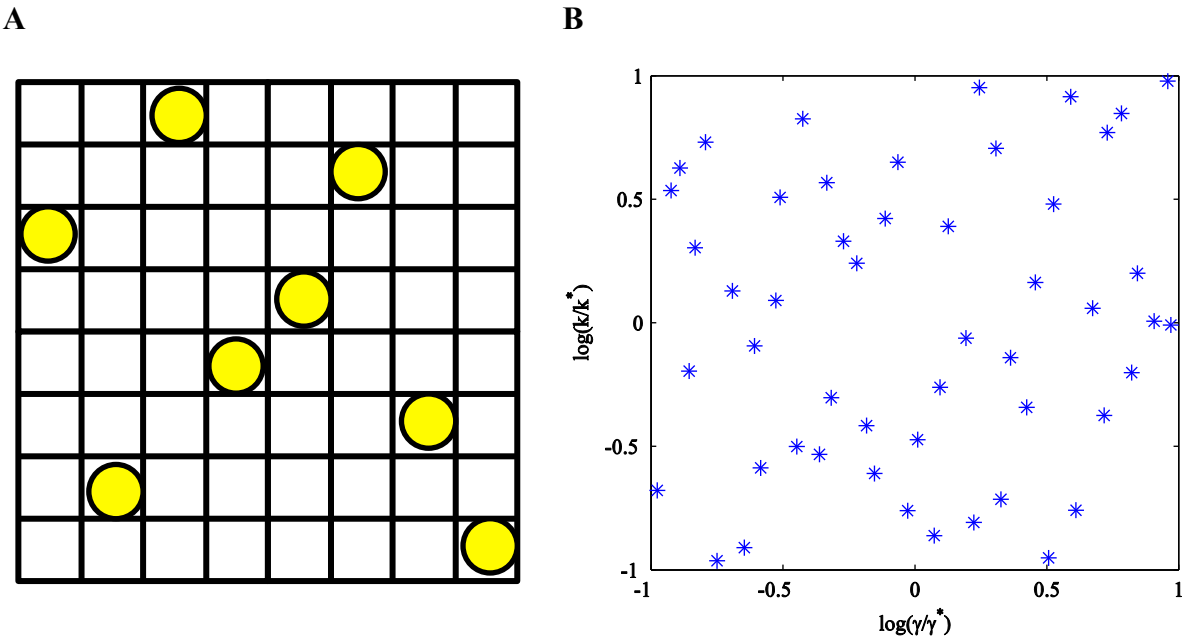

Figure 2-13: (A): An example of a Latin Square with one sample point in each row and each column. (B): A log-plot example of the sampling of the γ-k parameter space at the start of the optimisation process (Figure 2-14) used for the fitting of HIF-1α fluorescence time-series data. $k^* = 3.15\times10^{-4}$ and $\gamma^* = 1.88\times10^{3}$.

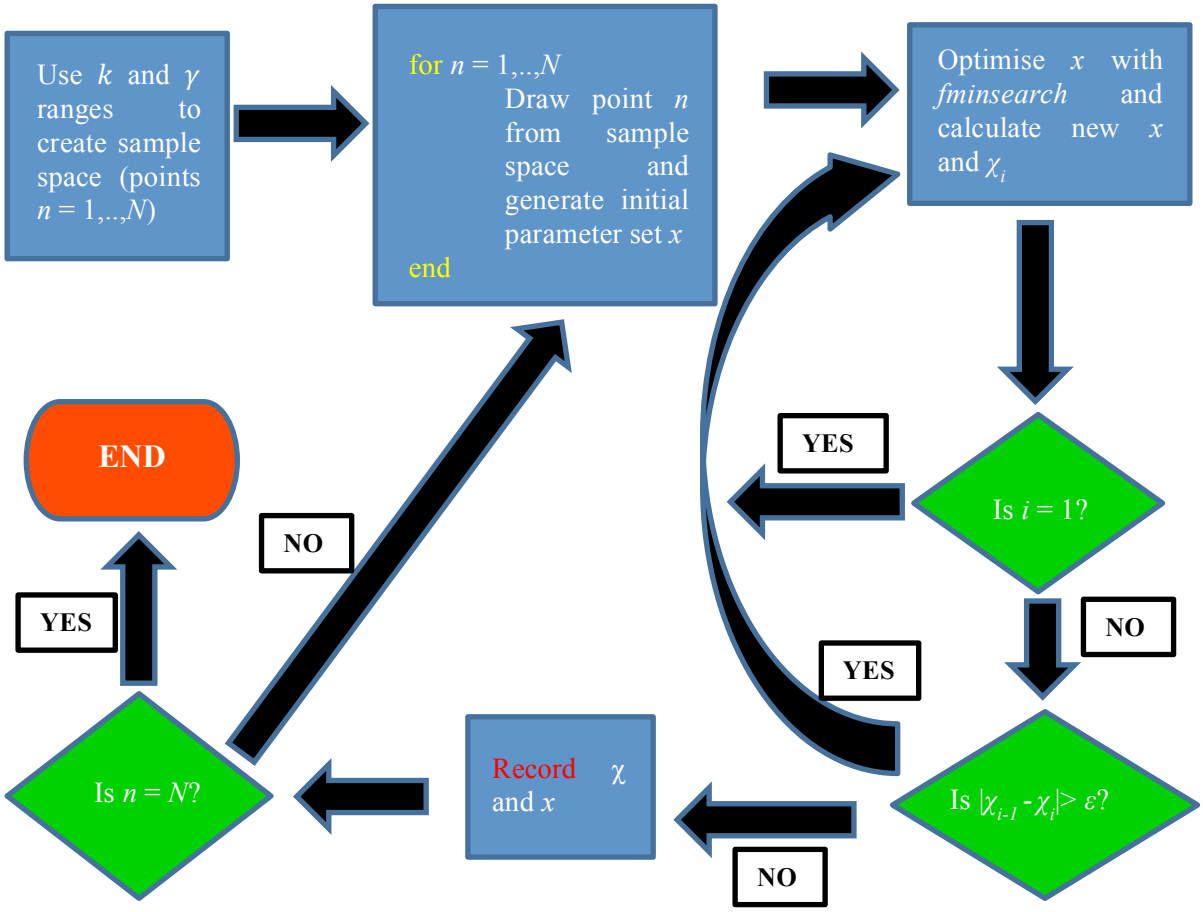

Figure 2-14: Flow chart outlining the general process of parameter optimisation. i represents the amount of iterations of *fminsearch* required in order to satisfy the inequality $|\chi_{i-1} - \chi_i| < \varepsilon$, where ε is a pre-determined threshold equal to $0.01\chi_{i-1}$.

2.3.3 Free Optimisation of Bell-shaped Data

The model parameters were initially optimised for a specific subset of the available data. This data corresponded to cells that shared a qualitative bell-shaped property in their transient HIF-1α dynamics during hypoxic induction. The purpose of this was to focus on a smaller and less heterogeneous set of data that is more complex dynamically than the rest (so we imagine the optimised parameter solutions to be more specific) yet had shared properties such as peak duration and qualitative symmetry. Moreover, our intention was to then focus on a smaller, localised parameter space for any further data-fitting. Initial estimates for parameters were obtained as described in section 2.3.1, and the only constraint on parameters during optimisation was that they remained positive. Fitting results of the 11 'bells' are shown in Figure 2-15 and optimised parameters are shown in Figure 2-16.

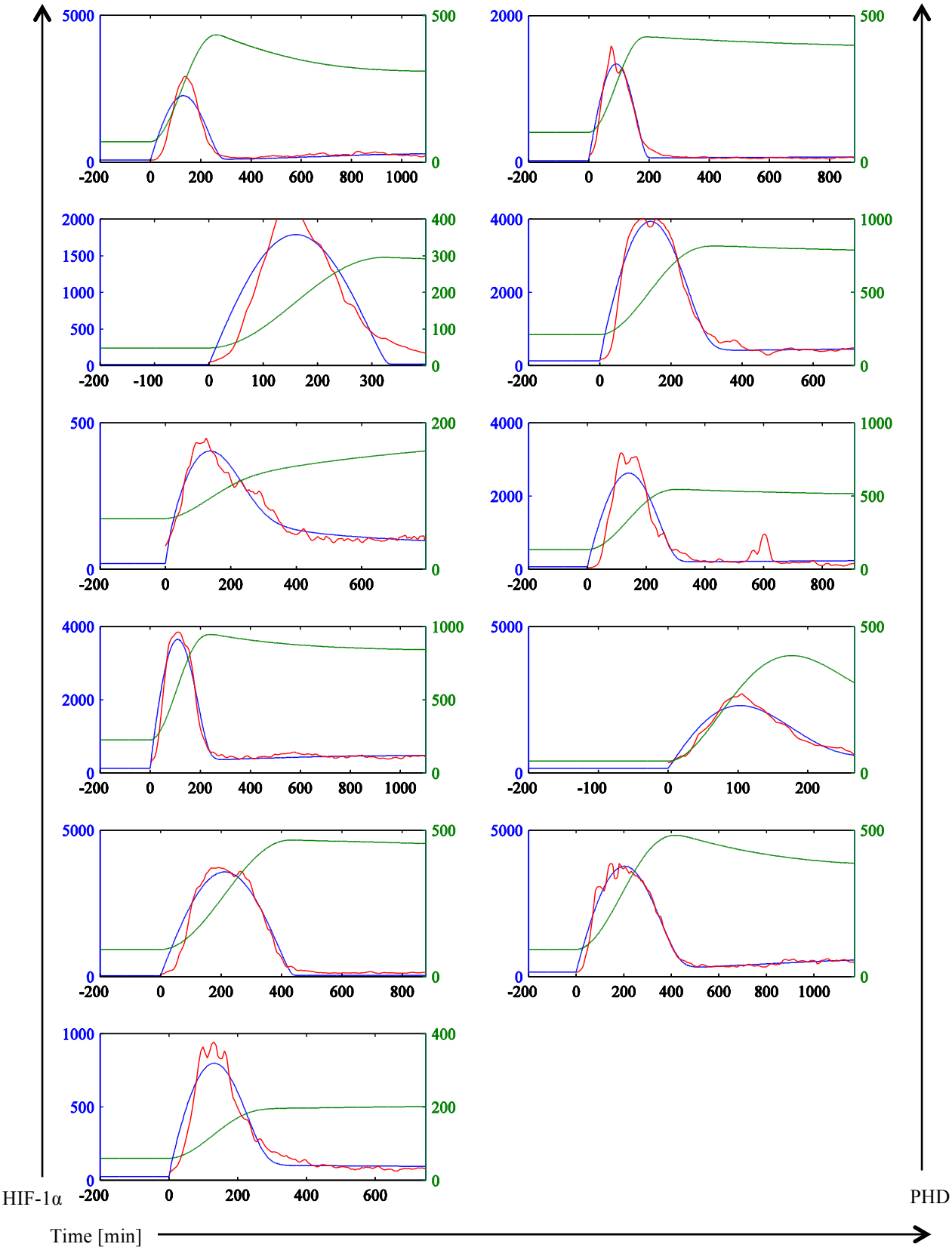

Figure 2-15: Plots showing the fits of the 11 'bells' obtained through the method of parameter optimisation outlined in Figure 2-14 using model (2.17). Red curves represent HIF-1α fluorescence experimental data (arbitrary units), blue curves represent the model output of HIF-1α (x) that has been fit through parameter optimisation; and green curves represent PHD (y) which was not fit to data.

We analysed how unique the best fits were among all the samples in an attempt to determine how sensitive this fit was to initial parameter estimates and justify the amount of samples we take. When convergence near a best fit (within 5% of the minimum χ) is found from multiple initial parameter values we note how the final parameter estimates compare. Several best-fit values with very different parameter values suggest that there are multiple combinations of parameter values that result in the same HIF-1α dynamics. We suspect this to be the case for more simple dynamics and therefore only initially fit to the more complex subset of bell dynamics in an attempt to hone in on a single localised region of parameter space.

Results of Figure 2-16 generally strengthen the claim that the optimisation algorithm converges on the same local minima. On average, more than half of all initial parameter estimate samples led to convergence within 5% of the best fit (minimum χ). This value is out of a potential maximum of 50 as 50 initial parameter sets were chosen for optimisation by sampling the k-γ space (see Figure 2-13). These results imply that 50 random samples is a sufficient selection for initial parameter estimate generation. Moreover in most cases, these multiple convergences also shared the same set of parameter values to represent the best fit. These results are useful as they imply that the variation in parameter value from cell to cell is a result of the variation of the dynamics displayed in the data rather than initial starting points of our fitting algorithm.

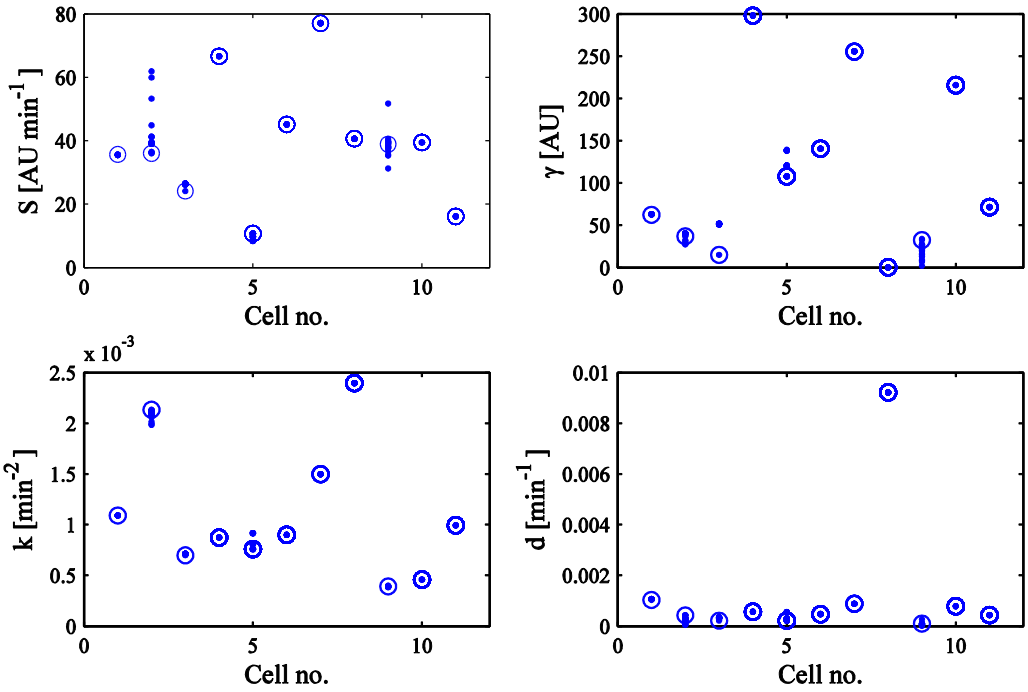

Figure 2-16: Scatter plots represent the best-fit parameters optimised independently for each individual single-cell data that displayed a bell shape profile. Data-fitting was carried out using the 2-component model in (2.17) and each sub-plot refers to a parameter of this system. Each blue point on an individual plot represents a parameter value for a single cell that corresponded to a fit that was within 5% of the best fit (i.e. minimum χ). Blue circles represent the parameter value corresponding to the minimum χ value.

2.3.4 Constrained Optimisation

All heterogeneity in the experimental data is accounted for in our optimisation process through the variation of parameters. By examining the experimental protocol and the model we can predict which parameter values may be expected to vary between experiments and between cells.

The HIF-1α dynamics are visualised through transient transfection of the cells with HIF-1α green fluorescent fusion protein. The method of transient transfection leads to cells with different copy numbers of the HIF-1α fusion constructs. In our model this corresponds to S, the basal synthesis rate of HIF-1α, taking fold-differences in value, i.e. not being conserved across cells. This affects the comparability of HIF-1α synthesis rates between cells.

The dynamics in the experimental data are represented by arbitrary units (AU) of fluorescence measured by the microscope. The experimental imaging protocol involves manually adjusting laser settings in order to optimise the image. Gain and offset values are fine-tuned at the start of each experiment to minimise noise-to-signal ratio and avoid saturation of the signal. This affects the comparability of fluorescence units between experiments. That is to say if 1 unit of fluorescence in

Experiment 1 corresponds to X HIF-1α molecules, 1 unit of fluorescence in *Experiment 2* corresponds to Y HIF-1α molecules, where X is not necessarily equivalent to Y. To understand how this affects parameter variation an investigation into the effects of scaling was conducted in order to determine if there are any parameters that are independent and can be compared between experiments.

2.3.4.1 Scaling Analysis

Three sets of model parameters were introduced to analyse the effects of scaling on parameter variability: the *real* parameters (superscript R); the *measured* parameters (superscript M); and the *fitted* parameters (superscript F). So the *real* system as represented by our model (i.e. a model representing values for the *in vitro* cells and independent of scaling), has the following form:

$$\begin{aligned} \frac{dx^R}{dt} &= S^R - h^R y^R \left(\frac{x^R}{x^R + \gamma^R} \right) \\ \frac{dy^R}{dt} &= k^R x^R - d^R y^R \end{aligned} \tag{2.21}$$

Now we assume that *measured* model variables are related to real model variables by a scaling factor due to experimental differences in the measurements of fluorescent data. For the most generally applicable case where HIF-1α and PHD are measured separately, the following re-scaling relates the *real* to *measured* variables:

$$x^R = Ax^M,$$

$$y^R = By^M.$$

System (2.21) now becomes:

$$\begin{aligned} \frac{dx^M}{dt} &= \frac{S^R}{A} - \frac{h^R B}{A} y^M \left(\frac{x^M}{x^M + \frac{\gamma^R}{A}} \right) \\ \frac{dy^R}{dt} &= \frac{k^R A}{B} x^M - d^R y^M \end{aligned} \tag{2.22}$$

We can now re-write the *real* parameters in terms of the *measured* parameters.

$$S^R = AS^M, \qquad h^R = \frac{A}{B} h^M, \qquad \gamma^R = A\gamma^M,$$

$$k^R = \frac{B}{A} k^M, \qquad d^R = d^M.$$

As before we apply our re-scaling of PHD that reduces the number of parameters in the system to be optimised during data-fitting:

$$y^F = h_N^M y^M.$$

This re-scaling applies to our *fitted* model variables.

The HIF-1α (x) ODE of system (2.22) in normoxia becomes

$$\frac{dx^M}{dt} = S^M - y^F\left(\frac{x^M}{x^M + \gamma^M}\right),$$

and in hypoxia becomes

$$\frac{dx^M}{dt} = S^M - \left(\frac{h_H^M}{h_N^M}\right) y^F\left(\frac{x^M}{x^M + \gamma^M}\right).$$

The PHD (y) ODE becomes

$$\frac{dy^F}{dt} = h_N^M \frac{dy^M}{dt} = h_N^M k^M x^M - h_N^M d^M y^M = h_N^M k^M x^M - d^M y^F.$$

Thus, we have the *fitted* system:

$$\frac{dx^F}{dt} = S^F - h^F y^F\left(\frac{x^F}{x^F + \gamma^F}\right)$$
$$\frac{dy^F}{dt} = k^F x^F - d^F y^F$$

Finally we can re-write the *real* variables and parameters in terms of the *fitted* variables and parameters:

$$x^F = x^M = \frac{x^R}{A} \quad \Rightarrow \quad x^R = Ax^F,$$

$$y^F = h_N^M y^M = \frac{B}{A} h_N^R \frac{y^R}{B} \quad \Rightarrow \quad y^R = \frac{A}{h_N^R} y^F,$$

$$S^F = S^M = \frac{S^R}{A} \quad \Rightarrow \quad S^R = AS^F,$$

$$\gamma^F = \gamma^M = \frac{\gamma^R}{A} \quad \Rightarrow \quad \gamma^R = A\gamma^F,$$

$$k^F = h_N^M k^M = \frac{B}{A} h_N^R \frac{A}{B} k^R \quad \Rightarrow \quad k^R = \frac{k^F}{h_N^R},$$

$$d^F = d^M = d^R \qquad \Rightarrow \qquad d^R = d^F.$$

$$h^F = \begin{cases} h_N^F = 1 \\ h_H^F = \dfrac{h_H^M}{h_N^M} = \dfrac{h_H^R}{h_N^R} \end{cases}$$

In summary, the original measured scaling of PHD (B) is irrelevant to the relationship between the *real* parameters and the *fitted* parameters (it has been absorbed in the further scaling process). We would not expect *fitted* parameters k and d to vary between cells. That is, we would not expect these values to vary due to arbitrary fluorescence units between experiments at least. This is a useful observation as it provides us with a way to constrain our optimisation technique in an attempt to further validate and/or strengthen the current feedback mechanism in the model. Also note that the *fitted* d should correspond to the *real* d which reinforces our justification for using a measured PHD degradation rate as an initial estimate during optimisation.

2.3.4.2 Optimisation Constrained by the Conserved Parameters of a Median Bell

Using the scaling analysis information, additional parameter optimisation simulations were carried out with a tightly imposed restriction on parameters k and d in order to compare the fitting of our mathematical model to all the available single-cell HIF-1α data. This restriction involved taking the median values of k and d found over all the bell-shaped data that was fit to using the previous free-optimisation method described in section 2.3.3 (see Figure 2-16 and also Figure 2-17).

The optimisation process was modified by only allowing k and d to vary by 50% either way of the median using a suitably customised *fminsearch* in a constrained optimisation. Note that this resulted in a slight change in the initial choices of parameters for the fitting process. We chose the median values of k and d obtained in the bell fitting as initial estimates. Also, we now only needed to randomly sample from a prescribed range for one parameter's initial estimate, namely γ. Again we took 50 samples per cell (this time from the one-dimensional γ-space) and analysed the relationships between initial parameter estimates, best-fit convergence and number of samples as before with the free optimisation of the bells (see Figure 2-20). During constrained optimisation, we would sometimes find that a particularly poor initial estimate for the model parameters would result in a very long optimisation process that eventually resulted in a poor 'best fit'. To prevent this and save time we implemented a timeout condition into the MATLAB code which would stop the optimisation process if it took longer than 5 minutes. Optimised parameter results from such events were not recorded but the χ values were. The results of fitting to data from de-oxygenation experiments can be seen in Figure 2-18 and re-oxygenation experiments in Figure 2-19.

A

S	γ	k	d
3.88×10^{1} AU min^{-1}	7.13×10^{1} AU	8.99×10^{-4} min^{-2}	4.71×10^{-4} min^{-1}

B

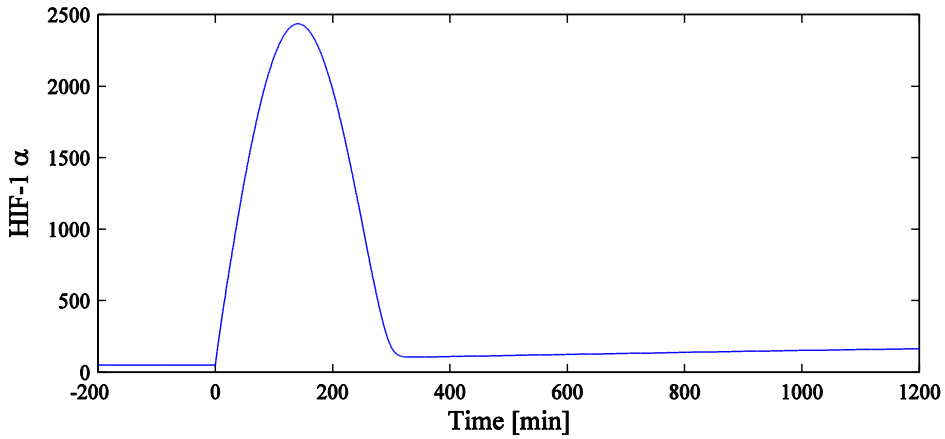

Figure 2-17: (A): A table showing the values obtained by calculating the median values of optimised parameters shown in Figure 2-16. (B): A plot of the 'median bell cell'; the output of the ODE model using the parameters in the table, starting from a normoxic equilibrium ($t < 0$) before hypoxia is simulated by decreasing the hydroxylation rate, h, at $t = 0$.

Figure 2-18 and Figure 2-19 show the full variety of HIF-1α responses to hypoxic induction and re-oxygenation in single cells. It is the de-oxygenation (hypoxic induction) experiments which seem to show the most cell-to-cell variation, particularly between *Experiments 1&2*. The bell-like feature of the dynamics is only seen in *Experiment 2* where it occurs at least 11 times whilst *Experiment 1* tends to show more ramp-like dynamics with a slower accumulation of HIF-1α in hypoxia and a lower fold-induction. Generally model (2.17) appears to fit the data well even under a strict constraint applied during parameter optimisation.

To discover if the simple feedback model really was still successful at fitting data under these constraints, we needed to formulate a quantitative way of comparing the quality of data-fits between optimisation methods, both free and constrained. Simply comparing values of χ is not sufficient to determine whether the 'best fit' (i.e. the minimum χ value) is a 'good fit'. Comparing χ values between different cells is an irrelevant measure since different cells have different amounts of data-points. Data with more points would have a larger χ value for the same quality of fit (e.g. 1% error at every point). Also, different cells (especially those from different experiments) are potentially measured on a different scale of arbitrary fluorescent units leading to different χ values. Comparing χ values between the same cells should be relatively satisfactory since we have the same units and length of data and we also analysed how other similar fits compared in our post-optimisation analyses (see Figure 2-16 & Figure 2-20). However, comparing between χ values for the same cell might show

which fit is better, but the best fit could still not fit the data very well. We determined which optimisation results were good fits by defining an *Error Envelope* (see the Appendix, section 7.2).

We categorised 79% (31/39 cells) of the de-oxygenation data and 74% (31/42 cells) of the re-oxygenation data as data displaying dynamics that our model can be successfully fit to. That is our model provided 'good fits' to these data according to our definition. For an example categorisation of good and bad fits see the Appendix, Figure 7-1. We feel these proportions add reasonable weight to the claim that the simple minimal 2-component feedback model exhibits a good central network motif to capture the essential characteristics of the dynamic experimental data. Therefore, we conclude that this motif provides a good basis for any further mathematical modelling of the HIF-1α signalling pathway. However, there are several instances where the model was unable to fit the data successfully ('bad fits', as defined by the *Error Envelope*, are labelled in Figure 2-18 and Figure 2-19). These data tend to fit into three categories: low induction (e.g. cells 1, 4, 49, 53 – see Figure 2-18 & Figure 2-19 for numbering); signal saturation (e.g. cells 26, 30); and multiple peaks (e.g. cells 33, 37).

In low induction cases the difference between the normoxic equilibrium and peak hypoxic accumulation (or vice-versa with respect to oxygen in re-oxygenation experiments) appears to be too small for the switch in h parameter being applied in the model. These data could suggest a variation in PHD hydroxylation rates h but if that is the case the source of this heterogeneity in oxygen sensitivity is unclear. Alternatively, the heterogeneity may be a result of a significant variation in HIF-1α copy number (number of HIF-1α molecules in the cell). This can happen as a result of transient transfection, where HIF-1α is overexpressed in the cells but the amount of extra HIF-1α incorporated into each cell varies. In the model this would translate to a variation in HIF-1α synthesis, S (note the effects of varying S on peak amplitude in Figure 2-12). For example, different S rates appear to cause different relative accumulation in hypoxic HIF-1α peaks. We might expect the parameter optimisation process to compensate for this heterogeneity by varying the S parameter which is unconstrained. However, another key feature of the data is peak width, something that is less easily influenced by S variation (see Figure 2-12). In the low induction cases, the peaks not only exhibit lower relative accumulation but broader peak-width. Thus an ideal parameter optimisation of low-induction-peaks might involve a decrease in S (mimicking lower transfection and resulting in lower HIF-1α induction) and a decrease in k (which can increase peak width as well as compensating for the change in equilibrium levels caused by S variation). However k (or more accurately the non-dimensional $h_N k$) is constrained due to our scaling analysis. Indeed since k, a key determinant of both peak amplitude and width, is relatively constrained the S value is decreased/increased during optimisation to best fit the low-induction dynamics but the cost of this is a poor normoxic/hypoxic equilibrium value (see Figure 2-18/Figure 2-19). Thus, the simplicity of this model with relatively constrained parameter

variation may not be able to fully account for experimental heterogeneity caused by variance in the efficiency of transient transfection.

Signal saturation refers to cases where the accumulation of HIF-1α is higher than the threshold of fluorescence detection of the microscope. This leads to a steady signal and the transient dynamics of HIF-1α in the cell are not captured. Multiple peak data describes data where two distinct periods of transient HIF-1α dynamic occur. This wasn't a common phenomenon and only happened in de-oxygenation experiments. Model (2.17) is not suitable to reproduce multiple peak dynamics such as growing oscillations as a result of a single hypoxic insult (change in h) as the steady state of the system is a unique, stable equilibrium. One possible explanation of data that appears to show two HIF-1α induction periods is experimental artefact where two cells have overlapped in the imaging field. Another possible explanation is an oxygen-independent form of HIF-1α regulation.

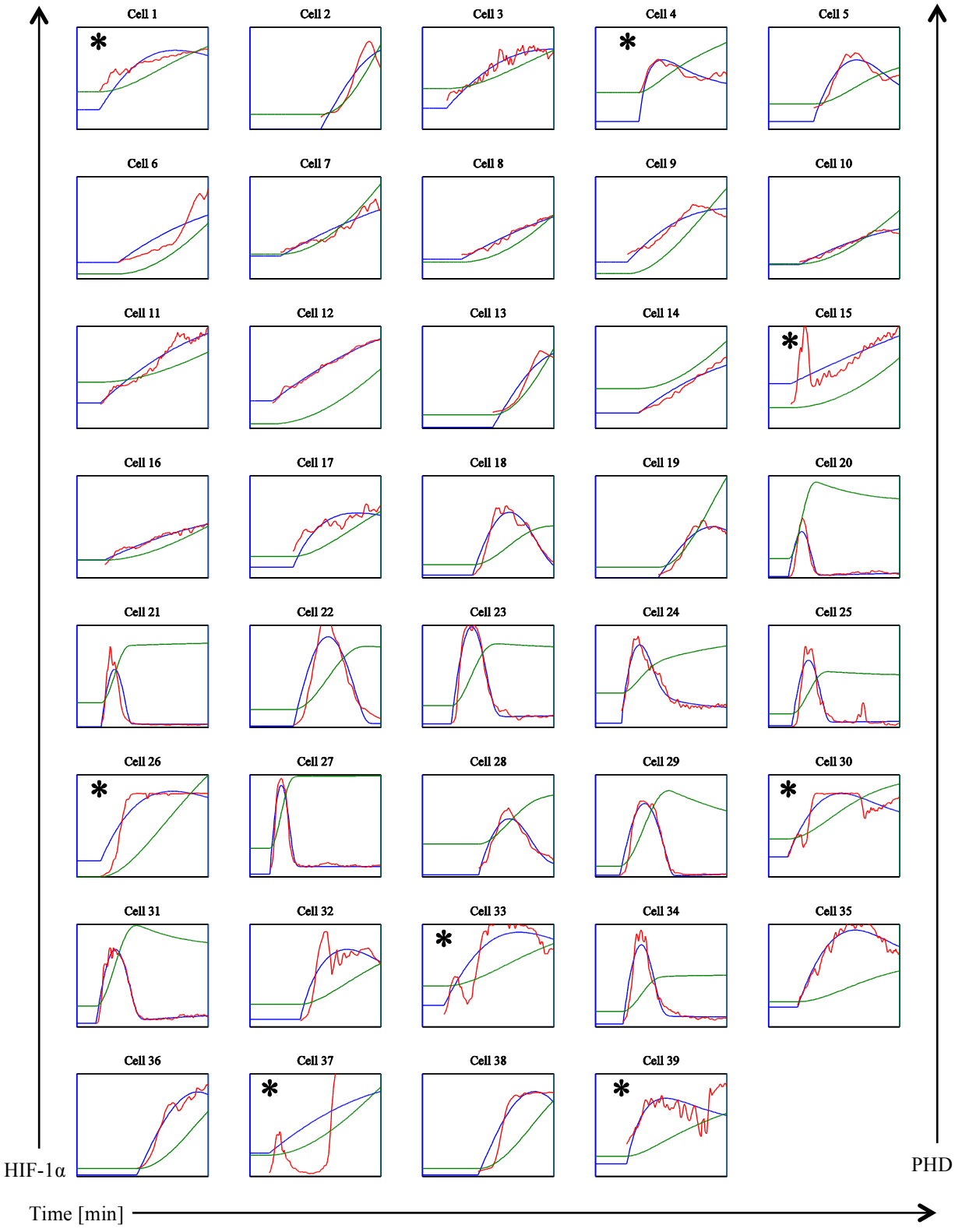

Figure 2-18: De-oxygenation data-fitting: cells are initially at equilibrium in normoxia ($h = 1$) and are de-oxygenated into hypoxia ($h = h_H/h_N$) at $t = 0$. Single-cell traces of HIF-1α dynamics (red line) were fitted computationally using the model described by (2.17) (HIF-1α, blue line; PHD, green line). The $*$ symbol highlights the cells that could not be fitted appropriately (see Figure 7-1 for examples of good and bad fits). Cells 1-17 belong to *Experiment 1* and cells 18-39 belong to *Experiment 2*.

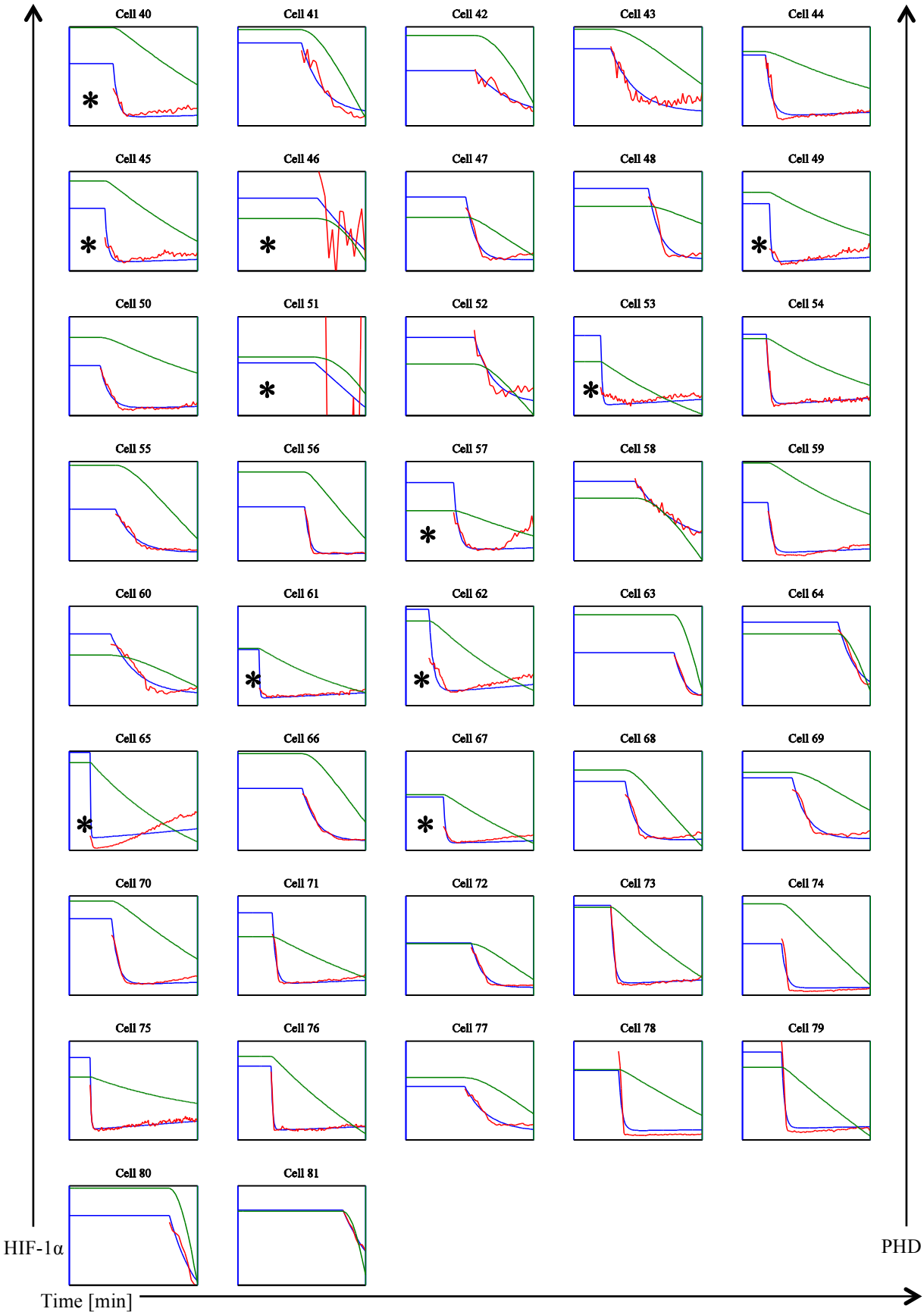

Figure 2-19: Re-oxygenation data-fitting: *Experiment 3* (cells 40-58) and *Experiment 4* (cells 59-81). Cells are initially at equilibrium in hypoxia and are re-oxygenated back into normoxia at $t = 0$.

Figure 2-20 shows the analysis of our constrained optimisation process. As a minimum, 20 out of the 50 parameter optimisation simulations converged towards the same χ value corresponding to the best fit. Specifically, there are at least 20 separate initial γ estimates that lead to convergence towards a χ value within 1% of the minimum χ value found and in the majority of cases this number is much higher. This suggests that the γ parameter space is adequately sampled. From now on, we will refer to χ values within 1% of the minimum χ as the best-fits for that data. For parameter S all best-fits correlated with the same S value and this was also the case for γ in most cells, although γ appeared to be less sensitive to change (especially when γ is small). Specifically, when the minimum χ for a particular cell corresponded with a relatively low γ value ($\gamma \sim < 10^{-1}$), other fits that were within 1% of the same χ value had corresponding γ values that were up to two orders of magnitude greater in some cases. However, in the vast majority of cases, the best-fits corresponded to the same parameter set. These results support the claim that cell-to-cell parameter variation is a result of the data and not the optimisation method.

The colour scheme in Figure 2-20 reveals the experiment-to-experiment clustering of parameter values as hypothesised in our scaling analysis (section 2.3.4.1). As suspected parameters S and γ appear to be correlated with which experiment the data had come from (*Experiment 1*, *2*, *3* or *4*). However, while *Experiments 1,3* and *4* appear to correspond to our experimental scaling assumptions *Experiment 2* is an unusual case if we assume that these parameters are scaled with an arbitrary constant in the same manner (i.e. $S^R = AS^F$, $\gamma^R = A\gamma^F$). For the relatively high S values we find in *Experiment 2* parameter optimisation, we would expect to also see relatively high γ values due to the scaling of arbitrary units by the microscope whereas we actually have lower values. One possibility is a significant variation in S independent of γ as a result of transient transfection. Variation in HIF-1α copy number between cells as a result of transient transfection may lead to variation in S but not γ. Therefore it could be that γ values are generally lower in *Experiment 2* than *Experiment 1* as a result of the scaling of arbitrary units but S values are higher due to a significantly higher copy number of HIF-1α in *Experiment 2* as a result of transient transfection. This hypothesis may also be linked to why we only see bells in *Experiment 2*. Alternatively, the exclusivity of bells to *Experiment 2* may suggest that there are other means of regulation (e.g. oxygen independent) involved that we haven't accounted for in the model.

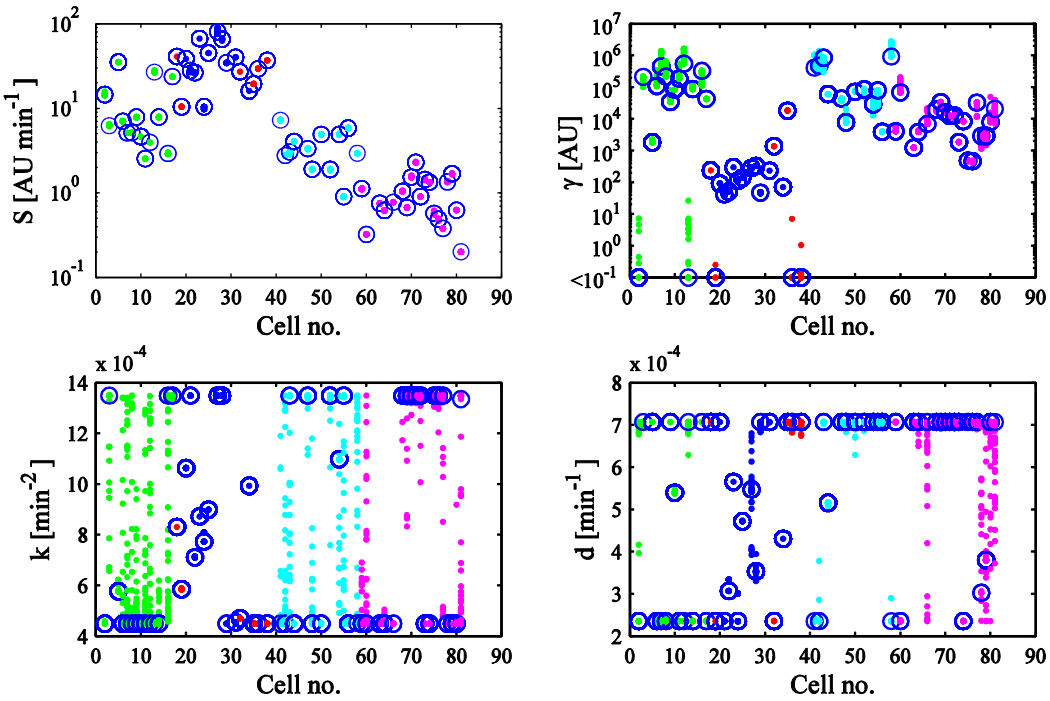

Figure 2-20: Scatter plots representing the optimised parameter values for all good data-fits (see 7.2 for the definition of good fits according to the error envelope). Blue circles indicate the parameter value corresponding to the minimum χ value from 50 simulations. Other parameter values corresponding to χ values within 1% of the minimum χ are also plotted in colours corresponding to their experiment and type. The colour scheme is: green – *Experiment 1* (de-oxygenation); blue – *Experiment 2* (de-oxygenation - 'bells'); red – *Experiment 2* (de-oxygenation - 'non-bells'); cyan – *Experiment 3* (re-oxygenation); magenta – *Experiment 4* (re-oxygenation).

Chapter 3

Modelling the Dynamics of the HIF-1α Signalling Pathway: Model Expansion & Analysis

---

3.1 Introduction

Using a combination of mathematical modelling and time-lapse single-cell imaging experiments we developed a representative core motif that describes the characteristic hypoxic dynamics of the transcription factor HIF-1α. This was achieved by focusing on the negative feedback relationship between HIF-1α and the oxygen sensitive prolyl-hydroxylase (PHD) enzyme (see Chapter 2 for details). The regulatory network of this simple feedback mechanism essentially involved: a) the induced production of a nonspecific PHD component at a rate linearly proportional to the amount of HIF-1α in the system and b) the non-linear destruction of HIF-1α by PHD in the presence of oxygen, a process which saturates for high levels of HIF-1α. However this mechanism provided enough complexity to reproduce the range of experimentally observed transient HIF-1α dynamics following two opposite, rapid oxygen-switch regimes. The variance in dynamics between individual cells was accounted for through parameter variation. Yet even when tight constraints were applied during parameter optimisation in the fitting of the model to experimental data, most dynamics could still be recaptured. This minimalist approach in modelling now allows us to build from a solid base derived from a known system mechanism without over-fitting the system. Indeed, by minimising the degrees of freedom during development of the core feedback device we can now extend to a more realistic model which will inevitably be more complex but will as a result allow the inclusion of parameter values that can be experimentally measured.

When building upon the minimal 2-component model we highlighted the role of PHD for further investigation. Initially, due to the novel and revealing single-cell data available to us, we focused only on HIF-1α dynamics and how we could recapitulate the observed behaviour through the known negative feedback of PHD. In order to improve this basic mathematical model we expanded out the generic PHD component of the 2-component model into its three distinct isoforms: PHD1; PHD2; and PHD3. By doing this we could start to include experimental measurements pertaining to a specific PHD family member such as in knockout experiments where a specific component of the pathway can be effectively removed. This motivated the side-by-side collaboration of experiments and modelling as the role of PHD feedback was examined and parameters related to the feedback mechanism were measured experimentally in order to enhance the model's fidelity.

The removal of PHDs from the HIF-1α pathway has been investigated experimentally to clarify the distinct roles of the variants and to identify the key oxygen sensor in HIF-1α regulation (Berra, et al. 2003), as well as to investigate PHD inhibition as a therapeutic strategy, for example in neuroprotection after cerebral ischemia (Kunze, et al. 2012). The inhibition or silencing of PHDs has been studied frequently due to the role of PHDs in suppressing HIF-1 activity. Pathologies such as ischemia and anaemia could benefit from overexpression of HIF-1 due to the target genes it encodes

for. These genes include VEGF (vascular endothelial growth factor) and EPO (erythropoietin) which induce processes that mediate adaptation to hypoxic environments such as blood vessel formation and red blood cell production. For example, PHD inhibition has also been applied in the development of drugs that promote erythropoiesis in rhesus macaques by inducing the expression of EPO (Hsieh, et al. 2007), an application that is being investigated for the treatment of anaemia. However, PHD inhibition can also correspond to favourable conditions for tumour development due to the potential tumour suppressor qualities of PHDs. Indeed, overexpression of HIF-1α in tumours (which can be achieved via PHD inhibition) leads to aggressive growth and poor patient prognosis (Powis and Kirkpatrick, Hypoxia inducible factor-1alpha as a cancer drug target 2004). This is a direct consequence of the target genes of HIF-1 that are specifically designed to mediate cellular adaptation to hypoxic environments such as those caused by the rapid growth of malignant tumours. The inclusion of the three different PHD components in our model separately allows us to compare our model with experiments that modify the pathway by only affecting a specific PHD isoform. In this way we also aim to make a predictive model that provides information on the essential role of the feedback caused by the PHDs both collectively and individually.

In this chapter we also investigate how altering the pathway's oxygen signal affects HIF-1α dynamics. This function of the pathway is of particular interest due to the role of various oxygen dynamics in hypoxia related pathologies. For example ischemia is associated with a fast switch in oxygen levels as hypoxia is induced very quickly due to the restriction of a blood supply. Cancer can be associated with a much slower, more gradual hypoxic induction as tumour cells outgrow their blood supply over time. Sleep apnoea is an example of a pathology that exhibits the intermittence of de-oxygenation and re-oxygenation caused by abnormal breathing. Using mathematical models as a predictive tool can be extremely useful where actual experiments can be very expensive or labour intensive.

3.2 Model Extension

When deciding to expand the minimal 2-component model it was with the intention that this more sophisticated model could be used to compare with experiments generally and make general qualitative if not quantitative predictions. For these general applications and potential comparisons with data from multiple sources, and also for mathematical simplicity, we wish to develop a 4-component model based on a single representative parameter set. Specifically the dynamics produced by these model simulations could be representative of the average response of the signalling pathway to whatever stimuli we are studying (oxygen regimes, knockout experiments, potential drugs etc.) and so we use a single representative parameter set corresponding to a typical hypoxic response.

Depending on the nature of the heterogeneity that exists in the pathway, this characteristic response could be an example of one particular cell or only representative of the averaged dynamics of the entire population. The discrete categorisation of our single-cell data into bells and non-bells (or 'ramps') (see Figure 3-1) might suggest that an average cell would be more comparable with a population response, i.e., an averaged response that incorporates dynamics of both types. Averaged population responses using bulk-cell assays can provide intuition to a response on a larger scale but often conceal the underlying dynamics of single cells, e.g., out of phase oscillations. In this case we might expect (by looking at the examples in Figure 3-1) averaged HIF-1α dynamics to produce a broad, skewed peak of reduced peak amplitude. Indeed this is what is shown in many publications only studying HIF-1α at the population level (Bruning, et al. 2011, Bagnall, et al. 2013, Chávez, et al. 2000). However, the criterion for this discretisation of bells and ramps was based more on the similarity of the duration of the bells rather than the difference in qualitative dynamics with the so-called ramps. Indeed, one could consider the ramps to still have a qualitative bell shape, i.e. HIF-1α accumulation following hypoxic induction followed by a decrease in HIF-1α, at a comparable rate to the induction, back to a relatively similar lower level. It could just be that there are fast bells and slow bells and we are not seeing the resolution of the slow bells (opening up the possibility for an average cell to be in fact representative of a single cell after all). Unfortunately, the data is too limited in number to be able to answer questions about this form of heterogeneity conclusively. We will study the results of our minimal 2-component model, which was flexible enough to represent the single-cell HIF-1α dynamics, in order to provide motivation for a representative response of the pathway.

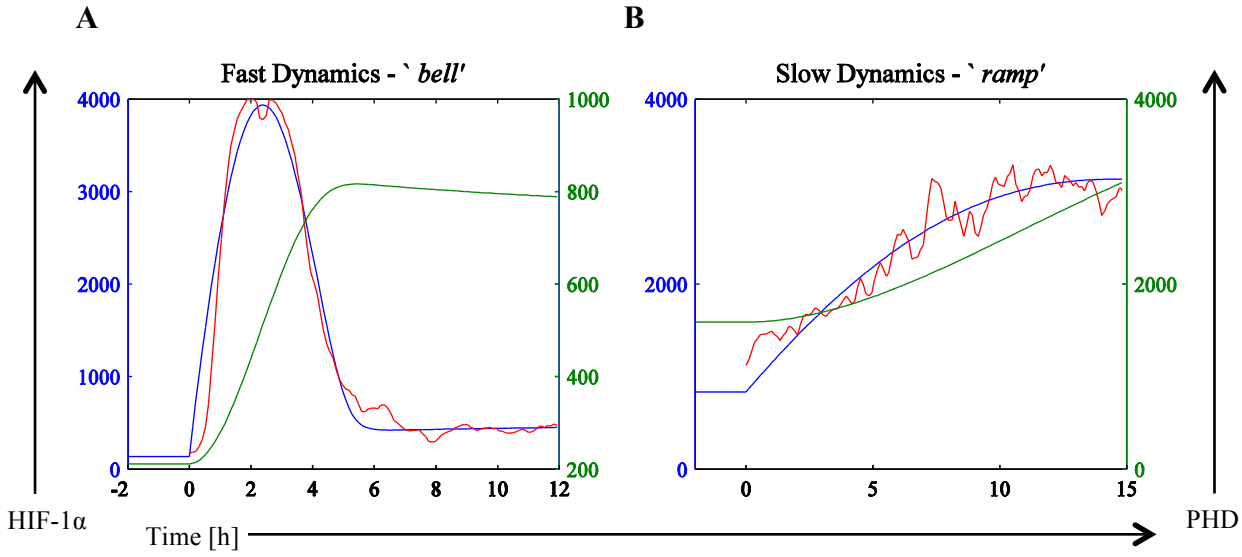

Figure 3-1: Two examples of single-cell HIF-1α dynamics after hypoxic induction that broadly encompassed two distinct categories of data: fast dynamics or 'bells' are represented in (A), typified by the quasi-symmetric peak in HIF-1α levels followed by a low hypoxic steady state; slow dynamics or 'ramps' are represented in (B) typified by their relatively slow accumulation of HIF-1α and seemingly lower peak amplitude.

3.2.1 A Representative Pathway Response in the Form of a Median Cell

In order to generate a representative hypoxic response of the HIF-1α signalling pathway with an expanded model, an average response had to be extracted from our 2-component model work. We will consider this response to be the characteristic HIF-1α dynamics in a typical cell. This average then informs us on what sort of dynamics we want the expanded model to produce. However, we also want to include as many parameter values as possible that can be derived from experimental measurements. To be able to include numerous measured physiological rates and still provide the required HIF-1α dynamics would go some way towards validating the foundations of the model structure. A representative response also allows us to analyse the general effects of varying model parameters individually. Initially, in order to derive an average cell response to an environmental oxygen switch we analysed the optimal parameters of the 2-component model given for all good fits during optimisation (see Chapter 2, Figure 2-20).

A median value was taken to represent the average parameter value for all data fits as this seemed a better representation of the average than the mean, which can be easily skewed by outliers. However, this median cell did not realistically represent the expected average hypoxic response; the transient contribution of the bells which make a large proportion of the de-oxygenation data did not seem to be represented for the hypoxic case (see Figure 3-2). The plot on the left of Figure 3-2 shows an unsatisfactory representative of HIF-1α dynamics after hypoxic induction in single cells. Due to the proportion of 'bell' data observed we would expect this response to share more bell-like properties such as a faster response time and a lower hypoxic steady state. This poor median may be explained by the median being taken across both types of experiments (de-oxygenation and re-oxygenation) whilst the parameter sets for each type are significantly different. The calculation of a median de-oxygenation response by taking into account the optimal parameters given by fits to re-oxygenation data may not be suitable here. That is, optimised parameter values for re-oxygenation experiments in Figure 2-19 correspond better with parameter values in the ramp-like behaviour seen in de-oxygenation *Experiment 1*. For example, *Experiment 1* (de-oxygenation) and *Experiments 3* and *4* (re-oxygenation) share the same properties of relatively high γ values and lower S values and a direct relationship. *Experiment 2* (de-oxygenation) exhibits bell-like dynamics and an inverse relationship between γ and S. The conformity in re-oxygenation (re-ox) experiments compared to the variation in de-oxygenation (de-ox) suggests that oxygen-dependent degradation dominates the dynamics of re-ox data while they may be more complex, additional regulation involved in the de-ox data.

A

Median S	Median γ	Median k	Median d
4.77×10^{0} AU min^{-1}	8.20×10^{3} AU	4.53×10^{-4} min^{-2}	7.07×10^{-4} min^{-1}

B **C**

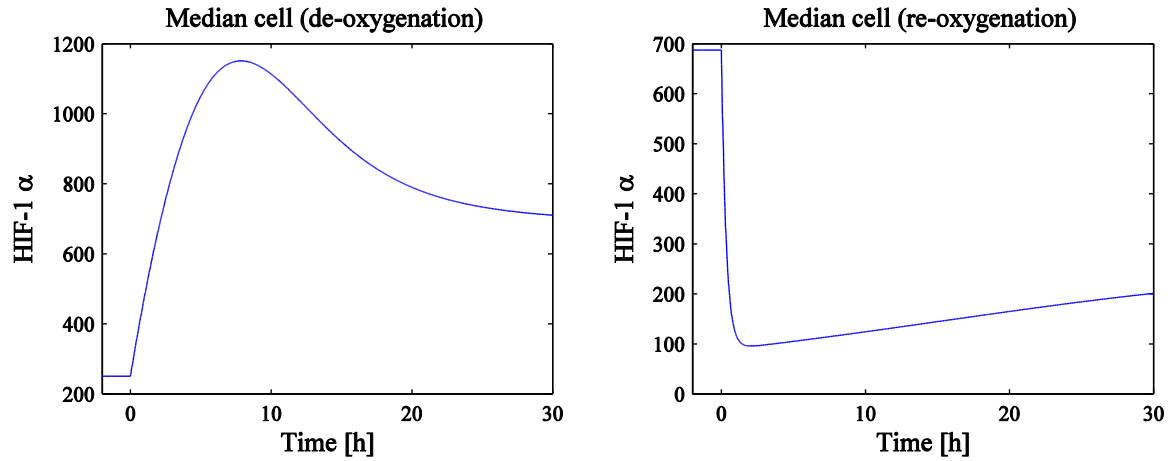

Figure 3-2: (A) The table shows the median parameter values calculated by analysing optimal parameters (good fits only) found during the fitting of the minimal 2-component model to the single-cell data (see Chapter 2). 'Median cell' HIF-1α dynamics are derived using parameter values in (A) with the 2-component model and plotted for de-oxygenation (B) and re-oxygenation (C) simulations.

A key parameter in determining the bell feature of HIF-1α dynamics is γ, a Michaelis constant that was introduced during model development as part of a saturation term; specifically the saturation of the hydroxylation effect or inhibition of HIF-1α by PHD. Recall that in the scatter plots of Figure 2-20 we observed that the optimised γ values are significantly different for points that correspond to bell data in *Experiment 2*. This non-linear kinetic term for the hydroxylation reaction was introduced purposely to address the more complex dynamics of the experimental data which we refer to as bells (see section 2.2.2). Therefore it is not particularly surprising that this subset of data corresponds with different γ values. However, due to the more homogenous response of re-oxygenation dynamics, this interesting dynamic feature of the pathway wasn't fairly represented when looking at re-oxygenation and de-oxygenation results simultaneously. For these reasons, we decided to look at the median parameter values for each of the two types of oxygen-switch experiment separately and plotted the corresponding median cells (see Figure 3-3). By doing this the interesting feature of the bell dynamics seen in approximately a quarter of the hypoxic data was better represented and the resulting average cell deemed more realistic. This does leave the mechanisms that explain the differences in our model unexplained (e.g. differences in γ in particular) but it might be argued that the relative homogeneity of the re-oxygenation data is a feature of the experiments if cells exhibiting higher hypoxic HIF-1α levels were targeted for imaging. Alternatively, the dominance of oxygen dependent degradation in

HIF-1α regulation may cause the homogeneity seen in re-oxygenation experiments when compared to de-oxygenation.

A

	Median S (AU min^{-1})	Median γ (AU)	Median k (min^{-2})	Median d (min^{-1})
D	2.38×10^{1}	2.98×10^{2}	4.71×10^{-4}	4.71×10^{-4}
R	1.35×10^{0}	1.63×10^{4}	4.50×10^{-4}	7.07×10^{-4}

B **C**

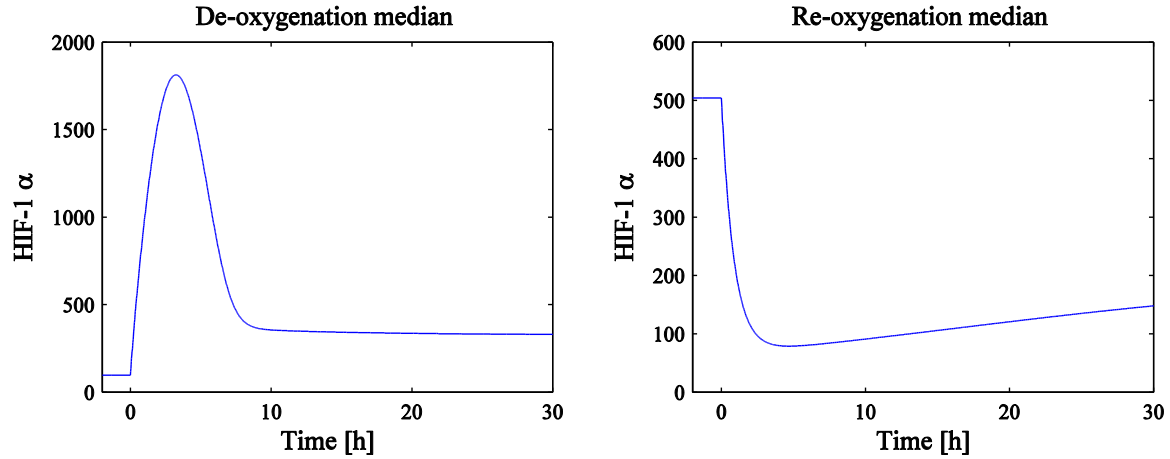

Figure 3-3: (A) The table shows median parameter values calculated by analysing optimal parameters found during the fitting of the minimal 2-component model to the single-cell data. The '**D**' row represents de-oxygenation median parameters and the '**R**' row represents re-oxygenation parameters. Plots of the median cells derived separately for both de-oxygenation (B) and re-oxygenation (C).

3.2.1.1 Parameter Variation Analysis of Median Cells

In order to better understand the role of the 2-component model parameters on the qualitative dynamics of the median cell, a basic parameter variation analysis was conducted. This was carried out by allowing model parameters to individually deviate from the median by graded amounts and the results were plotted in Figure 3-4. This analysis was analogous to the analysis of bell-shaped data in section 2.4.1.3 and was repeated here to determine whether the same results emerged when looking at a median cell. The results shown in Figure 3-4 indeed support previous findings that the parameter k, representing HIF-dependent induction of PHD was important in determining peak duration and response time and is very sensitive to changes. The peak duration (or transient dynamics) in particular is a dynamic property that shows large variance in the whole data yet tight conservation in the bells. During the analysis of the median cell it was also found that this property is effected considerably when varying the rate at which PHD is degraded, d. As the PHD degradation rate was reduced the peak duration was extended.

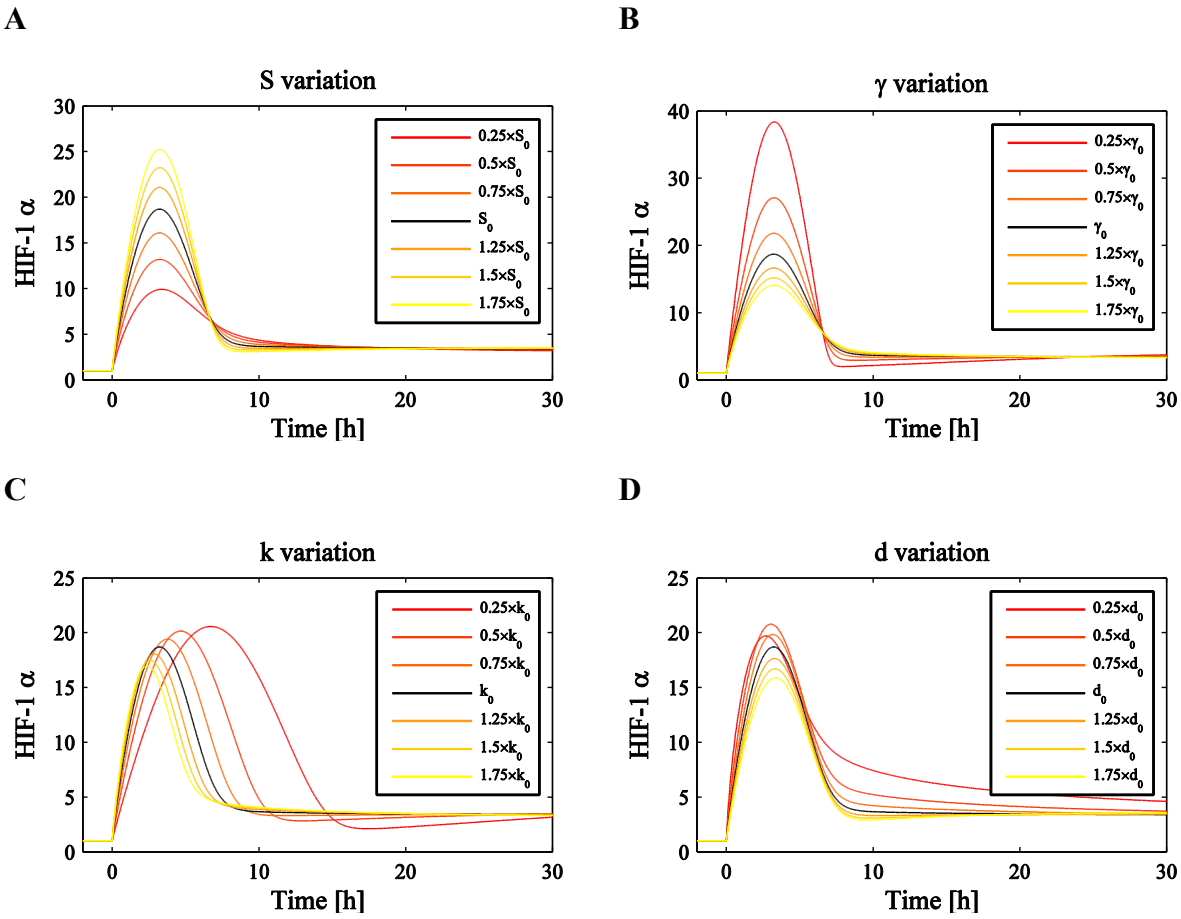

Figure 3-4: Parameter sensitivity analysis: parameters of the 2-component model S (A), γ (B), k (C) and d (D) were individually varied from the median derived in Figure 3-3 to observe the effects on HIF-1α dynamics. Pre-stimulation (normoxic) equilibria have been normalised to 1 to emphasise the qualitative effects of parameter variation. Labelling is equivalent to Figure 2-12. Parameter values: $S_0 = 2.38\times10^{1}$ AU min^{-1}, $\gamma_0 = 2.98\times10^{2}$ AU, $k_0 = 4.71\times10^{-4}$ min^{-2}, $d_0 = 4.71\times10^{-4}$ min^{-1}.

The emergence of the sensitivity of these two PHD-based parameters further motivated our investigation into the role of PHD feedback through an extension of the minimal 2-component model. It should be noted that while we earlier placed emphasis on γ as a key parameter for bell data, it can be seen in Figure 3-4 that varying that parameter alone is not as effective at distorting the peak duration and response time characteristics. However, it is clear that decreasing the value of γ, as we did when improving our representative median cell (Figure 3-3), is an effective way of increasing the overshoot characteristic prevalent in the bell data. The variation observed in the width of transient HIF-1α peaks is of a completely different nature to the variation found in peak amplitude for example, a property which also shows a great degree of variation within the single-cell data. The height of the peaks displayed variance in the data but seemed to correlate generally with the experiment the data came from suggesting an experimental artefact. This artefact may be explained by cell to cell variance in HIF-EGFP accumulation during transient transfection, as single cells are likely to have different copy numbers of HIF plasmid due to transfection variability, or the arbitrary nature of the fluorescent units by which the HIF-1α dynamics are measured (as discussed in section 2.3.4.1). This would have a

direct effect on the expression of HIF-1α and this is reflected in the parameter variation analysis where varying the basal rate of HIF-1α synthesis, S, had a clear effect on the amplitude of the peak (Figure 3-4). However, increased duration of transcription factor upregulation corresponds directly to prolonged activation of the target genes of the transcription factor. Therefore the peak duration property is considered important with respect to HIF-1 activity and therefore the regulation of genes mediating the hypoxic response. This dependence of HIF-1α peak dynamics on PHD induction strengthens the rationale for looking at distinguishing the different PHD isoforms in order to make a more informative model. In particular it allows for a model that can be adapted to the investigations of the relationships that exist between the PHDs, i.e., comparing relative amounts, knockdowns, transient increases and so forth.

3.2.2 Modification of the Minimal 2-component Model via PHD Specification

The minimal 2-component ODE model was extended to four components by removing the generic PHD feedback variable (y) and explicitly accounting for the three different isoforms of PHD: PHD1, PHD2 and PHD3 (termed y_1, y_2 and y_3 respectively).

While PHDs 2&3 are transcriptionally regulated by HIF-1 such that their production is increased, PHD1 has no such induced synthesis. That is, PHD1 is not a transcriptional target of HIF-1. Consequently, PHD1 regulation is effectively oxygen-independent in our model and equilibrium levels are maintained whether we are simulating normoxic or hypoxic environmental conditions. All three PHD components however can actively promote the hydroxylation of HIF-1α proteins in the presence of oxygen, ultimately leading to HIF-1α destruction, at rates h_1, h_2 and h_3 for PHD1, PHD2 and PHD3 respectively. This convention of subscripts of parameters relating to PHD type will continue throughout i.e. j_i is a parameter corresponding to PHDi. We assume the same saturation kinetics in the hydroxylation terms as in the minimal model for all three PHD types with Michaelis constants γ_1, γ_2 and γ_3. PHD2 and PHD3 are HIF-1 inducible and this is represented in the expanded model through the induction rates k_2 and k_3. Basal degradation rates for the PHDs are represented by d_1, d_2 and d_3 and we also introduce basal synthesis rates S_1, S_2 and S_3. Introducing synthesis rates for the PHDs was necessary since PHD1 is not induced by HIF-1. A constant rate of production was included in the ODE describing PHD1 dynamics to prevent the exponential decay of the protein to a zero steady state. For consistency we also included synthesis rates for PHD2 and PHD3. This generality would also prove to be useful when trying to distinguish between the PHD isoforms using experimental measurements.

In summary, the minimal 2-component model,

$$\begin{aligned}\frac{dx}{dt} &= S - hy\left(\frac{x}{x+\gamma}\right)\\ \frac{dy}{dt} &= kx - dy,\end{aligned} \tag{3.1}$$

is modified as described above to give the following 4-component model,

$$\begin{aligned}\frac{dx}{dt} &= S - h_1 y_1\left(\frac{x}{x+\gamma_1}\right) - h_2 y_2\left(\frac{x}{x+\gamma_2}\right) - h_3 y_3\left(\frac{x}{x+\gamma_3}\right)\\ \frac{dy_1}{dt} &= S_1 - d_1 y_1\\ \frac{dy_2}{dt} &= S_2 + k_2 x - d_2 y_2\\ \frac{dy_3}{dt} &= S_3 + k_3 x - d_3 y_3.\end{aligned} \tag{3.2}$$

Variables	Parameters
x – HIF-1α	S – basal HIF-1α synthesis rate
y_1 – PHD1	S_i – basal PHD*i* synthesis rate
y_2 – PHD2	d_i – basal PHD*i* degradation rate
y_3 – PHD3	h_i – hydroxylation rate of HIF-1α by PHD*i*
t - time	γ_i – HIF-1α hydroxylation threshold (Michaelis constant)
	k_i – PHD*i* production rate induced by HIF-1α

Table 3-1: A table describing all variables and parameters of the mathematical model described in (3.2).

Standard linear stability analysis shows that this system has a unique, stable equilibrium solution (see section 7.2 of the Appendix).

3.3 Parameterisation: Experimental Measurements & Fitting

A major motivating factor behind the expansion of the minimal 2-component feedback model was increasing the viability of the model as a predictive tool. In order to do this we needed to increase the complexity of the feedback mechanism which we know in its minimalist form is able to describe the range of observed HIF-1α dynamics. This increase in complexity arises through the specification of the three distinct PHD isoforms. Now that these isoforms have been made explicit in the model we can begin to attribute experimental measurements to relevant model parameters in an attempt to make the model more accurate. To this end, we searched for experimental measurements in published

literature and conducted our own experiments in order to refine and ultimately parameterise the expanded model.

The expansion of the mathematical model has increased the number of free parameters from 5 (S, γ, k, d, h) to 15 ($S, \gamma_1, \gamma_2, \gamma_3, S_1, S_2, S_3, d_1, d_2, d_3, k_2, k_3, h_1, h_2, h_3$). Hence we have considerably more degrees of freedom within the model when considering parameter optimisation. Therefore we aimed to constrain the model as much as possible by using experimental information and insight from the minimal model in order to minimise the number of parameter values we choose via fitting. It is hoped that these methods will increase the model's reliability by containing measurable, physical quantities from experimental data whilst still being capable of replicating the HIF-1α dynamics generated by the minimal 2-component model. The saturation-of-hydroxylation parameters, γ_i, were assumed to be equal for all PHDs reducing the parameter set by two. This decision was based on the lack of information regarding this parameter value in the literature as the mechanism of hydroxylation saturation was originally introduced into the model by us in an attempt to modify the qualitative output of the system (bell-shaped dynamics) rather than being based upon any prior biological knowledge.

3.3.1 Basal Degradation of PHD proteins

In order to determine suitable basal degradation rates for the three types of PHD protein we performed imaging experiments to measure the half-life values of the PHDs by blocking protein synthesis. We measured the half-life of each PHD type using time-lapse microscopy of cells transfected with either PHD1-EGFP, PHD2-EGFP or PHD3-EGFP. The chemical cycloheximide was used to cause translational arrest and the resulting decay of fluorescence was recorded. This loss of fluorescence was used to generate a distribution of half-life values for each PHD (see Figure 3-5). By looking at the mean values of these distributions we could calculate representative degradation rates d_1, d_2 and d_3 using the response time of the relevant ODEs between equilibrium and 0 when production is removed (i.e. cycloheximide applied). This corresponds to $t_i = \ln(2)/d_i$ using mean half-life values t_i for PHD*i*. Thus, using the values visible in Figure 3-5, we have:

$$d_1 = \frac{\ln(2)}{615.59\text{min}} = 1.13\times10^{-3}\text{min}^{-1},$$

$$d_2 = \frac{\ln(2)}{784.81\text{min}} = 8.83\times10^{-4}\text{min}^{-1},$$

$$d_3 = \frac{\ln(2)}{102.81\text{min}} = 6.74\times10^{-3}\text{min}^{-1},$$

using 3 significant figures throughout.

It is clear that PHD1 has a faster response time when compared with PHD2 but much slower than PHD3. These times provide information on how sensitive the PHDs are to changes in their production levels. Hypoxic induction and re-oxygenation provide an example of altering the production levels of PHDs 2&3 as they are both activated by the oxygen-sensitive HIF-1. However the regulation of PHD1 is oxygen independent and so we don't consider the implications of its response time here. The degradation rate is used to determine PHD1 levels as PHD1 maintains an equilibrium steady state with basal synthesis balancing degradation. We notice that PHD3 has a much faster response time when compared to the other PHDs and so we expect PHD3 to exhibit rapid dynamics following changes to the oxygen signal in the pathway. Conversely we expect a relatively slow response to changes in oxygen from PHD2, as its response time is much longer. The implications of these differences are discussed further in Chapter 4.

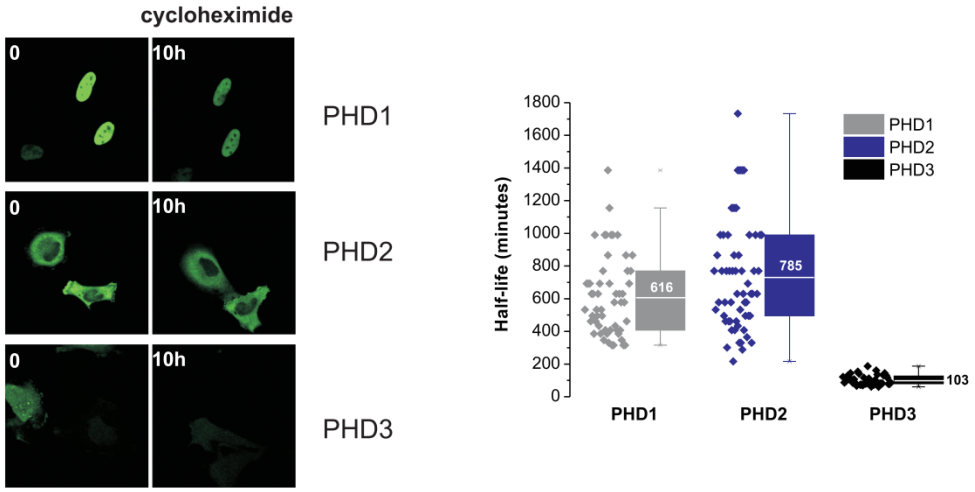

Figure 3-5: Measurements of the half-life of PHD1, 2 and 3. HeLa cells were transfected with PHD1, 2, 3-EGFP. 24 hours after transfection, cells were treated with cycloheximide (10µg/µl) and the PHD levels were monitored for up to 24 hours by measuring fluorescence intensity. A box-and-whisker plot shows the half-life measured in single cells for PHDs 1-3. The mean half-life values are indicated on the plot. This data was originally provided by Dr Sée's lab (Bagnall, et al. 2013).

3.3.2 Hydroxylation Rates

As mentioned previously in section 2.3 there are experimental measurements available in the literature showing the relative changes in the hydroxylation activity of PHDs 1-3 (Tuckerman, et al. 2004). We were able to utilise this information, presented in Figure 3-6, more fully in our expanded model.

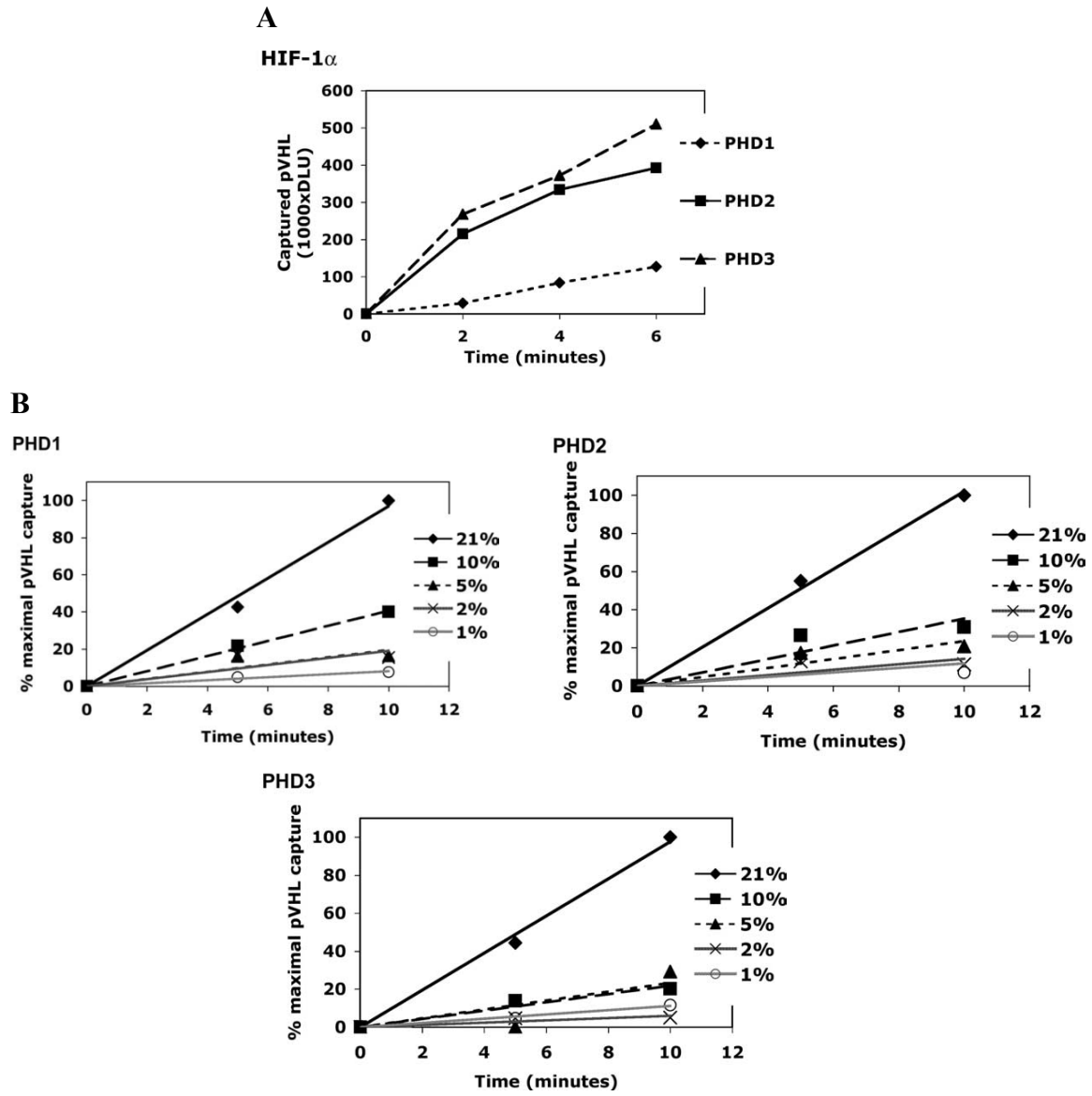

Figure 3-6: Experimental measurements of the hydroxylation activity of PHD. (A): the relative hydroxylation activities of the three PHD isoforms on HIF-1α. (B): the dependence of PHD activity on oxygen availability. Figure taken and adapted from Tuckerman et al. (Determination and comparison of specific activity of the HIF-prolyl hydroxylases 2004).

In Figure 3-6A HIF-1α was used to measure the relative hydroxylation rates of each PHD isoform (captured pVHL is a proxy for the amount of hydroxylated HIF-1α being produced). It can be seen that a linear trend is exhibited throughout the experiments with respect to time. Therefore we assume the ratio of rates for different PHDs to remain constant independent of time. The results in Figure 3-6A provide a means of measuring the relative differences in hydroxylation rate, but not absolute values.

We re-scale the PHDs with the hydroxylation rate of PHD2 in normoxia, h_2^N:

$$y_1^* = h_2^N y_1, \qquad y_2^* = h_2^N y_2, \qquad y_3^* = h_2^N y_3$$

Consequently, in normoxia our differential equation for HIF-1α becomes

$$\frac{dx}{dt} = S - \left(\frac{x}{x+\gamma}\right)\left(\frac{1}{h_2^N}\right)(h_1^N y_1^* + h_2^N y_2^* + h_3^N y_3^*),$$

and in hypoxia becomes

$$\frac{dx}{dt} = S - \left(\frac{x}{x+\gamma}\right)\left(\frac{1}{h_2^N}\right)(h_1^H y_1^* + h_2^H y_2^* + h_3^H y_3^*).$$

Thus, we define the re-scaled hydroxylation rates

$$h_i^* = \frac{h_i}{h_2},$$

for $i = 1,2,3$. The data presented in Figure 3-6A led us to define a hydroxylation rate ratio for each PHD in normoxia of 0.25: 1: 1.25 for PHD1: PHD2: PHD3. This ratio was derived from the relative amounts of hydroxylation activity ('captured pVHL') from Figure 3-6A at 6 minutes, although we assume time independence. Consequently we normalise our re-scaled hydroxylation rates based on h_2^N such that $h_1^* = h_1^N/h_2^N = 0.25$, $h_2^* = h_2^N/h_2^N = 1$ and $h_3^* = h_3^N/h_2^N = 1.25$ in normoxia.

We now have the following system, with re-scaling of the PHD ODEs included:

$$\begin{aligned}
\frac{dx}{dt} &= S - \left(\frac{x}{x+\gamma}\right)(h_1^* y_1^* + h_2^* y_2^* + h_3^* y_3^*) \\
\frac{dy_1^*}{dt} &= S_1^* - d_1 y_1^* \\
\frac{dy_2^*}{dt} &= S_2^* + k_2^* x - d_2 y_2^* \\
\frac{dy_3^*}{dt} &= S_3^* + k_3^* x - d_3 y_3^*.
\end{aligned} \tag{3.3}$$

Note that system (3.3) also now includes the following re-scaled parameters:

$$S_1^* = h_2^N S_1, \qquad S_2^* = h_2^N S_2, \qquad S_3 = h_2^N S_3, \qquad k_2^* = h_2^N k_2, \qquad k_3^* = h_2^N k_3.$$

We will subsequently drop the $*$ notation from the model.

Now that we have a suitably scaled model we can use the measurements of relative PHD hydroxylation rates over different oxygen concentrations and parameterise the model. Furthermore, we will consider the hydroxylation rate parameters to be continuous functions of oxygen by approximating and interpolating the discrete measurements of Tuckerman made at oxygen concentrations: 21%; 10%; 5%; 2%; and 1% O_2 (see Figure 3-6B and Figure 3-7). The data points in

Figure 3-7 were derived from the activity of PHDs at different oxygen concentrations after 10 minutes in Figure 3-6B. Note that we assume time independence between PHD activity at different oxygen levels due to the linear relationships in Figure 3-6B. The PHD activity values were then normalised by dividing by 100. A plot of the hydroxylation rates for each PHD isoform as functions of oxygen can be seen in Figure 3-8. Incorporating these functions in our model allows for continuous changes in the input signal (oxygen) which will be tested later in this chapter. The equations for the normalised hydroxylation rate curves are given by:

$$\begin{aligned} h_1(C) &= 0.25(0.0014C^2 + 0.016C + 0.1233) \\ h_2(C) &= 0.0015C^2 + 0.0137C + 0.1202 \\ h_3(C) &= 1.25(0.0022C^2 + 0.0012C + 0.1036) \end{aligned} \tag{3.4}$$

where C represents oxygen concentration (O_2%). In order to test the effects of different temporal signatures of oxygen on HIF-1α dynamics, we use these hydroxylation rates that are continuous functions of oxygen concentration (see section 3.5.1). These results were integrated into the model using the description of parameters h_1, h_2 and h_3 as functions of C which can be modified to be a function of time $C(t)$ that specifies the temporal dynamics of oxygen concentration.

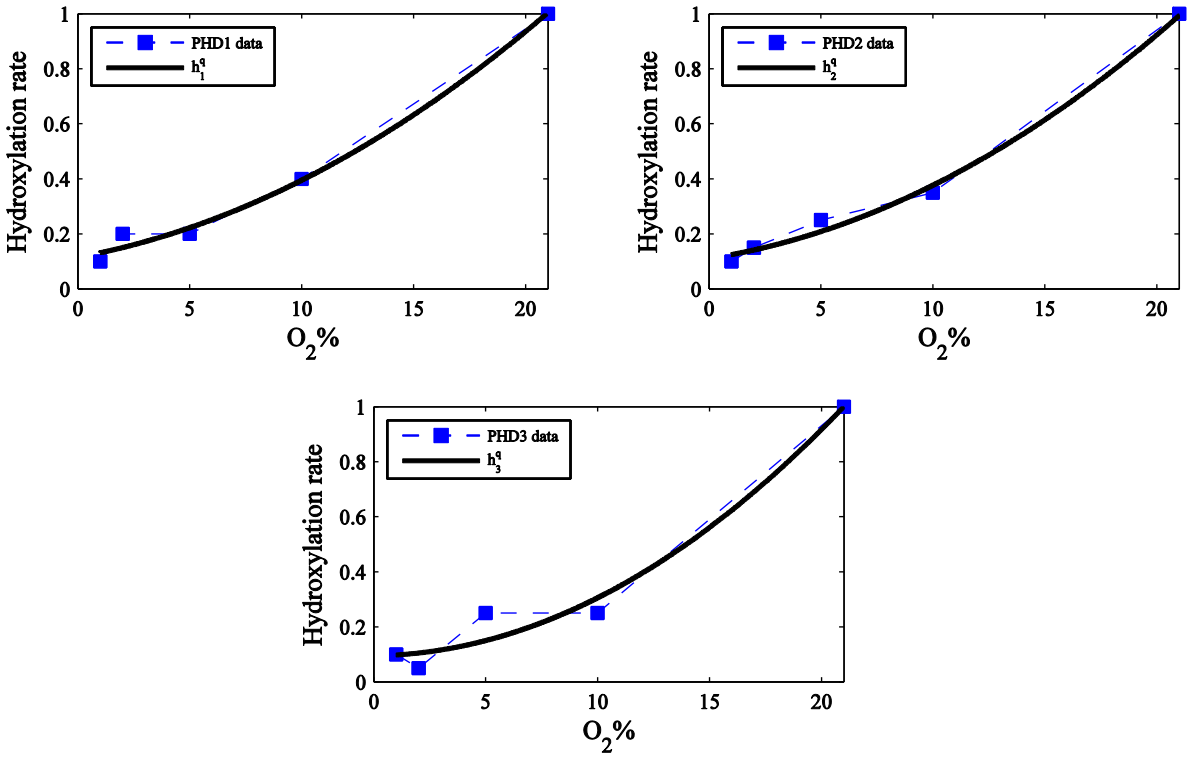

Figure 3-7: Plots of discrete data values for hydroxylation rates versus oxygen concentration of each PHD isoform (Tuckerman, et al. 2004). The rates are normalised based on the hydroxylation rate at 21% O_2. Each dataset is plotted individually for each PHD and fitted with a quadratic trend-line representing the hydroxylation rates h_i^q (correlation coefficients $R^2 = 0.9924, 0.9941, 0.973$ for h_1^q, h_2^q, h_3^q respectively).

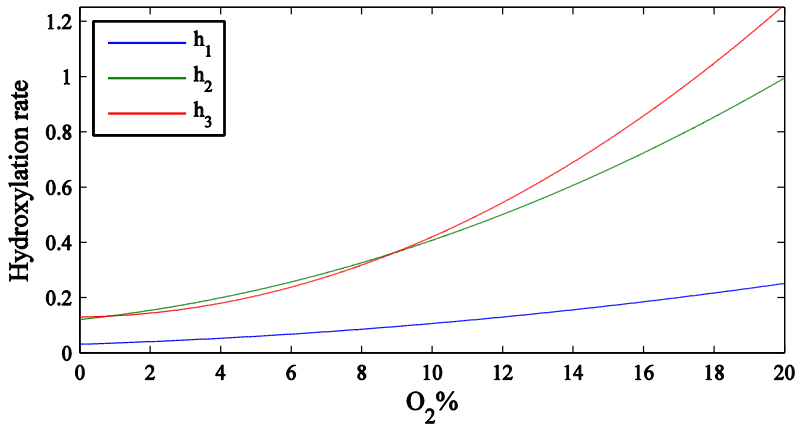

Figure 3-8: A plot showing oxygen concentration (O_2 %) versus hydroxylation rate h_i for each PHD isoform (PHD1, PHD2 and PHD3). The curves are normalised to the PHD2 rate of hydroxylation in normoxia (20% O_2).

3.3.3 PHD Induction Rates

One of the most critical parameters in determining HIF-1α dynamics in our model is the part of the fundamental negative feedback loop representing hypoxic induction of PHD by HIF-1α (corresponding to k in the original 2-component model). Previously this induction was represented with a generic PHD component representing the activity of all PHDs in a combined way. Note however that only two out of the three PHD isoforms are transcriptionally activated targets of HIF-1; PHD1 regulation is independent of HIF-1. To distinguish between the two HIF-inducible proteins in the signalling pathway, PHD2 and PHD3, we performed experiments measuring the rate of PHD mRNA production in hypoxia in order to provide us more information on any differences between k_2 and k_3 in the 4-component model.

HeLa cells were incubated in both hypoxia and normoxia and PHD-mRNA time-course profiles were measured by qPCR for each PHD protein. qPCR (quantitative real-time Polymerase Chain Reaction) is a laboratory technique used to measure the amount of amplification of a sequence of DNA in real time; in this case the DNA of interest are the genes for PHD mRNA. Our model does not explicitly describe the dynamics of mRNA but the k_i terms represent the whole process of HIF mediated transcription of PHD mRNA and the translation of PHD mRNA into PHD protein. Normoxic experiments were used as a control and no mRNA induction was observed as expected. Likewise, no PHD1-mRNA DNA was amplified in hypoxia corroborating general consensus in the literature and our own mathematical description that PHD1 is not induced by HIF-1. The experiments showed that PHD2-mRNA and PHD3-mRNA kinetics were largely similar in hypoxia, suggesting a similar rate of HIF-dependent PHD induction for both PHD2 and PHD3. For this reason the PHD induction rate parameters (k_2, k_3) were assumed to be equal to each other and we subsequently define

$$k_2 = k_3 = k.$$

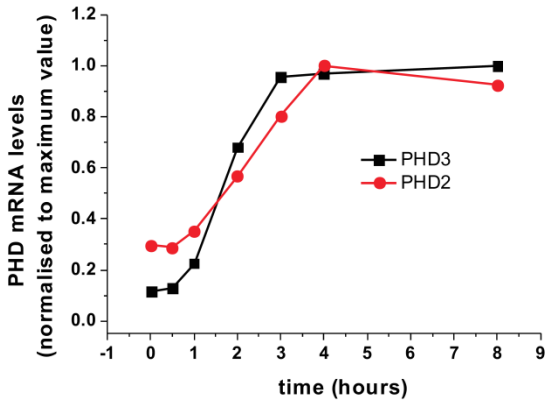

Figure 3-9: qPCR analysis of PHD2 and PHD3 mRNA induction during a hypoxic time course (1% O_2) showing similar induction rates (Bagnall, et al. 2013).

3.3.4 PHD Basal Synthesis Rates

The extension of our model from two to four components warranted the inclusion of basal synthesis rates for the PHD species. This is because PHD1 is not a gene target of HIF-1 and as such is not transcriptionally activated in hypoxia in a HIF-dependent manner. In order for PHD1 to be non-zero in our model, basal synthesis is required to balance basal degradation. We also include basal synthesis rates for PHDs 2&3 for consistency.

Previous measurements of the relative expression levels of PHD proteins in several cell lines have been measured by Appelhoff et al. (Differential function of the prolyl hydroxylases PHD1, PHD2, and PHD3 in the regulation of hypoxia-inducible factor 2004) and were used to help us estimate PHD synthesis rates, S_i. We used their measurements of relative abundances of PHDs in normoxic HeLa cells to provide us with a ratio of PHD equilibrium levels (see Figure 3-10). They obtained the relative normoxic expression levels of PHD1: PHD2: PHD3 in the ratio 0.2: <1: 0.1. By taking the ratio of steady state values[1] to be 0.2: 0.8: 0.1, and by using the degradation rates found in section 3.3.1, we now demonstrate how we estimate the ratio of production rates of the PHDs. In our model there exist the following steady state values for the PHD components in normoxia:

$$y_1^{EQ} = \frac{S_1}{d_1},$$

[1] The relative expression level for PHD2 could not be obtained precisely (see Figure 3-10) so we took 0.8 as an approximation. After recent consultation with the relevant author it was contended this value could be represented by 0.5. However all proceeding figures and parameterisations in this thesis will consider our initial estimated value of 0.8.

$$y_2^{EQ} = \frac{S_2 + kx_N^{EQ}}{d_2},$$
$$y_3^{EQ} = \frac{S_3 + kx_N^{EQ}}{d_3}.$$

We define the ratio of normoxic equilibria $y_1^{EQ} : y_2^{EQ} : y_3^{EQ}$ as

$$\begin{cases} \frac{S_1}{d_1} : \frac{S_2 + kx_N^{EQ}}{d_2} : \frac{S_3 + kx_N^{EQ}}{d_3} \\ 0.2 : 0.8 : 0.1 \end{cases}.$$

By including our degradation rate parameters this reduces to

$$\begin{cases} S_1 : S_2 + kx_N^{EQ} : S_3 + kx_N^{EQ} \\ 2.26\times10^{-4} : 7.064\times10^{-4} : 6.74\times10^{-4} \end{cases}.$$

Defining $S^* = S_3 + kx_N^{EQ}$ we obtain

$$\begin{cases} S_1 : S_2 + kx_N^{EQ} : S_3 + kx_N^{EQ} = S^* \\ S^*(0.34 : 1.05 : 1) \end{cases},$$

taken to 2 decimal places. Equivalently we can write,

$$S_1 = 0.34(S^*),$$
$$S_2 = 1.05(S^*) - kx_N^{EQ},$$
$$S_3 = S^* - kx_N^{EQ}.$$

These synthesis relations will be used throughout the remainder of this chapter.

A

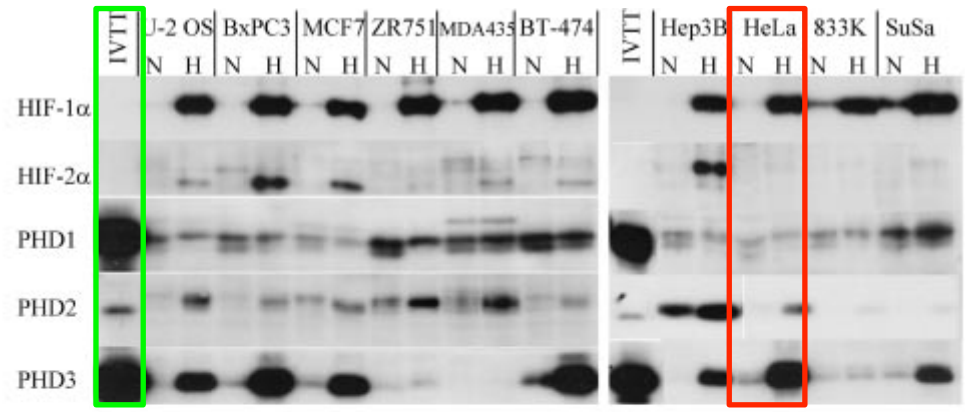

B

	U-2 OS		BxPC3		MCF7		ZR751		MDA -435		BT-474		Hep3B		HeLa		833K		SuSa	
	N	H	N	H	N	H	N	H	N	H	N	H	N	H	N	H	N	H	N	H
PHD1	0.2	0.2	0.3	0.2	0.2	0.1	0.8	0.5	0.5	0.4	0.7	0.9	0.7	0.2	0.2	0.2	0.2	0.2	0.6	1.2
PHD2	2	11	1.4	4.3	3.4	7.1	5.4	19	4.8	20	1.5	3	17	43	<1	8.4	<1	1	<1	1.1
PHD3	.04	2.4	.09	9	.09	2.8	.06	0.1	<.03	<.03	0.3	9.8	<.03	1.4	0.1	9.8	0.1	0.2	0.2	2.1

Figure 3-10: (A): Immunoblot data demonstrating PHD proteins in different cell lines (HeLa cell line highlighted in red box). The data was normalised based on the first lane of each gel (highlighted in green box) where equimolar amounts of PHD proteins were used. (B): A table showing the relative expression levels of PHD proteins in different cell lines (HeLa cell line highlighted in red box) for both normoxia ('N') and hypoxia ('H'). Due to the low detection threshold for PHD2 (A - green box) the measurement for normoxic PHD2 levels could not be given precisely (Appelhoff, et al. 2004).

3.3.5 Fitting to the 2-component Model

With parameter values found through new experimental measurements and publications in the field our model has become more constrained. The constraints applied to this model through real measurements were not feasible in the simplified 2-component feedback model which was designed in order to identify a key motif involving purely the negative feedback of PHD on HIF-1α in hypoxia. The PHD component was a fictional combination of all the different types of PHD allowing for a minimal model useful for finding an underlying base for further modelling work to be built upon. The degrees of freedom added by introducing more species and parameters to the model was countered by using tighter restrictions on these new values using experimental data related to the pathway.

To minimise the number of free parameters in our optimisation, we choose to use the same parameter values from the 2-component model median cell output (see Figure 3-3) for HIF-1α (x) basal synthesis S and hydroxylation threshold γ. For the data-fitting of the HIF-1α in the 4-component model, this now leaves just the basal synthesis rates of the PHDs (S_i) and the induced synthesis rate of PHD2 and PHD3 (k) to be determined. This is effectively only two free parameters due to the

knowledge gained of the relative production ratio of the PHDs, i.e. we only need to find values for S^* and k to complete the parameterisation of the model.

The choice of S^* and k was determined through parameter optimisation by fitting the 4-component model solution of HIF-1α to a 'de-oxygenation median cell' or a 're-oxygenation median cell' generated from the 2-component model optimisation (Figure 3-3) using the *fminsearch* minimisation algorithm described in the Appendix, section 7.1. This algorithm was used to minimise the sum of squared residuals in a least squares approach. For fitting results see Figure 3-11 below.

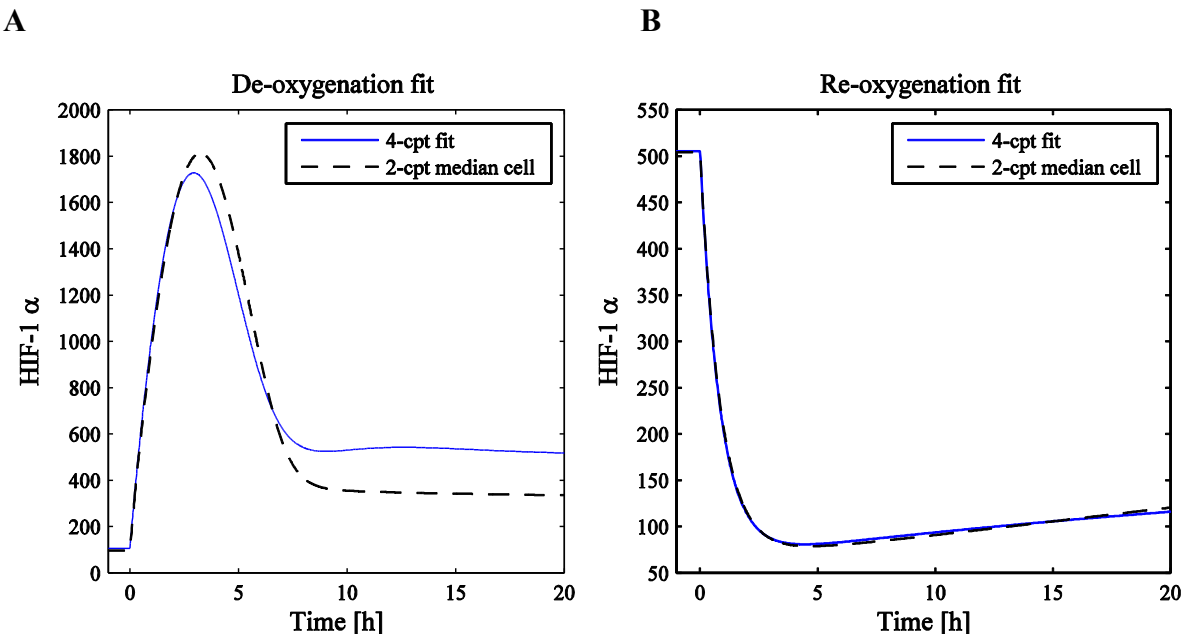

Figure 3-11: Plotted results of the fitting of the 4-component model output to the median cell 2-component model output for both de-oxygenation (A) and re-oxygenation (B) by varying parameters S^* and k. Optimised parameter values are included in Table 3-2.

To summarise, the updated 4-component model (3.5) and table of parameter values (Table 3-2) are detailed below:

$$\begin{aligned}
\frac{dx}{dt} &= S - \left(\frac{x}{x+\gamma}\right)(h_1 y_1 + h_2 y_2 + h_3 y_3) \\
\frac{dy_1}{dt} &= S_1 - d_1 y_1 \\
\frac{dy_2}{dt} &= S_2 + kx - d_2 y_2 \\
\frac{dy_3}{dt} &= S_3 + kx - d_3 y_3.
\end{aligned} \tag{3.5}$$

Parameters	Units	Value (de-oxygenation)	Value (re-oxygenation)
S	AU min^{-1}	2.38×10^{-1} (carried over from 2-component model)	1.35×10^{0}
S^*	AU min^{-2}	6.22×10^{-2} (fitted in 4-component model)	2.27×10^{-1}
S_1	AU min^{-2}	2.11×10^{-2} (based on S^* and literature data)	7.72×10^{-2}
S_2	AU min^{-2}	2.64×10^{-2} (based on S^* and literature data)	4.14×10^{-2}
S_3	AU min^{-2}	2.33×10^{-2} (based on S^* and literature data)	3.01×10^{-2}
d_1	min^{-1}	1.13×10^{-3} (measured)	
d_2	min^{-1}	8.83×10^{-4} (measured)	
d_3	min^{-1}	6.74×10^{-3} (measured)	
k	min^{-2}	3.65×10^{-4} (fitted in 4-component model)	3.90×10^{-4}
γ	AU	2.98×10^{2} (carried over from 2-component model)	1.63×10^{4}
h_1	1	$0.25(0.0014C^2 + 0.016C + 0.1233)$ (fitted to literature data)	
h_2	1	$0.0015C^2 + 0.0137C + 0.1202$ (fitted to literature data)	
h_3	1	$1.25(0.0022C^2 + 0.0012C + 0.1036)$ (fitted to literature data)	

Table 3-2: A table describing the parameter values for system (3.5), the 4-component mathematical model of the HIF-1α signalling pathway. Note that for hydroxylation functions h_i, the independent variable C represents oxygen concentration (O_2%).

The dynamics of all pathway components as a result of a hypoxic switch are plotted in Figure 3-12 using the fully parameterised 4-component model. After a rapid switch from normoxia to hypoxia at $t = 0$ we see transient dynamics for the oxygen-sensitive components of the HIF-1α signalling pathway: HIF-1α, PHD2 and PHD3. HIF-1α and PHD3 exhibit overshoot dynamics where protein levels peak during the transient period before stabilising at a long-term hypoxic steady state. The accumulation of PHD2 is relatively monotonic. PHD2 is by far the most abundant of the PHDs based on our use of results by Appelhoff et al. (Differential function of the prolyl hydroxylases PHD1, PHD2, and PHD3 in the regulation of hypoxia-inducible factor 2004) and is dynamically slower to respond to the hypoxic stimulus than PHD3 owing to its longer half-life (see Figure 3-5). Since the production and degradation processes of PHD1 occur at rates independent of HIF-1α activity, PHD1 remains at steady state in both normoxia and hypoxia.

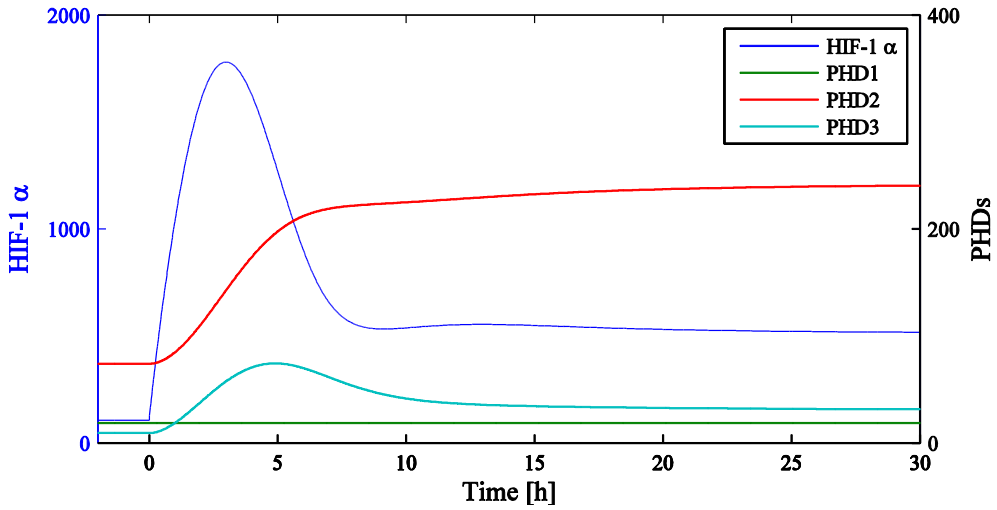

Figure 3-12: The output of the fully parameterised 4-component model (as described by (3.5) and Table 3-2) when oxygen is reduced from 20% O_2 (normoxia) to 1% O_2 (hypoxia) at $t = 0$.

3.4 Predictions and Experimental Validation

One of the advantages of the extra detail in the model is that it can be used to validate or predict behaviour in the pathway subject to experimentally realisable modifications. For example we can investigate the variation of more specific parameters or remove parameters/species altogether. As we become more informed about the individual roles of PHDs in the pathway we can strengthen the model and modify it as necessary.

The removal of a particular type of PHD from the system is an example of something we can now simulate with the expanded model. This is a good process of validating and correcting the proposed model as there is experimental data available, both published and obtained in our lab, to compare our results with. The PHD feedback mechanism has clinical significance due to its potential role as a tool to tune HIF-1 levels (see section 3.1). A study by Berra et al. (HIF prolyl hydroxylase 2 is the key oxygen sensor setting low steady-state levels of HIF-1alpha in normoxia 2003) led to the description of PHD2 as the key oxygen sensor after experiments conducted including the specific silencing of PHD isoforms using short interfering RNAs (siRNAs). The study claims that it is primarily PHD2 that is responsible for low levels of HIF-1α in normoxia supporting earlier reports that PHD2 has the highest specific activity towards the hydroxylation site of HIF-1α (Huang, et al. 2002).

To remove PHD components from our mathematical model we removed the appropriate PHD ODE (dy_i/dt) and hydroxylation reaction (term involving h_i) from the HIF-1α ODE (dx/dt). Thus, we effectively used 3-component models for these types of simulations with HIF-1α being hydroxylated by the remaining two PHDs only. This method was used in order to be comparable with experiments

where a steady normoxic state was found after PHD silencing before any hypoxic insult was applied. We compared the transient dynamics of HIF-1α following hypoxic induction given by the model for simulations with and without PHD2. This was done by assuming a normoxic equilibrium (20% O_2) in both cases prior to an instantaneous switch to hypoxia (1% O_2) at time $t = 0$ (see Figure 3-13). The model predicted significantly greater levels of HIF-1α in both normoxia and hypoxia when PHD2 was absent. Also, using our model we predicted that the removal of PHD2 from the system causes a sustained accumulation in HIF-1α levels after hypoxic induction as the characteristic transiency in the HIF-1α response is lost. These dynamics were compared with western blots showing relative HIF-1α levels in stable PHD2 knockdown cells ('shPHD2' cells - cells containing short hairpin RNA (shRNA) to knock down the expression of PHD2) and wild type cells ('WT' cells) in Figure 3-13. The qualitative feature of sustained HIF-1α accumulation was recaptured by the western blot data.

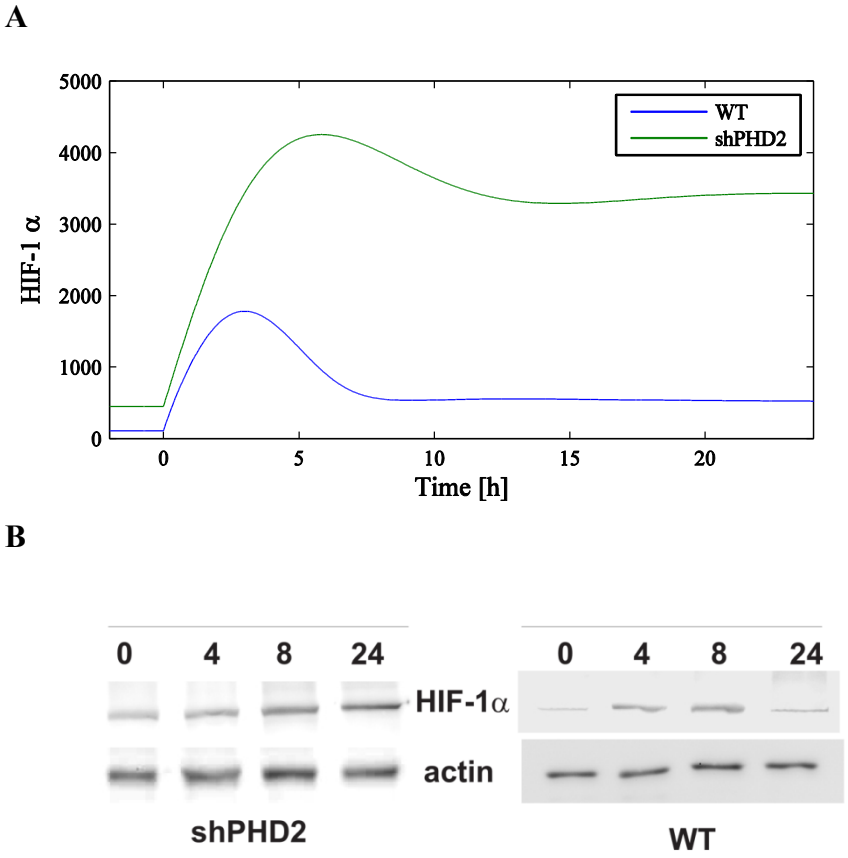

Figure 3-13: (A): A plot comparing the transient dynamics of HIF-1α after a hypoxic insult at $t = 0$ for systems with PHD2 (blue) and without PHD2 (green). When PHD2 is removed the normoxic levels of HIF-1α are much greater and the hypoxic response is more sustained. (B): Western-blot analysis of HIF-1α levels in shPHD2 HeLa cells cultured in 1% O_2 for indicated time points (in hours). The sustained accumulation of HIF-1α predicted by the model has been re-produced experimentally.

PHD knock-out model simulations were performed for each PHD isoform and their hypoxic dynamics plotted (see Figure 3-14). The PHD2 knockout had the most dramatic effect on HIF-1α dynamics,

compared with PHD1 and PHD3, corresponding with its widely used description as the pathway's main oxygen sensor.

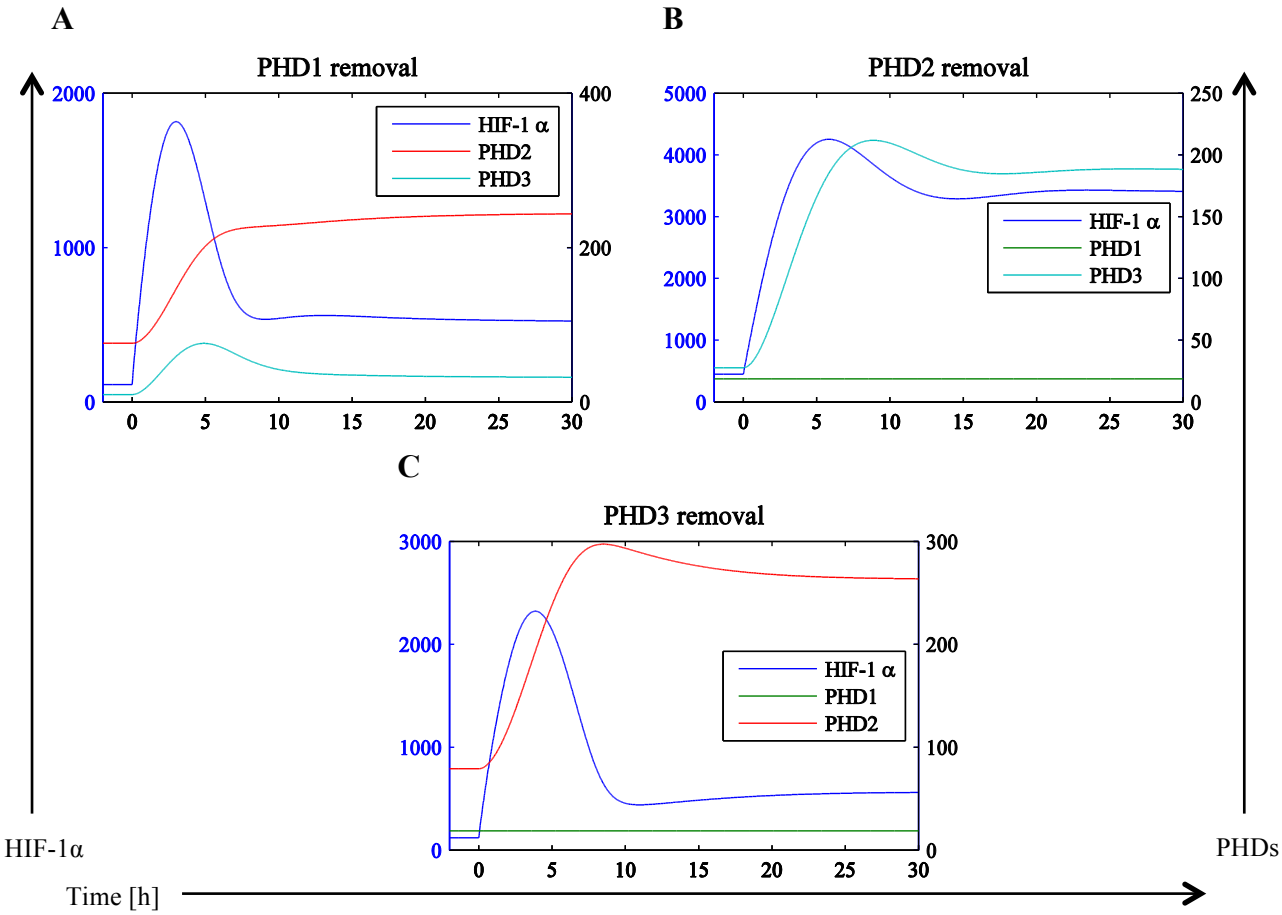

Figure 3-14: Plots representing pathway dynamics after hypoxic induction for the removal of PHD1 (A), PHD2 (B) and PHD3 (C).

Single-cell imaging data of re-oxygenation experiments were also recorded for shPHD2 cells and compared with the mathematical model. The experimental and computational results agree that the time taken for HIF-1α levels to drop is extended considerably when PHD2 is absent (see Figure 3-15). Following 2 hours of re-oxygenation in the model simulation, HIF-1α levels are decreased by 4-fold in wild type cells but only by 2-fold in shPHD2 cells. In the single-cell experiments there is some variability in the amount of HIF-1α after 2 hours but the fold-reduction generally agrees with the model simulations as can be seen in the figure.

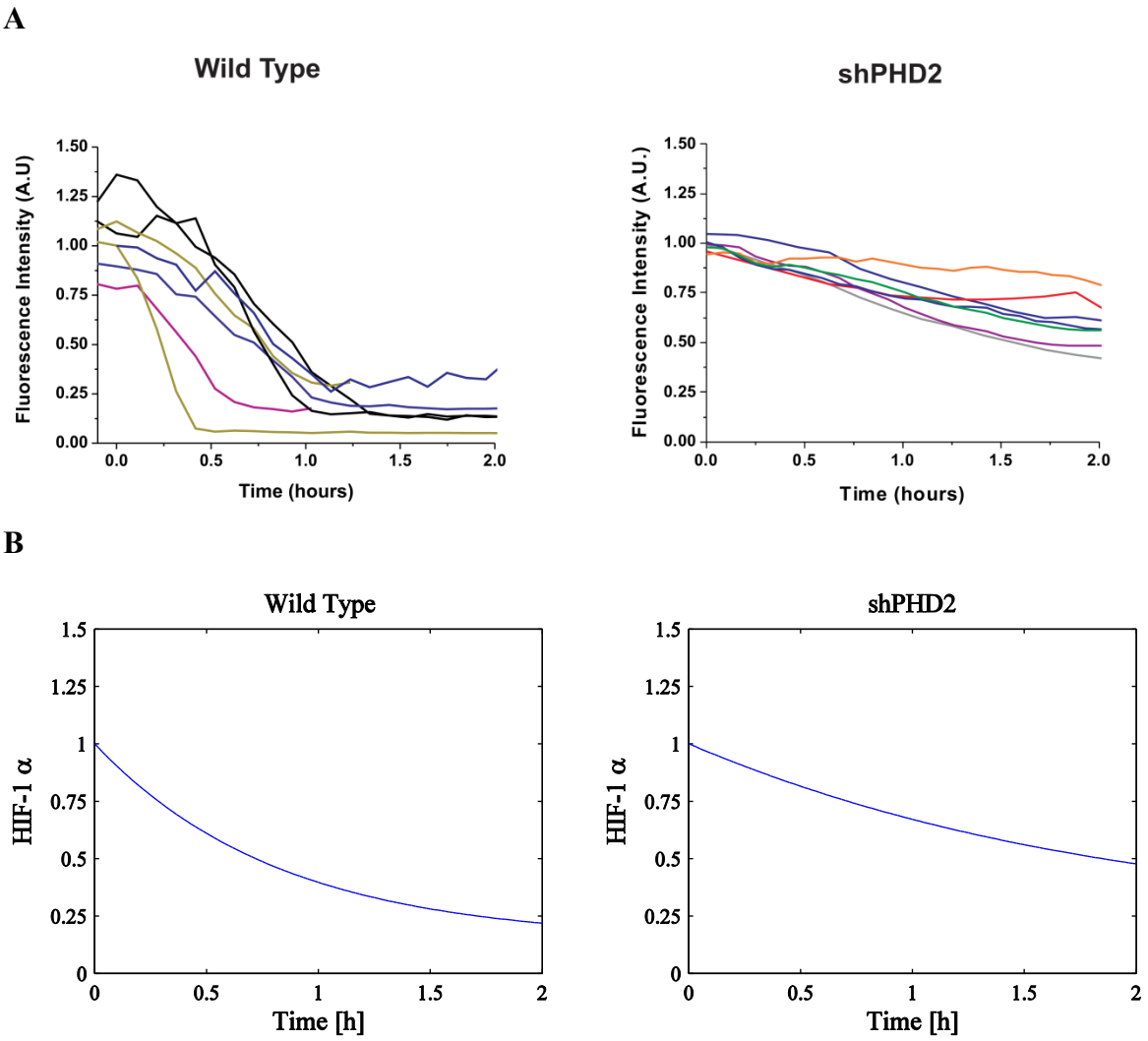

Figure 3-15: (A): Experimental data showing single-cell dynamics re-oxygenated at $t = 0$ after hypoxic incubation for both wild type and PHD2 knockout (shPHD2) cells. (B): Mathematical model predictions of the same conditions. The data presented in (A) was originally provided by Dr Sée's lab (Bagnall, et al. 2013).

3.5 Model Properties Analysis

3.5.1 Complex Oxygen Dynamics

An important aim of the model is to provide biological insight into the possible functions of the pathway. One such function we can investigate is the pathway's response to various temporal dynamics of oxygen. There are many different oxygen dynamics to consider such as: different severities and durations of hypoxic insults, different transition rates of oxygen (i.e. how long it takes for a cell to become hypoxic/normoxic), intermittent hypoxia/re-oxygenation etc. If the effects on the consequent profile of HIF-1α could be translated to biological responses and consequences then the

model would begin to show signs of predictive power. For example, how could dynamic activity such as various reset periods or oscillatory behaviour translate to downstream biology such as gene expression or critical cell behaviour? We have previously looked at varying model parameters and removing pathway components such as PHD2 to study consequent HIF-1α dynamics. These investigations correspond with current therapeutic targeting where different drugs are tested for inhibiting PHD production for example. However, using the oxygen signal itself to modify HIF-1 dynamics and therefore target gene expression could provide an alternative, relatively under-explored method. A signalling pathway computational model can very quickly simulate the effects of any signal dynamics supplied whereas these types of wet lab experiments can be very impractical and inefficient, especially for intermittent hypoxia for example. An investigation of the downstream effects of different oxygen kinetics would require further coupling to HIF-1 target genes that encode for the biological process of interest.

Oxygen is present in our model through the hydroxylation rate functions h_1, h_2 and h_3 derived in section 3.3.2. These hydroxylation functions are dependent on the variable C representing oxygen concentration. To investigate various different temporal signatures of oxygen we defined C to be a function of time, $C(t)$. In Figure 3-16 we have model dynamics as a result of 5 different temporal signatures of oxygen: instant switch; graded switch; square wave; trapezium wave; and triangle wave (see Figure 3-17). These oxygen concentration functions are defined as time-dependent functions which transition between two distinct states of oxygen (i.e. normoxia and hypoxia) that represent the starting oxygen level in our temporal signature and the level at which we switch to, possibly multiple times.

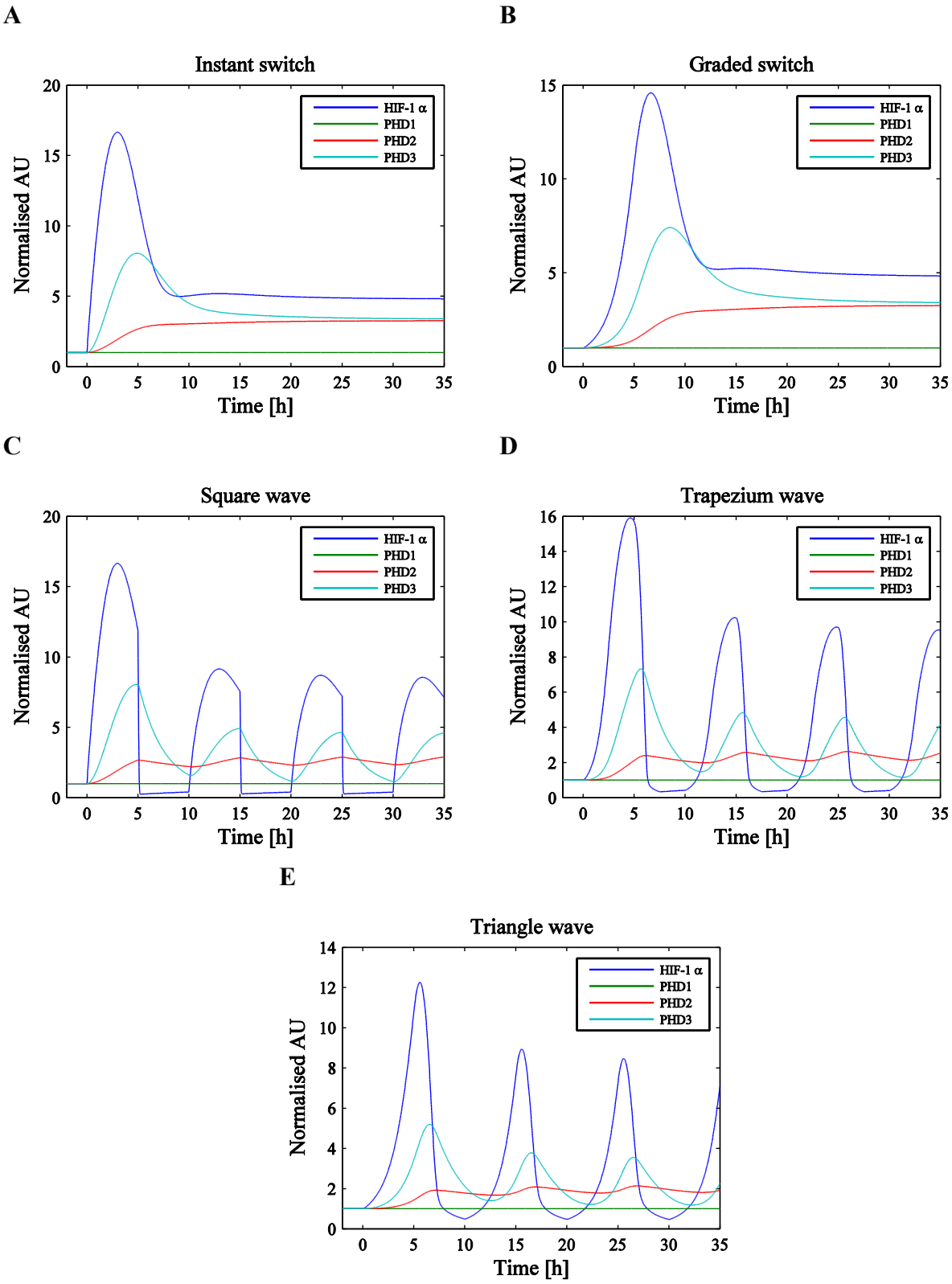

Figure 3-16: A series of plots showing the effects of different oxygen signalling profiles on HIF-1α pathway dynamics. In each plot (A-E) the dynamics of different pathway components are represented by the ODE solutions of model (3.5). The different oxygen dynamics simulated are: instant switch (A); graded switch (B); square wave (C); trapezium wave (D); and triangle wave (E) (see Figure 3-17).

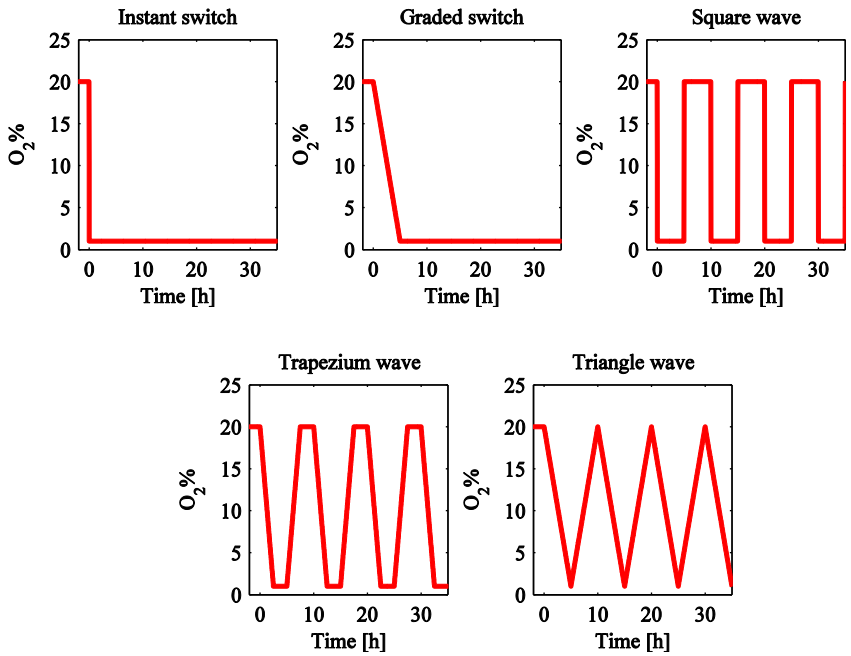

Figure 3-17: Different types of oxygen dynamics are plotted as O_2 concentration versus time. These dynamics were applied in the model simulations of Figure 3-16. The different oxygen dynamics correspond to Figure 3-16 as follows: instant switch (Fig3-16A); graded switch (Fig3-16B); square wave (Fig3-16C); trapezium wave (Fig3-16D); and triangle wave (Fig3-16E).

The instant switch represents the rapid oxygen dynamics we have been studying thus far and indeed the dynamics used experimentally. The graded switch shows a clear effect on the time it takes for significant activation of HIF-1α as the peak maximum is delayed.

While the instant switch represents the externally imposed oxygen conditions in our experiments, we hypothesise that changes to the intra-cellular oxygen concentration and the signalling response by the cell may not occur instantaneously. Therefore the graded switch may represent more realistically what occurs within cells. Furthermore cell-to-cell variation in timescale of the switch could lead to cell-to-cell heterogeneity, for example in variation in time-to-peak-maximum as seen in single-cell data. This is represented in more detail by Figure 3-18 where several different graded switches have been applied. The different switches varied in the time taken to reach the hypoxic value of 1% O_2. For each different grade (5h, 10h, 15h, 20h, 25h, 30h) the resultant HIF-1α dynamics were plotted. Figure 3-18 shows a collated plot and shifts in peak HIF-1α levels are seen as well as a reduction in peak amplitude. The time taken to reach hypoxia reduces the overshoot aspect of the HIF-1α dynamics but it would take an unrealistically long time to remove this dynamic feature altogether. That is to say, unrealistic times with respect to the growth and division cycle of a single cell. If we assume that the source of data heterogeneity is related to the oxygen signal, these model results imply that the ramp-like dynamic behaviour seen in some single-cell HIF-1α dynamics represent ‘slow bells’ with shifted peaks, rather than monotonous increases to hypoxic equilibrium as discussed in section 3.2.

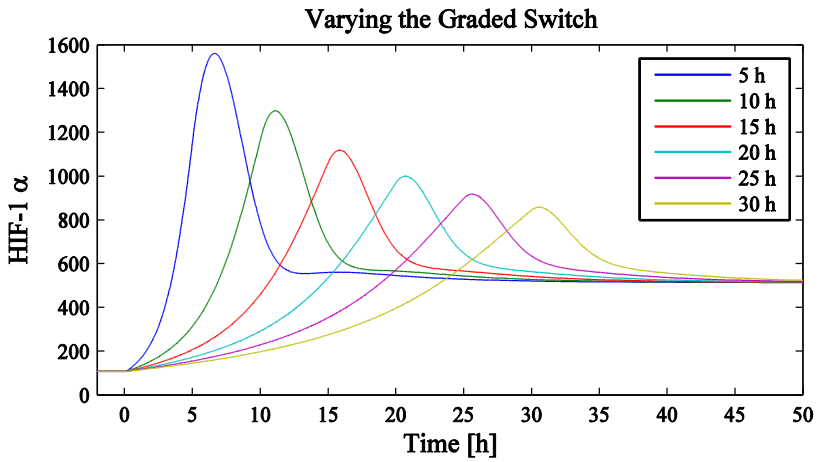

Figure 3-18: HIF-1α dynamics were plotted for various model simulations using different grades of hypoxic switches. These different grades are identified by the amount of time taken to linearly decrease oxygen levels from normoxia (20% O_2) to hypoxia (1% O_2).

Note that during square wave and trapezium wave simulations we see initial large amplitude peaks followed by subsequent peaks of smaller amplitude. One explanation for this could be the elevated levels of PHD2 on subsequent hypoxic insults. This is a result of the relatively long half-life of PHD2 as discussed in section 3.3.1. These higher levels of PHD2 would cause the hydroxylation of HIF-1α to occur at a faster rate. Also notice, that the re-oxygenation events that occur in these simulations take place during the transient dynamics of the system, i.e. before a steady state has been reached. A visible consequence of this is that the levels of HIF-1α are reduced to a lower value than the normoxic equilibrium. Before normoxic equilibrium can be reached a further hypoxic insult is applied and this is also likely to affect the subsequent amplitude of HIF-1α peaks. This shift, from square to trapezium wave, is effectively extending the time taken for the oxygen concentration to reach the new level which has the effect of shifting at what dynamic stage HIF-1α is in when an oxygen switch occurs. For example, if hypoxia is induced and then the system is re-oxygenated in the case of the square wave, i.e. instant switching, HIF-1α levels might be at their peak at the time of re-oxygenation. If we are using the trapezium or triangle waves however, i.e. a more graded switch, then HIF-1α levels may yet to have reached their peak amplitude when re-oxygenation is applied leading to a dampening of the oscillations.

We were able to compare one case of intermittent hypoxia with an experiment conducted in our lab. Firstly, the model was used to predict the HIF-1α dynamics for periodic hypoxic pulses. This periodic oxygen profile consisted of a hypoxic switch from 21% to 1% oxygen concentration for a duration of 6 hours, followed by an opposite re-oxygenation switch for 1 hour. The effects on HIF-1α dynamics predicted by the model were repetitive peaks in HIF-1α accumulation. Moreover the first peak had much greater amplitude than subsequent peaks, just as we had previously seen in our plots in Figure 3-16. This prediction was qualitatively validated experimentally using the ODD-EGFP cell line described in section 2.2 (see Figure 3-19).

We also combined our investigations of alternative oxygen kinetics and PHD inhibition by using the same oxygen regimes with and without PHD2 (see Figure 3-20). An oxygen signature of 2 hours hypoxic incubation and half an hour re-oxygenation was used to simulate pathway dynamics. The system with PHD2 once again showed damped peaks in HIF-1α levels. In contrast, when PHD2 was removed the second pulse of hypoxia generated the greatest amplitude of HIF-1α levels. This hypothesis has yet to be tested experimentally. This result is likely influenced by the current level of HIF-1α when successive hypoxic insults are applied as well as the PHD activity of the system. In the wild type case HIF-1α levels are reduced to levels comparable to (or below) normoxic equilibrium upon re-oxygenation. The reason for damped peaks is likely due to elevated PHD levels. When PHD2 is removed, HIF-1α levels are still relatively high after just 1 hour of re-oxygenation and so the second hypoxic insult allows for an even higher peak in HIF-1α. Successive HIF-1α peaks are lower as PHD3 has had sufficient time to accumulate and so further re-oxygenation events decrease HIF-1α levels at a greater scale.

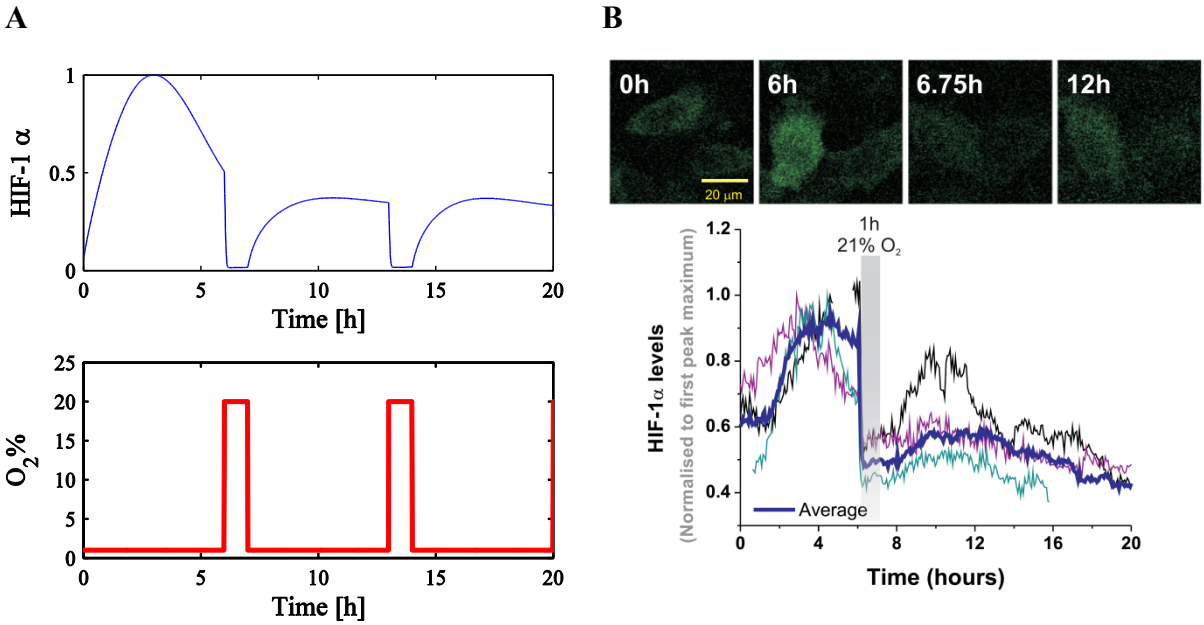

Figure 3-19: (A): Model simulation output showing the effects of pulses of intermittent hypoxia on HIF-1α dynamics. The pathway was subjected to 6 hours hypoxia followed by 1 hour of normoxia. This routine was repeated twice. (B): An experimental validation of the model prediction. Upper panels show images of fluorescent data at the times indicated. The lower plot shows this fluorescent data as single-cell HIF-1α dynamics for multiple cells. The re-oxygenation period at 6 h is indicated. The broad, blue line denotes average single-cell HIF-1α dynamics. This data was originally provided by Dr Sée's lab (Bagnall, et al. 2013)

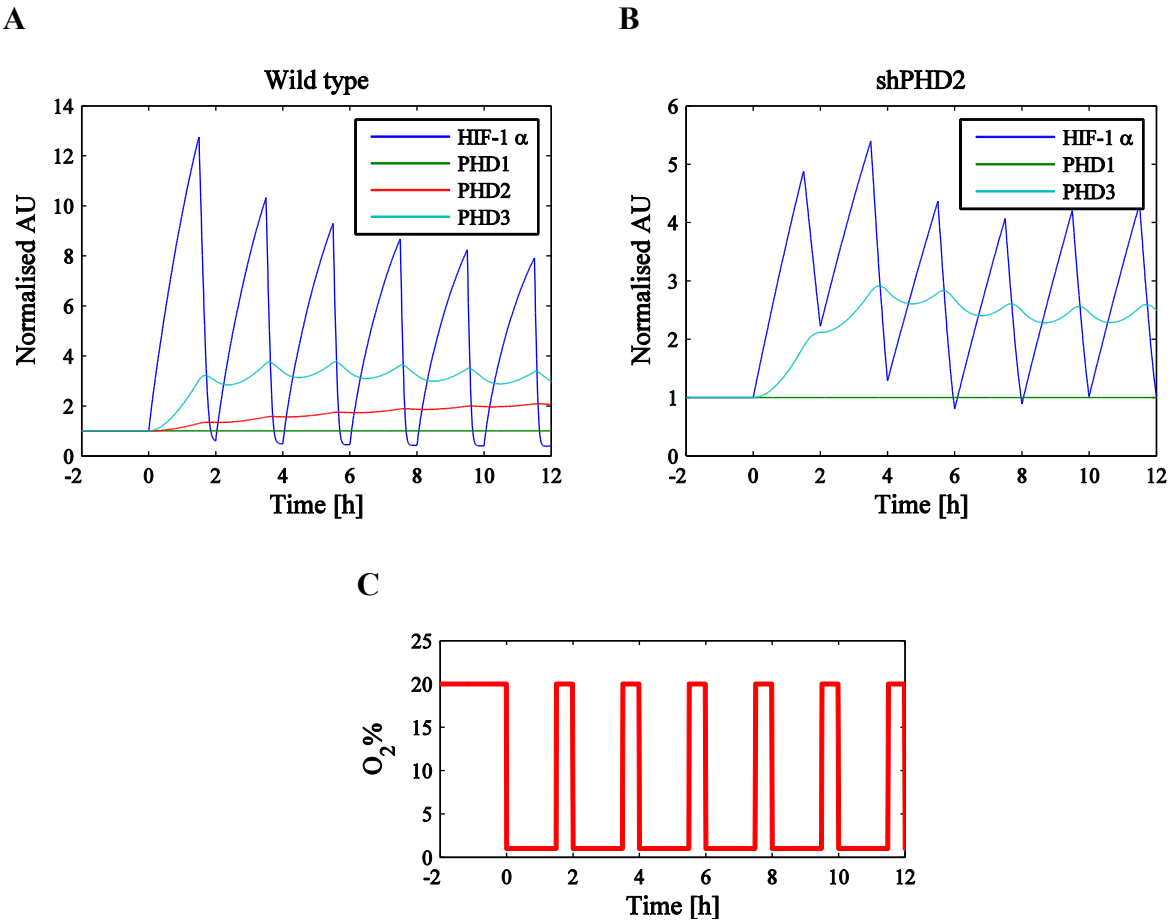

Figure 3-20: Dynamics of the HIF-1α signalling pathway for the wild type case (A) and the shPHD2 case (B) after stimulation by a specific pulsing oxygen signature (C).

3.6 Summary & Future Research

3.6.1 Modelling Summary

In the previous two chapters we have described in detail our research into the modelling of the dynamics of the HIF-1α signalling pathway. We have presented the specifics of the process from model conception through to a strong predictive model including aspects such as: investigating alternative models; formulating a rigorous parameter optimisation process for a minimal model; extending a robust yet flexible motif to a more realistic model; and the parameterisation and perturbation of the model. All these steps were studied alongside experimental data and existing biological knowledge whilst the whole process was much more cyclical between theory, experiment and interdisciplinary communication than might first appear from the direct form of these chapters.

The proposal to formulate this model was inspired by the novel, single-cell dynamics captured by imaging experiments in Liverpool. A detailed mathematical description of these short-term transient dynamics that occur in single cells after instantaneous induction into hypoxia could not be found. Therefore an entirely new model was conceived. It was decided that the best way to proceed with model formulation was to construct a minimal model using a known negative feedback mechanism between the measured protein of interest, HIF-1α, and its induced inhibitor PHD. This method was used to reduce complexity initially, and focus on a core network motif that was no more complicated than it needed to be in order to be capable of re-producing HIF-1α dynamics observed in the data. In this way, the model would be easier to analyse as to which components/parameters are having what effects, i.e. it would be more intuitive than a complex model, and this minimal motif could always be the foundation for a more complex model at a later stage.

Several models were considered that all described the negative feedback in a relatively simple way. Simulations and mathematical analysis were used to determine which model would be more suited to our needs. Once this had been decided a thorough yet logical form of data fitting had to be employed to truly determine whether the feedback motif was worthy. This is where the abundance of single-cell data proved to be of great use as the model parameters were optimised so that the numerical solutions of HIF-1α dynamics were fit to nearly 100 time-series data. This process was also improved through a constrained optimisation method so that parameters which we did not expect to vary much, due to biological and technological reasoning, were restricted during fitting.

The resulting minimal 2-component model was identified as a strong motif to proceed with as we looked to increase the complexity of the model to make it more useful. This prompted an investigation into where in the model we should increase complexity and what would be most interesting to explore scientifically. The PHDs were separated into their distinct isoforms which encouraged the commencement of more experiments and more literature research as we now wanted to make the model more realistic by including measured quantities. We had devised a representative response to various oxygen dynamics for four of the components of the HIF-1α signalling pathway and used it to make predictions and further validate it through various perturbations.

3.6.2 Future Research Directions

There are many possible future research directions worthy of focusing on with this model. As already touched upon, heterogeneity is evident in the single-cell data which we have modelled with parameter variation. Variation in peak timing is one aspect of cell-to-cell variability that can be replicated with careful choice of oxygen dynamics (i.e. variations in the rate oxygen is reduced or delays in the oxygen switch) but what does it mean for cells to ‘experience’ hypoxia at different times and what is the source? One possibility is that the rate at which the cell’s oxygen supply decreases after an

environmental switch is linked to the cell cycle. Indeed, there is a certain correlation between late responding cells, i.e. cells that exhibit a long delay in accumulation of HIF-1α after hypoxic stimulation; and mitosis, the stage of the cell cycle where division occurs, but this correlation is not conclusive. Another explanation could be a large variation from cell to cell in another cellular component that has a much higher affinity for oxygen utilisation than the PHDs, e.g. mitochondria where the cell's ATP is synthesised.

Another area where this project could progress is with the added complexity of multiscale modelling and/or the coupling of different signalling pathways. Viewing the signalling response with the inclusion of a spatial dimension (for example, at the tissue level) could lead to an investigation of how oxygen diffuses through tissue and permeates into the cells which may in turn lead to a better understanding of cell to cell variation in temporal oxygen dynamics. Coupling with other cell signalling pathways is another potential use for the model as HIF-1α has already been strongly linked with many other transcription factor networks. Through model coupling the extensive role of oxygen variation in other adaptive pathways could be elucidated, for example the role of hypoxia and HIF-1α in the inflammation pathway of NF-κB (van Uden, Kenneth and Rocha 2008). There is already a working mathematical model for the NF-κB signalling pathway developed at Liverpool (see (Ashall, et al. 2009)). HIF-1 can also be stimulated independently of oxygen, for example by cytokines, growth factors, environmental stimuli and other signalling molecules (Ke and Costa 2006).

A further, particularly interesting area of study would be trying to understand the range of downstream effects caused by various oxygen signals and HIF-1α dynamics, ranging from gene expression to physiological responses. There is a possibility that specific HIF-1α dynamics could upregulate certain target genes and longer term effects should include the maintenance of an oxygen homeostasis to address the imbalance. This could lead to more model-coupling, for example to an angiogenesis model; the main function of which is largely influenced by the regulation of HIF-1α.

Chapter 4

Modelling Spatio-temporal Oxygen Dynamics in Hypoxic Spheres & Coupling to the HIF-1α Model

---

4.1 Introduction

Multi-cellular spheres were cultured as part of a collaborative effort between Dr Violaine Sée's laboratory at the University of Liverpool and Professor Dmitri Papkovsky's lab at University College Cork. More specifically, the spheres were neurospheres, consisting of cancerous neuroblastoma cells. The neurospheres were subjected to different degrees of hypoxia and a novel method of recording single-cell oxygen concentration, developed in Cork (Fercher, Ponomarev, et al. 2010a, Fercher, Borisov, et al. 2011), was used to measure the oxygen concentration distribution within the neurosphere. These oxygen distributions are representative of those that occur in avascular tumours. A hypoxic core develops due to a combination of oxygen consumption and diffusion. These oxygen dynamics provide a physiologically important range of signals for the intracellular pathways of the HIF-1 transcription factor. The combination of our HIF-1α signalling pathway model with realistic tumour oxygen profiles could provide insight into the dynamic activity of HIF-1α throughout an avascular tumour. To do this, a model that describes both the spatial distribution of oxygen concentration in a sphere and the temporal evolution of that distribution is required. With this we aim to further our investigation of HIF-1α dynamics to determine whether the characteristic transiency, which we have identified in Chapters 2&3, may influence the global (tissue) dynamics.

A basic description of the neurosphere experiments is provided in section 4.2. The resulting data and its potential applications to our HIF-1α model prompted the development of a partial differential equation (PDE) model that describes the distribution of oxygen in hypoxic neurospheres. The details of this process are given in sections 4.3-4.5. This is followed by a coupling of the HIF-1α model to the oxygen model in section 4.5.3. Motivation for further, biologically relevant applications of this coupled model is considered in section 4.7.

4.2 Experimental Data of Hypoxic Neurospheres

Neuroblastoma is a cancer of specialised nerve cells involved in the development of the nervous system and is one of the most common solid tumours in childhood. In the lab these cells can be cultured such that they form three-dimensional clusters analogous to *in vivo* avascular tumour spheres. Neuroblastoma spheres or neurospheres were cultured in Dr Violaine Sée's laboratory and oxygen-sensitive nanoprobes were used to measure the amount of oxygen in the component cells via the FLIM (Fluorescence-lifetime Imaging Microscopy) imaging technique. The FLIM imaging technique involves producing an image based on the differences in exponential decay rate of fluorescence or phosphorescence. Phosphorescence was introduced into our cultured neurospheres by using oxygen-sensitive nanoprobes that were loaded intracellularly. These probes are very small devices that emit

light energy in the form of phosphorescence that decays in the presence of oxygen. This means that in regions of the sphere where there is less oxygen, the phosphorescence will decay more slowly. These measurements of decay are known as lifetime data and a greater lifetime value corresponds to a lower phosphorescent decay rate which in our case corresponds to less oxygen. The advantage of using lifetime values rather than luminescent intensity is that the effects of photon scattering are minimised for particularly thick samples such as the neurospheres. The lifetime values we used are given in units of microseconds (μs). The novelty in these experiments lies in using probes that can measure oxygen levels directly inside the cells of a sphere rather than the traditional method of using electrodes which measure tissue level hypoxia only. These experiments were all performed as part of the collaboration between Dr Sée with research associate Dr Anne Herrmann in Liverpool and the laboratory of Professor Dmitri Papkovsky (University College Cork) with PhD student Andreas Fercher. Papkovsky's lab developed the intracellular oxygen-sensitive probes (Fercher, Ponomarev, et al. 2010a, Fercher, Borisov, et al. 2011) and performed data analysis.

These experiments were originally conducted to investigate the oxygen concentration within neurospheres in different oxygen environments. Neurospheres were cultured in a range of external oxygen conditions from normoxia (17.9% O_2) to relative hypoxia (8%, 3%). What emerged from the FLIM images was a clear oxygen gradient inside the neurospheres, with less oxygen in the centre compared to the outside (see Figure 4-1). This is what we expect to see for large enough spheres of respiring cells due to diffusion and oxygen consumption. Respiring cells are cells that use respiration to generate energy, a process that (preferentially) requires oxygen. The neurospheres were typically between 100-400μm in diameter consisting of between 1,000 and 10,000 cells. Comparable experiments were conducted with non-respiring spheres which did not result in the emergence of oxygen gradients (see Figure 4-6). The process of oxygen diffusion without oxygen consumption led to a constant rate of phosphorescence degradation throughout these spheres.

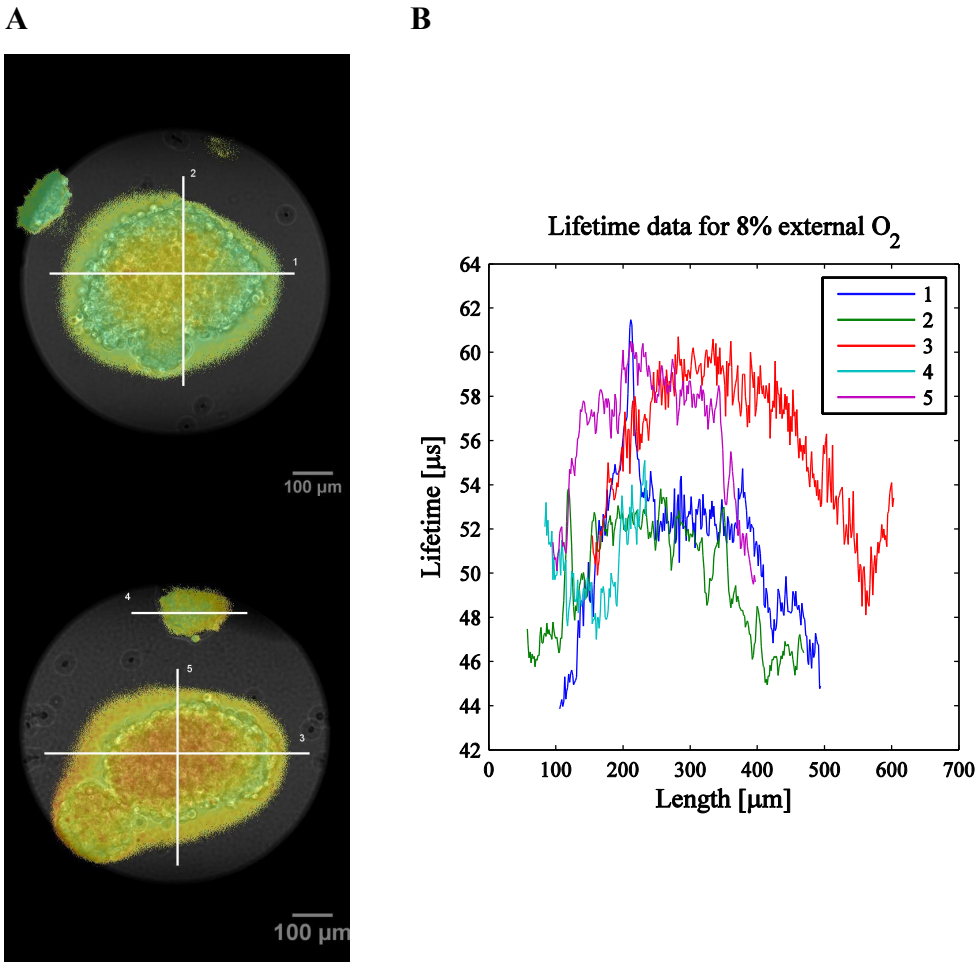

Figure 4-1: (A): An example of the imaging data recorded at University College Cork showing two neurosphere cultured in 8% oxygen. The oxygen gradient in the sphere can be seen by the changes in colour here. (B): Numbered lines from the imaging data (A) indicate where samples of the 2D image were taken as 1D representative cross-section of lifetime values (µs). These 1D lifetime values are plotted against position given by the length of the cross-section given in micrometres (µm) for the relevant numbered white lines in the imaging data.

4.3 Steady State Spherically Symmetric Model of Oxygen Concentration

In order to enhance the value of the HIF-1α signalling pathway model developed in Chapters 2&3, and also to provide some physiological and pathological context, the role of hypoxia in cancer was considered. To suit our previous work we were especially interested in rapid changes in oxygen dynamics and the consequent short timescale dynamics of the HIF-1α transcription factor protein. In order to apply our HIF-1α model to the field of cancer development, relevant oxygen signalling dynamics found in cancer would be required. This led us to consider the oxygen dynamics that are

found in early-stage solid tumours and investigate mathematically the oxygen concentration in this avascular phase.

A solid avascular tumour is three-dimensional containing multiple cells so our governing differential equation must provide oxygen signals that vary in space as well as time to use in our intracellular HIF-1α model. This would provide the means of investigating HIF-1α dynamics in multiple cells in the same tissue subject to the same environmental oxygen source. This required the use of a partial differential equation (PDE) to describe the spatio-temporal dynamics of oxygen. We assume that the regulation of this oxygen distribution within the tumour is dominated by two effects: the diffusion of oxygen into the tumour sphere from an external source; and the consumption of oxygen by the component tumour cells during respiration. For simplicity we assume both diffusion and consumption rates are constant. Therefore, we describe the oxygen dynamics within an avascular tumour using the following equation:

$$\frac{\partial C}{\partial t} = D_1 \nabla^2 C - \psi C, \quad \boldsymbol{x} \in \Omega,$$

where C represents oxygen concentration, D_1 the constant diffusion coefficient and ψ the constant consumption rate. Time is given by t while $\boldsymbol{x}$ represents the spatial vector with the equation being considered within the domain Ω (the sphere). Since we will be looking at oxygen dynamics that occur on a much faster timescale than cell cycle dynamics (growth and division) we assume the radius of the neurosphere to be a constant, R. We can re-scale the PDE by non-dimensionalising the lengths based on the sphere radius constant, R, and non-dimensionalising time based on the diffusion timescale to give

$$\frac{\partial C}{\partial \tilde{t}} = \tilde{\nabla}^2 C - \tilde{\psi} C,$$

where

$$\tilde{\boldsymbol{x}} = \frac{\boldsymbol{x}}{R}, \qquad \tilde{t} = \frac{D_1}{R^2} t, \qquad \tilde{\psi} = \frac{R^2}{D_1} \psi.$$

From here on we will drop the tildes for notational simplicity.

We now take the time equilibrium of the equation to match experimental data which show spatial oxygen variation at a steady state. We will also convert to spherical coordinates and assume radial symmetry so that the problem is reduced to a 1-dimensional equation in variable r, the radial coordinate. We use the following system to describe steady state spatial oxygen dynamics in a radially-symmetric sphere.

$$\nabla^2 C - \psi C = 0 \quad r \leq 1, \tag{4.1}$$

$$\frac{\partial C}{\partial r} = 0, \quad r = 0,$$

$$C = C_0, \quad r = 1.$$

The inner boundary conditions avoid any biologically unrealistic singularities at the centre of the sphere and we prescribe the oxygen concentration at the outer boundary of the sphere.

We also consider spatial oxygen dynamics outside the sphere where there is no consumption rate so that we have the effects of diffusion only. We assume oxygen diffuses at a different rate, D_2, in the outer medium compared to across tumour cells so we have the following PDE:

$$\frac{\partial C}{\partial t} = D_2 \nabla^2 C.$$

After performing non-dimensionalisation as for (4.1) we have:

$$D\nabla^2 C = 0, \quad r > 1, \tag{4.2}$$

$$C \to C_\infty, \quad r \to \infty,$$

$$C = C_0, \quad r = 1,$$

where $D = D_2/D_1$. Both of these equations (for inside and outside the sphere) can be solved analytically.

4.3.1 The Steady State Solution Inside The Sphere

For equation (4.1) we note that this time-independent PDE is in the form of a Helmholtz equation. Since we are assuming radial symmetry, writing the Laplacian operator with respect to the radial coordinate, we can re-write (4.1) as follows:

$$\frac{1}{r^2}\frac{d}{dr}\left(r^2 \frac{dC}{dr}\right) - \psi C = 0,$$

$$\Rightarrow \frac{d^2 C}{dr^2} + \frac{2}{r}\frac{dC}{dr} - \psi C = 0. \tag{4.3}$$

In order to solve this radial component of a Helmholtz equation in spherical coordinates we can use Bessel functions (see Abramowitz & Stegun (Handbook of Mathematical Functions with Formulas,

Graphs, and Mathematical Tables 1964)). Indeed if we take equation (4.3) and multiply through by r^2 we have

$$r^2\frac{d^2C}{dr^2}+2r\frac{dC}{dr}-r^2\psi C=0, \tag{4.4}$$

which when compared with the spherical Bessel differential equation,

$$r^2\frac{d^2C}{dr^2}+2r\frac{dC}{dr}+\big(k^2r^2-n(n+1)\big)C=0,$$

can be seen to be equivalent for $n=0$ and $k=i\sqrt{\psi}$. Solutions of this spherical Bessel differential equation (4.4), known as spherical Bessel functions of the first kind (finite at $r=0$), are of the form

$$C(r)=A\frac{J_{1/2}(kr)}{\sqrt{kr}},$$

where J is a Bessel function of the first kind and A is an arbitrary constant. For $n=0$ the spherical Bessel function of the first kind, denoted j_0, is defined by

$$j_0(\zeta)=\sqrt{\frac{\pi}{2\zeta}}J_{1/2}(\zeta)=\frac{\sin\zeta}{\zeta},$$

$$\Rightarrow J_{1/2}(kr)=\frac{\sin kr}{kr}\sqrt{\frac{2kr}{\pi}},$$

$$\Rightarrow C(r)=A\sqrt{\frac{2}{\pi}}\frac{\sin(kr)}{kr}.$$

For boundary condition $C(1)=C_0$ we choose

$$A=\frac{C_0k}{\sin k}\sqrt{\frac{\pi}{2}},$$

and so finally we have

$$C(r)=C_0\frac{\sin kr}{r\sin k}=C_0\frac{\sinh\sqrt{\psi}r}{r\sinh\sqrt{\psi}}.$$

Indeed if we take this value for C, evaluate its first and second derivatives with respect to r, and substitute it back into equation (4.3) we see that

$$\frac{dC}{dr} = \frac{C_0\left(\sqrt{\psi}r\cosh\sqrt{\psi}r - \sinh\sqrt{\psi}r\right)}{r^2\sinh\sqrt{\psi}},$$

$$\frac{d^2C}{dr^2} = \frac{C_0\left((\psi r^2+2)\sinh\sqrt{\psi}r - 2\sqrt{\psi}r\cosh\sqrt{\psi}r\right)}{r^3\sinh\sqrt{\psi}},$$

$$\Rightarrow \frac{d^2C}{dr^2} + \frac{2}{r}\frac{dC}{dr} - \psi C = \frac{C_0}{r^3\sinh\sqrt{\psi}}\left(\sinh\sqrt{\psi}r\,(\psi r^2+2-2-\psi r^2) + \sqrt{\psi}r\cosh\sqrt{\psi}r\,(2-2)\right)$$
$$= 0,$$

as required.

4.3.2 The Steady State Solution Outside The Sphere

We can solve the differential equation for oxygen dynamics outside the sphere by direct integration of equation (4.2). Firstly, re-writing (4.2) in spherical coordinates with radial symmetry:

$$\frac{D}{r^2}\frac{d}{dr}\left(r^2\frac{dC}{dr}\right) = 0.$$

For non-zero D and finite r this implies

$$\frac{d}{dr}\left(r^2\frac{dC}{dr}\right) = 0$$

From which we obtain

$$C = -\frac{A}{r} + B,$$

where A and B are arbitrary constants. Using boundary conditions $C(\infty) = C_\infty$ and $C(1) = C_0$ we derive A and B:

$$C(\infty) = B = C_\infty,$$

$$C(1) = -A + C_\infty = C_0,$$

$$\Rightarrow A = C_\infty - C_0.$$

Therefore we have the following piecewise solution for time-independent oxygen dynamics inside and outside the sphere:

$$C = \begin{cases} \dfrac{C_0 \sinh\left(\sqrt{\psi} r\right)}{r \sinh\left(\sqrt{\psi}\right)}, & r \leq 1, \\ \dfrac{1}{r}(C_0 - C_\infty) + C_\infty, & r > 1, \end{cases} \tag{4.5}$$

and we let the following constant flux boundary condition hold at the boundary to determine C_0, the value of C at the border of the sphere:

$$D_1 \frac{\partial C_<}{\partial r} = D_2 \frac{\partial C_>}{\partial r} \quad \text{at} \quad r = 1,$$

where D_1 represents the diffusion rate inside the sphere and D_2 represents the diffusion rate outside the sphere. Here we also refer to the concentrations of oxygen inside and outside of the sphere by $C_<$ and $C_>$ respectively.

Then we can rearrange to get,

$$C_0 = \frac{DC_\infty}{\sqrt{\psi}\coth\left(\sqrt{\psi}\right) - 1 + D} \quad \text{where} \quad D = \frac{D_2}{D_1}.$$

4.3.3 Model Solutions & Parameter Variation

Our piecewise solution (4.5) describes the distribution of oxygen concentration in a respiring sphere at steady state. To plot 1D radial solutions of this equation we have three constants to determine, C_∞, ψ and D. We assign C_∞ to be equivalent to the external environment of oxygen concentration, and investigate how the solution varies with changes in parameters ψ and D (the non-dimensional consumption rate and ratio of diffusion inside and outside the sphere). Sample solutions of (4.5) were plotted for various values of ψ and D (see Figure 4-2). Increasing the consumption rate ψ of the tumour cells resulted in more severe hypoxia towards the centre of the sphere with a sharper oxygen gradient at the sphere border ($r = 1$). However note that we are using the non-dimensional quantity where, re-introducing the tilde accents, $\tilde{\psi} = (R^2\psi)/D_1$ and so we can also think of increasing $\tilde{\psi}$ to be representative of increasing the sphere radius. Increasing D is equivalent to increasing the diffusion rate of oxygen outside the sphere relative to that inside the sphere. As D tends to infinity, the oxygen concentration everywhere outside the sphere will equal the value of the oxygen source C_∞.

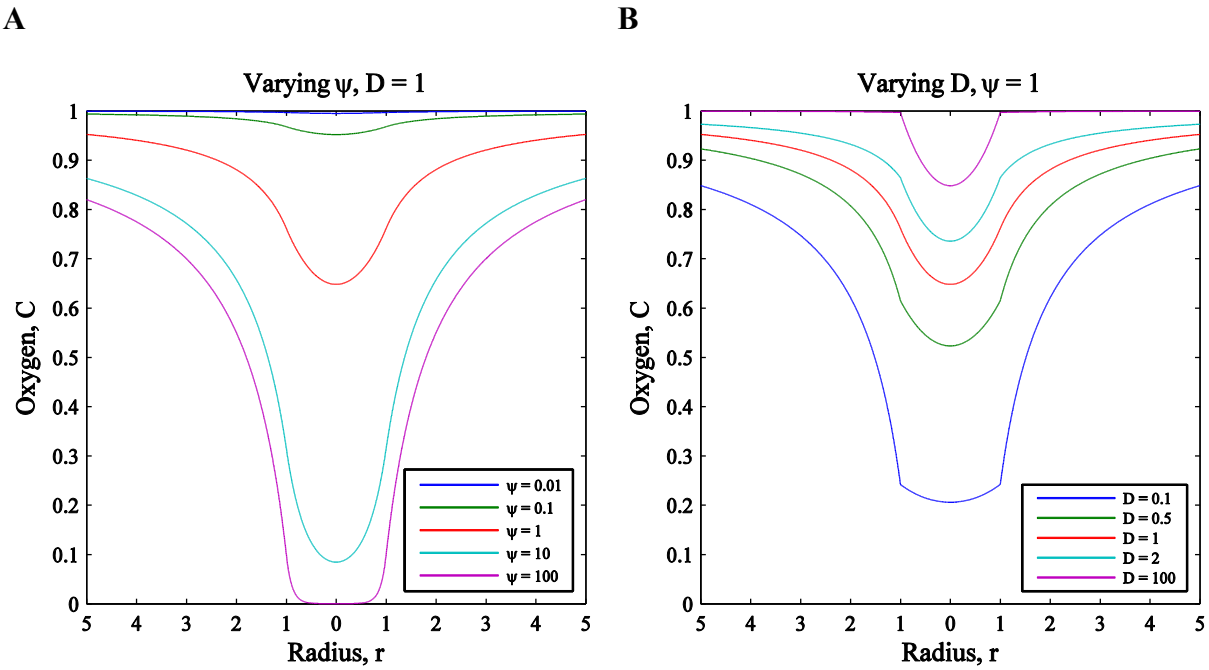

Figure 4-2: Example plots of oxygen concentration using equation (4.5). (A): Effect of varying ψ, the oxygen consumption rate of the tumour cells. (B): Effect of varying D, the relative diffusion rate parameter. The plots are centred on $r = 0$, the centre of the sphere. In both cases $C_\infty = 1$ was used for simplicity as steady state solutions are linear in C_∞.

4.4 Parameter Optimisation

To test the validity of our oxygen model we fit model solutions to the experimental data via parameter optimisation. For our radially symmetric 1D model we used representative vectors of lifetime data crossing the sphere. Parameterising the model using experimental data was done to add legitimacy to our steady state values before we re-introduced time into the model for future use in conjunction with the HIF-1α signalling pathway model.

4.4.1 Data Analysis

In order to compare the model with experimental data we needed to convert lifetime values into oxygen concentration units. A relationship between lifetime values and pO_2 units of oxygen concentration was derived experimentally by Fercher et al. using non-respiring spheres. We modified this approximate derivation for appropriate use with our data. Furthermore, we analysed our non-respiring sphere data to find a correlation between pO_2 units and O_2% saturation. All calibration and processing of FLIM data to generate lifetime values was done by Fercher et al., our collaborators in Professor Papkovsky's lab, University College Cork

4.4.1.1 Non-respiring Spheres & Lifetime (μs) to pO_2 (μM) to O_2% Calibrations

To calibrate the lifetime data, cellular respiration is blocked making non-respiring neurospheres that are then loaded with oxygen-sensitive nanoprobes. Phosphorescence lifetime values are measured as previously with respiring spheres via FLIM in a range of oxygen tensions. Due to the lack of consumption of oxygen inside the sphere, diffusion dominates and the oxygen levels are approximately constant throughout. We assume this relatively constant level to be equivalent to the external pO_2 levels. The measurement of the phosphorescence lifetime can then be compared with the oxygen concentration of the media in the experiment to provide a calibration curve to convert lifetime data (μs) to partial pressure of oxygen, pO_2 (μM) (see Figure 4-3).

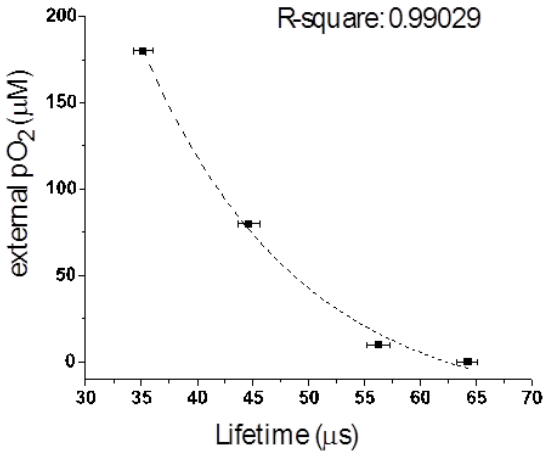

Calibration function, f:

$$f = 2628e^{-\frac{\tau}{13.9}} - 29$$

Figure 4-3: A calibration curve describing the relationship between lifetime data (μs) and pO_2 (μM). The calibration function (f) describes the fitted curve (dashed line), varying with time parameter τ representing lifetime value. Error bar data represents lifetime values of non-respiring spheres at different external oxygen concentrations. Calibration experiments, analysis and plot provided by Fercher et al.

The conversion formula given by the calibration function in Figure 4-3 now allows us to view the data in a comparable way with our model, i.e. oxygen concentration. The two representations, lifetime data and concentration data, are qualitatively inverse to each other (see Figure 4-4). Lifetime data values are greater in the centre of the sphere whereas corresponding pO_2 values are lesser, both representing the hypoxic core.

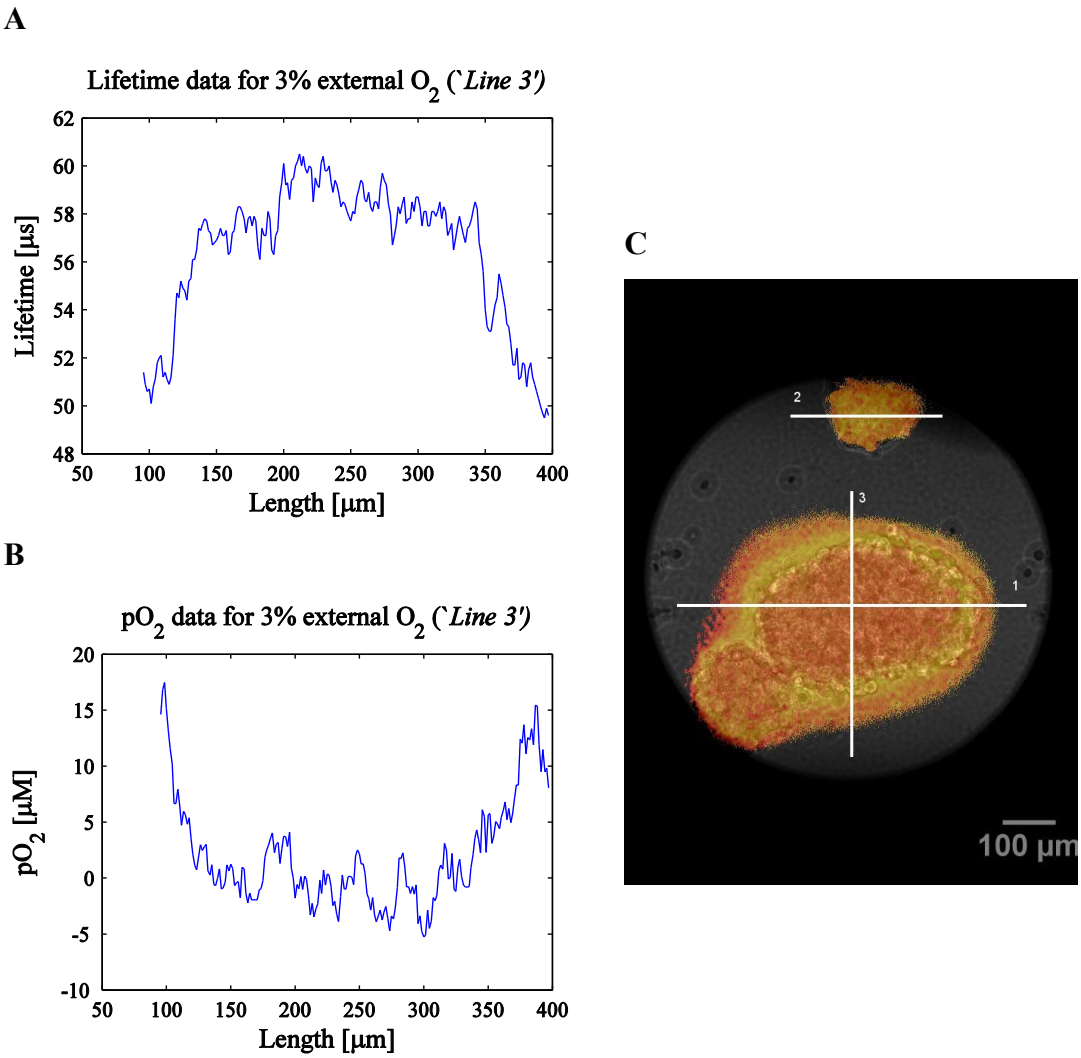

Figure 4-4: Plots of interior oxygen dynamics across a neurosphere cultured in 3% O_2 represented in both lifetime data (A) and pO_2 data (B). Both plots represent the same cross-section of the same neurosphere cells denoted *Line 3* with position indicated by the imaging data (C).

It should be noted that the calibration of lifetime values to pO_2 values in Figure 4-3 should only be considered within a certain range. This is because there were only a finite number of experiments used for this fitted calibration curve and we should be wary of extrapolating any pO_2 values beyond these experimental values. For example, the fitted curve is an exponential function and therefore extrapolating µM values for lifetime values that are less than ~35µs may lead to biologically unrealistic high values of oxygen concentration. An exponential function may be suitable for the set range of lifetime values given by the non-respiring sphere data but we would not expect oxygen concentration to grow exponentially for low lifetime values. Also the fitted calibration curve gives negative pO_2 values for lifetimes greater than 62.64µs which is unfeasible by definition and so we assume that these lifetime values correspond to a complete absence of oxygen. Therefore we cut out from fitting consideration any experimental pO_2 data that corresponds to a lifetime value shorter than 35µs and set all negative pO_2 data equal to 0µM (see Figure 4-5).

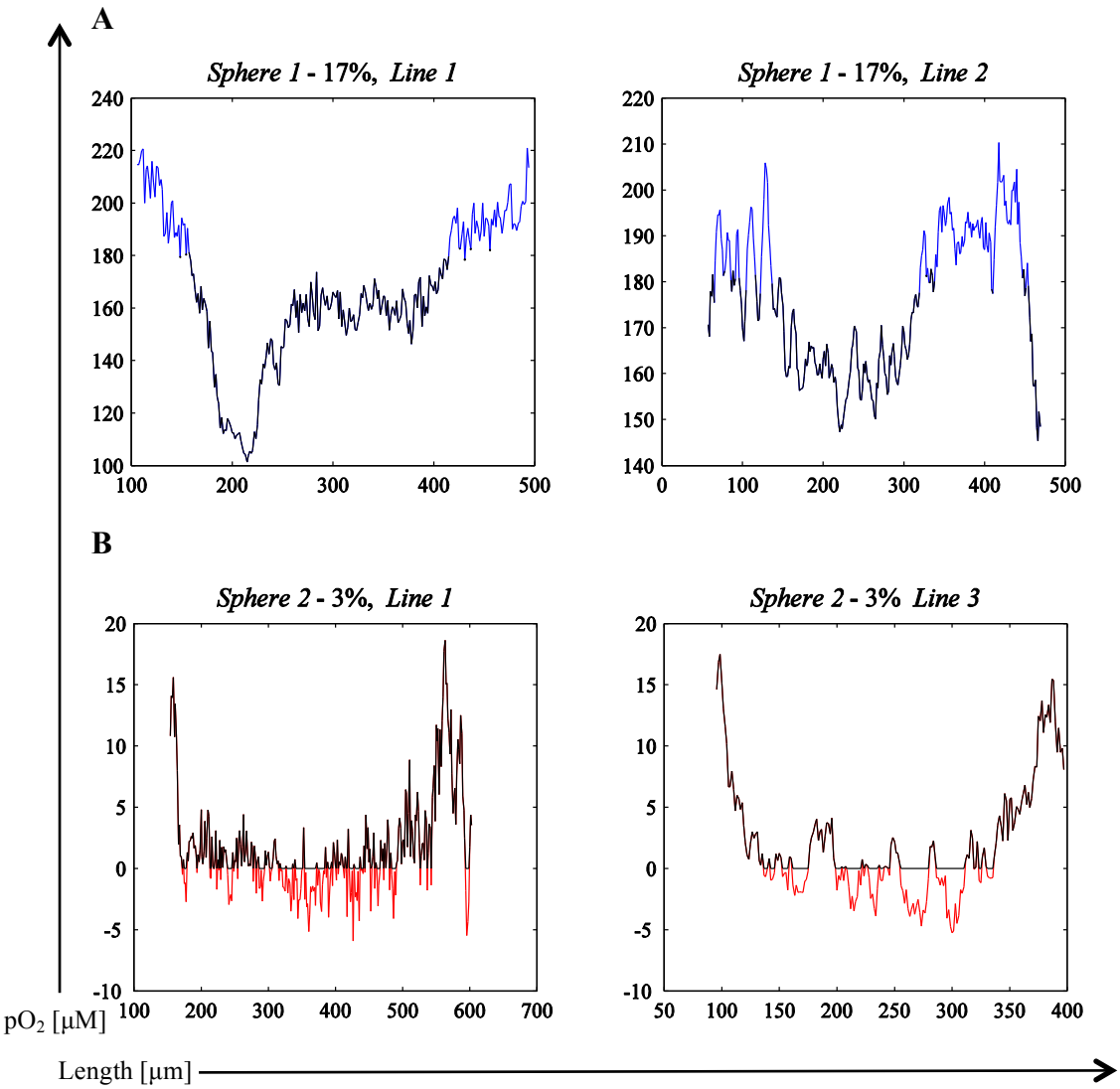

Figure 4-5: (A): *Sphere 1 - 17%, Lines 1&2*: Plots representing two cross-sections (*Lines 1&2*) of the same neurosphere (*Sphere 1*). Within each plot is a dataset corresponding to the interior oxygen concentration profile with an external oxygen concentration of 17%. (B): *Sphere 2 – 3%, Lines 1&3:* Plots representing *Lines 1&3* of *Sphere 2*. The curves represent data with an external oxygen concentration of 3%. Black data indicates pO_2 data generated from lifetime values that are within the feasible fitting range, i.e. (34-63 µs). Blue data is generated from lifetime values shorter than 35µs and is therefore cut. Red indicates negative pO_2 data. We set all negative data to be equal to 0µM.

One parameter in our model we have measurable information about in the data is C_∞, the value of the external oxygen concentration. However these experiments were conducted using O_2% incubators and our oxygen concentration data is given in pO_2 units (µM). In order to convert C_∞ values into pO_2 (µM) values we used the following relations previously calculated by our collaborators as well as in other literature and compared with our non-respiring hypoxic neurosphere data. Using oxygen solubility data atmospheric O_2 values were converted into dissolved O_2 concentration: 1.30µM/mmHg in water at 37°C, i.e., 1% O_2 corresponds to 9.9µM (Fercher, Ponomarev, et al. 2010a). This relationship corresponds linearly with other published approximations at the same solubility, 21% =

207μM (Qutub and Popel 2006, Tuckerman, et al. 2004) and 20.5% = 200μM (Fercher, O'Riordan, et al. 2010b).

We analysed our non-respiring neurosphere data by comparing with the linear correlation function $y = 9.9x$ given in the literature, to see if this unit conversion is suitable for our data (Figure 4-6). Lifetime data from neurospheres cultured in three different oxygen environments (1%, 8% and 17%) was recorded. Due to the lack of respiration, the effects of oxygen consumption were inhibited and a relatively uniform level of lifetime values was observed throughout the spheres. These lifetime data were converted to pO_2 (μM) using the calibration curve in Figure 4-3. The mean pO_2 (μM) values and standard deviations were calculated for each non-respiring sphere and plotted against the O_2% value for the experiment from which they came. To compare with the correlation found in the literature, the linear function $y = 9.9x$ was plotted on the same graph such that x corresponds to O_2% units and y to pO_2 (μM) units (see Figure 4-6). The non-respiring sphere data correlated well with the linear μM-to-% calibration curve for oxygen concentration. This allowed us to choose C_∞ values appropriately when data-fitting, e.g. for experimental data recorded in 3% O_2 we define C_∞= 9.9×3 = 29.7μM.

A

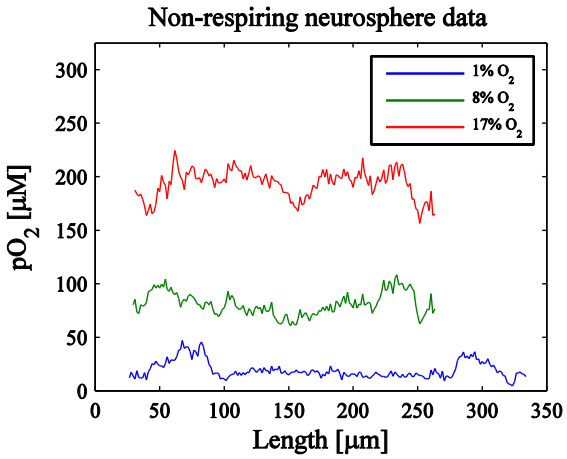

B

	1% O_2	8% O_2	17% O_2
Mean	19.42µM	81.14µM	193.59µM
Standard Deviation	7.96µM	10.53µM	13.14µM

C

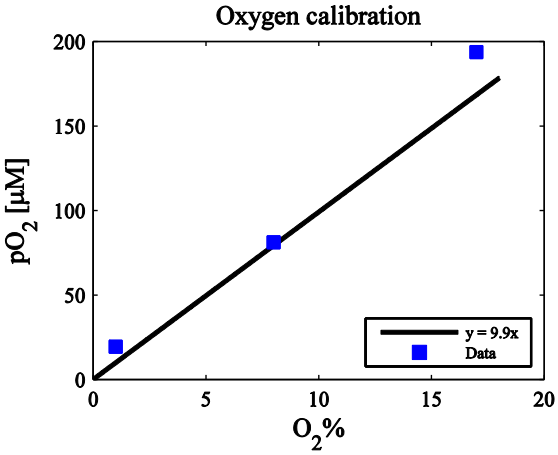

Figure 4-6: (A): pO_2 (µM) data for non-respiring spheres in external oxygen conditions 1% (blue), 8% (green) and 17% (red). (B): The mean pO_2 value of each 1D cross section was calculated as well as the standard deviation. (B): The mean values from the table were compared with the linear relationship derived from the relation found in publications by Fercher et al. (Evaluation of the derivates of phosphorescent Pt-coproporphyrin as intracellular oxygen-sensitive probes 2010a, Imaging of cellular oxygen and analysis of metabolic responses of mammalian cells 2010b) amongst others.

4.4.2 Data Fitting

To try and understand the effects of varying the external oxygen environment on oxygen dynamics within tumours we focus especially on data from the same spheres that have been subject to different oxygen conditions. In the data there exist two such spheres: *Sphere 1* has been exposed to both 17% and 8% external conditions; and *Sphere 2* has been exposed to both 8% and 3% (see Figure 4-7). These steady state distributions given by different external oxygen conditions will represent the start and end-points for our future simulations with time-dependent dynamics.

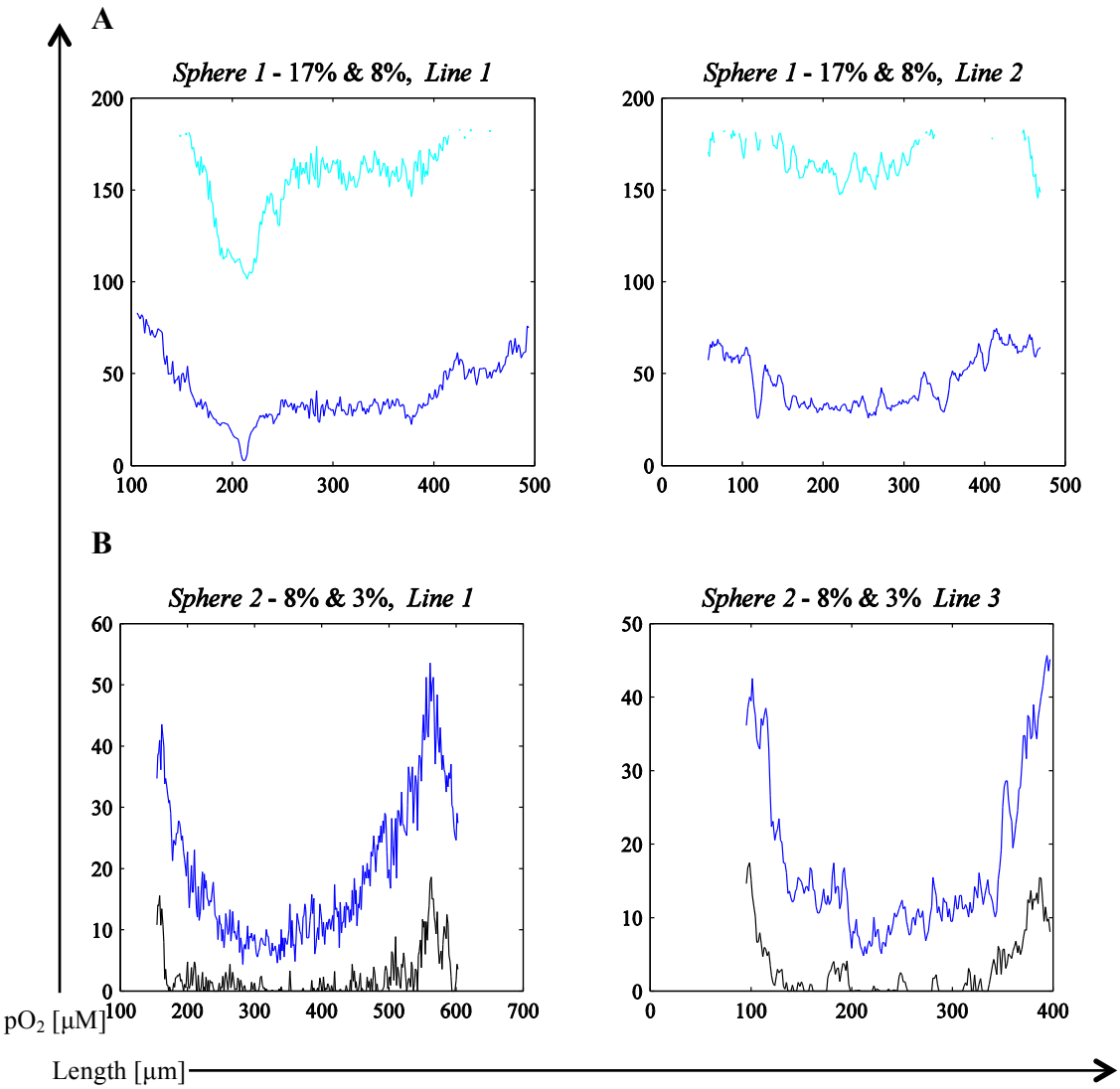

Figure 4-7: (A): Oxygen data values for *Sphere 1* taken at two different cross-section sites (*Lines 1&2*) for two different oxygen environments, 17% (cyan) and 8% (blue) O_2. (B): Oxygen data values for *Sphere 2*, *Lines 1&3* for 8% (blue) and 3% (black) oxygen environments. The effects of switching to hypoxia can be seen in this figure as oxygen values decrease suggesting progressively hypoxic neurospheres.

Before we begin fitting, some further examination of the data should be considered. *Sphere 2* data was recorded at 8% and 3% conditions and the pO_2 values generated for these lifetime values fell within the feasible range of fitting. No short-lifetime data had to be cut from *Sphere 2* due to any extrapolation from the calibration curve. For these reasons it was the results of *Sphere 2* fitting that was used for further parameterisation of the model. For further details on the unsuitability of data from the other spheres see the Appendix, section 7.4. We fit the spatial data series by optimally varying the specific model parameters.

4.4.2.1 *Optimised Parameters*

Fitting the steady state model to the data was performed via parameter optimisation using the *fminsearch* error minimisation technique (see the Appendix, section 7.1) comparable to the fitting work done in Chapters 2&3. We wanted to optimise the parameters of the model representing constant rates and since the non-dimensional consumption rate $\tilde{\psi} = R^2\psi/D_1$ is dependent on the radius, we instead optimise the ratio $\Psi = \psi/D_1$. This value should be the same for all data regardless of sphere radius. We also optimise constant parameter D, the ratio between the diffusion rate across cells inside the sphere and across the external medium. Parameters Ψ and D were optimised for four different data corresponding to 2 cross-sections (*Lines 1&3*) of *Sphere 2* in both oxygen conditions 8% and 3% O_2. We fit all four data simultaneously so that the same model parameter values were used to represent all dynamics. This is the assumption we made in model formulation, i.e. that parameters Ψ and D are constant rate parameter values independent of oxygen concentration C (or space r and time t). Fitting results are plotted in Figure 4-8.

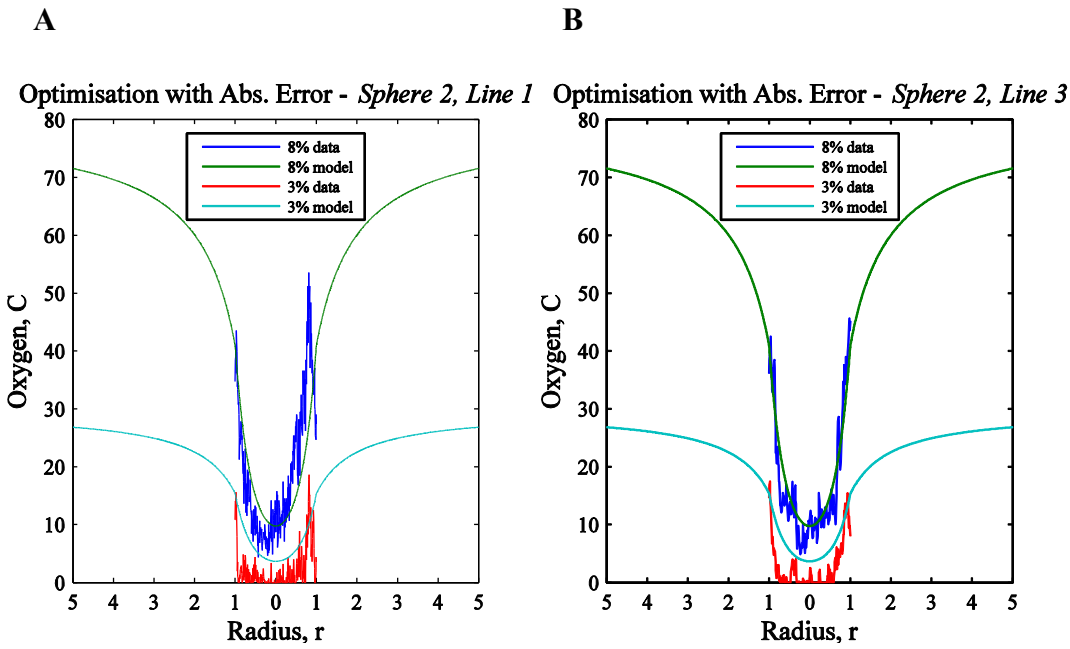

$C_\infty = 8\% \rightarrow C_\infty = 3\%$
$\Psi = 3.16\times10^{-4}\mu m^{-2}$
$D = 2.50\times10^{0}$

Figure 4-8: Optimised fits of the model to data from *Sphere 2* in both 8% and 3% O_2 for two different cross-sections: *Line 1* (A) and *Line 3* (B). Ψ and D values were optimised simultaneously for each data and are given below the plots. Parameter optimisation was achieved by reducing the absolute error between model solution and experimental data.

As can be seen in Figure 4-8, fitting all data to a single set of parameters (Ψ and D) results in good fits for 8% O_2 data but not such good fits for 3% O_2 data. We hypothesised this was due to using an absolute error value for χ, the measure of difference between the model solution and the data which is

minimised during parameter optimisation. Data from the 8% O_2 experiments has a higher oxygen concentration values compared to 3% O_2 experiments so there appears to be a bias in producing better fits for 8% data. In an attempt to reduce this bias we modified χ such that the relative error was calculated,

$$\chi = \sum_{i=1}^{n} \left(\frac{M_i - E_i}{M_i} \right)^2,$$

where E_i represents the i-th experimental data point and M_i represents the corresponding i-th model output point for oxygen concentration ($C(r)$ from (4.5) for r corresponding to the spatial-point of the experimental data). The resolution of the data is indicated by n, the number of time-points. However, fitting results using the relative error did not appear to significantly improve the quality of fit (see Figure 4-9).

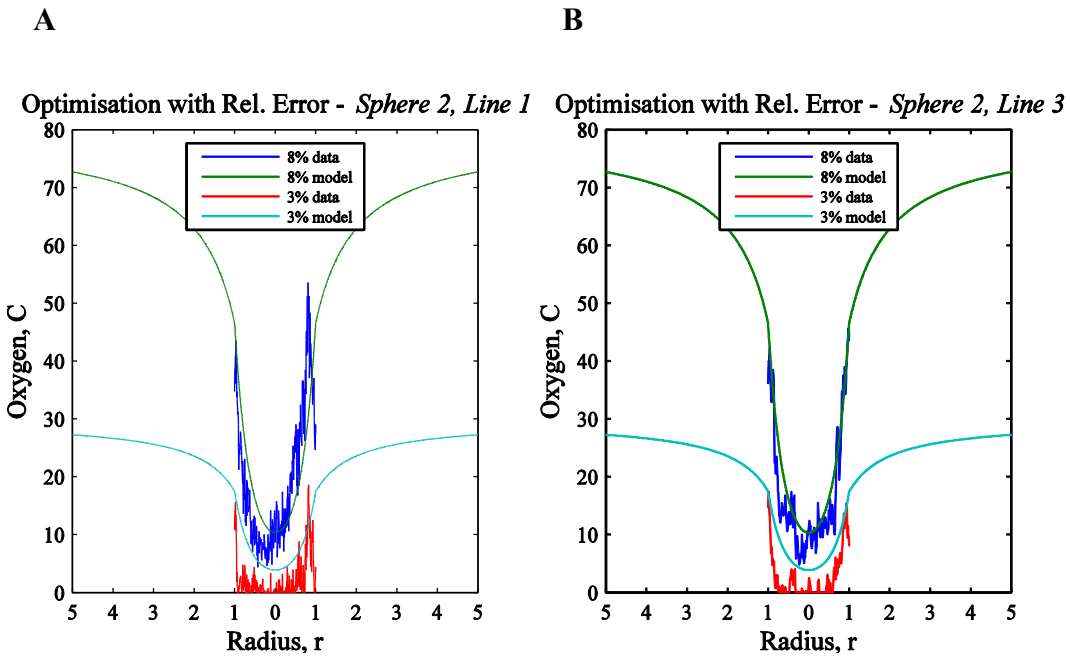

$C_\infty = 8\% \rightarrow C_\infty = 3\%$
$\Psi = 3.35\times10^{-4}\mu m^{-2}$
$D = 3.48\times10^{0}$

Figure 4-9: Fitting results as in Figure 4-8, but optimisation was achieved through minimising the relative error instead of the absolute error.

If we fit 8% and 3% O_2 data separately we predict much greater values of consumption rate Ψ for 3% than 8% whereas D remains relatively constant. One way in which the model could be improved upon in the future is through the introduction of a more sophisticated consumption rate that is dependent on the oxygen concentration, i.e. we would have the function $\psi(C)$. We will parameterise the current model using the results in Figure 4-9. That is, we impose the fixed values $\Psi = 3.35\times10^{-4}\mu m^{-2}$ and $D = 3.48$ for all further modelling work.

4.5 Time Dependent PDE Model of Oxygen Concentration

We now return to the time-dependent PDE model describing the oxygen concentration:

$$\begin{aligned} \frac{\partial C}{\partial t} &= \nabla^2 C - \psi C, \qquad r < 1, \\ \frac{\partial C}{\partial t} &= D\nabla^2 C, \qquad\quad r > 1, \end{aligned} \tag{4.6}$$

with mixed boundary conditions

$$\frac{\partial C}{\partial r} = 0, \quad r = 0,$$

$$C = C_0, \quad r = 1,$$

$$C \to C_\infty, \quad r \to \infty.$$

The value of C_0 is derived by imposing a constant-flux boundary condition:

$$D_1 \frac{\partial C_<}{\partial r} = D_2 \frac{\partial C_>}{\partial r} \quad r = 1.$$

4.5.1 Numerical Scheme

Solutions to the time-dependent system (4.6) were found numerically using a backward time centred space (BTCS) implicit Euler finite difference method which we now describe in detail.

To find an explicit numerical representation of system (4.6) we use Taylor series expansions to make a finite difference approximation to $\partial C/\partial t$. This is done so that we can calculate approximate values of the solution function C at each point of a discretised spatio-temporal mesh. We use a backward difference formula for our time derivative and central difference formulae for spatial derivatives. Small perturbations, or steps, are denoted by Δ.

$$\begin{aligned} \frac{\partial C(r,t)}{\partial t} &= \frac{C(r,t) - C(r,t-\Delta t)}{\Delta t}, \\ \frac{\partial C(r,t)}{\partial r} &= \frac{C(r+\Delta r,t) - C(r-\Delta r,t)}{2\Delta r}, \\ \frac{\partial^2 C(r,t)}{\partial r^2} &= \frac{C(r+\Delta r,t) - 2C(r,t) + C(r-\Delta r,t)}{(\Delta r)^2}. \end{aligned}$$

4.5.1.1 *Interior Dynamics*

We use a central finite difference approximation for the spatial derivatives, and a backward difference approximation for the time derivative to derive an approximation to our governing equation inside the sphere. We write the radially symmetric spherical form of the Laplacian operator for clarity:

$$\frac{\partial C}{\partial t} = \frac{\partial^2 C}{\partial r^2} + \frac{2}{r}\frac{\partial C}{\partial r} - \psi C. \tag{4.7}$$

We discretise equation (4.7) and simplify our notation using i and j subscripts to denote spatial and temporal steps in the mesh respectively. For example, $C_{i+1,j}$ represents the value of C at time-step j and spatial-step $i+1$ which is equivalent to r plus an additional space increment, Δr. We now have the governing finite difference equation:

$$\frac{C_{i,j} - C_{i,j-1}}{\Delta t} = \frac{C_{i+1,j} - 2C_{i,j} + C_{i-1,j}}{(\Delta r)^2} + \frac{2}{r}\left(\frac{C_{i+1,j} - C_{i-1,j}}{2\Delta r}\right) - \psi C_{i,j}. \tag{4.8}$$

Note that one term in (4.8) refers to variable C at time-step $j-1$ and all others at step j. If we know the value of C at all mesh points on the $(j-1)$-level, then C values at the j-level can be calculated from equation (4.8) using a system of equations.

For all future simulations we will investigate spatio-temporal oxygen dynamics by perturbing from the temporal steady state. This perturbation is implemented by altering the external oxygen concentration conditions. Hence we prescribe the initial condition in our simulations to be the oxygen distribution at equilibrium. For the internal oxygen values, this is described by

$$C(r,0) = \frac{C_0 \sinh\left(\sqrt{\psi} r\right)}{r \sinh\left(\sqrt{\psi}\right)}.$$

We use l'Hôpital's rule to determine the value of $C(0,0)$:

$$\lim_{r\to 0} \frac{C_0 \sinh\left(\sqrt{\psi} r\right)}{r \sinh\left(\sqrt{\psi}\right)} = \lim_{r\to 0} \frac{C_0\sqrt{\psi} \cosh\left(\sqrt{\psi} r\right)}{\sinh\left(\sqrt{\psi}\right)} = \frac{C_0\sqrt{\psi}}{\sinh\left(\sqrt{\psi}\right)}.$$

To find the system of equations that enable us to calculate C at the j-level from the $(j-1)$-level we re-write equation (4.8) in the following form:

$$\begin{aligned} C_{i,j-1} &= \frac{\Delta t}{\Delta r}\left(\frac{1}{r} - \frac{1}{\Delta r}\right) C_{i-1,j} + \left(1 + \psi\Delta t + \frac{2\Delta t}{(\Delta r)^2}\right) C_{i,j} - \frac{\Delta t}{\Delta r}\left(\frac{1}{r} + \frac{1}{\Delta r}\right) C_{i+1,j} \\ &= XC_{i-1,j} + YC_{i,j} + ZC_{i+1,j}. \end{aligned}$$

We re-write this system for the interior space $i = 1..R-1$:

$$\begin{pmatrix} Y & Z & 0 & \cdots & 0 \\ X & Y & Z & \cdots & 0 \\ 0 & X & Y & \cdots & 0 \\ \vdots & \vdots & \vdots & \ddots & \vdots \\ 0 & 0 & 0 & \cdots & Y \end{pmatrix} \begin{pmatrix} C_{2,j} \\ C_{3,j} \\ C_{4,j} \\ \vdots \\ C_{R-1,j} \end{pmatrix} = \begin{pmatrix} C_{2,j-1} \\ C_{3,j-1} \\ C_{4,j-1} \\ \vdots \\ C_{R-1,j-1} \end{pmatrix} - \begin{pmatrix} XC_{1,j} \\ 0 \\ 0 \\ \vdots \\ ZC_{R,j} \end{pmatrix} \tag{4.9}$$

If boundary values C_1 (the value of C at the centre of the sphere) and C_R (the value of C at the border of the sphere) are known, this matrix equation can be solved to obtain C at time-step j from existing knowledge of C at time-step $j-1$. We initially assume that C_R is a known constant. To determine C_1 we use the Neumann boundary condition, $\partial C(0,t)/\partial r = 0$. We take a central finite difference approximation to discretise the Neumann condition:

$$\begin{aligned} \frac{\partial C}{\partial r} &= \frac{C_{i+1,j} - C_{i-1,j}}{2\Delta r} = 0, \\ \Rightarrow C_{i-1,j} &= C_{i+1,j}. \end{aligned} \tag{4.10}$$

With $i = 1$, $C_{0,j}$ is called a 'ghost node' as this point lies outside the solution mesh. Using equation (4.10) we define $C_{0,j}$:

$$C_{0,j} = C_{2,j},$$

and we can now determine a value for $C_{1,j}$ using our governing finite difference equations (4.9):

$$\begin{aligned} C_{1,j} &= XC_{0,j+1} + YC_{1,j+1} + ZC_{2,j+1} \\ &= YC_{1,j+1} + (X+Z)C_{2,j+1}, \end{aligned}$$

or

$$C_{1,j-1} = YC_{1,j} + (X+Z)C_{2,j}.$$

Our system of equations (4.9) now becomes

$$\begin{pmatrix} Y & (X+Z) & 0 & 0 & \cdots & 0 \\ X & Y & Z & 0 & \cdots & 0 \\ 0 & X & Y & Z & \cdots & 0 \\ 0 & 0 & X & Y & \cdots & 0 \\ \vdots & \vdots & \vdots & \vdots & \ddots & \vdots \\ 0 & 0 & 0 & 0 & \cdots & Y \end{pmatrix} \begin{pmatrix} C_{1,j} \\ C_{2,j} \\ C_{3,j} \\ C_{4,j} \\ \vdots \\ C_{R-1,j} \end{pmatrix} = \begin{pmatrix} C_{1,j-1} \\ C_{2,j-1} \\ C_{3,j-1} \\ C_{4,j-1} \\ \vdots \\ C_{R-1,j-1} \end{pmatrix} - \begin{pmatrix} 0 \\ 0 \\ 0 \\ 0 \\ \vdots \\ ZC_{R,j} \end{pmatrix}, \tag{4.11}$$

which can be numerically solved to obtain C_j from C_{j-1}.

4.5.1.2 Coupling Interior & Exterior Dynamics

System (4.11) describes an approximate solution for the interior sphere oxygen dynamics. To couple to the exterior dynamics we need to include the finite difference approximation of our exterior PDE with no consumption. For clarity we use $\hat{C}$ to represent oxygen concentration outside the sphere.

$$\hat{C}_{i,j-1} = \frac{D\Delta t}{\Delta r}\left(\frac{1}{r} - \frac{1}{\Delta r}\right)\hat{C}_{i-1,j} + \left(1 + \frac{2D\Delta t}{(\Delta r)^2}\right)\hat{C}_{i,j} - \frac{D\Delta t}{\Delta r}\left(\frac{1}{r} + \frac{1}{\Delta r}\right)\hat{C}_{i+1,j}$$
$$= DX\hat{C}_{i-1,j} + W\hat{C}_{i,j} + DZ\hat{C}_{i+1,j},$$

where $i = 1..N-1$ and $i = 1$ corresponds to $R+1$. When coupling the interior and exterior models recall that there is a zero Neumann boundary condition at the sphere centre, which has been accounted for, and a Dirichlet condition for $r = \infty$. In practice, we will not be able to simulate $r = \infty$ and so we will assume the outer boundary of the exterior dynamics, $\hat{C}_N$, to be fixed based on the steady state solution. That is, when we want to simulate a switch from 8% O_2 to 3% O_2 for example, we will define the initial condition as the steady state solution calculated in section 4.3.

$$C(0,0) = \frac{C_0\sqrt{\psi}}{\sinh(\sqrt{\psi})}, \qquad r = 0,$$
$$C(r,0) = \frac{C_0\sinh(\sqrt{\psi}r)}{r\sinh(\sqrt{\psi})}, \qquad 0 < r < 1,$$
$$C(1,0) = C_0, \qquad r = 1,$$
$$C(r,0) = \frac{1}{r}(C_0 - C_\infty) + C_\infty, \qquad r > 1,$$

where $C_0 = DC_\infty/(\sqrt{\psi}\ \coth((\sqrt{\psi}) - 1 + D)$.

Initially, to simulate 8% O_2 we set C_∞ = 8% O_2 = 9.9 × 8 pO_2 (μM). As we have to numerically solve over a finite mesh we define the outer boundary condition (Dirichlet) to be

$$C(N,t) = \frac{1}{N}(C_0 - C_\infty) + C_\infty, \qquad t < T$$

where N denotes the boundary external radial value. This value represents the oxygen source and is where the oxygen switch is implemented. Upon switching to 3% O_2 oxygen conditions in our example, at time $t = T$, we update the value of C_∞ accordingly: C_∞^T = 3% O_2 = 9.9 × 3 pO_2 (μM). Therefore we update the Dirichlet condition and perturb the 8% steady state:

$$C(N,t) = \frac{1}{N}(C_0^T - C_\infty^T) + C_\infty^T, \qquad t \geq T$$

There is also a Neumann boundary condition at the interface between the interior dynamics and the exterior dynamics,

$$D_1 \frac{\partial C}{\partial r} = D_2 \frac{\partial \hat{C}}{\partial r}, \tag{4.12}$$

which specifies that the flux of oxygen at the boundary is matched by both sides. We will use this condition to determine $C_{R,j}$, the value of C at the boundary. First we look at the last equation for the discretisation of our interior model, and the first equation for our exterior model, with respect to space.

$$XC_{R-2,j} + YC_{R-1,j} = C_{R-1,j-1} - ZC_{R,j},$$

and

$$W\hat{C}_{1,j} + DZ\hat{C}_{2,j} = \hat{C}_{1,j-1} - DX\hat{C}_{0,j}, \tag{4.13}$$

where $\hat{C}_{0,j} = C_{R,j}$. To determine $C_{R,j}$ we approximate condition (4.12) by one-sided finite difference approximations:

$$D_1 \frac{C_{R,j} - C_{R-1,j}}{\Delta r} = D_2 \frac{\hat{C}_{1,j} - \hat{C}_{0,j}}{\Delta r}$$

$$\Rightarrow \hat{C}_{0,j} = C_{R,j} = \frac{1}{D_1 + D_2}\left(D_1 C_{R-1,j} + D_2 \hat{C}_{1,j}\right) \tag{4.14}$$

We can now write equations (4.13) as

$$XC_{R-2,j} + YC_{R-1,j} = C_{R-1,j-1} - Z\frac{1}{D_1 + D_2}\left(D_1 C_{R-1,j} + D_2 \hat{C}_{1,j}\right),$$

$$\Rightarrow C_{R-1,j-1} = XC_{R-2,j} + \left(Y + Z\frac{D_1}{D_1 + D_2}\right)C_{R-1,j} + Z\frac{D_2}{D_1 + D_2}\hat{C}_{1,j}$$

and

$$W\hat{C}_{1,j} + DZ\hat{C}_{2,j} = \hat{C}_{1,j-1} - DX\frac{1}{D_1 + D_2}\left(D_1 C_{R-1,j} + D_2 \hat{C}_{1,j}\right), \tag{4.15}$$

$$\Rightarrow \hat{C}_{1,j-1} = DX\frac{D_1}{D_1 + D_2}C_{R-1,j} + \left(W + DX\frac{D_2}{D_1 + D_2}\right)\hat{C}_{1,j} + DZ\hat{C}_{2,j}$$

Since we only have a value for $D = D_2/D_1$ and not specific values for D_1 and D_2 explicitly, we write

$$\frac{D_1}{D_1 + D_2} = \frac{1}{1 + D}$$

and

$$\frac{D_2}{D_1 + D_2} = 1 - \frac{1}{1+D} = \frac{D}{1+D}.$$

For the coupled system of interior and exterior oxygen dynamics we have the following matrix equation to solve for $\vec{C}_j$ for each time-step j. For each iteration of j we also update $C_{R,j}$ using equation (4.14).

$$\begin{pmatrix} Y & (X+Z) & 0 & 0 & \cdots & 0 & \cdots & & & \cdots & 0 \\ X & Y & Z & 0 & \cdots & 0 & \cdots & & & \cdots & 0 \\ 0 & X & Y & Z & \cdots & 0 & \cdots & & & \cdots & 0 \\ 0 & 0 & X & Y & \cdots & 0 & \cdots & & & \cdots & 0 \\ \vdots & \vdots & \vdots & \vdots & \ddots & \vdots & \vdots & \vdots & \vdots & \vdots & \vdots \\ 0 & 0 & 0 & 0 & \cdots & Y + Z\frac{1}{1+D} & Z\frac{D}{1+D} & 0 & 0 & \cdots & 0 \\ \vdots & \vdots & \vdots & \vdots & \cdots & DX\frac{1}{1+D} & W + DX\frac{D}{1+D} & DZ & 0 & \cdots & 0 \\ & & & & \cdots & 0 & DX & W & DZ & \cdots & 0 \\ & & & & \cdots & 0 & 0 & DX & W & \cdots & 0 \\ \vdots & \vdots & \vdots & \vdots & \cdots & \vdots & \vdots & \vdots & \vdots & \ddots & \vdots \\ 0 & 0 & 0 & 0 & \cdots & 0 & 0 & 0 & 0 & \cdots & W \end{pmatrix} \begin{pmatrix} C_{1,j} \\ \vdots \\ \\ \\ \vdots \\ C_{R-1,j} \\ \hat{C}_{1,j} \\ \vdots \\ \\ \vdots \\ \hat{C}_{N-1,j} \end{pmatrix}$$

$$= \begin{pmatrix} C_{1,j-1} \\ \vdots \\ \\ \\ \vdots \\ C_{R-1,j-1} \\ \hat{C}_{1,j-1} \\ \vdots \\ \\ \vdots \\ \hat{C}_{N-1,j-1} \end{pmatrix} - \begin{pmatrix} 0 \\ \vdots \\ \\ \\ \\ \\ \\ \vdots \\ DZC_{N,j} \end{pmatrix}$$

4.5.2 Numerical Simulation Results

We numerically simulated the spatio-temporal dynamics of oxygen inside and outside of a radially symmetric respiring sphere. These simulations were carried out by solving our oxygen dynamics PDE as described by the numerical scheme in section 4.5.1 using MATLAB. We plotted the results of these simulations as both spatio-temporal surface plots and spatial time-step plots (see Figure 4-10 & Figure 4-11). These simulations used a 1001x1001 grid resolution. Increasing to a higher resolution did not yield any noticeable difference in the figures and so this choice of mesh was deemed sufficiently accurate.

Simulations were initially carried out focusing on the effect of hypoxic switches on oxygen dynamics inside and outside of the sphere (see Figure 4-10 & Figure 4-11). These simulations were carried out by starting at a steady state distribution corresponding to the analytical solution, found in in section

4.3, derived using a particular C_∞ value and then switching to another C_∞ value. The simulation is then run until the new steady state distribution is obtained.

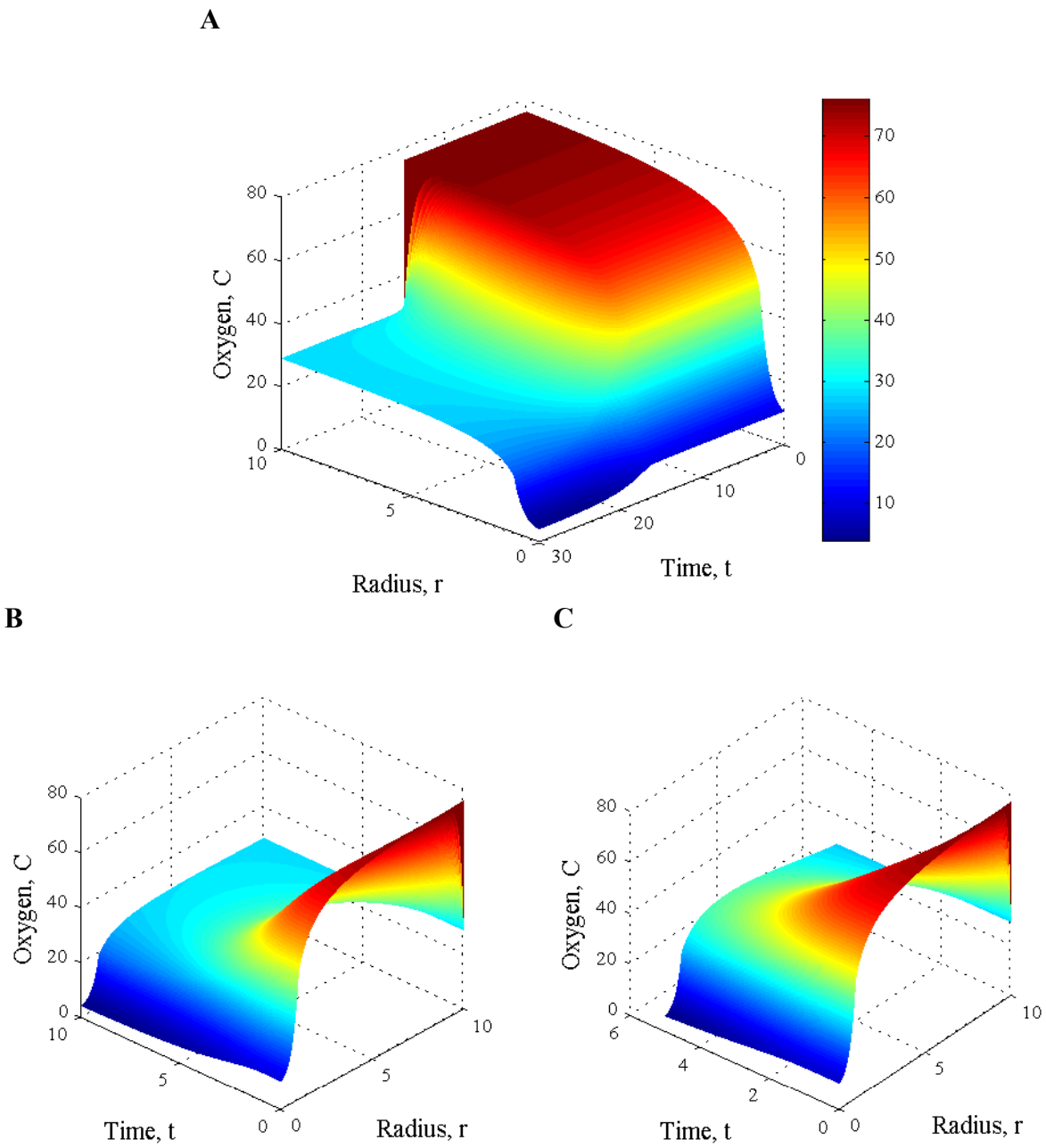

Figure 4-10: Three-dimensional surface plots showing the solutions of our oxygen dynamics PDE (4.6). Plotted are: time, space (radius), and oxygen concentration. Oxygen concentration can also be visualised by the colour of the plotted surface (high to low corresponds to red to blue – see the colour bar in (A)). (A): In this simulation, the C_∞ value has been decreased at $t = 15$, representing a switch to hypoxia that takes effect at the $r = 10$ boundary. The sphere interior (where oxygen consumption and a slower diffusion rate occur) is bounded at $r = 1$. (B, C): Simulations using the same parameter values show in more detail the transient spatio-temporal dynamics immediately following the hypoxic switch by looking at a shorter timescale following the hypoxic switch. A 1001x1001 space-time mesh was used for these plots, C_∞ was changed from 8% to 3% O_2.

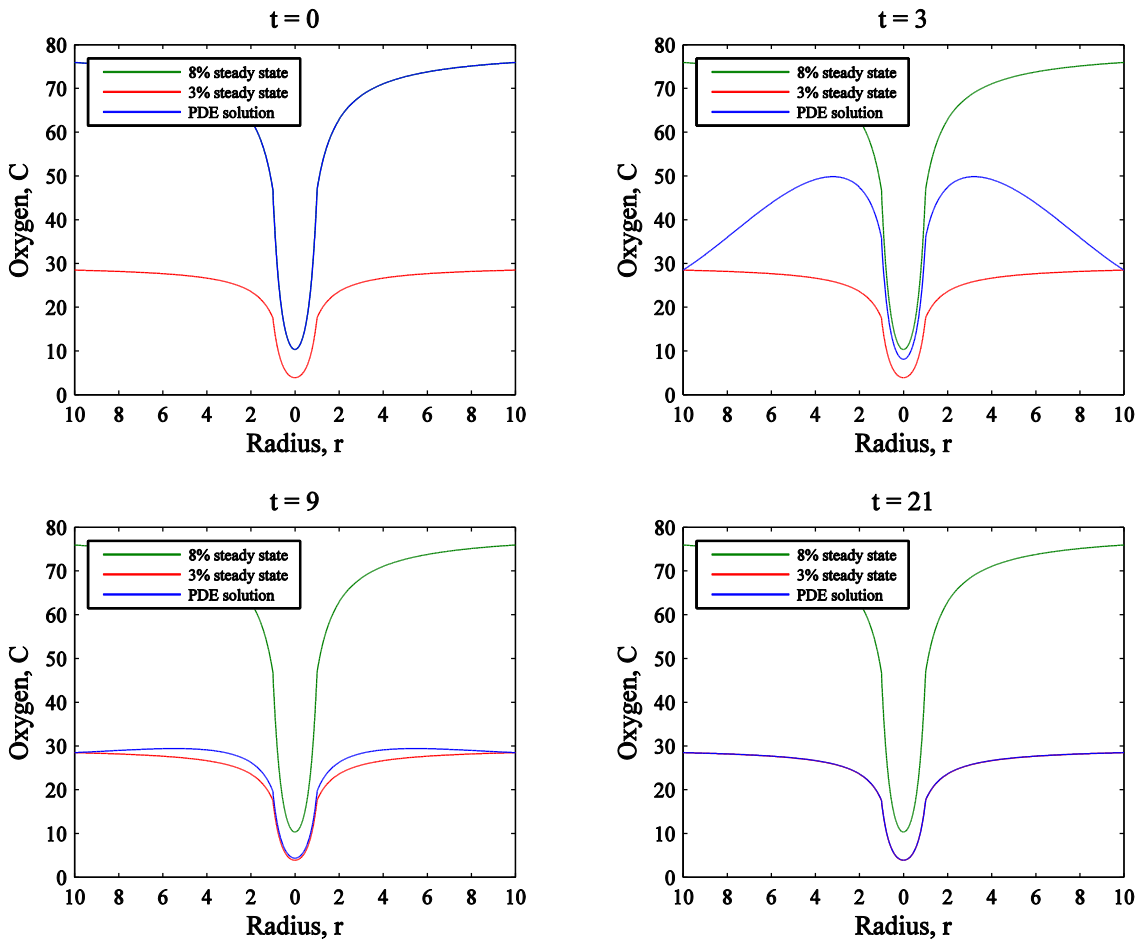

Figure 4-11: 2D figures plotting oxygen concentration at different time points. The C_∞ value has been decreased from 8% to 3% O_2 at $t = 0$. Green and red curves represent the analytical steady state solutions of the oxygen model and this equilibrium envelope is permanently superimposed onto the time-series plots for comparison with the blue curves which represent the PDE approximation solutions. At $t = 0$ the blue and green curves coincide and as time increases the blue curve tends toward the new steady state (red curve).

4.5.3 Oxygen Model with Non-linear Consumption

In section 4.4.2.1 we suggested that a more complex dynamic oxygen model would yield more successful data-fitting results when compared with Figure 4-8 and Figure 4-9. In particular, the current model did not seem adept at reproducing the steady state oxygen distribution in more severe hypoxic conditions (i.e. compare fitting results of 3% external O_2 compared with 8% in Figure 4-8 and Figure 4-9). We hypothesised that a more sophisticated oxygen consumption rate could address this deficiency, specifically through the introduction of a non-linear oxygen-dependent rate of consumption. If we replace the constant, linear consumption term ψC with a term that saturates for higher oxygen levels we define a likely more realistic description of the process that will also correspond with what we see experimentally. As shown in working with our constant consumption assumption, for the more hypoxic experiments we see a relatively lower amount of oxygen in the

centre of the neurospheres than we would expect from a change in external oxygen values alone. In order to represent saturating oxygen consumption we define the following modified partial differential equation:

$$\frac{\partial C}{\partial t} = D_1 \nabla^2 C - \psi \frac{C}{C + \kappa}, \quad \boldsymbol{x} \in \Omega.$$

As before, C represents oxygen concentration and D_1 is the constant diffusion coefficient inside the sphere. The maximal consumption rate is given by ψ with κ representing the oxygen value at which consumption has reached half its maximal value. Time is given by t while $\boldsymbol{x}$ represents the spatial vector with the equation being considered within the domain Ω (the sphere). We re-scale this PDE in an analogous way to the method in section 4.3:

$$\frac{\partial C}{\partial \tilde{t}} = \tilde{\nabla}^2 C - \tilde{\psi} \frac{C}{C + \kappa},$$

where

$$\tilde{\boldsymbol{x}} = \frac{\boldsymbol{x}}{R}, \qquad \tilde{t} = \frac{D_1}{R^2} t, \qquad \tilde{\psi} = \frac{R^2}{D_1} \psi.$$

From here on we will drop the tildes for notational simplicity. As before we take the time equilibrium of the equation for data comparisons, convert to spherical coordinates and assume radial symmetry:

$$\begin{aligned} \nabla^2 C - \psi \frac{C}{C + \kappa} = 0 \quad & r \leq 1, \\ \frac{\partial C}{\partial r} = 0, \quad & r = 0, \\ C = C_0, \quad & r = 1. \end{aligned} \tag{4.16}$$

As we are only proposing changes to internal oxygen dynamics the equations for oxygen outside the sphere remain the same:

$$\begin{aligned} D \nabla^2 C = 0, \quad & r > 1, \\ C \to C_\infty, \quad & r \to \infty, \\ C = C_0, \quad & r = 1, \end{aligned} \tag{4.17}$$

where $D = D_2 / D_1$. Equation (4.17) has the same analytical solution as before,

$$C = \frac{1}{r}(C_0 - C_\infty) + C_\infty.$$

However the analytical solution for our internal spatial dynamics equation, (4.16), cannot be solved analytically and thus we look for a numerical solution.

4.5.3.1 Numerical Solution for the Temporal Steady State

We have the following second order non-linear differential equation to solve numerically and find the spatial oxygen dynamics at the steady state:

$$\nabla^2 C - \psi \frac{C}{C+\kappa} = 0.$$

In order to do this we re-introduce the time-dependence in our PDE, develop a finite difference approximation numerical scheme, and simulate until the steady state has been reached. We use finite difference approximations in an analogous way to section 4.5. Thus, we return to the time-dependent PDE model describing the oxygen concentration:

$$\begin{aligned} \frac{\partial C}{\partial t} &= \nabla^2 C - \psi \frac{C}{C+\kappa}, \qquad r < 1, \\ \frac{\partial C}{\partial t} &= D\nabla^2 C, \qquad\qquad\quad r > 1, \end{aligned} \tag{4.18}$$

with mixed boundary conditions

$$\frac{\partial C}{\partial r} = 0, \quad r = 0,$$

$$C = C_0, \quad r = 1,$$

$$C \to C_\infty, \quad r \to \infty.$$

The value of C_0 is derived by imposing a constant-flux boundary condition:

$$D_1 \frac{\partial C_<}{\partial r} = D_2 \frac{\partial C_>}{\partial r} \quad r = 1.$$

Due to the introduction of a non-linear consumption term, $\psi C/(C+\kappa)$, we did not use BTCS implicit Euler finite difference method to find solutions of system (4.18). Instead we make finite difference approximations for spatial derivatives only, such that we have a system of time-derivative ordinary differential equations which we solve in MATLAB. We use central difference formulae for spatial derivatives:

$$\frac{\partial C(r,t)}{\partial r} = \frac{C(r+\Delta r,t) - C(r-\Delta r,t)}{2\Delta r},$$
$$\frac{\partial^2 C(r,t)}{\partial r^2} = \frac{C(r+\Delta r,t) - 2C(r,t) + C(r-\Delta r,t)}{(\Delta r)^2}.$$

For the interior oxygen dynamics we then have:

$$\frac{\partial C_i}{\partial t} = \frac{C_{i+1} - 2C_i + C_{i-1}}{(\Delta r)^2} + \frac{2}{r}\left(\frac{C_{i+1} - C_{i-1}}{2\Delta r}\right) - \psi \frac{C_i}{C_i + \kappa}. \tag{4.19}$$

for $i = 1..R$, i.e. $r = 0..R-1$. When $i = 1$, we define $C_{i-1} = C_0$ using the Neumann boundary condition at $r = 0$ and a ghost node as before (see (4.10)). Thus

$$C_0 = C_2.$$

When $i = R$, we define $C_{i+1} = C_{R+1}$ using the constant flux boundary condition as before (see (4.14)) and consequently we have

$$C_{R+1} = \frac{1}{1+D}\left(C_R + D\hat{C}_1\right),$$

where $\hat{C}$ refers to external oxygen as before and $\hat{C}_1$ represents the value of oxygen at C at $i = R + 2$.

For the external oxygen dynamics we write the following system:

$$\frac{\partial C_i}{\partial t} = D\left(\frac{C_{i+1} - 2C_i + C_{i-1}}{(\Delta r)^2}\right) + \frac{2D}{r}\left(\frac{C_{i+1} - C_{i-1}}{2\Delta r}\right). \tag{4.20}$$

where $i = 1..N-1$ and $i = 1$ corresponds to $R + 2$. When $i = 1$, we need $\hat{C}_{i-1} = \hat{C}_0$ which is equivalent to the value of oxygen at the boundary and so we have

$$\hat{C}_0 = C_{R+1} = \frac{1}{1+D}\left(C_R + D\hat{C}_1\right).$$

We define our outermost point $\hat{C}_N$ (required when $i = N-1$) as before based on the steady state for external oxygen dynamics. Therefore,

$$\hat{C}_N = \frac{1}{N}\left(\hat{C}_0 - C_\infty\right) + C_\infty.$$

Let us couple this system under a single variable such that $w_1 = C_1$, $w_R = C_R$ and $w_{R+1} = \hat{C}_1$. We then write the system of temporal ODEs for w_i for $i = 1..N-1$:

$$\frac{dw_1}{dt} = \frac{2(w_2 - w_1)}{(\Delta r)^2} - \psi \frac{w_1}{w_1 + \kappa}, \qquad i = 1, \; r = 0,$$

$$\frac{dw_i}{dt} = \frac{1}{\Delta r}\left(\frac{w_{i+1} - 2w_i + w_{i-1}}{\Delta r} + \frac{w_{i+1} - w_{i-1}}{r}\right) - \psi \frac{w_i}{w_i + \kappa}, \qquad i = 2..R-1, \; r = 1..R-2,$$

$$\frac{dw_R}{dt} = \frac{1}{\Delta r}\left(\frac{w_R + Dw_{R+1} + (1+D)(w_{R-1} - 2w_R)}{(1+D)\Delta r} + \frac{w_R + Dw_{R+1} - (1+D)w_{R-1}}{(1+D)r}\right) - \psi \frac{w_R}{w_R + \kappa} \qquad i = R, \; r = R-1,$$

$$\frac{dw_{R+1}}{dt} = \frac{D}{(1+D)\Delta r}\left(\frac{(1+D)(w_{R+2} - 2w_{R+1}) + w_R + Dw_{R+1}}{\Delta r} + \frac{(1+D)w_{R+2} - w_R - Dw_{R+1}}{r}\right), \qquad i = R+1, \; r = R+1,$$

$$\frac{dw_i}{dt} = \frac{D}{\Delta r}\left(\frac{w_{i+1} - 2w_i + w_{i-1}}{\Delta r} + \frac{w_{i+1} - w_{i-1}}{r}\right), \qquad i = R+2..N-2, \; r = R+2..N-2,$$

$$\frac{dw_{N-1}}{dt} = \frac{D}{(1+D)N\Delta r}\left(\frac{w_R + Dw_{R+1} + (1+D)(N(C_\infty - 2w_{N-1} + w_{N-2}) - C_\infty)}{\Delta r} + \frac{w_R + Dw_{R+1} + (1+D)(N(C_\infty - w_{N-2}) - C_\infty)}{r}\right) \qquad i = N-1, \; r = N-1,$$

We are able to find the temporal steady state of the new model with non-linear consumption, (4.18), using the above system of ODEs. Now we can optimise the model parameters in order to fit our steady-state model output to experimental data. We optimised parameters $\Psi = \psi/D_1$ and D as before, as well as the new parameter κ. Optimisation was carried out in an analogous way to the previous model in Figure 4-9, using the same experimental data and relative error condition. The data-fitting results are plotted in Figure 4-12. It is clear from this figure that the introduction of a more sophisticated, saturating oxygen-consumption term has resulted in better fits to the experimental data. In particular the fits appear to be good for both 8% and 3% O_2 conditions without bias, unlike previously, using the same constant model parameters throughout.

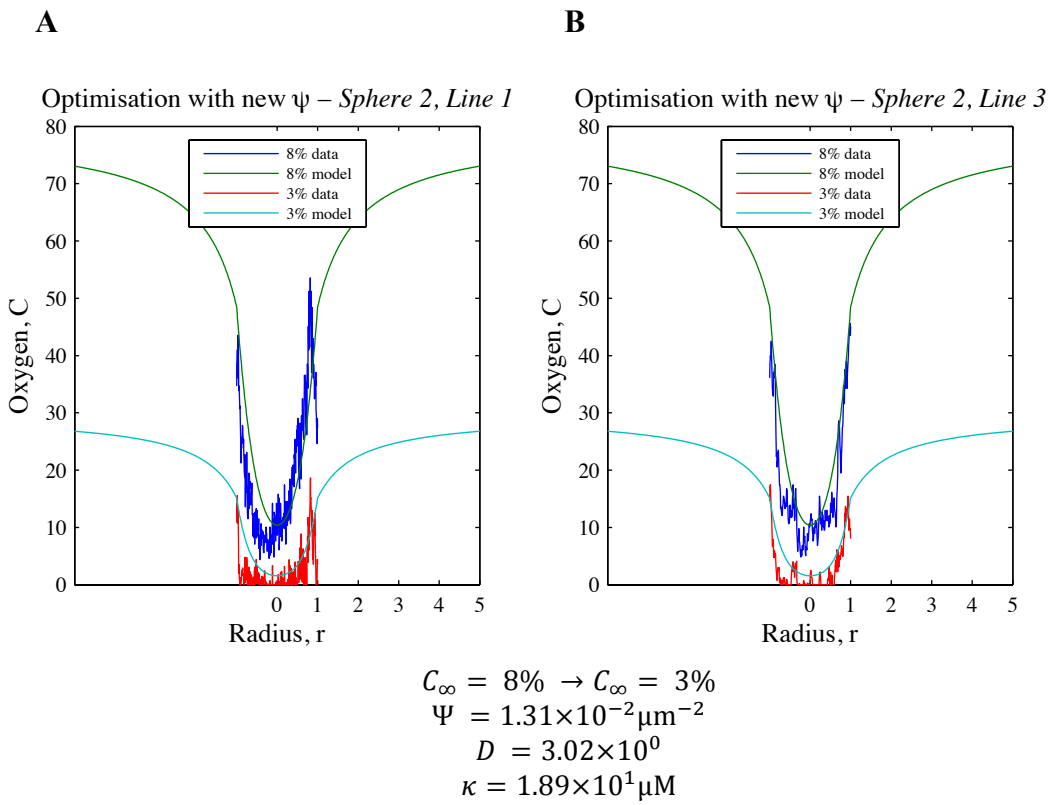

Figure 4-12: Parameter optimisation of a modified oxygen diffusion model with non-linear consumption. Fitting methods comparable to Figure 4-9, but optimisation also included the saturation threshold parameter κ.

This modified oxygen model comprises an addendum to the original research presented and as such we shall revert to the linear oxygen consumption model for the remainder of the thesis.

4.6 Coupling to the HIF-1α Model

By simulating a hypoxic switch in our PDE model for oxygen dynamics in tumour spheres (4.6) and coupling to our previous single-cell HIF-1α signalling pathway model, we aim to predict the spatial variation of single-cell HIF-1α dynamics within a hypoxic avascular tumour. The oxygen diffusion model provides a more biologically realistic setting for an investigation into the effects of rapid, acute oxygen switches on the dynamics of the HIF-1α signalling pathway.

Our oxygen model can be coupled to the HIF-1α model through the oxygen concentration C, where the hydroxylation rate functions h_i vary with the dependent variable C (see Chapter 3 equations (3.4) & (3.5)). As our HIF-1α model is based on an intracellular pathway with no feedback between cells we are only interested in the temporal dynamics of oxygen concentration at discrete spatial positions for coupling. This is achieved by assuming that in our timescale of interest (minutes to hours) that cells don't move significantly and we neglect any cell cycle effects such as growth and division. This

means that we can expect the fixed spatial discretisation of the mesh on which we numerically solve the oxygen dynamics PDE to be representative of a spatial discretisation of the tumour into component tumour cells. Furthermore, we choose an approximate 1:1 ratio between grid-points and single-cells for convenience as we have sufficient accuracy at this resolution. Therefore for a fixed radius $r = r^*$, we identify the position of a single cell and associate the temporal oxygen dynamics that occur at that radial position with the HIF-1α model to simulate intracellular HIF-1α dynamics for a cell at distance $r = r^*$.

4.6.1 Comparing Timescales

In order to couple these models their respective timescales need to be compared. The HIF-1α model uses dimensional time units of minutes or hours whereas our oxygen model unit of time has been non-dimensionalised based on the timescale for oxygen to diffuse throughout the sphere, $\tilde{t} = D_1 t/R^2$. As we do not have an estimate for the diffusion rate D_1 within the sphere, we have chosen to compare the time taken for the lifetime values in hypoxic neurosphere experiments to reach steady state values t, with the re-scaled time taken for the numerical approximation of oxygen concentration to reach steady state $\tilde{t}$, in order to formulate a scaling factor. This scaling factor will enable us to simulate the oxygen model in dimensional time units and therefore also allow coupling to the HIF-1α model.

For example, from our experimental work we know that it took at most 8 minutes for the oxygen distribution in a sphere of radius 200μm to reach a time-independent equilibrium after a switch in exterior oxygen levels from 17.9% O_2 to 8% O_2. To compare with our model, we choose to switch C_∞ from 9.9 × 17.9 pO_2 (μM) to 9.9 × 8 pO_2 (μM). This defines the equilibrium envelope but we choose to set the outer boundary of the PDE problem to $r = 10$ which corresponds to 2mm away for a sphere of radius 200μm. This is a reasonable choice as the neurospheres were cultured in a medium 2mm deep. We can calculate numerically that it takes our model approximately 13.08 non-dimensionalised time units to reach the new steady state. This is done by comparing the analytical steady state (4.5) (we call the steady state C^{EQ} here) with each row of the solution matrix corresponding to the spatial oxygen distribution at different time-points. After each step in time the matrix rows are compared and the relative error, ε, recorded. If this relative error is less than 1% of C^{EQ} at each spatial point then the steady state is said to have been reached. So we have the following condition:

If

$$\frac{C_{r,t^*} - C^{EQ}}{C^{EQ}} < 1{\times}10^{-2} = \varepsilon,$$

then $t = t^*$ is the system steady-state.

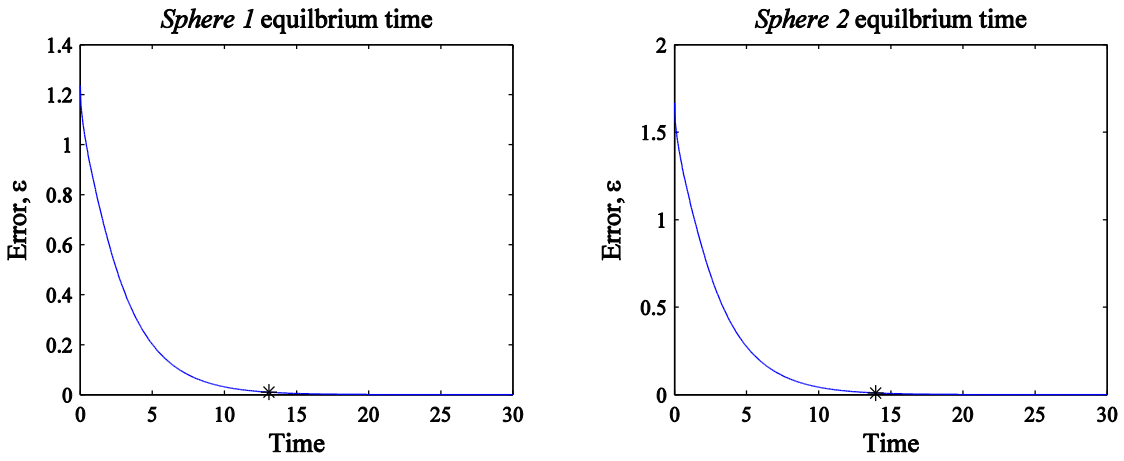

Figure 4-13: Error plots for both *Spheres 1&2*. The difference between the PDE solution for the oxygen diffusion model and the analytical steady state solution was measured over time. When the normalised difference, ϵ, was less than 1% for each spatial grid point, equilibrium was said to have been reached, $t = t^*$. Black stars indicate the non-dimensional time at which we claim the steady state is equivalent to the steady state times recorded during experiments.

An error bound term ($\varepsilon = 1\times10^{-2}$) was used rather than 0 in an attempt to more closely match the experimental approximations of what it meant for the oxygen concentration to be at a steady state (see Figure 4-13). This experimental steady state was judged approximately by the eye of the experimentalist and so comparing with an exact numerical equilibrium could lead to erroneous comparisons. This is important as there can be a great difference between the time taken to reach an apparent steady state and the $\varepsilon = 0$ state. Indeed the chosen error bound corresponds more closely with the criteria of an approximate steady state in mind. Let us re-introduce tildes for non-dimensionalised time, $\tilde{t}$. Also let time-to-equilibrium values be known as t^* (or $\tilde{t}^*$).

Using times derived from experiments and numerical simulations for the case of *Sphere 1* we can deduce:

$$\frac{\tilde{t}^*}{t^*} = \frac{13.08}{8 \text{ minutes}} = 1.64 \text{ min}^{-1} \text{ (3. s. f)}.$$

Using a scaling factor we can use our oxygen solutions $C(r,t)$ as a signal into the HIF-1α model for fixed r as the HIF-1α model deals in intracellular dynamics only and neglects spatial variation.

4.6.2 Predicting Diffusion Rates

We can use scaling factors to make some predictions about the diffusion rates inside and outside of hypoxic neurospheres. We have two known hypoxic-switch conditions from our experimental results: 17.9% to 8% O_2 in a neurosphere of radius 200μm; and 8% to 3% O_2 in a neurosphere of radius 187.5μm. The first condition has a t^* value of approximately 8 minutes and for the second condition

$t^* = 5$ minutes. Similarly the $\tilde{t}^*$ values are approximately 13.08 and 13.95 respectively. We recall that $\tilde{t} = D_1 t/R^2$ and $D_2 = DD_1$ and so we derive the following diffusion rates:

1) O_2: 17.9% to 8%, $= 200\mu m$, $t^* = 8$ minutes, $\tilde{t}^* = 13.08$

$$D_1 = \frac{R^2\tilde{t}^*}{t} = \frac{200^2 \times 13.08}{8} = 6.54\times10^4 \mu m^2 min^{-1},$$

$$D_2 = DD_1 = 3.48D_1 = 2.28\times10^5 \mu m^2 min^{-1}.$$

2) O_2: 8% to 3%, $= 187.5\mu m$, $t^* = 5$ minutes, $\tilde{t}^* = 13.95$

$$D_1 = \frac{R^2\tilde{t}^*}{t} = \frac{187.5^2 \times 13.95}{5} = 9.81\times10^4 \mu m^2 min^{-1},$$

$$D_2 = DD_1 = 3.48D_1 = 3.41\times10^5 \mu m^2 min^{-1}.$$

If we convert the units to $cm^2 sec^{-1}$ and compare these values with the diffusion coefficient for water (1 cP viscosity) at 20°C we can see that the predictions are of the correct order of magnitude (see Table 4-1). Note that D_2 represents the diffusion constant outside the sphere of cells, i.e. the diffusion of oxygen through the basal medium. Diffusion constant D_1 represents the diffusion of oxygen within the sphere. We expect $D_1 < D_2$ if we assume the solid, spheroid mass to have a higher viscosity than the outer liquid medium due to the extra cellular material.

Condition 1)	$D_1 = 1.09\times10^{-5} cm^2 sec^{-1}$	$D_2 = 3.79\times10^{-5} cm^2 sec^{-1}$
Condition 2)	$D_1 = 1.63\times10^{-5} cm^2 sec^{-1}$	$D_2 = 5.69\times10^{-5} cm^2 sec^{-1}$
Diffusion in water (Schmidt-Nielsen 1997)	$2.5\times10^{-5} cm^2 sec^{-1}$	

Table 4-1: Table showing predicted diffusion rates under different conditions inside and outside the sphere and a referenced rate for oxygen diffusion in water. All numbers calculated to 3 significant figures.

4.6.3 Results

The spatio-temporal oxygen dynamics model was coupled to the single-cell HIF-1α model by taking the temporal oxygen dynamics at a fixed radial position and using these dynamics as the input signal for the HIF-1α signalling pathway model. Oxygen is included in the model through the hydroxylation rate parameters h_i. These parameters are increasing functions of oxygen concentration. The results of a coupled model simulation are plotted in Figure 4-14 & Figure 4-15.

In this simulation the oxygen dynamics being applied to the HIF-1α model are acute hypoxic switches from 8% to 3% O_2, 2mm away from the sphere border in analogous conditions to the neurosphere

experiments. In Figure 4-14B we can see that the HIF-1α dynamics throughout the sphere exhibit heterogeneity in both steady state levels and transient dynamics. This is highlighted by Figure 4-14A where the dynamics of the HIF-1α signalling pathway are plotted for the two extreme sphere regions; the sphere centre and the sphere boundary. Following the instantaneous switch in oxygen levels at the outer boundary, the oxygen dynamics in these two sphere regions change on a timescale. This timescale (~5 minutes) varies little in both regions as the hypoxic steady state distribution of oxygen is reached relatively quickly when compared with the dynamics of the proteins in the pathway. A key feature of the variation in HIF-1α dynamics in these two regions is that although there are greater steady state HIF-1α levels in the centre of the sphere where there is less oxygen; for a transient period there is more HIF-1α in cells towards the sphere boundary. Because the oxygen dynamics reach equilibrium relatively quickly the main influence on this heterogeneity appears to be dependent on the levels of oxygen concentration and the magnitude of the switch between these levels, rather than the timescale of the transient oxygen dynamics.

In Figure 4-15 in particular we observe that the initial distribution of HIF-1α values has a greater value in the centre of the sphere and lower values towards the sphere boundary demonstrating an inverse relation to oxygen concentration as expected. As oxygen is decreased at the sphere border, HIF-1α levels rise in the cells closest to the border and at approximately 45 minutes there is an even distribution of HIF-1α throughout the sphere. The switch of greater magnitude at the sphere border results in a transient increase in HIF-1α dynamics such that at approximately 1.75 hours HIF-1α levels are greater towards the border of the sphere than they are at the core. This transiency resolves as we see a uniform distribution again at ~6.25 hours and subsequently the HIF-1α levels at the sphere's core are the greatest once more.

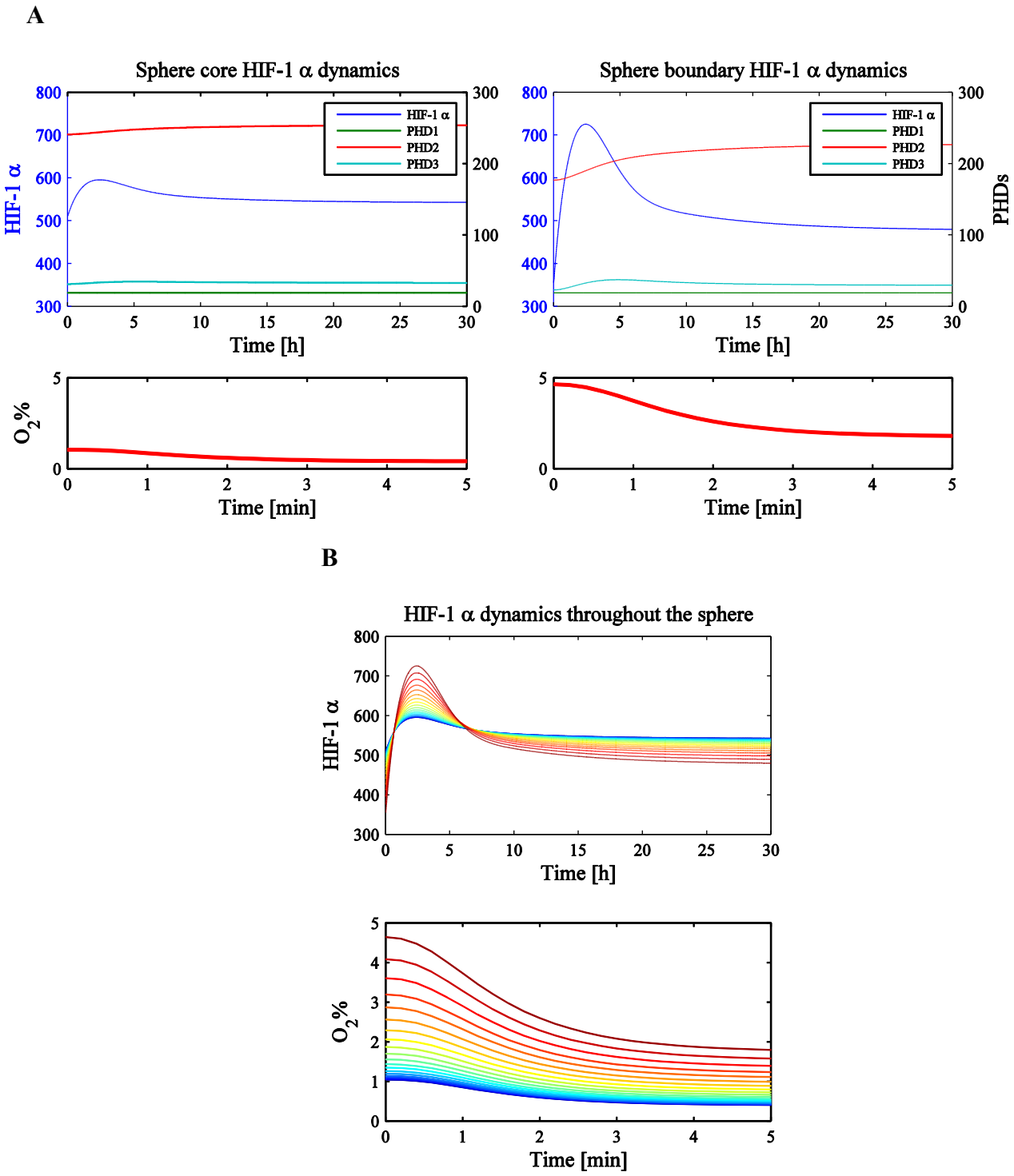

Figure 4-14: (A): Two subplots across the top of the figure represent the dynamics of the HIF-1α signalling pathway (upper panels) for two different regions of a respiring sphere: the sphere core and the sphere boundary. 1D Oxygen dynamics are plotted in the lower panels. (B): A subplot showing a collation of HIF-1α dynamics (upper panel) and oxygen dynamics (lower panel) for selected radial distances. Here the colour-map ranges from blue through green to yellow to red indicating the radial distance from 0μm (core) to 187μm (boundary) respectively. C_∞ is switched from 8% to 3% at $r = 10$ analogous to neurosphere experiments.

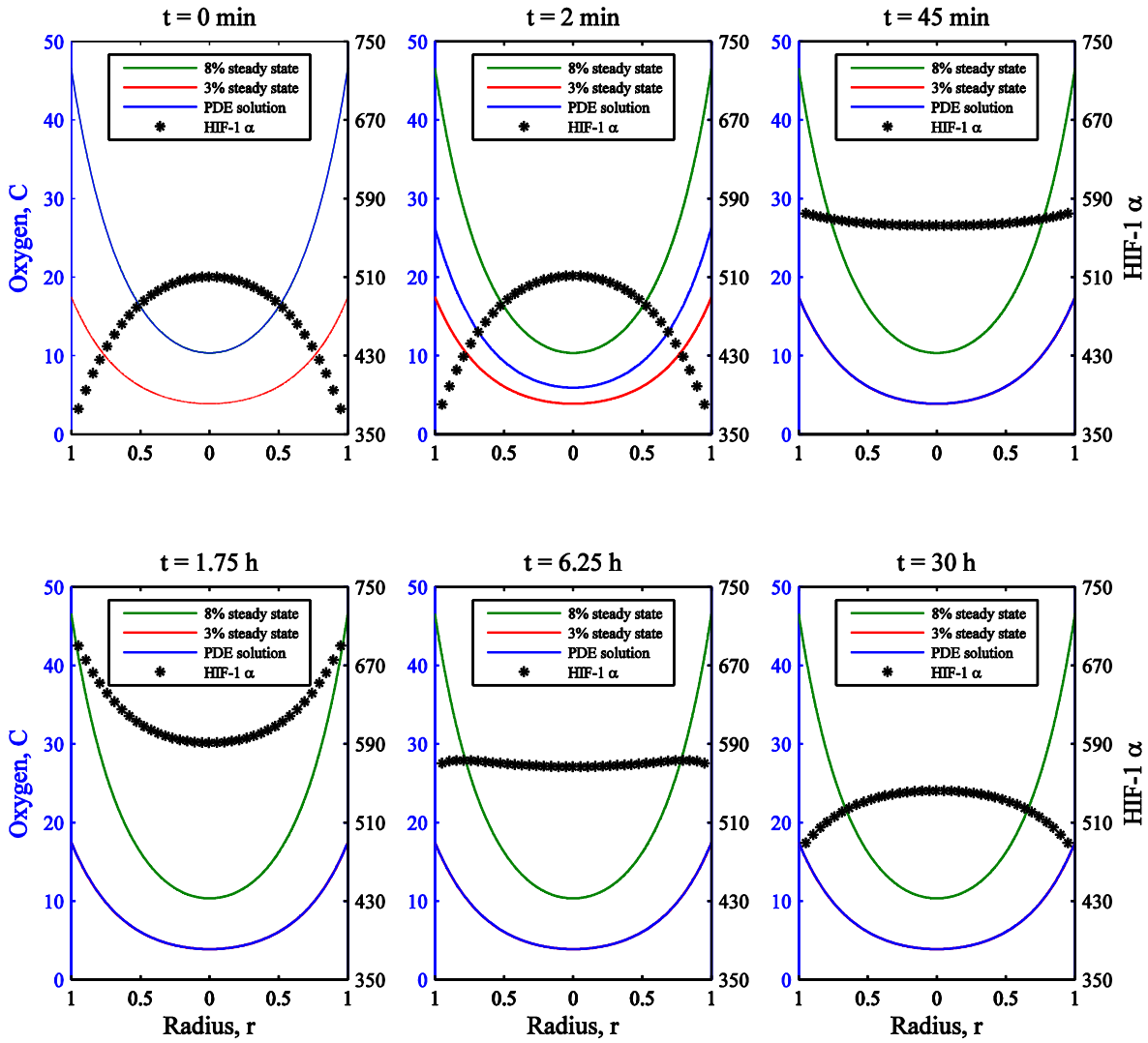

Figure 4-15: A series of time-steps are plotted to show the development of HIF-1α dynamics in different parts of the sphere as oxygen is reduced. As in Figure 4-11 the oxygen dynamics are plotted with an equilibrium envelope indicating the start and end points of the spatial distribution of oxygen. Green represents the initial steady state and red the final steady state. The blue curve is the time-dependent PDE solution where the oxygen at the sphere border is dropped at $t = 0$. Note that the blue curve coincides with the red by panel 3 ($t = 45$ min) meaning the oxygen dynamics are at the new steady state. Black stars denote HIF-1α levels for r values which represent the fixed position of individual cells within the sphere. These positions signify a sample distribution of cells where the HIF-1α model is coupled to the temporal oxygen dynamics and the secondary y-axis reveals the HIF-1α values associated with these stars at different time-points. C_∞ is switched from 8% to 3% at $r = 10$.

4.7 Motivation for Model Applications

The development of a single-cell model of HIF-1α dynamics that can be coupled to a biological model of spatial oxygen dynamics allowed us to consider the variation of HIF-1α across a multi-cellular environment. The aim of this section is to investigate the significance of the difference in HIF-1α

dynamics across a multi-cellular environment, such as a hypoxic neurosphere, and provide motivation for further applications of this model. Of particular interest to us is any situation relevant to fast hypoxic switches of great magnitude. It is these signals in particular that we have studied most and the mathematical model was based on data from this type of experiment. We also know that this type of signal can lead to a strong exhibition of the negative feedback at work in the signalling pathway in a short space of time. The timescale for the transient dynamics in between normoxic and hypoxic steady states is another focus of ours. It is in this phase that 'overshoot' dynamics can occur, where HIF-1α levels rapidly, but only temporarily, exceed their stable hypoxic steady state due to a fast hypoxic induction. The speed of the response of the HIF-1α signalling pathway is a result of its regulation mechanism, which appears rather inefficient at first glance. HIF-1α is continually produced at a basal rate but is degraded in an oxygen-dependent manner. The advantage of this, compared to say a direct signal to produce HIF-1α in hypoxia, is that as soon as oxygen levels are depleted, HIF-1α levels rapidly accumulate as less hydroxylation can occur. This emphasises the importance of the HIF-1α responses as the first line of defence against a hypoxic insult. Similarly, the tightly regulated negative feedback that takes effect and prevents this overshoot phenomenon from lasting too long or from HIF-1α reaching too great an amplitude hints at the danger of overexpression for this important transcription factor.

The 'overshoot' dynamics that occur in single cells can also transmit to the tissue-scale. As cells that are closer to the source of oxygen sense an acute switch effect more rapidly, this is where single-cell overshoot dynamics are most likely to occur. This effect can be so strong when compared to cells that are far away from the oxygen switch and hence have higher HIF-1α levels (such as the hypoxic core of a tumour sphere), that it can compensate for the lower starting level of HIF-1α and result in transient dynamics that have higher HIF-1α levels nearer the oxygen source than those further away (see Figure 4-14 & Figure 4-15).

This behaviour represents the most biologically interesting result of early model simulations, comparing transient HIF-1α dynamics on sphere boundaries with relatively constant levels in the centre. The case where the transient boundary dynamics 'overshoot' the relatively constant central dynamics is particularly interesting because of the potential to cause differential gene transcription. These dynamics are an example of how the oxygen signal to the HIF-1α pathway can be manipulated such that the transient hypoxic response is greater in less hypoxic regions.

4.7.1 PHD Dynamics

Dependent on the cell's position within a tumour, HIF-1α dynamics will vary as the oxygen signal is different. Consequently these signals also determine the dynamics of genes downstream of HIF-1, called target genes. Investigating the PHD dynamics in different regions of a sphere exposed to

hypoxia at the surface gives insight into the effect on gene expression as the genes that encode for PHD proteins are themselves targets of HIF-1. In particular PHD2 is a slow or late-responding gene when compared to the fast or early-responding PHD3. This property is largely determined by the basal degradation rates of each PHD isoform. The difference in response times of these two HIF-1-induced PHD isoforms provides a good opportunity to infer behaviour about different types of HIF-1 gene targets.

The HIF-1α dynamics shown in Figure 4-14B are a representation of the dynamics exhibited in cells distributed throughout a respiring sphere when a hypoxic insult has been applied. The associated PHD dynamics are plotted in Figure 4-16. In this case, the resultant PHD3 dynamics are such that at $t\sim3$ h and $t\sim9$ h there is a uniform level of PHD3 throughout the sphere (see Figure 4-16B). In between these times there is an overshoot event as PHD3 dynamics towards the sphere border are greater than those in the core. This does not occur for the PHD2 dynamics which are ordered such that there is always more PHD2 in the centre of the sphere than there is at the surface (see Figure 4-16A). However, the variation in PHD2 levels between these two extreme locations is greatly reduced after hypoxic induction. The conditions of this coupled model simulation are the same as those for the results in Figure 4-14.

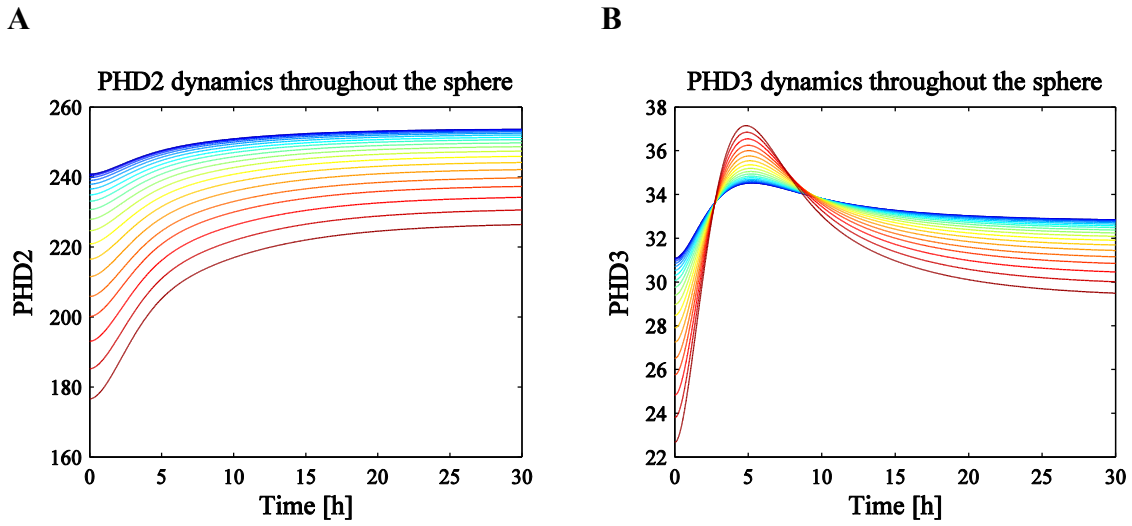

Figure 4-16: Two plots showing the dynamics for one simulation of the coupled oxygen-HIF-1α model for the oxygen-sensitive PHD components of the signalling pathway: PHD2 (A); and PHD3 (B). Within each plot, each curve represents the dynamics of that PHD in a single cell over time. The colour scheme is the same as Figure 4-14 where blue represents the sphere core and red represents the sphere boundary. Corresponding HIF-1α dynamics and oxygen dynamics are found in Figure 4-14B.

Normalisation in Figure 4-17 shows an ordered rate of fold-induction for all proteins in the HIF-1α signalling pathway model. We see that the relative induction of PHD is greater for cells closer to the oxygen switch. This representation of the pathway dynamics is particularly useful when thresholds are applied to dynamic behaviour of genes/proteins after stimuli. For example, thresholds are particularly

important for morphogen gradients in pattern formation and also in protein aggregation (Goldbeter 2005, Rieger, Morimoto and Hatzimanikatis 2006). In Figure 4-17 we have indicated arbitrarily where an activation threshold may occur as an illustrative example for protein dynamics generally (25% induction). We consider the switch-like behaviour exhibited by HIF-1α, PHD2 and PHD3 as they undergo a transition from normoxic equilibrium to hypoxic equilibrium. PHD2 levels display a monotonic increase such that when the switch is 'activated', i.e. PHD2 levels exceed the threshold, it remains activated. Note that the distinction between a fold-induction threshold and an absolute threshold is important as they result in opposite effects for PHD2 (compare Figure 4-16 with Figure 4-17). Specifically, the boundary levels of PHD2 show the greatest fold-induction but the lowest absolute increase compared to PHD2 levels in the sphere core which have the greatest concentration but exhibit the lowest fold-induction following this hypoxic switch. Contrast this with the transient overshoot dynamics of PHD3 where the peak PHD3 concentration at the boundary exceeds PHD3 levels in cells closer to the sphere centre in Figure 4-16. In Figure 4-17, PHD3 boundary levels also have the highest fold-induction but there is no overshoot. For protein dynamics of this nature a switch may be activated temporarily in some regions (inner sphere cells) or permanently activated in others (sphere boundary). Note that unlike PHD2 dynamics, the relationship between fold-induction thresholds and absolute thresholds is not necessarily inverse, i.e., where the sphere region/cell with the highest absolute value of a protein has the lowest fold-induction. When the sphere boundary overshoot phenomenon occurs, where PHD3 levels are temporarily higher at the sphere boundary than they ever reach in the centre, the threshold implications could be the same for both fold-induction and absolute values. Regarding the transcription factor itself, HIF-1α, it has been proposed that different target genes may require different thresholds of HIF-1α activation, e.g. the EPO gene may require a higher threshold than the VEGF or Pgk1 gene (Minamishima, et al. 2009). This would provide an example of differential gene expression, and ultimately hypoxic response, throughout a tumour as a result of HIF-1α thresholds that are target gene specific.

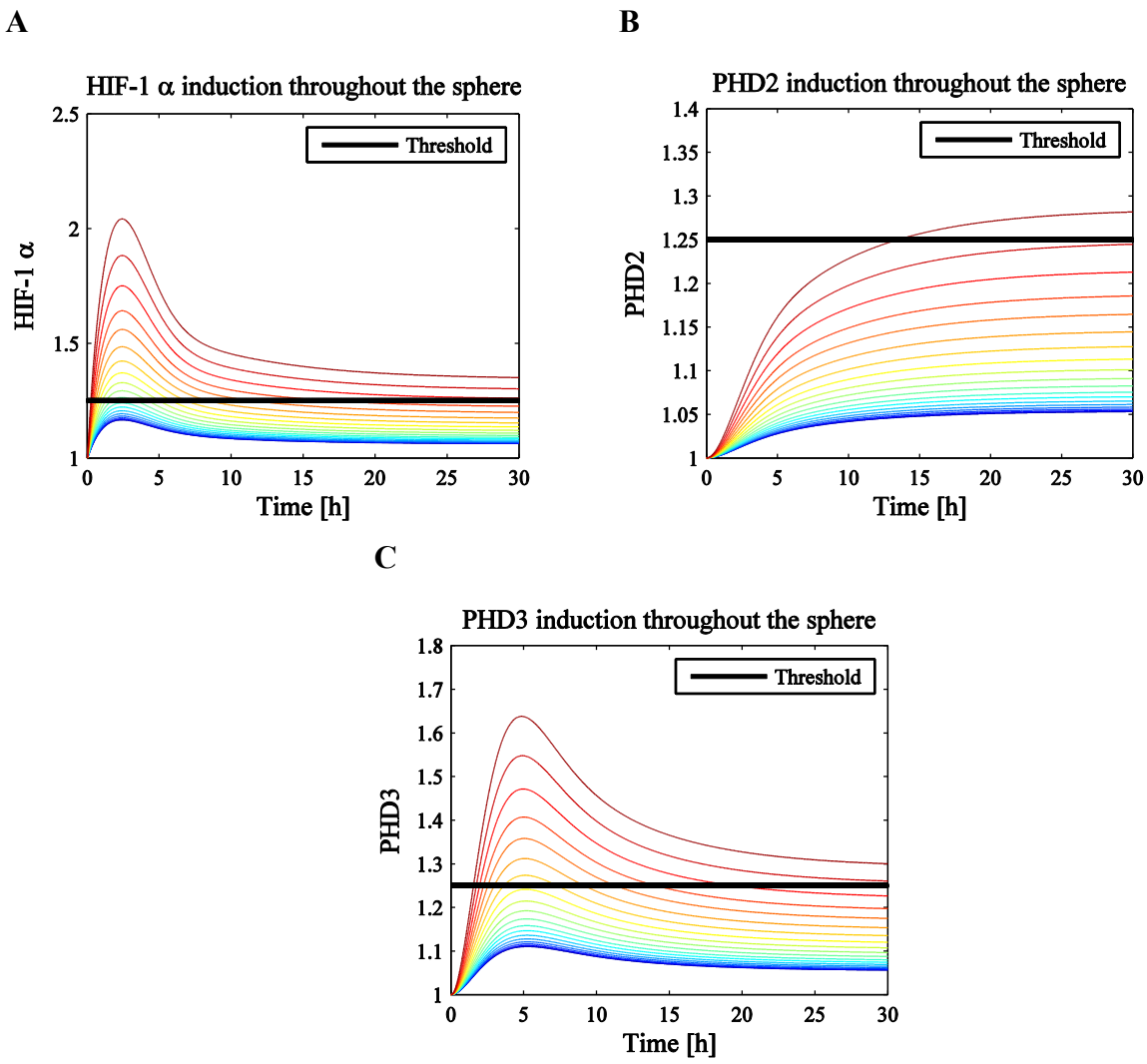

Figure 4-17: HIF-1α (A), PHD2 (B) and PHD3 (C) dynamics following different spatio-temporal oxygen signals have been normalised here such that the variable of interest is equal to 1 at $t = 0$. This is done to demonstrate the relative increase or 'fold-induction' after the hypoxic switch in different regions of the sphere. The broad black line indicates an example 25% threshold of activation. Colouring is as with previous figures.

4.7.2 Oxygen Pulsing

The importance of various oxygen kinetics, especially repetitive pulses of hypoxia, was discussed in Chapter 3, Section 3.5.1 from an experimental, theoretical and clinical point of view. With the coupled model, this investigation was taken a step further to try and understand the effects of pulsing oxygen on HIF-1α at a multi-cellular level. Initial simulations showed the boundary overshoot phenomenon of HIF-1α occurring in the first hypoxic pulse, but subsequent HIF-1α oscillations were relatively damped (see Figure 4-18). If we consider the dynamics of the transcription factor 'overshoot phenomenon' to be genetically significant, it is desirable to understand whether repeated overshoots can be achieved on a shorter period/pulsing frequency than simply waiting for the system

to reset at equilibrium. This could potentially result in an interesting situation where the average level of HIF-1α, and by association the grade of hypoxic response, is paradoxically maintained at a higher level towards the outer rim of a cellular sphere despite the greater availability of oxygen.

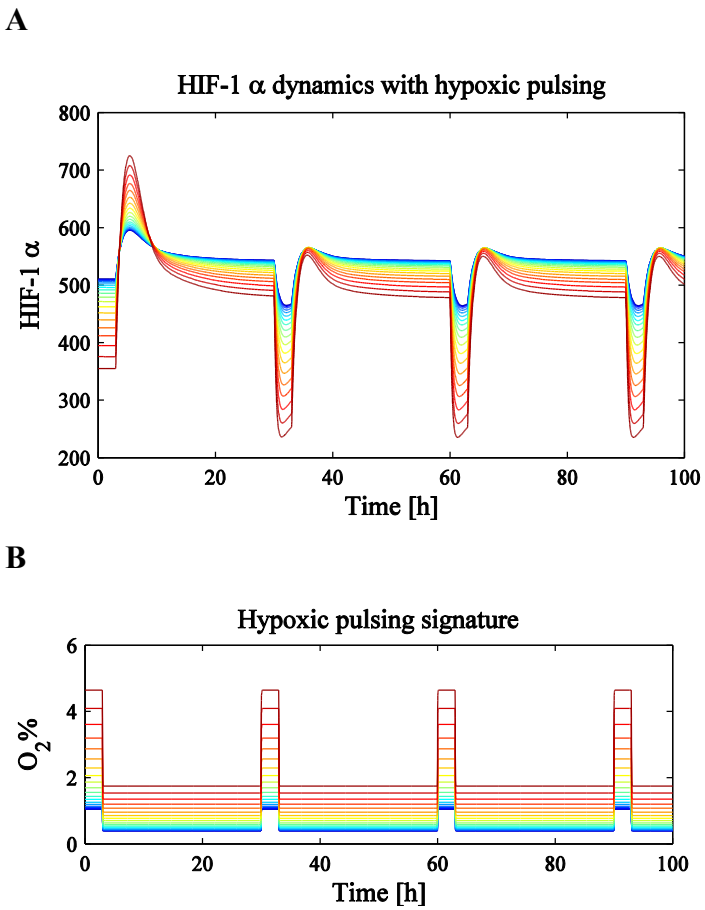

Figure 4-18: Repetitive hypoxic pulses were applied to the coupled model as described by the oxygen dynamics in (B). The corresponding HIF-1α dynamics are plotted in (A). As in previous figures, individual lines represent the dynamics in individual cells/regions of the sphere. Colour coding is as in previous figures (e.g. Figure 4-14). Note that the boundary overshoot phenomenon occurs in the first hypoxic phase only.

Repeated overshoots were achieved for a pulsing regime of 5 hours of hypoxia followed by 10 hours of relative normoxia periodically (see Figure 4-19). The effects of this are different for different HIF-1 targets. For fast responding proteins such as PHD3, each time an overshoot occurs PHD3 levels become approximately uniform throughout the sphere. However, for slow responding proteins such as PHD2 the short hypoxic phase is not sufficient to achieve the variation-reduction result seen in Figure 4-16. That is, the oscillating oxygen dynamics maintain a relatively wide range of PHD2 throughout the sphere when compared to the effects of a sustained hypoxic insult. Also note the effect this oxygen signature has generally on slow responding proteins such as PHD2. Due to the short hypoxic pulses, boundary levels of PHD2 are unable to reach the fold-induction they experience under sustained hypoxia. For example, whereas in sustained hypoxia boundary levels of PHD2 exhibited a 28% induction, in the pulsing experiments the induction level fluctuated between 5 and 18%. For

PHD3 the same cells exceeded the arbitrary 25% threshold used in Figure 4-17 albeit levels fell below this threshold each time re-oxygenation occurred. This oxygen regime mechanism could prove to be a method of suppressing unwanted, slow transcription factor targets from exceeding a certain activation threshold, whilst keeping desirable fast targets activated.

Acute re-oxygenation has the transient effect of decreasing HIF-1α levels significantly below the normoxic equilibrium level. Re-introducing hypoxia to the environment with these low HIF-1α levels results in an absence of the transient overshoot (where boundary HIF-1α levels are greater than those of the core), e.g. see Figure 4-18. Incubating in a state of relative normoxia for a longer period allows time for HIF-1α levels to increase towards the steady state following this re-oxygenation undershoot (see Figure 4-19). Re-introducing hypoxia after longer normoxic incubation can allow for the HIF-1α boundary overshoot to be repeated. Also, by varying the duration of the hypoxic incubation, one can investigate the effects of downstream transcription factor targets that have received the activation signal (increased transcription factor activity) for different time intervals. Short periods of hypoxia can lead to suppression in PHD2 induction, enabling HIF-1α to recover from acute re-oxygenation more quickly which is conducive to achieving repeated overshoots.

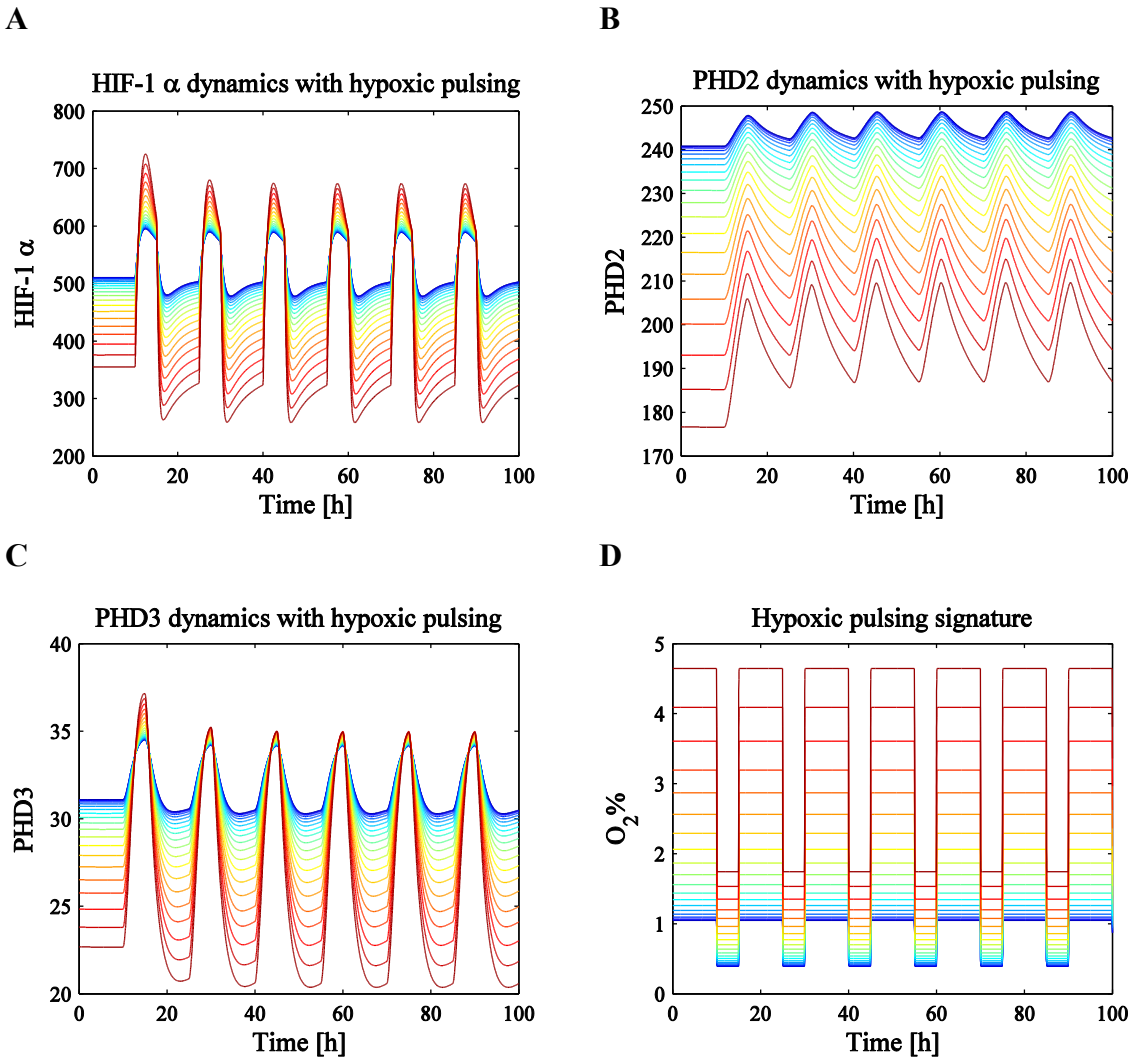

Figure 4-19: Hypoxic pulse dynamics for HIF-1α (A), PHD2 (B), PHD3 (C) and oxygen itself (D). The boundary overshoot mechanism in HIF-1α dynamics (A) occurs for each hypoxic insult in the oxygen signature (D). Colouring and labelling comparable with Figure 4-16 in particular.

4.7.3 Different Oxygen Switches & Sphere Sizes

For this section we try to discover the extent of the range of dynamics that our HIF-1α model can produce within a reasonably feasible physical setting. This will mainly be investigated by looking at severe hypoxic switches and sphere-size variation. From now on and for further investigations into theoretical simulations we will form hypotheses based on internal oxygen dynamics only. That is, we will neglect the effect of diffusion outside the neurospheres observed experimentally, and instead assume that the external oxygen concentration can be controlled and maintained directly at the sphere boundary. This means our initial conditions for further simulations will now be of the form

$$C(r,0) = C_0 \frac{\sinh \sqrt{\psi} r}{r \sinh \sqrt{\psi}},$$

where C_0 defines our oxygen concentration at the boundary of the sphere.

As a result of this change we no longer have an experimental time-to-equilibrium value to couple the non-dimensional oxygen model with the dimensional HIF-1α model. Therefore we must use our predicted diffusion rates to facilitate further simulations. Taking the average value of our two D_1 estimates (see Section 4.6.2) we arrive at the D_1 approximation,

$$D_1 = 8.17\times10^4 \mu m^2 min^{-1}.$$

As our original single-cell HIF-1α experiments were based upon instant, acute hypoxic switches from atmospheric oxygen level normoxia (~20%) to severe hypoxia (1%) we decided to simulate a tumour sphere under the same conditions (see Figure 4-20). We initially took the sphere to have radius $R = 200\mu m$ in line with the experimental data used to parameterise our oxygen diffusion model. Figure 4-20 shows a more pronounced boundary overshoot for both HIF-1α and PHD3 levels following the more severe hypoxic switch. Greater levels of fold-induction of PHD3 are observed when compared with lesser oxygen switches such as in Figure 4-17 for example. Specifically, a higher threshold is being met, which may be important if we consider the potential implications of PHD3 to fast target genes generally, where some may have higher activation thresholds than others. Similarly, a more severe hypoxic switch can lead to the target gene exceeding the lower threshold of Figure 4-17 in more regions of the sphere and for longer transient periods in some parts of the sphere. PHD2 levels are however still ordered such that there is always more PHD2 in more hypoxic regions. However the variation between PHD2 at the sphere core and at the boundary has been greatly reduced when compared to normoxic variance. Switching the external condition directly at the boundary resulted in a much faster time to reach the new internal oxygen dynamic equilibrium. Rather than the order of 5 minutes, equilibrium is now reached in less than 10 seconds.

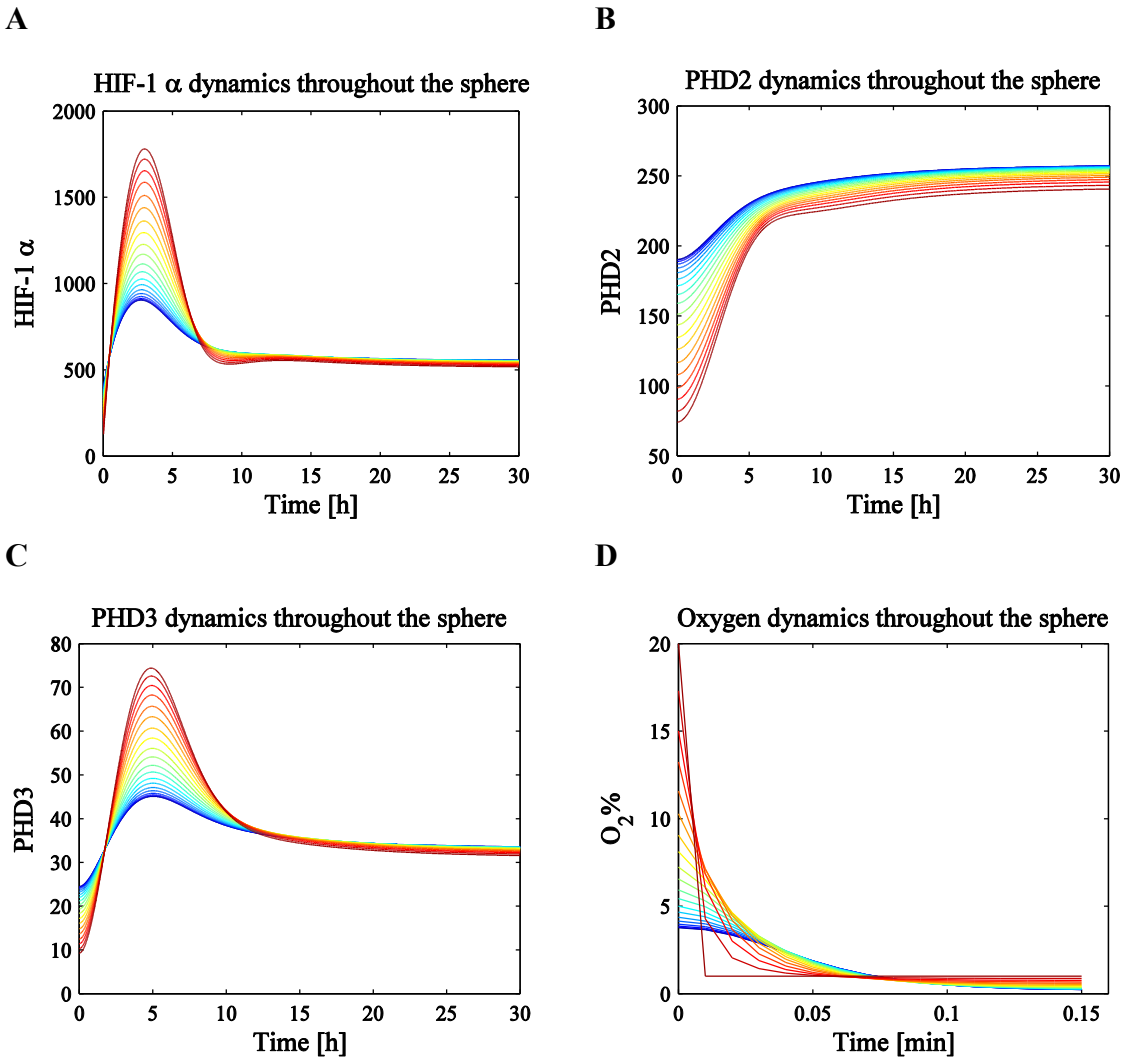

Figure 4-20: Plots for HIF-1α (A), PHD2 (B), PHD3 (C) and oxygen (D) for a 20% to 1% hypoxic switch at time $t = 0$ at the boundary of a sphere 200μm in radius. Colour-coding as with previous model coupling figures where different coloured lines represent dynamics of pathway components in different regions of the sphere: core (blue) to border (red).

So far we have only looked at spheres of radius ~200μm. We assume this represents an early stage avascular tumour as they usually grow to a diffusion-limited size of a few millimetres in diameter. Spheres that are much larger than 200μm will begin to lead to extremely hypoxic regions in the core of the model tumour that in turn lead to necrosis as cells are starved of oxygen. Our model does not currently account for cell death and we are focused on the stage of tumour growth where all cells are still alive but experiencing different levels of hypoxia. We therefore confine the investigation of sphere radius variance in our model at $R = 500\mu m = 0.5mm$. We assume that this is representative of an upper-limit for the size at which an avascular tumour can exist without a necrotic core.

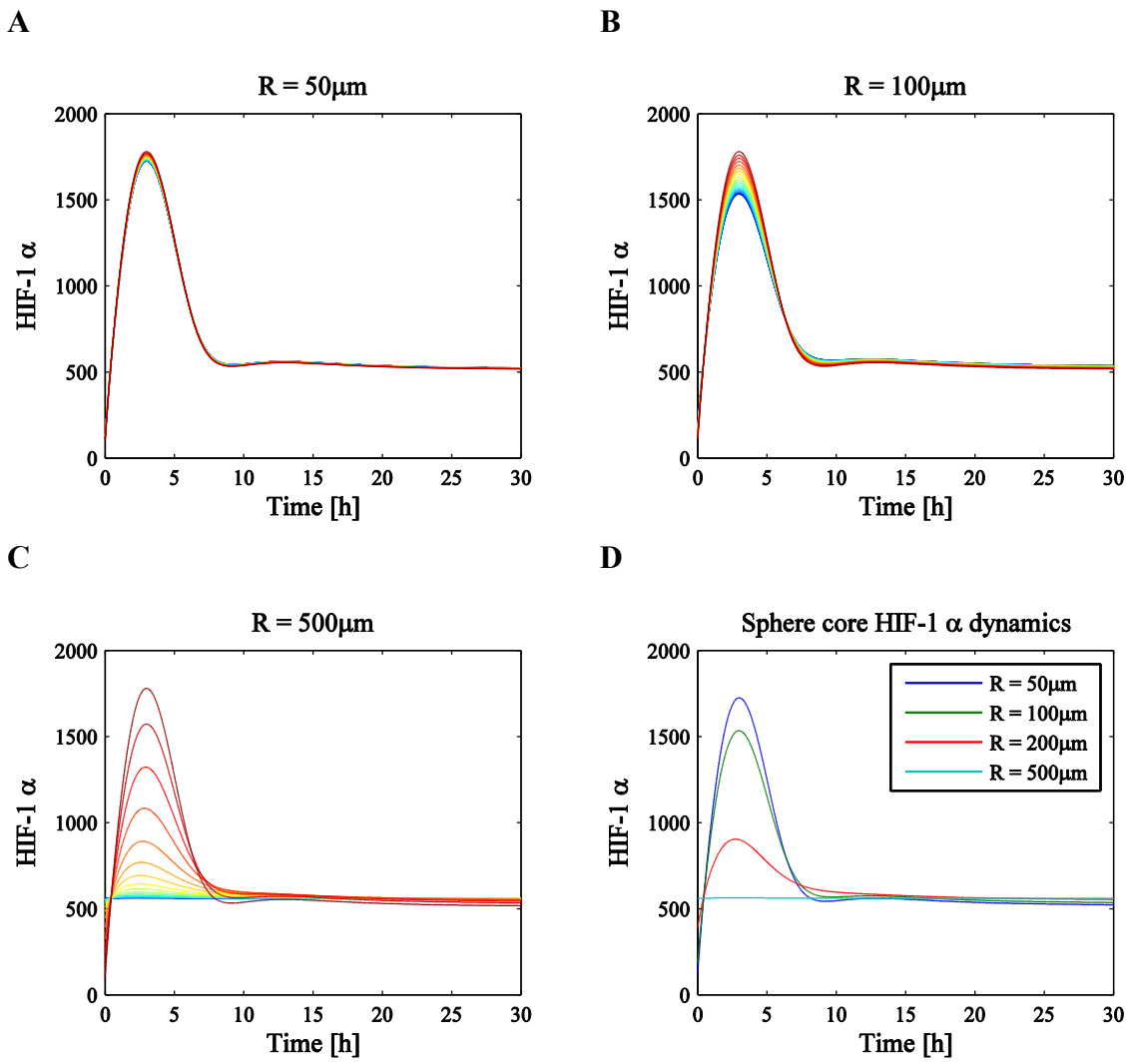

Figure 4-21: HIF-1α dynamics throughout spheres of different radii: $R = 50, 100, 500\mu m$ (A, B, C) following a hypoxic switch at $t = 0$ from 20% to 1% O_2. For (A, B, C), each curve represents one of 20 representative regions/cells that are selected in an even distribution through the sphere from border (red) to core (blue). (D): HIF-1α dynamics at the core of the sphere ($r = 0$) for R ranging from $50\mu m$ to $500\mu m$.

We investigate the effects of varying the radius of spheres from a HIF-1α-dynamics point of view (see Figure 4-21). We know that in the model, cells closer to the oxygen switch can exhibit overshoot behaviour which leads to sphere boundary cells temporarily having higher HIF-1α levels than the sphere core. As the radius is increased, and the same hypoxic switch is applied, the cells at the boundary experience the exact same oxygen signal as those cells at the boundary of spheres of smaller radii. However, cells in the centre of larger spheres are further away from the source of the hypoxic switch and due to the effects of diffusion and respiration; the core of a larger sphere is more hypoxic than the core of a smaller sphere. As there is a further distance between the sphere core and the oxygen source at the boundary, more oxygen is being consumed by respiring cells as the oxygen is diffusing inwards from the external source. See for example Figure 4-2 where we can think of an increase in non-dimensional $\tilde{\psi}$ as a result of an increase in R (since $\tilde{\psi} = R^2\psi/D_1$). The consequences

of this are that the severity of the hypoxic switch is effectively reduced for cells towards the centre of the sphere when the sphere radius is increased. Specifically, as the sphere size increases and the core becomes more hypoxic, the difference between oxygen conditions in the core decreases when the external oxygen source is lowered. Subsequently HIF-1α dynamics change very little in the sphere core such that for spheres with large radii the central HIF-1α levels are relatively constant despite fluctuations in the surrounding environmental oxygen signal. These cells are now incapable of producing HIF-1α levels that a boundary cell can still (transiently) produce. This termination in activity of the cell's main instigator of hypoxic adaptation suggests that these cells are more vulnerable to the damaging effect of oxygen deprivation and cell death.

Chapter 5

Applications of the Model of HIF-1α Dynamics

5.1 Introduction

In this chapter we will consider the link between transcription factor protein dynamics, target gene expression and ultimately the cellular processes regulated by these transcription factors. Specifically we will investigate this relationship for HIF-1 using the HIF-1α signalling pathway model developed in Chapters 2&3. The physiology of an avascular tumour will also provide us with a context in which to consider the effects of various single-cell HIF-1α dynamics on HIF-1 target gene functions. In particular, we will focus on two important cellular processes affected by hypoxia and HIF-1: proliferation and cell death. These processes outline the enhancing effect of HIF-1 in the growth of multicellular tumour spheroids, having a dual role of regulating cell division and apoptosis (Leek, Stratford and Harris 2005). The role of HIF-1 in these complex processes will be discussed by reviewing the cell cycle and the apoptosis pathway. In section 5.2 we will modify an existing oxygen-dependent cell-cycle model and couple it with our HIF-1α model to explore the potential applications of transient HIF-1α dynamics in the cell cycle. Section 5.3 will consider the relationship between hypoxia and apoptosis in order to determine how these two processes are related. This information will allow us to couple the dynamics of HIF-1α and p53 (protein 53): the two principal transcription factor pathways of hypoxia and apoptosis.

5.2 The Cell Cycle

Cellular proliferation occurs through a procession of events whereby the cell: increases in size; duplicates most of its component parts; and divides into two daughter cells. Each daughter cell has all the genetic material and mechanistic parts to function and start the process of proliferation again. This repeated process is known as the cell cycle and the events of this cycle are often split up and categorised into distinct phases (see Figure 5-1). In the initial G_1 phase ('G' signifying gap) the cell grows until it is large enough to enter S phase where DNA replication occurs through the copying of the chromosomes. Following the S phase cells enter G_2 phase, a secondary gap phase where the cell continues to grow after its DNA has been replicated. Finally cells enter M phase where the process known as mitosis occurs and the cell divides and the cycle begins again for the daughter cells at the G_1 phase. Alternatively, after division cells can leave the cell-cycle progression altogether and enter what is known as the G_0 phase, a quiescent state in which most cellular functions are suspended.

Several checkpoints are included in one cell cycle to ensure that progression is occurring normally. During G_1, the cell is as of yet un-committed to the replication-division process and is primarily focused on growth. This phase has variable duration as the cell continuously monitors its size as well as the environment to ensure that internal and external conditions are suitable for DNA synthesis and

division. Once these conditions are met, the cell cycle enters the S phase, a phase of much less variable duration as chromosome replication is carried out as quickly as possible to minimise exposure of DNA in this vulnerable state. The transition between G_1 and S is known as the G_1 checkpoint and is often satisfied once the cell has reached a critical mass (Mitchison 1971). There is also a checkpoint between G_2 and M that prevents the cell from initiating mitosis if the process of DNA replication and chromosome alignment has not been completed properly. Any problems during DNA replication could lead to severe consequences for the daughter cells in the form of mutations that are usually fatal.

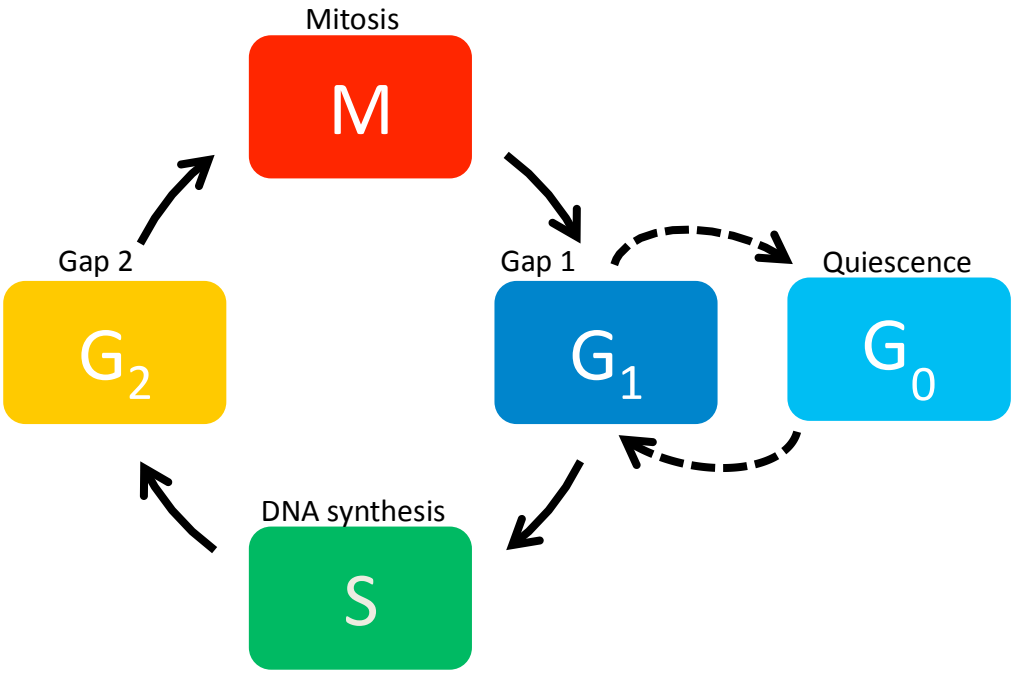

Figure 5-1: An illustration of the different phases of the cell cycle. The cycle can be separated into four main phases: Gap 1 (G_1), DNA synthesis (S), Gap 2 (G_2) and Mitosis (M). Additionally, a quiescent phase can be entered during G_1 phase under certain circumstances. This supplementary phase is referred to as G_0.

Events of the cell cycle are controlled by a complex molecular signalling network. The central components of this network are two families of proteins: the cyclin-dependent kinases (CDKs) and the cyclins. These partner families form complexes that oscillate during different phases of the cell cycle and govern the central molecular signalling involved. Indeed cyclins are so named due to their parallel cycle of synthesis and degradation with the cell cycle. When cyclins bind with CDKs, the CDK becomes active and can induce downstream processes by activating target proteins and orchestrate cell-cycle events. Mathematical models of the cell cycle vary in complexity but tend to be based upon the oscillations of these cell-cycle mediators which signal irreversible transitions into each phase. The transient activation of different CDKs represents different stages of the cell cycle in these models. Upon cell division, the oscillatory dynamics of the cycle start again. Many early models of

the mammalian cell cycle were focused on particular portions such as the G_1/S transition or restriction point where bifurcation analysis is particularly useful when modelling sharp switches or transitions between states (Swat, Kel and Herzel 2004, Novák and Tyson 2004). These models tended to focus on the bistability between checkpoints due to the complexity of the cell cycle as a whole (Qu, Weiss and MacLellan 2003). More recently, more complex models have been developed that intend to describe the repetitive, sequential activation of different cyclin-CDK complexes that control each cell-cycle phase. One such model was established by Gérard & Goldbeter (Temporal self-organization of the cyclin/Cdk network driving the mammalian cell cycle 2009) that describes the transient dynamics of 4 different cyclin-CDK complexes within 4 different modules: one for each classical cell-cycle phase. Unlike previous cell-cycle models, the complexities of this model allow for sustained oscillations as a result of the model's regulatory structure rather than being driven by a bifurcation parameter such as cell mass (Gérard and Goldbeter 2009). Such a tightly regulated process as the cell cycle with its complex regulatory network of proteins is sensitive to many external environmental factors that could compromise its viability. One such environmental factor is hypoxia.

5.2.1 The Role of Hypoxia and HIF-1 in the Cell Cycle

A characteristic cellular response to hypoxia is a reduction in proliferative rate (Koch, et al. 1973, Löffler, Postius and Schneider 1978). In the simplest case this is due to an insufficient energy supply but hypoxia can cause a specific cessation of growth without any alteration in long-term viability (Goda, Ryan, et al. 2003). The dormancy exhibited by tumour cells may also be a result of hypoxia-induced growth arrest. Moreover, hypoxia-induced cell-cycle arrest occurs specifically via the inhibition of the G_1/S transition. This transition represents the passing of the G_1 checkpoint and is inhibited through the regulation of the expression of p27 (Gardner, et al. 2001), a protein whose production is upregulated under hypoxia. The G_1 checkpoint requires the phosphorylation of retinoblastoma (RB) proteins in order to progress to S phase, a process that is activated by specific CDK-cyclin complexes. p27 also known as $p27^{Kip1}$ (protein 27 kinase inhibitor protein 1) inhibits the activity of these CDK-cyclin complexes, thus promoting RB hypophosphorylation and, consequently, cell-cycle arrest in G_1. Thus p27 was identified as "a key regulator of the G_1/S transition in hypoxic cells" by Gardner et al. and its hypoxic induction was suggested to be transcriptional (Gardner, et al. 2001).

An obvious candidate for the transcriptional activator in the hypoxia-inducible expression of p27 is HIF-1, the master regulator of gene induction under hypoxic stress. Examples of negative cell-cycle regulator genes which are induced by hypoxia in a HIF-1α dependent manner include cyclin G2 (Wykoff, et al. 2000) and p21 (Carmeliet, et al. 1998).

The dependence of the hypoxic induction of p27 on HIF-1 is widely disputed. A study by Carmeliet et al. (Role of HIF-1alpha in hypoxia-mediated apoptosis, cell proliferation and tumour angiogenesis 1998) claims that while some hypoxia-regulated genes involved in controlling the cell cycle are HIF-1α dependent (p53, p21, Bcl-2) others such as p27 are not. Carmeliet's claims were determined by submitting modified ES (embryonic stem) cells with an inactivated HIF-1α gene to hypoxia (20% to 2% O_2 switch) for up to 16 hours. Results using Northern blot analysis of total mRNA showed hypoxia-induced levels of p27 whether the HIF-1α gene was inactivated or not. Gardner et al., who proclaimed p27 to be a key regulator in hypoxic cell-cycle arrest, asserted in 2001 that HIF-1 transactivation does not contribute to hypoxia-induced G_1 arrest and the induction of HIF-1 does not increase p27 expression (Gardner, et al. 2001). The effects of HIF-1α induction were investigated independently of oxygen by using $CoCl_2$ (cobalt chloride), a known inducer of HIF-1α in normoxia. Under these conditions neither G_1 arrest nor an increase in p27 expression were observed. Furthermore, transcriptional regulation of p27 in hypoxia was shown to occur on a HIF-1 independent region of the p27 promoter in MEFs (Mouse Embryonic Fibroblasts).

Conversely, Goda et al. (Hypoxia-inducible factor 1alpha is essential for cell cycle arrest during hypoxia 2003) claim that hypoxia causes a HIF-1α-dependent increase in the expression of p27 and that the hypophosphorylation of RBs in hypoxia is accordingly HIF-1α dependent. Western blot analysis in hypoxia showed that HIF-1α null cells did not exhibit the elevation of p27 expression shown in wild-type cells. Hyperphosphorylation of RBs occurred in HIF-1α null cells but not in wild-type cells. Blotting measurements were made in normoxic levels of 20% O_2 and hypoxic levels of 0.5% O_2 for up to 48 hours. This study was conducted using MEFS as well as splenic B lymphocytes, a more suitable cell line for studying cell-cycle arrest as they are much less susceptible to spontaneous growth arrest in culture, and cells with deleted HIF-1α genes were made. In the same year, Wang et al. (Cyclin dependent kinase inhibitor p27(Kip1) is upregulated by hypoxia via an ARNT dependent pathway 2003) also reported that HIF-1 is involved in the transcriptional upregulation of the p27 gene under hypoxic conditions. Specifically, the expression of p27 was studied dependent on the presence of ARNT (HIF-1β). This was conducted in two related murine hepatoma cell lines: Hepa-1 (producing ARNT) and c4 (ARNT deficient). Cells were treated in hypoxia (1% O_2) for 24 h and western blotting revealed that p27 protein levels were only elevated in Hepa-1 cells. Furthermore, RNase protection assays were performed that confirmed that an increase in p27 synthesis in hypoxic Hepa-1 cells was reflected by an increase in p27 mRNA. No change was observed in the c4 cells in hypoxia. In 2008 Horrée et al. also declared that p27 expression under hypoxia is HIF-1α dependent (Horrée, et al. 2008). This was shown by knocking down HIF-1α in HEC1B (Human Endometrial Carcinoma) cells which completely blocked the induction of p27 by hypoxia (1% O_2). HIF-1α knockdown was achieved by transiently transfecting cells with a knockdown vector (RNAi) targeting HIF-1α. Hypoxic measurements were made after 24 hours via Western blot analysis. The contradicting work of Gardner

and Goda is addressed in Goda's publication. To support their claim, the argument of Goda et al. is that Gardner's normoxic experiments of HIF-1α induction (using $CoCl_2$) do not take into account any hypoxic cofactors necessary for cell-cycle arrest and the lack of hypoxic environment could potentially compromise the full activation of HIF-1α. All differences in these above studies and the contradicting results could also be explained simply by the different cell lines used. This theory is somewhat supported by Box et al. who showed how different cell lines differ in their hypoxic p27 expression and G_1/S cell-cycle arrest (Box and Demetrick 2004).

Establishing a role for HIF-1 in hypoxic cell-cycle arrest will be critical in investigating the effects of transient HIF-1α dynamics in the cell cycle using our mathematical model.

5.2.2 A Modified Oxygen Dependent Cell-cycle Model

There are several different published mathematical models describing the events of the cell cycle with respect to the oscillations of cyclin-CDK protein complexes but there is one in particular that considers the effects of hypoxia and includes oxygen dependence explicitly. This model was developed by Alarcón et al. and published in 2004 in the paper entitled 'A mathematical model of the effects of hypoxia on the cell cycle of normal and cancer cells' (Alarcón, Byrne and Maini 2004). This is the model we will use to investigate the effects of HIF-1α dynamics on hypoxia-induced cell-cycle arrest.

5.2.2.1 The Alarcón Model of the Cell Cycle with Mass-driven Oscillations

The mathematical model developed by Alarcón et al. in 2004 was constructed to investigate the differences in hypoxia-induced growth arrest in 'normal' cells and the onset of quiescence in cancer cells. The terms 'arrest' and 'quiescence' are used frequently in the literature but without universal agreement on the definitions. Alarcón et al. interpret this terminology in the following way: a cell that is in a quiescent state has halted its progress through the cell cycle (i.e. the cell is in G_0); while cell-cycle arrest refers to a delay in cell-cycle progression (i.e. an extension of G_1 duration). The model focuses on the G_1/S transition event in particular and includes observations made by Gardner et al. (2001) regarding the role of p27 which inhibits normal progression when upregulated. The Alarcón model is based upon the Tyson & Novak (2001) cell-cycle model which describes the cell cycle as two irreversible transitions between two stable theoretical stages (G_1 phase and S-G_2-M phases). These transitions are mediated in the Tyson-Novak model by dynamic bifurcations such that the system of non-linear ODEs switches between two steady states which are stable when the cell is small and when full-sized. This switch behavior is achieved by describing the feedback existing between two antagonistic components of the cell-cycle machinery: CDKs and APCs (Anaphase-Promoting

Complexes). APCs mark specific proteins for degradation including the cyclins, the cell-cycle proteins necessary for CDK activation. CDK-cyclin complexes are used to orchestrate most cell-cycle events such as DNA replication by activating target proteins but they also inhibit Cdh1, a key component of APC. The activities of these two proteins (CDK and APC) are inversely related such that during G_1 phase CDK/cyclin activity is low whilst APC/Cdh1 is high, but once the G_1/S transition is triggered APC/Cdh1 activity is high and CDK/cyclin is low (see Figure 5-2). Thus we have two states to consider, G_1 and S-G_2-M, which the model must periodically bifurcate between in order to cycle. The link between cell growth and the irreversible transition from G_1 phase to S phase is incorporated into the model by assuming there is mass dependence on the inhibition of Cdh1 by the cyclin-CDK complex. In this way, once the mass is large enough the stable G_1 steady state will be destroyed and the system will move into the S-G_2-M steady sate via saddle node bifurcation. In the S-G_2-M state the mass is divided once the cyclin concentration is below a certain threshold and the G_1 stable steady sate is restored (Tyson and Novak 2001).

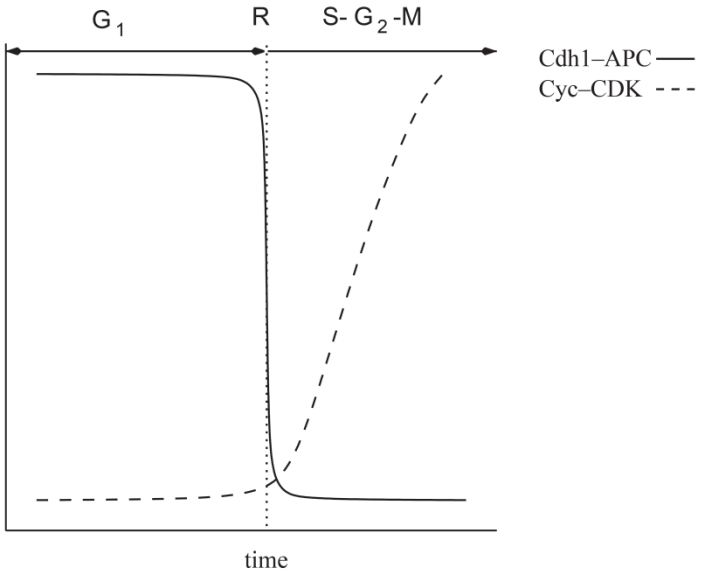

Figure 5-2: A schematic representation showing the distinction of the cell cycle into two states: G_1 phase; and S-G_2-M phases. These phases are divided by the vertical dotted line representing a restriction point (R) at which the G_1/S transition occurs. Also shown are the relative activities of the two antagonistic proteins: the Cdh1-APC complex representing cyclin inhibition and thus the inhibition of kinase activity; and Cyc-CDK the kinase complex that promotes cell-cycle events by activating appropriate proteins. This diagram has been reproduced from the Alarcón et al. publication (A mathematical model of the effects of hypoxia on the cell-cycle of normal and cancer cells 2004).

5.2.2.2 Effects of Hypoxia

The Alarcón model takes a simplified version of the Tyson-Novak cell-cycle model but incorporates oxygen dependence through the introduction of a time-dependent variable representing p27 and a

constant parameter for oxygen tension. Oxygen dependence is introduced into the Tyson-Novak model framework by using results from Gardner et al. (2001) which report that p27 induces cell-cycle arrest in hypoxia by downregulating the activity of cyclin-CDK complexes leading to the hypophosphorylation of RBs. Phosphorylated RBs induce the activation of cyclin targets via the transcription factor E2F. The relationship between p27 and cell-cycle arrest can be displayed in the form of a schematic diagram, in a simplified form of the mechanism proposed by Gardner (see Figure 5-3). Note that the simplifications introduced by Alarcón et al. are the use of only one generic cyclin-CDK complex and E2F is not accounted for explicitly.

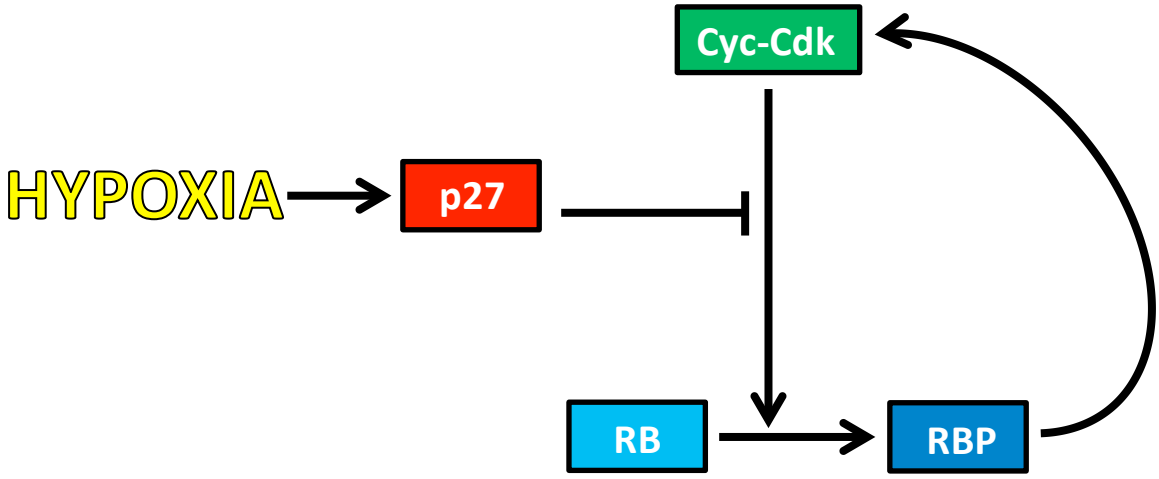

Figure 5-3: A simplified version of the mechanism proposed by Gardner et al. (Hypoxia inhibits G-1/S transition through regulation of p27 expression 2001) through which hypoxia induces the expression of p27 which inhibits cyclin-CDK activity leading to the hypophosphorylation of RB and thus cell-cycle arrest. RBP represents phosphorylated retinoblastoma. This diagram has been adapted from the Alarcón et al. publication (A mathematical model of the effects of hypoxia on the cell-cycle of normal and cancer cells 2004).

Below is the oxygen-dependent Alarcón cell-cycle model[2]:

$$\begin{aligned}
\frac{dx}{d\tau} &= \frac{(1+b_3u)(1-x)}{J_3+1-x} - \frac{b_4mxy}{J_4+x} \\
\frac{dy}{d\tau} &= a_4 - (a_1 + a_2x + a_3z)y \\
\frac{dm}{d\tau} &= \eta m\left(1-\frac{m}{m^*}\right) \\
\frac{dz}{d\tau} &= c_1\left(1-\frac{m}{m^*}\right) - c_2\frac{P}{B+P}z \\
\frac{du}{d\tau} &= d_2 - (d_2 + d_1y)u
\end{aligned} \tag{5.1}$$

[2] Note that the last equation, describing $du/d\tau$, has been misprinted in the original publication (Alarcón, Byrne and Maini 2004) but corrected here.

Model variables x and y represent the concentrations of two generalised antagonistic cell-cycle complexes: APC-Cdh1 and cyclin-CDK respectively. Variables m, z and u represent cell mass, p27 concentration and the concentration of RBNP (non-phosphorylated retinoblastoma). The a, b, c, d parameters are rate constants and the J, B parameters are Michaelis-Menten constants. The maximum size to which a cell may grow is represented by the critical mass m^* and the specific growth rate when $m \ll m^*$ is given as η. The parameter P represents non-dimensional oxygen tension such that low P corresponds to a hypoxic state resulting in an increase in p27 concentration.

In addition to the ODEs, cell division occurs when $x < x_{THR}$ and $y > y_{THR}$ ($x_{THR} < y_{THR}$) for threshold values x_{THR} and y_{THR}. These division criteria are a simplification from the Tyson-Novak model to minimise complexity and focus on the G_1/S transition of the cell cycle. When these conditions are met the cell cycle is reset by $m \to m/2$. The biological switch between high and low steady states of the antagonistic components is triggered by the cell mass dynamics. The inhibitory effects of p27 (z) are incorporated by including p27-dependent decay in the cyclin-CDK ODE ($dy/d\tau$). The p27 differential equation itself, $dz/d\tau$, is dependent on both oxygen, through the parameter P, and mass, which has a negative effect in the p27 production term. This growth regulation of p27 was based on experimental evidence suggesting that in the presence of growth factors, the expression of p27 is reduced (Leshem and Halevy 2002). Parameter values are defined in the corresponding model literature[3] (Tyson and Novak 2001, Alarcón, Byrne and Maini 2004, Owen, et al. 2009). Tyson and Novak (Regulation of the eukariotic cell-cyclemolecular antagonism, hysteresis, and irreversible transitions 2001) (and likewise Alarcón et al.) normalised the concentration of APC-Cdh1 to 1 and set the Michaelis-Menten constants much smaller than 1 to ensure switching behavior as in Figure 5-2 (Cherry and Adler 2000).

We solved the system (5.1) using MATLAB and implementing the corrected parameter values and initial conditions published by Owen et al. (Angiogenesis and vascular remodelling in normal and cancerous tissues 2009). We reduced the oxygen value, P, from 1 to 0.001 comparable to the original publication (Alarcón, Byrne and Maini 2004). The results are plotted in Figure 5-4. In the upper panels of the figure one can see the oscillations of the two antagonistic protein complexes. For each period in Cdh1-APC oscillations for example, one can see two distinct phases: one where Cdh1-APC levels are elevated representing the G_1 phase of the cell cycle; and, following the G_1/S transition, one where Cdh1-APC levels are depressed representing cell-cycle phases S through to M. The lower panels show how one cell-cycle period corresponds with the growth and division of the mass and also the oscillatory nature of the p27 protein (the RBNP protein is relatively constant at this scale). When hypoxia is simulated, by setting $P = 0.001$, one can see a much greater amplitude in the p27 peak

[3] Parameter values originally reported by Alarcón et al. (A mathematical model of the effects of hypoxia on the cell-cycle of normal and cancer cells 2004) were corrected by Owen et al. (Angiogenesis and vascular remodelling in normal and cancerous tissues 2009).

amplitude and a larger period of Cdh1-APC oscillations. Reducing the oxygen level from $P = 1$ to $P = 0.001$ shows a clear arrest in the cell cycle as there is a massive delay in the time to cell division even after the cell has reached its critical mass.

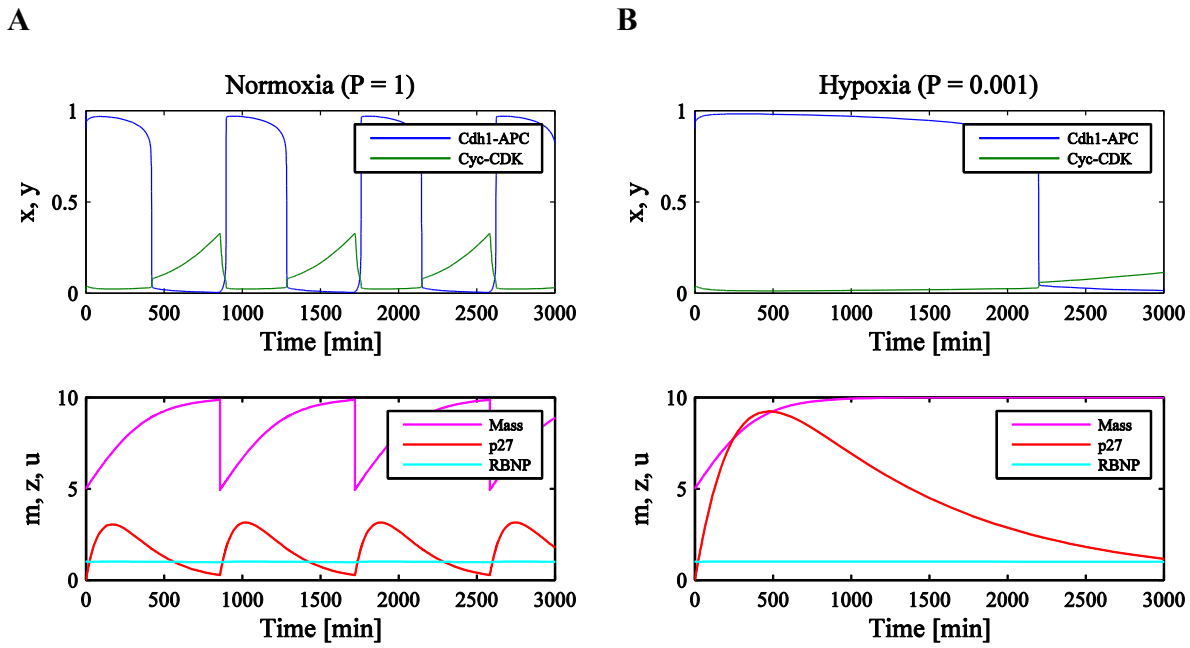

Figure 5-4: Two sub-plots showing the results of simulations of the Alarcón cell-cycle model (A mathematical model of the effects of hypoxia on the cell-cycle of normal and cancer cells 2004) in normoxia (A) and hypoxia (B) with indicated P values. Upper panels in (A) and (B) represent the periodic dynamics of the two antagonistic cell-cycle regulators Cdh1-APC and cyclin-CDK. Lower panels represent the other model components: mass, p27 and non-phosphorylated RB (RBNP). There is a clear extension of the cell-cycle period when oxygen is decreased.

5.2.2.3 Introducing HIF-1α Dependence

In order to modify the Alarcón model (5.1) to include HIF-1α we look at the oxygen-dependent terms in the ODE describing the evolution of p27 (z) concentration:

$$\frac{dz}{d\tau} = c_1\left(1 - \frac{m}{m^*}\right) - c_2\frac{P}{B+P}z \tag{5.2}$$

Rather than being directly dependent on oxygen, we want to introduce HIF-1α-dependent p27, $z(X)$, where it is HIF-1α (X) that is modulated by the oxygen state, P. We assume HIF-1α transcriptionally activates p27 in hypoxia (Goda, Ryan, et al. 2003, Horrée, et al. 2008) and as such it would seem more intuitive to have the production term of the p27 ODE being dependent on oxygen (P) rather than the degradation term. We can consider equation (5.2) in the following way such that we have oxygen dependence represented in the production term:

$$\frac{dz}{d\tau} = c_1\left(1 - \frac{m}{m^*}\right) - c_2\frac{P + B - B}{B + P}z = c_1\left(1 - \frac{m}{m^*}\right) + \frac{B}{B + P}z - c_2 z$$

Since HIF-1α (X) and oxygen (P) are inversely proportional we can then approximate this as

$$\frac{dz}{d\tau} == c_1\left(1 - \frac{m}{m^*}\right) + \frac{BX}{BX + A}z - c_2 z,$$

for some constant of proportionality A. As B is a relatively small Michaelis-Menten constant ($B = 0.01$) and A and X are approximately of the same order of magnitude $A \gg BX$ and subsequently we have

$$\frac{dz}{d\tau} = c_1\left(1 - \frac{m}{m^*}\right) + \frac{B}{A}Xz - c_2 z,$$

The regulation described by the Alarcón model, where increasing oxygen increases the rate of p27 degradation, would seem to fit better with a post-translational modification hypothesis, such as with our model of HIF-1α dynamics. Recall that in our HIF-1α model the oxygen-dependent decay term is a result of the hydroxylation reaction whereby oxygen molecules are used to target HIF-1α proteins for proteasomal destruction. Furthermore, transcriptional activation of p27 due to HIF-1α would suggest oxygen dependence in the p27 production term that is independent of the amount of p27 already in the system, i.e. independent of z.

Therefore we derive the following equation for p27 dynamics,

$$\frac{dz}{d\tau} = c_1\left(1 - \frac{m}{m^*}\right) + \alpha X - c_2 z, \tag{5.3}$$

where we assume a linear dependence on X at a constant rate α. However, the function of this cell-cycle model depends on terms contributing to the production of p27 being entirely dependent on mass such that when the cell has reached critical mass, $m = m^*$, p27 is exclusively decaying. This condition ensures that the division criteria in the model will eventually be met and the cycle can progress and so we make sure that our modifications also satisfy this requirement.

For example,

$$\frac{dz}{d\tau} = (c_1 + \alpha X)\left(1 - \frac{m}{m^*}\right) - c_2 z.$$

If we have production terms that are independent of mass, then the division criteria $x < x_{THR}$ and $y > y_{THR}$ ($x_{THR} < y_{THR}$) may not be met and the cell cycle will be permanently arrested. As m increases the system goes through a bifurcation corresponding to the G_1/S transition. The second bifurcation corresponds to cell division and occurs when the threshold criteria above are satisfied. If p27 (z) is decaying exponentially when $m = m^*$ (i.e. p27 production stops when the cell reaches

critical mass) the division criteria will eventually be met regardless of the oxygen state for the parameter values according to Alarcón et al. (2004) and Tyson and Novak (2001). If there is a mass-independent production term we have

$$\frac{dz}{d\tau} = \alpha X - c_2 z$$

when $m = m^*$ with constant steady state $z^* = \alpha X / c_2$. Unless αX is very small, this non-zero, non-decreasing value for z results in the stabilisation of x at a value above the division threshold x_{THR} and so the system becomes "stuck". Alternatively, if αX is very small the impact of oxygen dependence in the model is negligible. Therefore the dependence of p27 production on mass is essential for creating the oscillatory dynamics necessary for a cell-cycle model. An example of suspended oscillations due to p27 dynamics in the form of equation (5.3) can be seen in Figure 5-5.

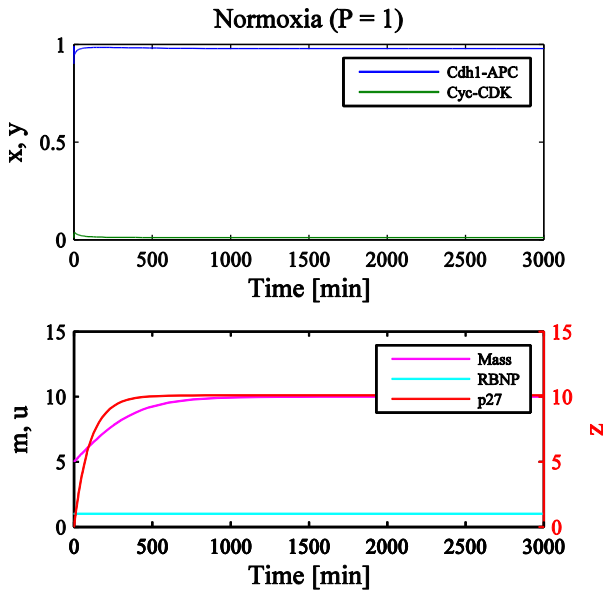

Figure 5-5: A sub-plot showing the results of simulations of a modified oxygen-dependent cell-cycle model in normoxia that includes a mass-independent p27 production term. As p27 does not exclusively decay once $m = m^*$ the oscillations of x and y do not occur and the cell is permanently arrested.

Indeed it is the removal of the p27 mass-dependence condition in the Alarcón paper (2004) that allows for the supposition of model 'cancer cells' undergoing quiescence or permanent arrest. Cancer cell-cycle dynamics are simulated by Alarcón et al. by taking model (5.1) and removing the mass-dependent production term in differential equation describing p27 dynamics ($dz/d\tau$) and replacing with a constant. That is, it is assumed that p27 is produced at a constant rate in cancer cells but this rate is modulated by the mass in normal cells (Alarcón, Byrne and Maini 2004). As a result, p27 is independent of mass in cancer cell simulations and can reach a steady non-zero state such that the inhibition of cyclin-CDK (y) is limited and the cell-division criteria may not be met.

We therefore introduce the following modified oxygen-dependent cell-cycle model. Note, only the ODE describing the evolution of p27 concentration has been adjusted.

$$\begin{aligned}
\frac{dx}{d\tau} &= \frac{(1+b_3u)(1-x)}{J_3+1-x} - \frac{b_4mxy}{J_4+x} \\
\frac{dy}{d\tau} &= a_4 - (a_1 + a_2x + a_3z)y \\
\frac{dm}{d\tau} &= \eta m\left(1-\frac{m}{m^*}\right) \\
\frac{dz}{d\tau} &= (c_3+\alpha X)\left(1-\frac{m}{m^*}\right) - c_4z \\
\frac{du}{d\tau} &= d_2 - (d_2+d_1y)u
\end{aligned} \tag{5.4}$$

To make better comparisons between the Alarcón model (5.1) and our modified version (5.4) we initially consider only equilibrium values of HIF-1α just as Alarcón et al. have considered only constant oxygen tensions. Here we have introduced the term αX where X, or $X(C)$, is a function of oxygen tension C and it represents the equilibrium value of HIF-1α concentration at different oxygen tensions using our HIF-1α model (see Chapter 3 and the Appendix, section 7.2 – note that the HIF-1α variable has been re-named X to avoid confusion with APC-Cdh1 variable x). The constant α is a proportionality rate constant. c_3 and c_4 are positive, arbitrary constants yet to be determined.

We match the two versions of the cell-cycle model in normoxic conditions ($P = 1$, $C = 20$). This requires a normalisation of our HIF equilibrium function. We call this normalised function X^* (see Figure 5-6):

$$X^*(P) = \frac{\left(S - \sum_{i=1}^{3}\frac{h_i^*S_i}{D_i}\right) + \sqrt{\left(\sum_{i=1}^{3}\frac{h_i^*S_i}{D_i} - S\right)^2 + 4kS\gamma\left(\frac{h_2^*}{D_2}+\frac{h_3^*}{D_3}\right)}}{2k\left(\frac{h_2^*}{D_2}+\frac{h_3^*}{D_3}\right)},$$

where

$$\begin{aligned}
h_1^*(P) &= 0.25(0.0014(20P)^2 + 0.016(20P) + 0.1233), \\
h_2^*(P) &= 0.0015(20P)^2 + 0.0137(20P) + 0.1202, \\
h_3^*(P) &= 1.25(0.0022(20P)^2 + 0.0012(20P) + 0.1036).
\end{aligned}$$

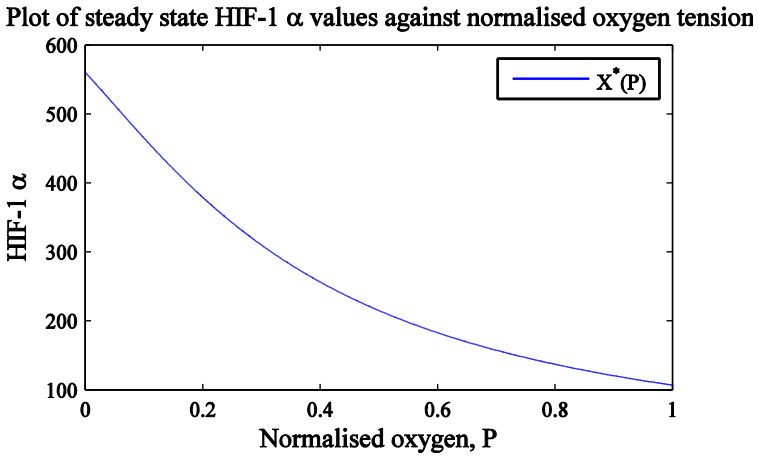

Figure 5-6: A plot of $X^*(P)$ versus oxygen concentration, P. This is a normalised version of the HIF equilibrium function representing the value of HIF-1α at equilibrium for different concentrations of oxygen (O_2 %).

To match the models in normoxia ($P = 1$) we need to determine the new constants representing rates of p27 production and degradation, c_3 and c_4. We do this by comparing production terms and destruction terms between models for the modified differential equation $dz/d\tau$. The Alarcón model (5.1) has p27 production term

$$c_1\left(1 - \frac{m}{m^*}\right)$$

and destruction term

$$c_2 \frac{P}{B+P} z = c_2 \frac{1}{B+1} z$$

in normoxia. Our modified model (5.4) has p27 production term in normoxia of

$$(c_3 + \alpha X^*(1))\left(1 - \frac{m}{m^*}\right)$$

and destruction term $c_4 z$ in normoxia. Therefore we define

$$c_3 = c_1 - \alpha X^*(1) \tag{5.5}$$

and

$$c_4 = c_2 \frac{1}{B+1}. \tag{5.6}$$

By setting

$$\alpha = \frac{c_1}{X^*(1)}, \tag{5.7}$$

we have $c_3 = 0$ and hence no basal p27 synthesis. Therefore we expect to see the maximum difference between normoxia and hypoxia using this condition. Simulations analogous to those for the results of Figure 5-4 were carried out for our modified HIF-equilibrium cell-cycle model using conditions (5.5), (5.6) and (5.7). For the results see Figure 5-7. In Figure 5-7 we see the same results as the original unmodified cell-cycle model without HIF-1α for the normoxic case. This is expected as we made sure that the models matched in normoxia. In hypoxia we see a delayed cell-cycle period but not to the same extent as with the original model. This is due to the nature of functions $X^{EQ^*}(P)$ and $P/(B+P)$. The fold-change in output of these two functions when P is reduced from 1 to 0.001 is vastly different. However, we note that now, in our modified version of the model, it is only the G_1 phase that is extended not the S-G_2-M phases. This is actually a more desirable outcome if the contention is indeed that the hypoxic upregulation of p27 causes cell-cycle arrest in G_1 and delays the G_1/S transition. The main reason we see this effect is due to the shifting of the oxygen dependence from the decay term in the p27 equation to the mass-dependent production term. The benefit of this approach is that once the cell has reached critical mass, m^*, all p27 production ceases and the decay rate is approximately the same independent of the oxygen environment. That is, when $m = m^*$,

$$\frac{dz}{d\tau} = -c_4 z,$$

$$\Rightarrow z \propto e^{-c_4 t}.$$

We can see this effect more clearly by increasing the rate at which HIF-1α induces the production of p27. One way to do this is by implementing a non-linear response, for example:

$$\frac{dz}{d\tau} = (c_3 + \alpha X^n)\left(1 - \frac{m}{m^*}\right) - c_4 z$$

where $n > 1$ for a non-linear enhancement of the HIF-1α-induced production of p27 (z). Increasing n allows us to highlight the effect of increasing only G_1 duration in hypoxia when p27 degradation is independent of oxygen. See for example Figure 5-8 with $n = 3$. The G_1 arrest effect of p27 is clear here but such a value of n results in very large p27 oscillations. This is an illustrative example to demonstrate the effects of p27 induction on different cell-cycle stages (G_1 and S-G_2-M) but for further modelling we will maintain the linear response ($n = 1$).

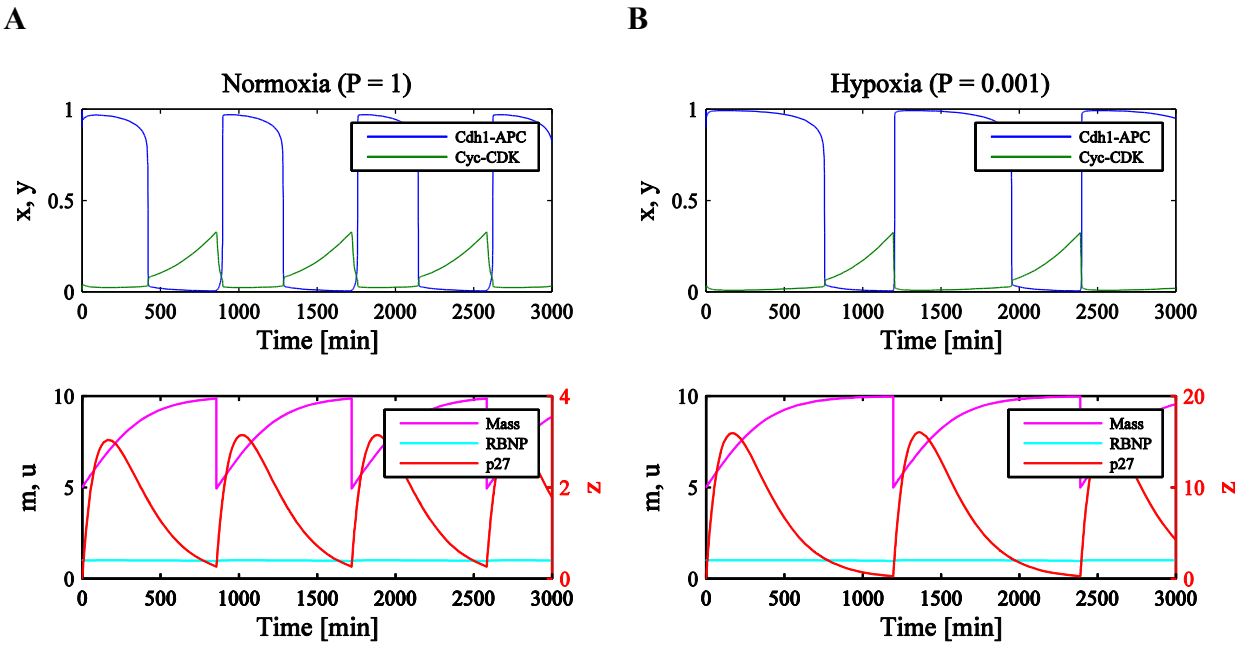

Figure 5-7: Two sub-plots showing the results of simulations of the modified HIF-1α-dependent cell-cycle model in normoxia (A) and hypoxia (B) with indicated *P* values. There is a delay in the cell-cycle period when oxygen is decreased but only the G_1 phase is affected.

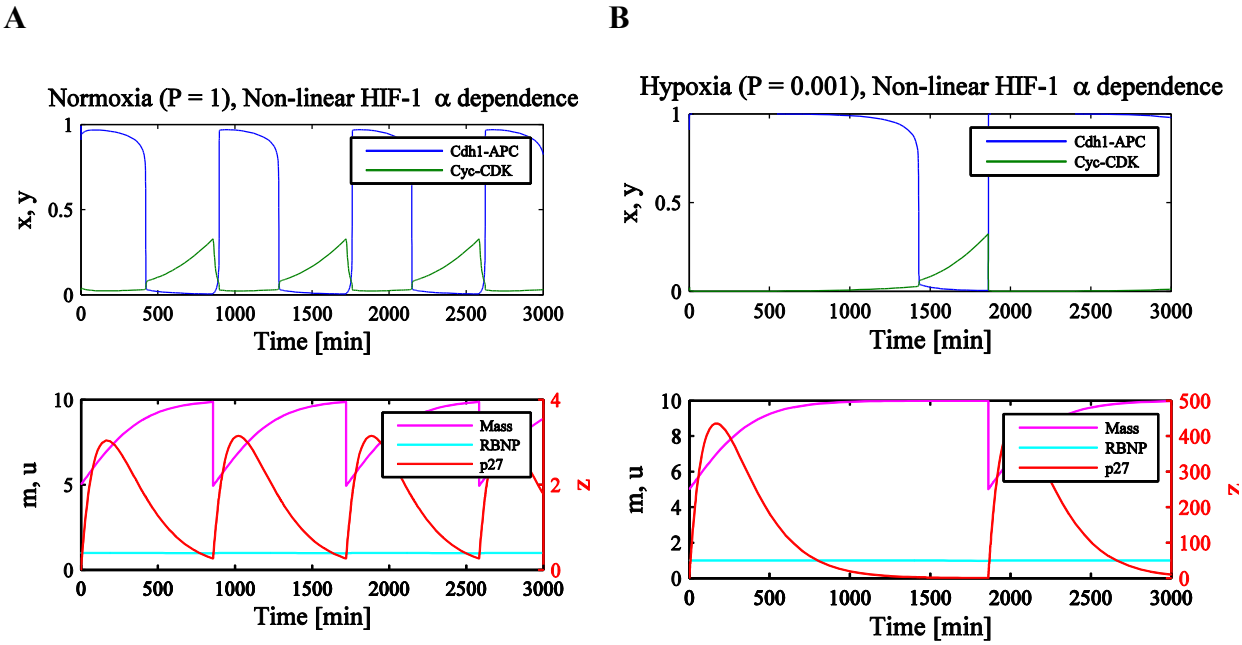

Figure 5-8: Simulation results of the modified HIF-1α-dependent cell-cycle model in normoxia (A) and hypoxia (B) with indicated *P* values as in Figure 5-7. Here, we have exaggerated the hypoxic induction of p27 by making the production of *z* proportional to X^3. This demonstrates the effect of our modifications of the Alarcón model, extending the G_1 phase only.

5.2.3 Model Coupling Results & Discussion

In order to study the effects of the transient overshoot dynamics of HIF-1α on hypoxia-induced cell-cycle arrest, we now extend the cell-cycle model. This extension consists of the introduction of p27 dependence on the dynamic behaviour of HIF-1α. We use our modified oxygen dependent cell-cycle model, which is more biologically realistic due to hypoxic arrest in G_1 only, and introduce dynamic HIF-1α by including our HIF-1α signalling pathway model[4] (see Chapter 3) explicitly:

$$\begin{aligned}
\frac{dx}{d\tau} &= \frac{(1+b_3u)(1-x)}{J_3+1-x} - \frac{b_4mxy}{J_4+x} \\
\frac{dy}{d\tau} &= a_4 - (a_1 + a_2x + a_3z)y \\
\frac{dm}{d\tau} &= \eta m\left(1-\frac{m}{m^*}\right) \\
\frac{dz}{d\tau} &= (c_3+\alpha X)\left(1-\frac{m}{m^*}\right) - c_4z \\
\frac{du}{d\tau} &= d_2 - (d_2+d_1y)u \\
\frac{dX}{d\tau} &= S - \left(\frac{X}{X+\gamma}\right)(h_1Y_1 + h_2Y_2 + h_3Y_3) \\
\frac{dY_1}{d\tau} &= S_1 - D_1Y_1 \\
\frac{dY_2}{d\tau} &= S_2 + kX - D_2Y_2 \\
\frac{dY_3}{d\tau} &= S_3 + kX - D_3Y_3
\end{aligned} \tag{5.8}$$

Note that p27 production now depends directly on dynamic HIF-1α (X). Oxygen dependence is included through the hydroxylation parameters h_1, h_2 and h_3 which vary with oxygen. We compared this dynamic-HIF cell-cycle model with the equilibrium-HIF cell-cycle model by switching to hypoxia mid-simulation.

Figure 5-9 shows the results of a simulation of model (5.8) where hypoxia is introduced during the S-G_2-M phase of the cell cycle. From now on, the cell cycle in which hypoxia is induced will be referred to as the intermediate cell cycle. When HIF-1α levels are at equilibrium the normoxic and hypoxic cell-cycle periods are approximately 14 h 25 min and 19 h 55 min respectively. So the hypoxic switch in these conditions has caused a 5 h 30 min delay in the G_1 phases of subsequent cell-cycle periods. The duration of the intermediate cell cycle is approximately 10 minutes shorter than the long-term hypoxic cell cycle for the HIF-equilibrium model. However, the duration of the intermediate cell

[4] Note that we have capitalised some parameters from the HIF-1α model where necessary, to avoid confusion with parameters of the cell-cycle model with the same names.

cycle is 21 hours 30 minutes for the dynamic-HIF model, 1h 35 min longer than for long times. This result highlights a significant difference in assuming whether p27 dynamics are affected directly by the instant oxygen switch or indirectly via the transient dynamics of a transcription factor (HIF-1). The intermediate cell cycle is extended in both cases but for the equilibrium assumption it is slightly shorter than subsequent hypoxic cycles, whereas the dynamic assumption yields an extended intermediate cycle. Despite the large extension of the intermediate cycle in the dynamic-HIF case, the 2^{nd} cell cycle following hypoxic induction was not greatly affected (approximately 3 minutes longer). This is due to the relatively fast HIF-1α dynamics when compared to the cell-cycle periods.

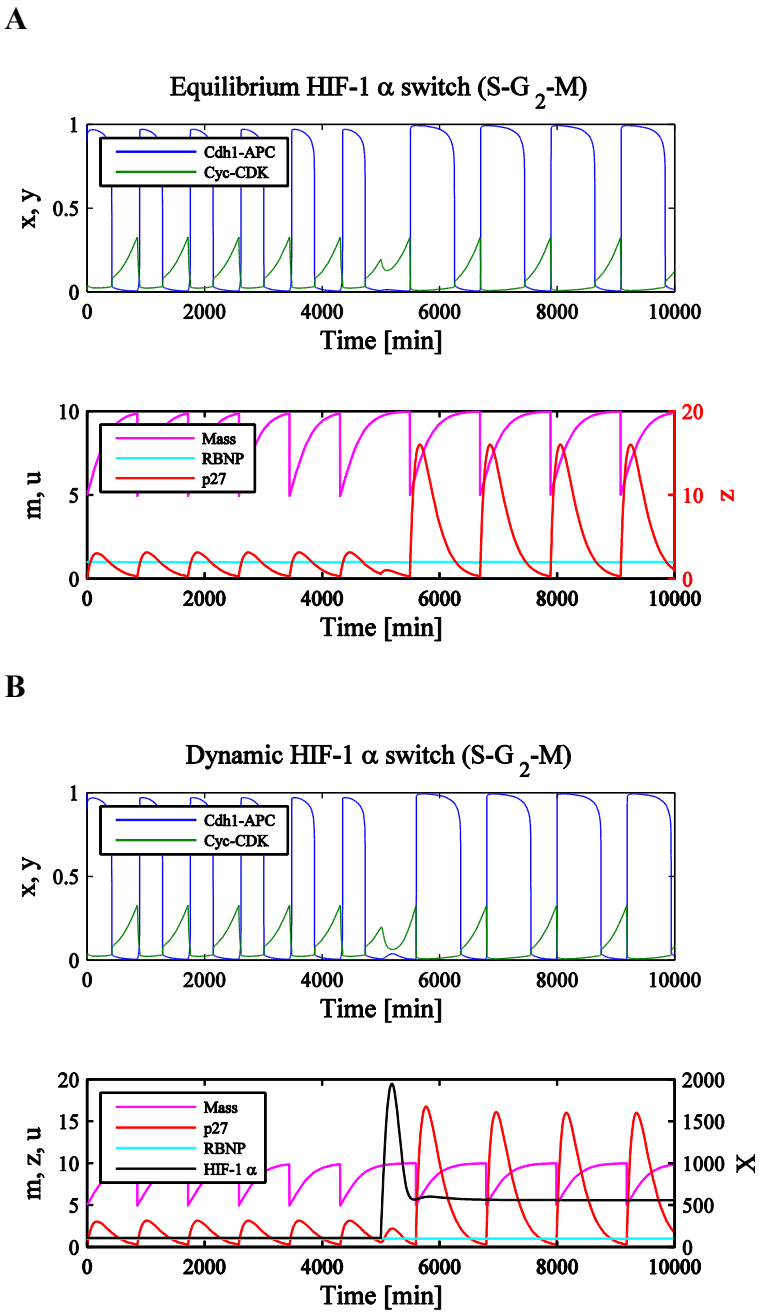

Figure 5-9: Two subplots of the modified cell-cycle model simulations with the oxygen switch occurring mid-simulation. Both the equilibrium-HIF model (A) and the dynamic HIF model (B) are simulated. In these simulations P was reduced at $t = 5000$ minutes during the S-G_2-M phases.

In Figure 5-10 the same conditions were applied in the simulation except the hypoxic switch was applied earlier in the intermediate cell cycle, during the G_1 phase. For the equilibrium-HIF case, this resulted in the intermediate cell-cycle period being slightly longer than subsequent hypoxic cycles. The duration was 5 minutes longer rather than 10 minutes shorter as in the case of Figure 5-9. For dynamic-HIF, the intermediate cell-cycle duration was 20 hours and 20 minutes; still longer than subsequent hypoxic periods but the extension was significantly diminished when compared to S-G_2-M phase hypoxic induction. Overall, when comparing intermediate cell-cycle durations using

equilibrium and dynamic HIF-1α, the period was extended by 8.5% by introducing dynamic-HIF when the hypoxia switch occurred in the S-G_2-M phases, and by 2% when inducing hypoxia in G_1. If we just compare the dynamic-HIF model with hypoxic switches in different phases, there was a 5% longer intermediate cycle period when inducing hypoxia in the S-G_2-M phase rather than the G_1 phase.

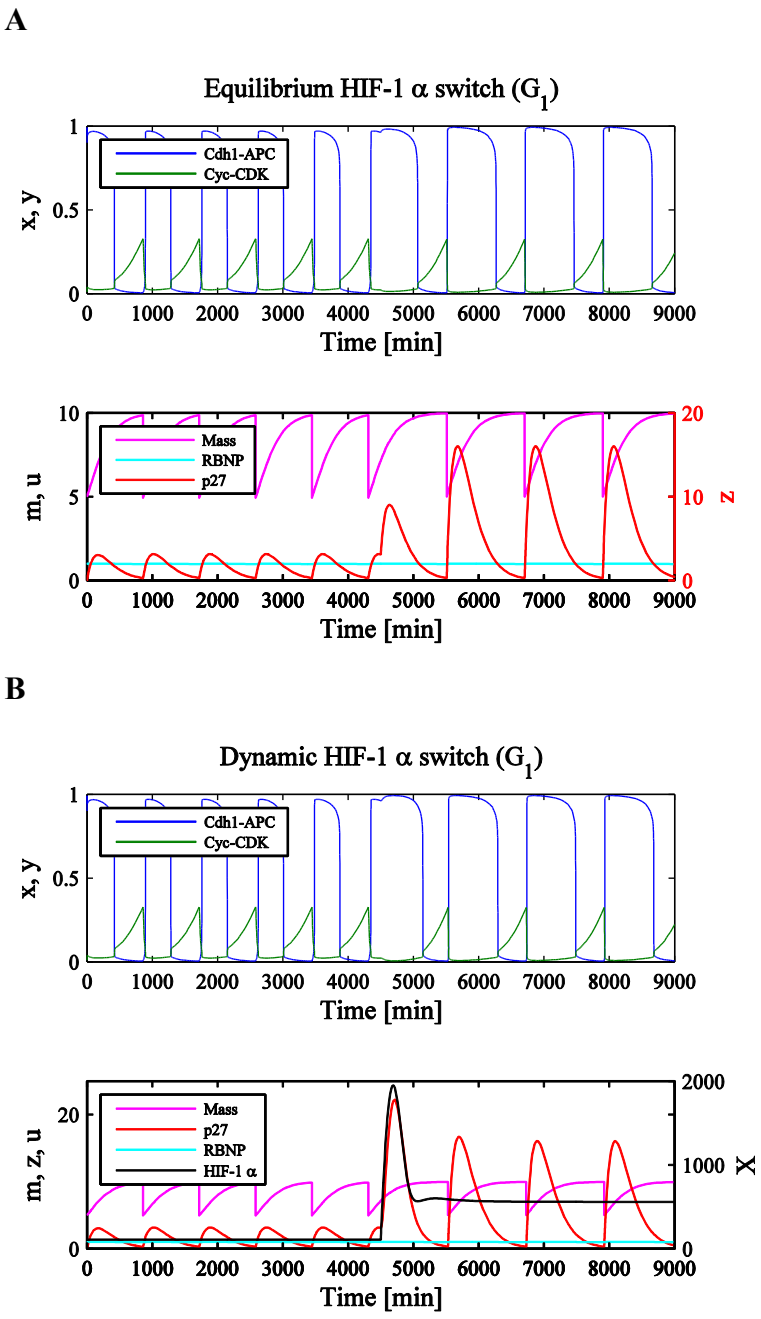

Figure 5-10: Two subplots of the modified cell-cycle model simulations with the oxygen switch occurring mid-simulation. Both the equilibrium-HIF model (A) and the dynamic HIF model (B) are simulated. In these simulations P was reduced at $t = 4500$ minutes during the G_1 phase.

The main differences in using dynamic HIF-1α rather than equilibrium levels was the effect it had on the cell-cycle period in which hypoxia was initiated. This intermediate cell-cycle period was greater in

simulations using the dynamic HIF-1α model. This effect was also slightly different depending on at what stage of this intermediate cell cycle the cell was in when the hypoxic switch was applied (see Figure 5-9 and Figure 5-10). However the period extension during the intermediate cell cycle was only increased by 8.5% at most after the introduction of dynamic HIF-1α and the differences were only noteworthy during this single, transitional period. This suggests that the hypoxic response of the cell-cycle mechanism is robust to relatively large fluctuations in p27 in both theoretical states. The introduction of overshoot dynamics appears to be limited in this case, probably as a result of the HIF-1α-independent dynamics of cell growth, $dm/d\tau$. A more realistic cell-cycle model where the production of p27 is not entirely dependent on mass may yield more significant effects of overshoot HIF-1α dynamics on p27-induced G_1 arrest.

It should be noted that the significance of these results depend on the timescale. Using the published parameter values from the Alarcón model and our new parameters as defined above ((5.5), (5.6), (5.7)), the model simulations result in normoxic cell-cycle periods of approximately 14 hours and 25 minutes. This not an entirely unrealistic duration but the length of the cell cycle varies dependent on cell type. For example, crypt cells in the intestinal epithelium can have cell-cycle periods as short as 9 hours, yet human liver cells can take up to one year. It is generally accepted that a typical mammalian cell proliferating in culture displays circadian rhythms with an average cell-cycle period of 24 hours (Alberts, et al. 2002). Even with cell-cycle duration of 24 hours we would expect the introduction of transient HIF-1α dynamics to have a significant effect. However, for cell types with much greater cycle periods we would expect the effect of transiency to be diminished due to HIF-1α dynamics and the dynamics of the rest of the cell-cycle proteins operating on separate timescales.

If we consider the range of oxygen tensions in a growing cellular sphere, we can hypothesise the consequences of HIF-1α induced cell-cycle arrest. The centre of a tumour sphere is the most hypoxic region and this is where the highest levels of HIF-1α would accumulate. With high HIF-1α levels we would expect to have longer cell-cycle periods until eventually apoptosis, a programmed cell death, is triggered. Cancerous cells may display apoptotic resistance and be therefore capable or remaining in severe hypoxic conditions for much longer with an effective quiescence as G_1 is greatly extended. In the most extreme case the cell cannot function indefinitely without oxygen and a necrotic core develops. On the outer rim of a growing sphere we would expect to find low levels of HIF-1α as the cells are closer in contact to the oxygen source (blood supply). Therefore cell-cycle periods would be shorter and this region is often referred to as the proliferative rim. In Chapter 4 we found that introducing a rapid hypoxic switch to sphere boundaries results in an overshoot phenomenon whereby cells in the proliferative rim temporarily have higher HIF-1α levels than in the hypoxic core. This transient overshoot period typically lasts between 0-20 hours in our simulations and would result in the intermediate cell cycles being of greater duration on the proliferative rim than in the core. If hypoxic switches were supplied periodically such that this overshoot phenomenon occurred relatively

frequently (see Figure 4-19) this could provide a method of altering typical tumour progression. With this oxygen signal we would expect cell-cycle periods in the core to remain relatively constant and dead cells to accumulate as with normal progression. However, outer rim cells would be arrested and the proliferative rim might be rendered quiescent.

Another potential significant factor in the effect of rapid oxygen switches on cell-cycle periods is the heterogeneity exhibited in HIF-1α dynamics in single cells (see Figure 5-11). For typical 'bell' responses (e.g. Figure 5-11C) we see great peak amplitude in HIF-1α following hypoxic induction before a relatively fast return to low levels. In the cell-cycle model we might expect this to translate as a considerably extended intermediate cell-cycle period with hypoxic cell-cycle periods relatively similar to those in normoxia. For non-bell responses such as 'ramps' (e.g. Figure 5-11B) we typically see a more gradual increase in HIF-1α accumulation to a lesser peak amplitude but the hypoxic equilibrium is greater. This would likely translate to an intermediate cell-cycle period of extended duration yet shorter than subsequent hypoxic cell-cycle periods of extended duration.

We tested the effects of heterogeneous HIF-1α responses on the cell cycle by using the 2-component model derived in Chapter 2, (2.14). This model was parameterised using the optimisation results found in Chapter 2 for the cell responses seen in Figure 5-11B-C (cells 3 and 31 respectively as identified in Figure 2-18). We coupled the 2-component model to our modified cell-cycle model in the same manner as the 4-component coupling and applied a rapid hypoxic switch during an intermediate cell cycle (see Figure 5-12).

In Figure 5-12A we used the HIF-1α dynamics of cell 3 (Figure 5-11B), a 'ramp' response, characterised by a relatively slow induction. In the data this cell also had relatively high HIF-1α levels (AU) and there was no dynamic resolution in hypoxia to determine a HIF-1α value for a hypoxic steady state. Our 2-component model fit to this data predicts the stable equilibria of HIF-1α in normoxia and hypoxia to be approximately 800 and 2,400 AU respectively. Contrast this with the median 4-component model output of approximately 100 and 600 AU. Thus, there is lower fold-induction in cell 3 when compared with the median, but greater absolute levels (albeit in arbitrary units). The model fit also gives peak HIF-1α amplitude of approximately 3,300 AU so the model prediction is that there is an overshoot in this HIF-1α response before stabilisation at a slightly lower hypoxic equilibrium (not seen in the data). The effects of the dynamic characteristics of cell 3 on the cell cycle during rapid hypoxic induction are similar to what we expected. There is clear hypoxic cell-cycle arrest, but the relatively slow induction of HIF-1α results in the intermediate cell cycle being shorter than subsequent hypoxic cell cycles. The second cell cycle following the introduction of hypoxia was the longest in duration due to the overshoot characteristic in the HIF-1α dynamics which were greater than the hypoxic equilibrium at this stage.

In Figure 5-12B the 'bell' HIF-1α dynamics of cell 31 (Figure 5-11C) were introduced to the cell-cycle model. This data had AU levels of a similar order to the 4-component model output at equilibria but much greater peak amplitude (~4,000 AU compared with ~2,000 AU) resulting in twice as much fold-induction. As predicted the intermediate cell cycle was much greater than cell-cycle periods before and afterwards. The intermediate cell cycle was 45% longer than in normoxia while long-term hypoxic cycles were 32% longer than normoxic cycles. For these HIF-1α dynamics, the second cell cycle following hypoxic induction had the shortest extension (30%) due to an undershoot before the resolution of the bell dynamics and stabilisation at the hypoxic equilibrium (see Figure 5-12B). These results suggest opposite roles for the intermediate cell-cycle periods (and the following cell-cycle period) dependent on the type of transient HIF-1α dynamics generated following a hypoxic switch.

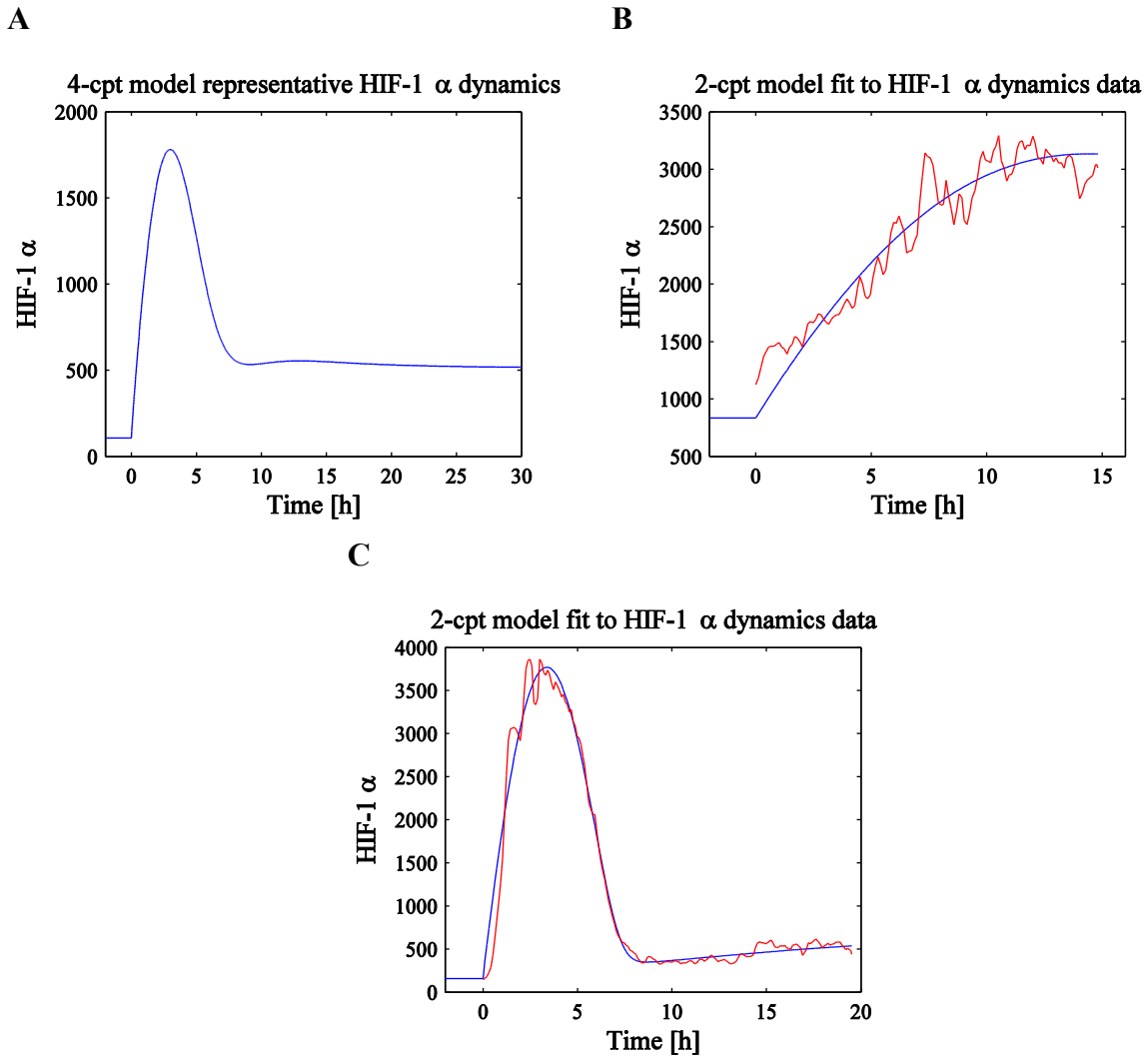

Figure 5-11: An example of the heterogeneity of single-cell HIF-1α dynamics after a rapid hypoxic switch. (A): Our representative response of an average cell from the 4-component (4-cpt) model used in our modified oxygen-dependent cell-cycle model. (B-C): Examples of different single-cell data (red) fit to by the 2-component (2-cpt) model (blue). This heterogeneity may be a significant factor in the effects of hypoxia on cell-cycle arrest.

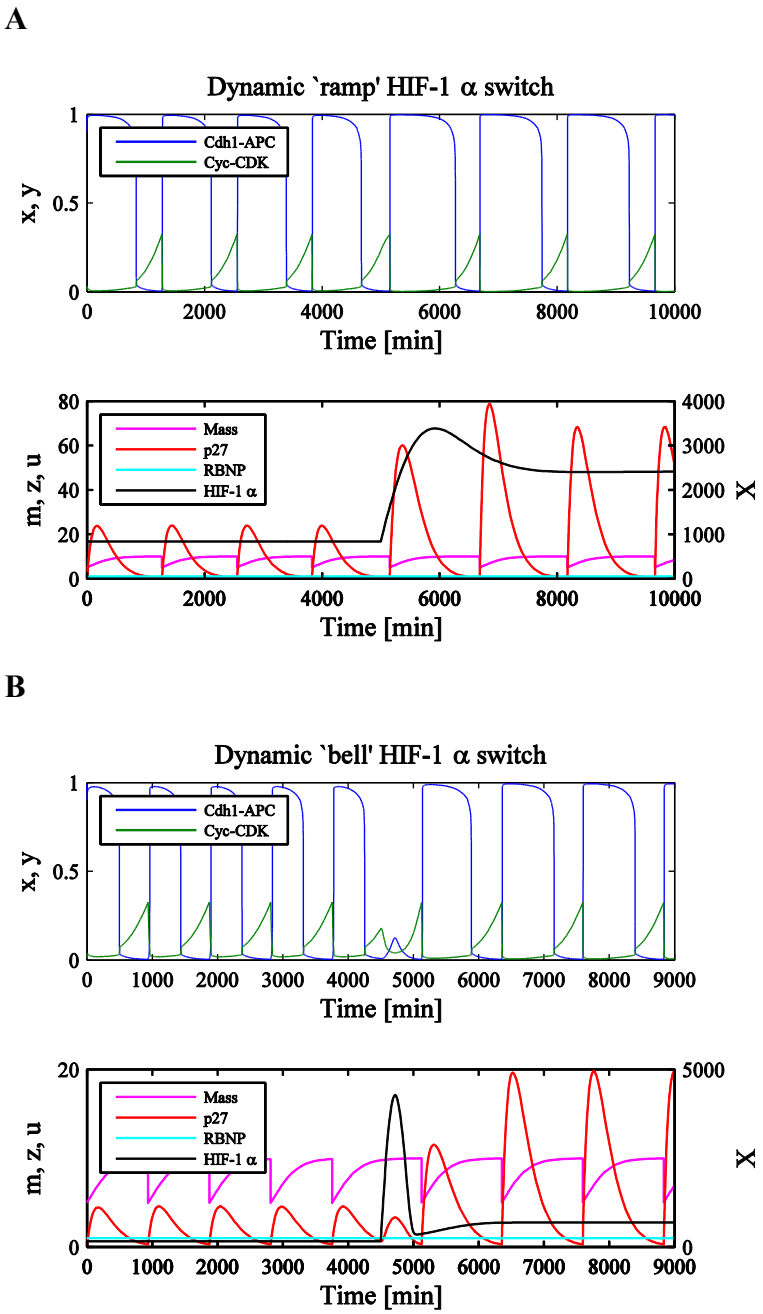

Figure 5-12: Two cell-cycle model simulations with a hypoxic switch and heterogeneous HIF-1α dynamics. Both the 'ramp' HIF-1α dynamics (A) and the 'bell' HIF-1α dynamics (B) are simulated. In these simulations P was reduced such that the intermediate cell cycle was approximately halfway through the S-G_2-M phase ($t = 5{,}000$ min and 4,500 min for (A) and (B) respectively).

5.3 Apoptosis and the p53 Signalling Pathway

All cellular processes require tight regulation and levels of organisation in order to function efficiently. Just as cellular proliferation is controlled through the events of the cell cycle, it is also necessary to control the rate of cell death within a population. This can be achieved by the activation of an intracellular death program where the cell effectively commits suicide for the benefit of the larger cellular system. This process of programmed cell death is referred to as apoptosis and can be triggered when cells are no longer needed (e.g. in development, where apoptosis is needed for the proper formation of cell structures such as in synapse formation) or become a threat to the organism (e.g. as a result of viruses or gene mutations). Apoptosis differs from cell death caused as a result of injury. This unprogrammed cell death is referred to as necrosis and is a result of external forces that cause the cell to swell and burst potentially damaging neighbouring cells and inducing an inflammatory response (Alberts, et al. 2002). In contrast, apoptosis is an energy-dependent process that is regulated by a cascade of proteins called caspases that mediate the destruction and removal of the cell and its components without trauma. A damaging consequence of necrosis is cell leakage and this is avoided during apoptosis by recruiting macrophages or neighbouring cells to ingest the dying cell.

Apoptosis can occur as a result of many different environmental stresses and as such is involved in many pathologic conditions including acute neurologic injuries, cardiovascular diseases, immunological diseases and cancer (Zimmermann and Green 2001). One of the most important genes involved in apoptosis and cancer is the p53 gene (named after the molecular mass of its protein product, the tumour suppressor protein 53). The p53 gene is mutated in over 50% of human cancer cells (Levine 1997) where its critical role in protecting the organism from cellular damage is inhibited. One of the main forms of this protection offered by p53 is the initiation of apoptosis in damaged cells. Therefore when p53 is inactivated in cancer cells, genetically damaged and senescent cells are allowed to escape apoptosis and continue to replicate their DNA (Alberts, et al. 2002).

As with HIF-1, the p53 protein is a transcription factor that plays a key part in the response to cellular stress and is maintained at a relatively low level in normal/healthy conditions. Another way in which p53 is comparable to HIF-1 is in the way it is primarily regulated by post-translational modifications. The key regulation mechanism of p53 is through the control of its protein stability and this is mediated by the specific repressor of p53, mouse double minute-2 (Mdm2, sometimes called Hdm2 in humans). Mdm2 is a transcriptional target of p53 and therefore this regulation is of the form of a negative feedback loop where p53 activates the expression of its own inhibitor (Amaral, et al. 2010). How exactly p53 mediates apoptosis has been a matter of intensive study for over twenty years but few target genes have been unequivocally confirmed as being essential to the induction of apoptosis in

a p53-dependent manner. However, there are many signalling pathways involved in the apoptosis process and p53 can be found to intervene at every major step in all of them and initiate apoptosis via both transcription-dependent and transcription-independent mechanisms (Haupt, et al. 2003).

5.3.1 The Role of Hypoxia and HIF-1 in Apoptosis

Apoptosis can be initiated due to a range of physiological stresses including hypoxia. Deficiency in oxygen results in the HIF-1 mediated cellular response to address the oxygen imbalance but severe hypoxia or anoxia causes a high rate of mutations. In order to protect the organism from the proliferation of genetically unstable DNA, the cell initiates the apoptosis pathway during severe hypoxia. Therefore there is a delicate balance of hypoxia and apoptosis regulatory proteins in order to determine whether cells are sacrificed or adapt to the hypoxic microenvironment. A hallmark of cancer is the adaptation to chronic hypoxia through apoptotic resistance, often through a mutation in the p53 signalling pathway (Reynolds, Rockwell and Glazer 1996). Hypoxia is a physiological inducer of p53 and the repeated periods of hypoxia found in growing tumours can lead to selective pressure that encourages the establishment of a mutated cell population with inactive p53 (Koumenis, et al. 2001).

The p53 gene is the key factor in inducing apoptosis as a response to a wide range of cellular stress caused by DNA damage or hypoxia (often both together as they are not mutually exclusive (Hammond, Dorie and Giaccia, ATR/ATM targets are phosphorylated by ATR in response to hypoxia and ATM in response to reoxygenation 2003)). Hypoxia causes the nuclear accumulation of p53 to increase as well as the DNA-binding and transactivation activity of p53 (Graeber, et al. 1994). The levels of the negative regulator of p53, Mdm2, are decreased in hypoxia allowing p53 to accumulate (Hammond and Giaccia, The role of p53 in hypoxia-induced apoptosis 2005). Specifically, it is Mdm2 at the protein level which is affected. Mdm2 is a transcriptional target of p53 and thus p53 accumulation is normally curtailed by an autoregulatory feedback loop. However, during hypoxic induction of p53, Mdm2 protein levels are suppressed for long times. The mRNA levels of Mdm2 are still increased in hypoxia (as a consequence of p53 induction) so the hypoxic regulation of Mdm2 must be due to a post-transcriptional mechanism (Koumenis, et al. 2001). As the key mediator in cellular hypoxic responses it has been proposed that HIF-1α has a regulatory role to play in p53-dependent hypoxia-induced apoptosis. However, there is no conclusive agreement within the field of the precise nature of the relationship between HIF-1α and p53.

A review by Greijer & van der Wall (The role of hypoxia inducible factor 1 (HIF-1) in hypoxia induced apoptosis 2004) asserts that HIF-1 plays a role in hypoxia-induced apoptosis but that the exact mechanism is unclear. The review contains the results of various reports into the interactions between HIF-1α and the p53-pathway. HIF-1α can increase the stability of p53 and induce apoptosis

and the interaction between HIF-1 and p53 can be direct or indirect (Liu, et al. 2012, Goda, Dozier and Johnson, HIF-1 in cell cycle regulation, apoptosis, and tumor progression 2003). It has been shown that HIF-1α can stabilise p53 directly by binding to Mdm2. Thus HIF-1α protects p53 degradation that is mediated by Mdm2 and promotes the activation of p53-mediated transcription (Chen, et al. 2003). However, another report shows that p53 can bind to the oxygen dependent degradation domain (ODD) of HIF-1α and speculates that this complex may promote apoptosis via the stabilisation of p53 (Hansson, et al. 2002). This proposal also suggests that p53 can cause repression of HIF-1, independent of hydroxylation status, via an alternative, Mdm2-based degradation mechanism. This could explain the role of p53 as a tumour suppressor by inhibiting HIF-1 induced angiogenesis (Hansson, et al. 2002). Conversely, more recent contradictory results suggest that Mdm2 induction actually promotes the activation of HIF-1 (Nieminen, et al. 2005). It is also the inability of HIF-1α to interact with tumour derived mutant p53 that is proposed to be the cause of the resistance to hypoxia-induced apoptosis in cancer (An, et al. 1998) and promote an angiogenic phenotype during tumourigenesis (Ravi, et al. 2000).

It has been repeatedly established in the referenced literature above that there is a link between HIF-1α, hypoxia, p53 and apoptosis yet the precise mechanism remains unclear. Using what information we have available we aim to reveal the implications of introducing the characteristic HIF-1α dynamics of our model to a model of the p53-apoptosis pathway. Specifically: how are p53 dynamics affected during acute hypoxic shock when p53 is regulated by HIF-1α levels? How do these p53 dynamics vary across a model sphere subject to the effects of oxygen diffusion and consumption? What inferences can be made about the apoptotic activity of such a sphere exposed to acute hypoxic induction?

5.3.2 A Modified Oxygen Dependent p53 Model

A recent study by Hunziker et al. (Stress-specific response of the p53-Mdm2 feedback loop 2010) reported the construction of a simple yet flexible mathematical model describing the dynamics of the p53-Mdm2 feedback loop. The paper focuses on the central role of p53 in the cellular responses to stress. Several different types of stress are considered and simulated to provide different output dynamics of p53. These p53 dynamics are thought to be significant in determining specific downstream gene expression patterns corresponding to the range of outputs that can be triggered by p53 (e.g. apoptosis, cell-cycle arrest and cellular senescence) (Hunziker, Jensen and Krishna 2010). In particular, a portion of the work is dedicated to the hypoxia-specific response of the p53-Mdm2 feedback loop and the associated output of this stress is a higher incidence of apoptosis, represented by large increases in p53 levels (relative to other stress-induced responses). We will use this model to

investigate the downstream effects of acute hypoxic induction and the consequent HIF-1α dynamics on p53 output behaviour.

5.3.2.1 The Hunziker Model of the p53-Mdm2 Negative Feedback Loop

The ultimate results of the stress perturbations in the Hunziker model are deemed to be represented by output behaviour of p53. The unperturbed system maintains a low, steady state of p53 consistent with biological literature (Ma, et al. 2005, Wang, et al. 2007). The various forms of stress applied (hypoxia; DNA damage; Nutlin treatment; and deregulated oncogenes) are replicated in the model through the variation of appropriate parameters. These perturbations can lead to significantly different long-term p53 dynamics such as sustained oscillations. Certain dynamic features are highlighted in the paper as examples of 'specific output behaviour'. These include: steady state solutions with any combination of high and low p53 and Mdm2, as well as oscillations (spiky and smooth) with high or low average p53. Although no explicit correlations between output states and specific physiological responses can be made it is reasoned that large increases of p53 are expected to correspond to an apoptotic response whereas more moderate increases may correspond to less drastic responses such as cell-cycle arrest (Hunziker, Jensen and Krishna 2010).

The mathematical model developed by Hunziker et al. consists of four time-dependent variables representing four key components of the signalling pathway: p53 (p); Mdm2 mRNA (m_m); Mdm2 (m); and the p53-Mdm2 complex (c). The evolution of these variables is described by the following system of ODEs:

$$\begin{aligned} \frac{dp}{dt} &= \sigma - \alpha p - k_f pm + k_b c + \gamma c, \\ \frac{dm_m}{dt} &= k_t p^2 - \beta m_m, \\ \frac{dm}{dt} &= k_{tl} m_m - k_f pm + k_b c + \delta c - \gamma m, \\ \frac{dc}{dt} &= k_f pm - k_b c - \delta c - \gamma c. \end{aligned} \tag{5.9}$$

The model parameters are defined in Table 5-1 while Figure 5-13 shows the interactions described in the model in the form of a schematic diagram. p53 (p) is produced at a constant rate σ and this production is enhanced by the release of free p53 from the p53-Mdm2 complex c at a combined rate of $k_b + \gamma$ (dissociation rate and Mdm2 degradation rate respectively). p53 is degraded at a constant rate α and associates with Mdm2 at a rate k_f increasing the production of complex c. The transcription of Mdm2 mRNA (m_m) is dependent on a quadratic p53 induction function proportional to rate k_t while basal mRNA degradation is represented by β. Mdm2 mRNA is translated into Mdm2

protein (m) at rate k_{tl} and the growth of this molecular species is increased by the release of free Mdm2 from complex c at a combined rate of $k_b + \delta$ (dissociation rate and Mdm2-mediated p53 degradation rate respectively). Increase in Mdm2 concentration is limited by basal degradation rate γ and complex association rate k_f. The p53-Mdm2 complex c is formed via the association of p53 and Mdm2 at rate k_f. This complex can be broken down in three ways: dissociation (at rate k_b); Mdm2 degradation (γ); or by Mdm2-dependent p53 degradation (δ). Thus, the model is based on a single negative feedback loop as p53 induces the synthesis of its own inhibitor, Mdm2. Nonlinearities in the description of complex formation prove sufficient for the generation of oscillatory behaviour (Hunziker, Jensen and Krishna 2010).

Parameter Symbol	Parameter Description	Default Value	Hypoxic Value (if different)
σ	p53 production	1000 nM. hr^{-1}	
α	Mdm2-independent degradation/deactivation of p53	0.1 hr^{-1}	
δ	Mdm2-dependent degradation/deactivation of p53	11 hr^{-1}	2 hr^{-1}
k_t	Mdm2 transcription	0.03 $nM^{-1}hr^{-1}$	0.01 $nM^{-1}hr^{-1}$
k_{tl}	Mdm2 translation	1.4 hr^{-1}	
β	Mdm2 mRNA degradation	0.6 hr^{-1}	
γ	degradation/deactivation of Mdm2	0.2 hr^{-1}	
k_b	p53-Mdm2 dissociation	7200 hr^{-1}	
$k_D = k_b/k_f$	p53-Mdm2 dissociation constant	1.44 nM	

Table 5-1: The table provides a description of each of the parameters in model (5.9). Note that concentration units are given in nanomolars (nM) and time units are given in hours (hr).

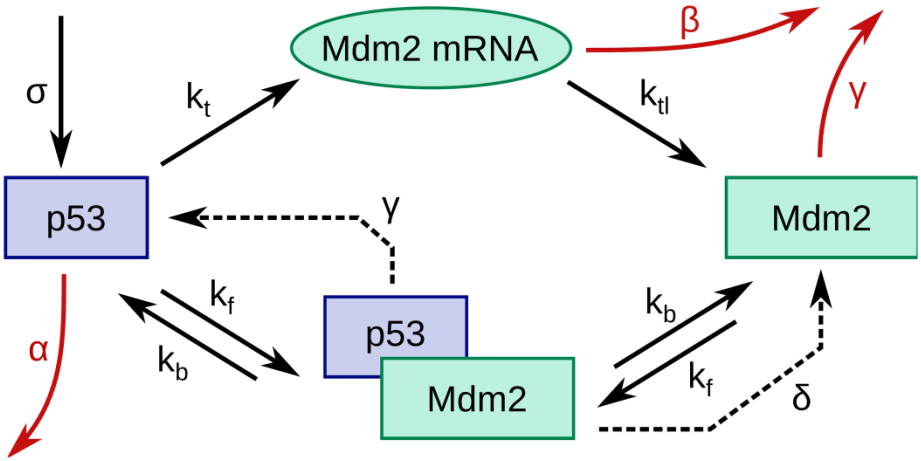

Figure 5-13: A schematic representation of model (5.9) as produced by Hunziker et al. (Stress-specific response of the p53-Mdm2 feedback loop 2010). Parameter definitions are given in Table 5-1.

5.3.2.2 Effects of Hypoxia

Stress responses were produced in the Hunziker model by mimicking the effects that a particular stress had on pathway interactions. This was achieved by varying appropriate model parameters from their default value. The default parameterisation of the model (as given in Table 5-1) describes the 'resting state' of the system, a healthy/normal environment where p53 is maintained at a low, steady level. Hunziker et al. assert that hypoxia affects the p53-Mdm2 feedback loop in two distinct ways: the transactivation property of p53 is decreased; and hypoxia induces HIF which binds to p53 and prevents degradation. These hypoxic effects are achieved in the model by decreasing parameters k_t and δ respectively. We note that α, the Mdm2-independent degradation/deactivation of p53, is not altered by hypoxia; but may not be too important as this occurs on a much slower timescale than the degradation of p53 when in complex with Mdm2. Hypoxic simulations carried out by Hunziker et al. result in a bifurcation in p53 dynamics from the resting low steady state to oscillations with a greater amplitude and average p53 level when compared to other stresses. Our own MATLAB simulations of model (5.9) are shown in Figure 5-14 which shows the application of hypoxic parameters at time $t = 0$ hours. As in the Hunziker paper, oscillations are generated upon the switch to hypoxia. All our simulations of the Hunziker model and its subsequent modifications use the following initial conditions and the first 100 hours are discarded as done by Hunziker et al. (Stress-specific response of the p53-Mdm2 feedback loop 2010). That is

$$p(0) = 1, \qquad m_m(0) = 0, \qquad m(0) = 1, \qquad c(0) = 0. \tag{5.10}$$

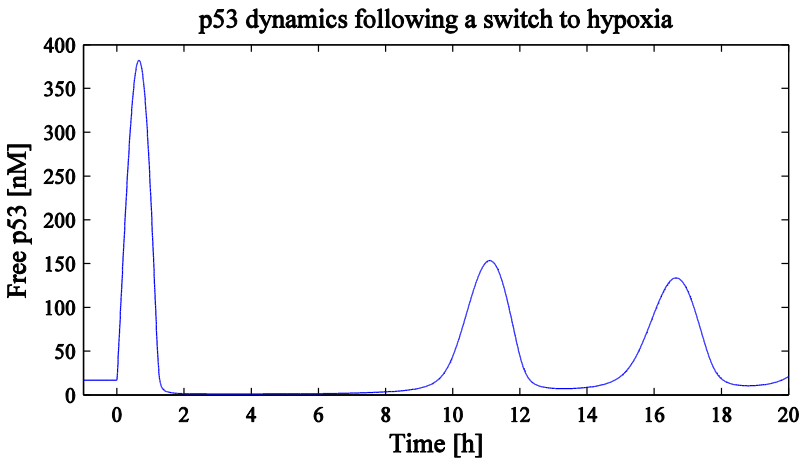

Figure 5-14: p53 dynamics. Hypoxia is simulated by decreasing parameters k_t and δ in model (5.9) from the resting state parameterisation at $t = 0$. The temporal dynamic behaviour of p53 changes from a low steady state to oscillations of great amplitude.

Before we introduce hypoxic-sphere HIF-1α dynamics to the Hunziker p53 model, we would like to match the oxygen dependence of parameters k_t and δ with various grades of hypoxia. This will allow us to break away from the limiting two-state situation of normoxia/hypoxia and incorporate a range of hypoxic p53 responses. Specifically, the Hunziker model simulates hypoxia by reducing parameters k_t and δ in the following manner:

$$k_t = \begin{cases} 0.03\ \mathrm{nM}^{-1}\mathrm{hr}^{-1}, & \text{in normoxia} \\ 0.01\ \mathrm{nM}^{-1}\mathrm{hr}^{-1}, & \text{in hypoxia} \end{cases}$$

$$\delta = \begin{cases} 11\ \mathrm{hr}^{-1}, & \text{in normoxia} \\ 2\ \mathrm{hr}^{-1}, & \text{in hypoxia} \end{cases}$$

In order to deduce the values of these parameters at any point between 'normoxia' and 'hypoxia' we must assign a value of oxygen concentration to these two distinct, named states and interpolate between them. We assume 'normoxia' corresponds to 20% and 'hypoxia' corresponds to 1% oxygen saturation in accordance with our previous work. We introduce explicit, continuous oxygen dependence into the Hunziker model by assuming that parameters k_t and δ are functions of the variable for oxygen concentration, C. For simplicity we assume that the relationship between model parameter and oxygen is linear and thus derive the following relations:

$$\delta(C) = 0.4737C + 1.5263$$

$$k_t(C) = 0.0011C + 0.0089$$

We used this modified model with extended oxygen dependence to analyse the temporal p53 dynamics after different hypoxic switches were applied (see Figure 5-15). In the plot of Figure 5-15, each curve represents the p53 dynamics resulting from an instant switch from normoxia (20% O_2, $C = 20$) to a different level of hypoxia (1-20%, $C = 1,..,20$). Initial normoxic conditions were used

as in the Hunziker paper before hypoxic insults of varying severity were applied at $t = 0$ hours. The results of these simulations are that hypoxic switches of greater severity result in p53 oscillations of greater amplitude that suggest a stronger apoptotic phenotype. Also, even slight drops in hypoxia appeared to lead to oscillatory behaviour. Furthermore, although we see growing amplitudes in p53 oscillations for stronger hypoxic switches, we note that the ordering of peak timings in the oscillations changes once a certain level of hypoxic drop is reached. That is, for milder hypoxic switches (red, yellow, green curves), increasing the severity of the hypoxic switch leads to delayed second-peaks while in the case of the severe hypoxic switches (blue curves), increasing hypoxic switches leads to a shortening in the time-to-second-peak (we refer to the second peak as initial peaks are relatively homogenous throughout with respect to time). Therefore we conclude that peak-timing is not a monotonic function of hypoxic-switch-severity although peak-amplitude is.

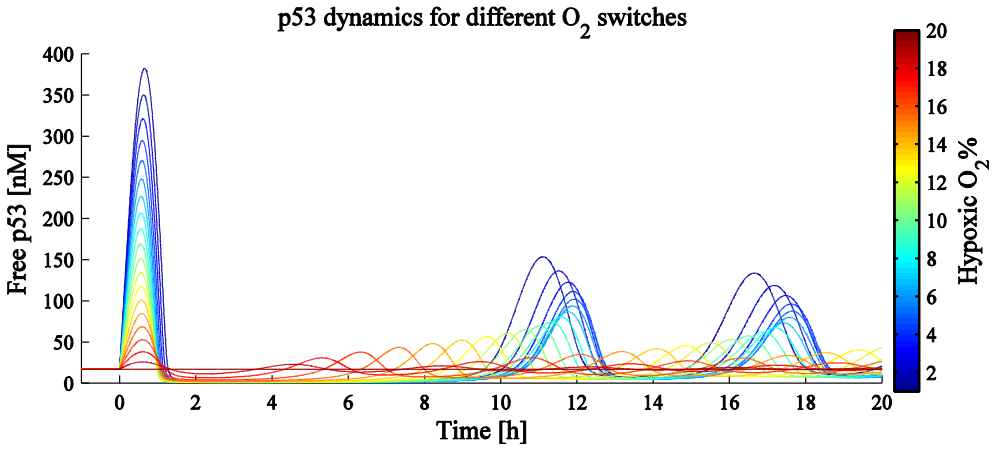

Figure 5-15: Temporal p53 dynamics as a result of various hypoxic switching from the normoxic resting state (20% O_2). The hypoxic switches applied were varied between 1% and 20% in 1% intervals. The colour bar indicates what severity of hypoxic switch was applied for each curve on the plot. For example dark blue represents a hypoxic switch from 20% to 1% and dark red represents a switch from 20% to 20% (i.e. no change). The hypoxic switch was applied at $t = 0$ h.

We also used this model to investigate hypoxic p53 dynamics in a physiologically relevant setting, e.g. a neurosphere. By analysing the model results at different oxygen tensions given by the steady-state distribution of our oxygen-diffusion model (see Chapter 4), we can infer the behaviour of the p53 pathway in different regions of the sphere. Specifically, we investigated p53 dynamics across a sphere of radius 200μm with a normoxic boundary (20% O_2) in line with previous work. The sphere was parameterised as in Chapter 4 with respect to the rates of oxygen consumption and oxygen diffusion.

The Hunziker study attempted to quantify the response to stress by measuring long-timescale features of p53 dynamics such as the peak levels of p53 in stress-induced oscillations. In Figure 5-16 we analysed the peak values of the long-term dynamics (steady states or stable oscillations) in order to determine where in the sphere oscillations begin to occur, dependent on different boundary conditions

(normoxic and hypoxic). The Hunziker paper also gave significance to a subset of oscillations defined as 'spiky oscillations'. Oscillations were said to be 'spiky' once the amplitude was twice as great as the average value. We also calculated where the onset of spikyness [*sic*] occurs in the sphere using the same method (see Figure 5-16). We found that p53 oscillations start to occur 20μm radially inwards from the normoxic sphere boundary, corresponding to approximately 16% O_2. Spiky oscillations, typically characterised by big peaks relative to the average concentration, begin to occur at approximately 1/3 of the way radially inwards of the sphere at an oxygen concentration of 10% O_2. The onset of spiky oscillations means that p53 peak levels increase at a high rate when compared with the average p53 levels which do not significantly change. The Hunziker paper concedes that the physiological significance of this is unclear but claims that some downstream genes may respond to peak p53 levels while others may sense the average level. This theory is based on work from the same research group when studying the effects of spiky oscillations of Nf-κB on gene expression and its dependence on association rates between Nf-κB and relevant operator sites (Krishna, Jensen and Sneppen 2006).

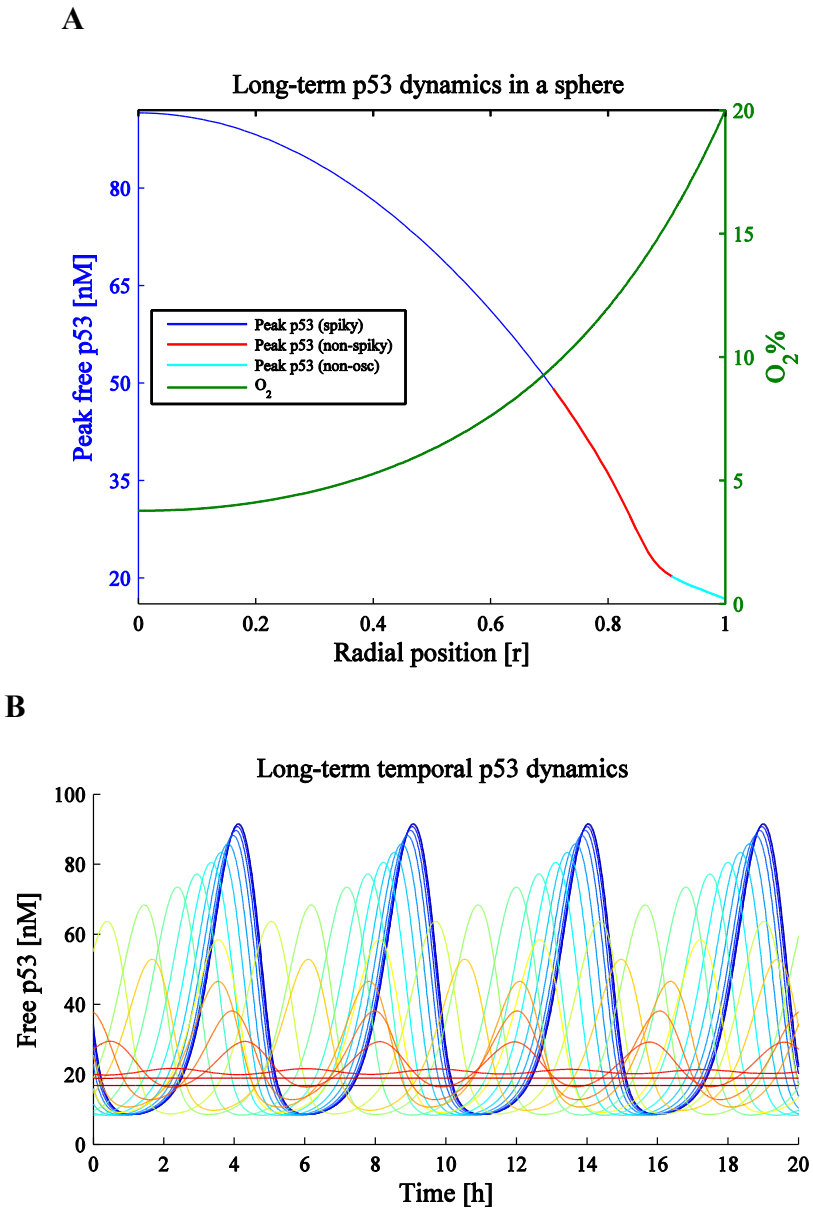

Figure 5-16: Characteristics of long-term p53 dynamics throughout a neurosphere. (A): p53 peak amplitude (the peak only differs from the average when there are oscillations) is plotted against the oxygen distribution for a sphere with normoxic boundary conditions. The p53 peak amplitude curve is coloured dependent on the type of p53 dynamics at the corresponding region of the sphere. Colour coding: spiky oscillations (as defined in the text) – blue; non-spiky oscillations – red; steady state – cyan. (B): Long-term p53 oscillatory dynamics. Different coloured p53 oscillations represent different regions of the sphere from the sphere core (blue curves) to the sphere border (red curves). As with our previous simulations we used conditions (5.10) and discarded the first 100 hours ($-100{:}\,0$ h) by which time stable oscillations had been established.

5.3.2.3 Introducing HIF-1α Dependence

In order to investigate the effects of transient HIF-1α dynamics on the p53 pathway, a site within the model has to be identified where HIF-1α dependence can be introduced. Hypoxia has an effect on two parameters in the Hunziker model but only δ, the Mdm2-mediated degradation rate of p53, is said to

be HIF-dependent. Therefore we preserve our definition of the linear relationship between oxygen and the other oxygen-dependent parameter k_t (Mdm2 transcription rate) as before but introduce a new function for δ dependent on HIF-1α concentration, x. That is

$$\delta = \delta(x) = \delta\big(x(C)\big),$$

as HIF-1α levels themselves are dependent on oxygen concentration C. In order to define the new relation we use the HIF-1α equilibrium function $x^{EQ}(C)$, as in the cell-cycle model coupling (see section 5.2.2 and in particular Figure 5-6), where

$$x^{EQ}(C) = \frac{\left(S - \sum_{i=1}^{3} \frac{h_i S_i}{d_i}\right) + \sqrt{\left(\sum_{i=1}^{3} \frac{h_i S_i}{d_i} - S\right)^2 + 4kS\gamma\left(\frac{h_2}{d_2} + \frac{h_3}{d_3}\right)}}{2k\left(\frac{h_2}{d_2} + \frac{h_3}{d_3}\right)}, \tag{5.11}$$

and

$$\begin{aligned} h_1(C) &= 0.25(0.0014(C)^2 + 0.016(C) + 0.1233), \\ h_2(C) &= 0.0015(C)^2 + 0.0137(C) + 0.1202, \\ h_3(C) &= 1.25(0.0022(C)^2 + 0.0012(C) + 0.1036), \end{aligned}$$

with HIF-1α-model parameters as defined in Chapter 3. In theory we can invert $x^{EQ}(C)$ such that we can write $\delta(x)$ corresponding to our previous definition. That is,

$$\delta(x) = \delta\big(C(x)\big) = 0.4737C(x) + 1.5263. \tag{5.12}$$

Instead we take a new definition

$$\delta(x) = \frac{A}{x} - B$$

for simplicity. Note that there is an inverse relation between δ and x as δ should decrease in more hypoxic conditions when HIF-1α levels (x) are elevated. We choose A and B such that

$$\begin{aligned} \delta\big(x^{EQ}(20)\big) &= 11 \\ \delta\big(x^{EQ}(1)\big) &= 2 \end{aligned}$$

Thus,

$$\delta(x) = \frac{1{,}216}{x} - 0.372. \tag{5.13}$$

We can compare approximations (5.12) and (5.13) in the form of a plot (see Figure 5-17) and note that there is no significant change when we change the dependence of δ from oxygen (C) directly to equilibrium levels of HIF-1α (x^{EQ}).

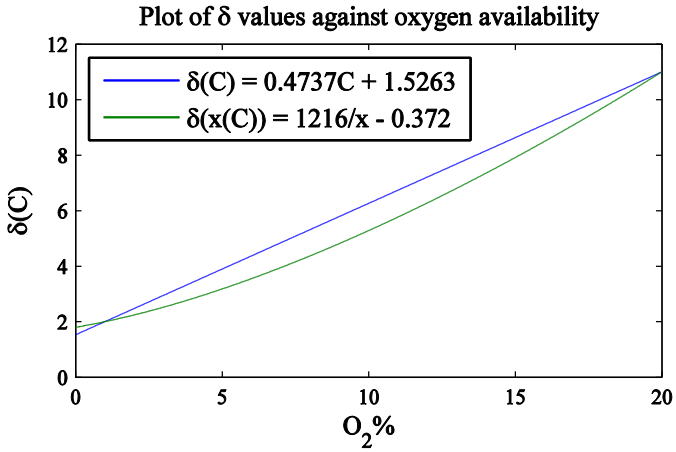

Figure 5-17: Plots of δ approximations as a function of oxygen directly (C) and of HIF-1α equilibrium levels ($x^{EQ}(C)$).

5.3.3 Model Coupling Results & Discussion

We introduce dynamic HIF-1α by coupling the modified Hunziker p53 model (with continuous oxygen-dependent k_t and HIF-1α-dependent δ) to our HIF-1α model:

$$\begin{aligned}
\frac{dp}{dt} &= \sigma - \alpha p - k_f p m + k_b c + \gamma c \\
\frac{dm_m}{dt} &= k_t(C)p^2 - \beta m_m \\
\frac{dm}{dt} &= k_{tl} m_m - k_f p m + k_b c + \delta(x) c - \gamma m \\
\frac{dc}{dt} &= k_f p m - k_b c - \delta(x) c - \gamma c \\
\frac{dx}{dt} &= S - \left(\frac{x}{x+\gamma}\right)(h_1(C)y_1 + h_2(C)y_2 + h_3(C)y_3) \\
\frac{dy_1}{dt} &= S_1 - d_1 y_1 \\
\frac{dy_2}{dt} &= S_2 + k_2 x - d_2 y_2 \\
\frac{dy_3}{dt} &= S_3 + k_3 x - d_3 y_3
\end{aligned} \tag{5.14}$$

where

$$h_1(C) = 0.25(0.0014C^2 + 0.016C + 0.1233),$$
$$h_2(C) = 0.0015C^2 + 0.0137C + 0.1202,$$
$$h_3(C) = 1.25(0.0022C^2 + 0.0012C + 0.1036),$$

$$k_t(C) = 0.0011C + 0.0089,$$

and

$$\delta(x) = \frac{1{,}216}{x} - 0.372.$$

In order to provide a realistic physical setting for our simulations we look at using the oxygen distribution given by our oxygen model with normoxic boundary conditions as an initial condition. We then want to switch to hypoxic conditions by changing the sphere boundary condition from 20% O_2 (normoxia) to 1% O_2 (hypoxia). We know that the distribution given by our oxygen-diffusion model gives a decreasing function of oxygen concentration with respect to the radius, i.e. the level of hypoxia increases towards the centre of the sphere. Since we also know that even very mild hypoxic environments can lead to p53 oscillations, our initial simulation condition using a sphere with normoxic boundary conditions is not a p53-steady-state as can be seen in Figure 5-16B. Initial conditions were chosen as previously for the p53 pathway in (5.10) and equilibrium values were chosen for the HIF-1α pathway as in our previous work. This is compared with previous switching simulations when we started from the normoxic resting state (see Figure 5-15).

Simulations of the coupled HIF-1α-p53 model subject to a switch in boundary conditions from normoxia to hypoxia are shown in Figure 5-18. As seen in Chapter 4, the switch in oxygen occurs on a much faster timescale than the HIF-1α dynamics, and so we assume the hypoxic steady state distribution of oxygen is reached instantly. As the severity of the oxygen switch varies with spatial position in the sphere, we see that HIF-1α mediated p53 dynamics also vary with position. We also compare the effects of steady HIF-1α and dynamic HIF-1α when inducing hypoxia at the sphere boundary. For steady HIF-1α simulations, $\delta(x)$ only depends on equilibrium values of HIF-1α. This is implemented by removing the HIF-1α pathway module of model (5.14), i.e. equations dx/dt, dy_1/dt, dy_2/dt and dy_3/dt. Then equilibrium HIF-1α values are derived using equation (5.11) for a given oxygen value, and input into $\delta(x)$. This type of simulation is comparable to direct oxygen dependence. Steady state oxygen conditions for both simulations can be seen in Figure 5-19.

A

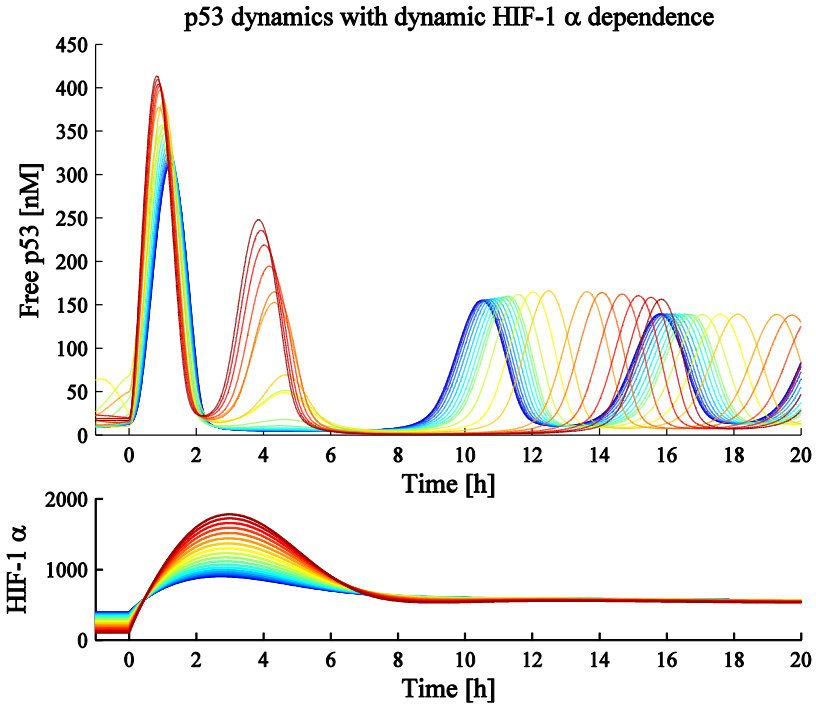

B

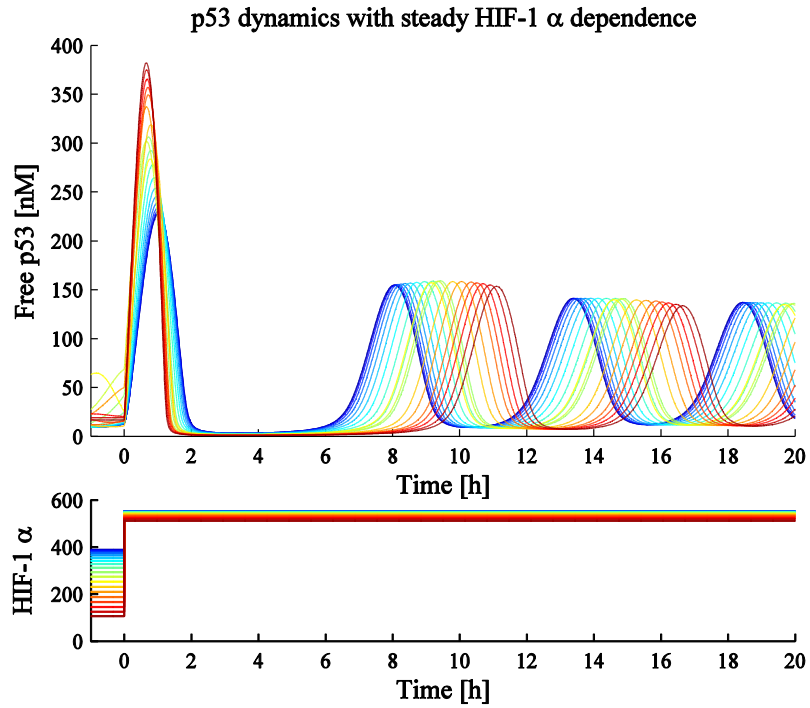

Figure 5-18: Results of introducing dynamic HIF-1α dependence (A) and steady HIF-1α dependence (B) to the p53 dynamic model. p53 and HIF-1α dynamics as a result of a hypoxic switch applied at the boundary of a respiring sphere are plotted. Blue curves correspond to protein dynamics towards the centre of the sphere. Red curves correspond to dynamics toward the sphere boundary. Oxygen conditions throughout the sphere are described in Figure 5-19.

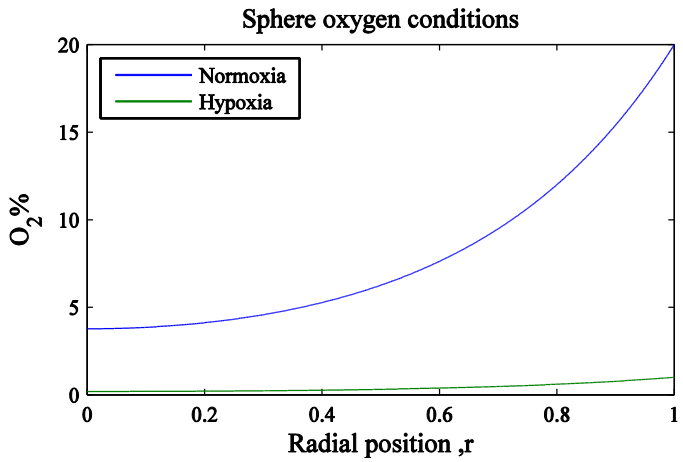

Figure 5-19: Oxygen conditions for the simulations of Figure 5-18. The normoxic distribution (blue) represents the steady state of oxygen in a sphere with 20% O_2 at the border. This is the initial oxygen condition for Figure 5-18 simulations. The hypoxic distribution (green) represents the steady state after a switch to 1% O_2 at the sphere border. The switch to hypoxia (green) occurs at $t = 0$ in Figure 5-18.

Figure 5-18 shows how the introduction of transient HIF-1α dynamics can significantly affect the nature of p53 oscillations in a hypoxic sphere of respiring cells. A striking consequence of this introduction of HIF-1α dependence into the p53 pathway is a double-peak in p53 following hypoxic induction. Without the inclusion of the dynamic behaviour of HIF-1α, we have consistently seen a relatively homogenous time-to-initial peak in p53 concentration followed by a relatively long delay before the onset of sustained oscillations. With the inclusion of dynamic HIF-1α, p53 dynamics nearer to the sphere boundary exhibit a second peak that closely follows the first, being both relatively early and large in amplitude. However, p53 dynamics towards the centre of the sphere, where the hypoxic switch is less extreme, follow more closely the dynamics seen in a simulation using only equilibrium values of HIF-1α. The main difference between the coupling of dynamic HIF-1α or steady HIF-1α to the p53 model is the overshoot dynamics phenomenon given by dynamic HIF-1α in a sphere (as discussed in Chapter 4). Since this effect is most dramatic at the sphere boundary it is not surprising that this is where p53 dynamics differ most.

Furthermore, the differences between these secondary p53 peaks are quite distinct such that there is almost a bimodal separation between big, early second-peaks near the sphere border and smaller, late second-peaks at the sphere core. An apparent consequence of these big, early secondary peaks due to overshooting HIF-1α dynamics is the relatively long delay between secondary and tertiary peaks in these regions. When dynamic HIF-1α is not included, boundary p53 reach the highest levels during initial peaks and peak earlier which results in a longer delay to the next peak, i.e. with steady HIF-1α, the region with the earliest (and largest) initial p53 peak also has the latest second p53 peak. Due to the nature of the dynamic HIF-1α-induced double-peak phenomenon it is the third peaks, not the second, which are severely delayed. Moreover this delay has been increased. Without dynamic HIF-

1α the time between the initial p53 peak and the secondary peak at the boundary is approximately 10 hours. With dynamic HIF-1α the time between the secondary p53 peak and the tertiary peak at the boundary is approximately 12 hours. In both cases the p53 levels is very low for most of these periods between peaks which suggests little p53-related transcriptional activity. This effect appears to be independent of the initial oscillations before hypoxic stimulation (not shown).

The consequences for apoptotic behaviour are not clear as there is no obvious way to couple the p53 dynamics with specific physiological effects in any detail. However, the increased p53 activity at early stages following hypoxic induction suggests that apoptotic activity should be increased in regions where the hypoxic switch is most severe, i.e. the sphere boundary. We hypothesise that apoptotic activity is increased at the boundary despite the longer delay in tertiary peak timing. This is due to the timescales involved. Although the longer delays in tertiary peaks may result in average p53 levels being comparable to those without the second-peak phenomenon (no dynamic-HIF dependence) within a certain window of time, we argue that this window is too long. Cell cycles typically last approximately 24 hours and the duration of apoptotic cell death is between 6 and 24 hours dependent on cell type (Saraste and Pulkki 2000). Based on these timescales we assume that the p53 signal for initiating apoptosis is more important in smaller segments of time such as with the double-peak feature. These results correspond with the HIF-1α overshoot phenomenon that can apparently stimulate processes to a degree that is usually thought to occur in regions that are more hypoxic.

The results of Figure 5-18 suggest that different oxygen regimes provide significantly different oscillatory p53 behaviour dependent on a critical change in hypoxic-switch magnitude. Regardless of spatial tissue-level context, at the single-cell level this could potentially translate to heterogeneous oxygen signals. These results prompt a hypothesis that more hypoxic cells would only exhibit a single peak in p53 within the first few hours following stimulation whereby oxygen is further reduced. However, less hypoxic cells would exhibit a double-peak of p53 following a relatively large drop in oxygen levels. This hypothesis could be tested experimentally using similar imaging techniques to those we used to record our single-cell HIF-1α dynamics. Indeed, there have already been published reports of a cell-line stably transfected with p53 fused to cyan fluorescent protein (Lahav, et al. 2004). Furthermore, this report measures the variation in peak number and amplitude of p53 following gamma irradiation and the mean number of peaks appeared to be dependent on the dose of irradiation. If this study were to be repeated with variations in oxygen signal, rather than gamma irradiation, using switches as suggested in Figure 5-18, our hypotheses could be tested experimentally.

Chapter 6

Discussion

The research in this thesis was initially motivated by experimental imaging data obtained at the University of Liverpool providing new information on the cellular hypoxic response. The dynamics of the master regulator of oxygen homeostasis, HIF-1α, were shown to display heterogeneous, transient accumulation after a rapid switch in oxygen conditions. These dynamics were distinct from previous population-level measurements of HIF-1α under these conditions. This was because the data was recorded at a very high temporal resolution using confocal microscopy and the single-cell nature of the experiments allowed for the discovery of fast transient peaks in HIF-1α levels that are not necessarily seen in multi-cell measurements. This new high-resolution, dynamic data motivated the formulation of a novel mathematical model capable of reproducing the observed dynamics by describing interactions of the HIF-1α signalling pathway. Supporting information was provided by additional experiments studying the dynamics of the oxygen degradation domain (ODD) of HIF-1α; the transcriptional activity of HIF-1α in hypoxia; and HIF-1α dynamics after re-oxygenation. These experiments supported the interesting transient responses found in the initial imaging experiments.

The nature of the dynamics in the single-cell data, in combination with biological knowledge of the HIF-1α signalling pathway, prompted a mathematical investigation based on an oxygen-dependent negative feedback loop. A minimal modelling approach was used for the preliminary mathematical models describing the feedback inhibition that exists between HIF-1α and PHD. The aim of this approach was to use the large quantity of detailed data in conjunction with a simple mathematical description in order to identify a core model mechanism that was flexible in order to re-produce the variety of observed dynamics but had limited degrees of freedom by reducing model parameters. This core mechanism, or network motif, was the single negative feedback loop between HIF-1α and PHD. The first model we studied consisted of just two ODEs and all pathway interactions were described using mass action laws. After unsatisfactory preliminary modelling we considered the introduction of a delay in the feedback effect of PHD based on qualitative analysis of the data. Negative feedback loops and delays in dynamical systems represent typical devices of generating oscillations (Goodwin 1965, Mahaffy and Pao 1984). Although we were not aiming to generate HIF-1α oscillations as such, we were trying to model fast transient peaks in HIF-1α levels based on a negative feedback loop. Consequently we devised several alternative simple negative feedback models inspired by the work of Geva-Zatorsky et al. on oscillations of the p53-Mdm2 system (Oscillations and variability in the p53 system 2006). After further analysis of the alternative models, a minimal feedback motif was identified and the 2-component mathematical model formulated.

Key to this early modelling work, in identifying the structure of the model, was the parameterisation achieved via data-fitting. The volume and detail of the single-cell data allowed us to place emphasis on this fitting aspect of model development compared to alternative modelling approaches where data, and thus model calibration, is relatively limited. As a consequence, we originally focused more on re-producing the dynamic features of the system well, rather than say including accurate physical

measurements. However, because we were optimising our parameter values to fit many different single-cell data we aimed to reduce the freedom and therefore avoid any extreme cell-to-cell variation in parameter values that might result from this approach. This was achieved through some sensible choices in initial parameter estimates pre-fitting and the identification of a distinctive subset of single-cell HIF-1α dynamics. This sub-set appeared to represent a group of more complex dynamics, characteristically displaying relatively large peaks of transient accumulation followed by a stable resolution of HIF-1α dynamics at low levels comparable to those in normoxia. Therefore initial parameter optimisation was conducted based on these bell-shaped data in order to identify a localised region of parameter space. We then aimed to fit the rest of the data, including re-oxygenation data, by remaining within this region of parameter space.

The main result of Chapter 2 is the development of a core feedback motif that can re-produce the single-cell HIF-1α dynamics observed experimentally. Furthermore the motif is simple and these flexible dynamics are achieved by varying only a few parameters in a constrained manner. The relative success of this simple structure was measured using our own device, the *Error Envelope*, with a successful fitting rate of 77%. A greater success rate may have been achieved with a more complex model or more freedom in parameter variation but this result provided a strong case for a foundation model that could be relied upon to produce characteristic HIF-1α dynamics under relatively strict conditions.

The simple yet strong 2-component model description stimulated the conduction of more experiments within the HIF-1α signalling pathway and an extensive literature search to make the model more comparable to actual biology. That is, with more complexity and accurate parameter values that represent real rates. Although the minimal 2-component model used biological data as the chief motivation and driving force for parameterisation, the framework of this malleable system was theoretically driven. When we decided to increase the complexity of the model based upon the 2-component motif, this was done to be more representative of the extended biology pathway rather than to try and increase our *Error Envelope* success rate.

Increased model complexity was introduced by making a distinction between the three different isoforms of PHD in the model resulting in an expansion to four ODEs. This expansion allowed for the inclusion of experimental measurements that distinguish different PHD isoforms and crucially, allows us to investigate their individual roles. The parameterisation of the 4-component model was based on a representative single-cell response of HIF-1α dynamics to oxygen-switching, defined with the 2-component model. Parameters that could not be identified by our previous modelling work, new experiments or literature review were found by calibration with this representative response. Validation of the finalised model format was carried out by comparing with experimental results.

Different dynamic oxygen signatures and other perturbations of the system such as PHD silencing were performed both experimentally and in the mathematical model numerically.

The silencing of PHD2 in the model caused an increase in levels of HIF-1α in both normoxia and hypoxia and the removal of this key feedback component lessened the overshoot nature of the transient dynamics following hypoxic induction. These results compare favourably with the literature and our own experiments. The model output of re-oxygenation simulations without PHD2 compared very well with our experimental data showing a 50% decrease in HIF-1α levels over the first 2 hours following stimulation. By varying the oxygen signal input of the model we were able to make certain predictions of HIF-1α pathway behaviour. For example, the heterogeneity in single-cell HIF-1α peak dynamics may be a result of graded oxygen signals. That is, when the oxygen signal is supplied less rapidly to the system. An explicit mechanism for this is not yet incorporated into the model but it could be that competition for oxygen within cells for example leads to different hypoxic-switch gradients. We also investigated oxygen pulsing as a method of signal manipulation that can generate different HIF-1α dynamics. Different hypoxic pulse signatures can generate more spiky oscillations for example, such as those dynamics typically seen in neural activity. Altering these oxygen signals can also affect the threshold induction of HIF-1α and the PHDs (as we also investigated in Chapter 4) and these results can qualitatively change when we silence PHD2.

The applications of this model have a much more general use than just the study of the hypoxic response. In the generalised case, this mathematical model represents the evolution of a transcription factor that is predisposed to rapidly accumulate in an overshoot fashion, as the result of an acute change in signal. This qualitative overshoot characteristic may be lost in multi-cell environments or at least the rapidity of the peak transiency may be hidden among cells responding at slightly different times or at different gradients. Furthermore, these dynamics may be ignored completely in some signalling pathway models, especially if the transcription factor is an intermediate part in a long chain or the timescale of the phenomenon being studied is sufficiently separated from the transcription factor dynamics. These oversights could potentially result in the loss of any feedback information that propagates from these dynamics. This propagation could be in the form of downstream effects, which for transcription factors means target gene regulation. This HIF-1α model is also useful in a general sense as it includes the description of target genes that have similar roles (negative feedback) but tend to respond at different rates. The studies of this research thesis could potentially be applicable to other transcription factors that share transient dynamics as a result of acute signal changes and regulate the transcription of differently responding target genes.

The 4-component model would be improved by identifying the source of heterogeneity in the observed single-cell HIF-1α dynamics. This then needs to be translated to parameter values or new functional forms within the model, possibly in the form of stochasticity as discussed in section 3.6.2.

Further applications of this model within this thesis consider the more generalised overshoot dynamic response in cellular HIF-1α levels when a rapid oxygen switch is introduced to the system. However, we maintain that the core motif is flexible and capable of producing a variety of single-cell HIF-1α dynamics and as such is suitable for further study to re-visit this heterogeneity aspect in the future.

As part of the analysis of the 4-component model of the HIF-1α signalling pathway, different oxygen dynamics were supplied to the system. Variation in oxygen signals is a plausible way of generating heterogeneous HIF-1α dynamics and the rapid overshoot response characteristic in rapid hypoxic induction is not seen when the gradient of the oxygen switch is sufficiently reduced. A physiologically important example of hypoxia and dynamic oxygen variation is found in the growth of solid tumours. Specifically, avascular tumours exhibit a range of oxygen tensions and notably hypoxic cores due to the rapid proliferation of cancerous cells. Consequently HIF-1α is heavily implicated in the development of cancer (Powis and Kirkpatrick, Hypoxia inducible factor-1alpha as a cancer drug target 2004). To provide biologically relevant oxygen signals for our HIF-1α model we developed a simple diffusion-based model of oxygen dynamics in a tumour sphere. This model was parameterised using steady state data of oxygen-level distributions throughout neurospheres, data collected from experiments performed as part of a collaborative study between the University of Liverpool and University College Cork. The spatio-temporal oxygen diffusion model was also validated by comparing diffusion rate predictions with measured values (Schmidt-Nielsen 1997).

Our oxygen model was coupled to the HIF-1α model such that we could study the effects of different oxygen signals on HIF-1α dynamics within the physical setting of a sphere of respiring cells. When choosing a biologically feasible setting, the external oxygen range and relatively small sphere sizes resulted in oxygen steady states that were reached relatively fast following an oxygen switch at the boundary. This caused the oxygen switch to be rapid for HIF-1α dynamics in all regions/cells constituting the tumour sphere. However, the magnitude of the switch was more variable. At the boundary a much more severe oxygen switch would be experienced, with respect to the difference in steady state oxygen values, when compared to the sphere core. As a result the transient overshoot HIF-1α dynamics, seen in rapid acute oxygen switches, occur to a greater extent at the sphere border than the core. Consequently it is possible that, for a temporary period, HIF-1α levels are at a much higher concentration towards the sphere border than in the sphere core. This occurs despite the fact that there is less oxygen in the sphere core. This result is biologically interesting as it hints at a potential mechanism for manipulating the signalling pathway to deliver a stronger hypoxic response (HIF-1α activity) in less hypoxic cellular regions. This manipulation could take the form of a specific oxygen signal while the response of interest might be governed by a downstream target gene. This was studied in Chapter 4 by investigating the dynamics of PHDs 2&3 and different external oxygen signals, particularly hypoxic pulsing. For example, thresholds are generally important in downstream gene expression to determine if certain processes are initiated (e.g. pattern formation in chemotaxis).

Oxygen pulsing may represent a method of repressing slow, unwanted target gene expression in certain regions of a sphere whilst maintaining fast desirable target genes. It is a simplistic example but highlights the potential consequences of a transcription factor overshoot mechanism that is dependent on the signal switch, and specifically the severity of that switch.

To further investigate the consequences of the characteristic transient response of HIF-1α to acute hypoxic shock, we considered introducing HIF-1α to models of other cellular processes that contained an element of oxygen dependence. In Chapter 5 two processes in particular were identified as oxygen-sensitive and potentially sensitive to HIF-1α activity: the cell cycle and the apoptosis pathway. After searching the literature, it was found that HIF-1α dependence could be incorporated into models of these processes, although there were no models that currently described the coupled effects of transient HIF-1α.

Modification of an existing oxygen-dependent cell cycle model (Alarcón, Byrne and Maini 2004) and explicit inclusion of the HIF-1α pathway dynamics of our model aimed to investigate the effects of HIF-1α on hypoxic cell-cycle arrest. Specifically, transient dynamic HIF-1α was compared to steady state levels of HIF-1α for different values of oxygen to highlight the potential missed information from neglecting intermediate transcription factor dynamics. Due to the timescales involved it was only the cell cycle in which the hypoxic switch occurred that was affected at all by the introduction of dynamic HIF-1α. That is, HIF-1α levels would reach or be close to steady state within one cell cycle. The model coupling did not yield significant differences (the additional intermediate cell cycle extension caused by dynamic HIF-1α was no more than 10%) but it was difficult to ascertain whether or not this was due to certain weaknesses in the original cell-cycle model.

The apoptosis pathway is largely governed by the well-studied transcription factor p53. There have been many studies that link HIF-1α and p53 directly or indirectly but the exact nature of the relationship between the two remains unclear. Hypoxia clearly affects the stress response system involving p53 and its key regulator Mdm2, and so we chose a relevant model of p53 dynamics that incorporated oxygen dependence (Hunziker, Jensen and Krishna 2010). We stimulated the coupled HIF-1α-p53 model with oxygen dynamics generated by our oxygen-diffusion tumour model to investigate how p53 dynamics vary within this type of physical setting. The introduction of dynamic HIF-1α when compared with steady state HIF-1α (although dependent on oxygen) is striking. For the physical parameters used (i.e. sphere size and signal switch) a large distinction emerged between p53 dynamics near the sphere boundary and p53 dynamics near the core as with HIF-1α. However, unlike HIF-1α this distinction appeared to be discretely separated into two, especially with respect to secondary and tertiary peaks of p53 oscillations. The introduction of dynamic HIF-1α appears to generate a bimodal distinction in the secondary p53 peaks. We hypothesise that this results in a much

higher incidence of apoptosis for cells within an outer layer of the model sphere, the width of which is determined by HIF-1α dynamics.

The latter results in this thesis highlight the fact that even in apparently well parameterised mathematical models the simple introduction of a new system-component or the modification of inputs can have greater downstream implications than may be immediately obvious. Consequently, the danger of over-simplifying models is emphasised as certain omissions of model variables could result in different conclusions when models are being used as a predictive tool. In contrast, the value of minimal models was stressed from the outset of this research; especially when certain data and knowledge is absent, to avoid over-fitting systems and producing unreliable results caused by too many degrees of freedom. Moreover, used correctly model reduction is a very useful tool that can help us understand underlying model mechanisms and garner an intuition for the intricacies of the phenomenon being studied. Overall, it is clear that there must be a delicate balance between model complexity, including a lot but understanding little; and model simplicity, more suitable to analysis but limited and prone to oversights. In my opinion, the systems biology philosophy appears to favour the simple model approach, focusing on general model features and worrying less about the exact replication of a particular measurement. The challenging part of this holistic viewpoint is deciding what to throw out at the first stage of model conception. This almost always depends on what property in particular is of most interest to the scientist, especially in cell biology where so many systems cannot be isolated satisfactorily to a neat, sequestered pathway. As a result, the development process of modelling a phenomenon is steeped in bias which is why there are so many apparent different models for the same system, often with very different assumptions and conclusions: they were designed with different intentions in mind at the start. I take the view that the progression of the modelling of these systems is an evolutionary process and initial diversity should be embraced. The strongest models exchange information and adapt to survive, with model offspring that possess those valuable traits of their ancestors; while the weakest ones fail to pass on their undesirable features which are lost.

Bibliography

Abramowitz, Milton, and Irene A Stegun. *Handbook of Mathematical Functions with Formulas, Graphs, and Mathematical Tables.* New York: Dover Publications, 1964.

Alarcón, T, H M Byrne, and P K Maini. "A mathematical model of the effects of hypoxia on the cell-cycle of normal and cancer cells." *Journal of theoretical Biology* 229 (2004): 395-411.

Alberts, B, A Johnson, J Lewis, M Raff, K Roberts, and P Walter. *Molecular Biology of the Cell.* 4th. New York: Garland Science, 2002.

Alon, U. *An Introduction to Systems Biology: Design Principles of Biological Circuits.* 1. Chapman & Hall/CRC, , 2006.

Al-Quobaili, F, and M Montenarh. "Pancreatic duodenal homeobox factor-1 and diabetes mellitus type 2." *Int J Mol Med* 21 (2008): 399–404.

Amaral, J D, J M Xavier, C J Steer, and C M Rodrigues. "The role of p53 in apoptosis." *Discov Med.* 9, no. 45 (2010): 145-52.

An, W G, M Kanekal, M C Simon, E Maltepe, M V Blagosklonny, and L M Neckers. "Stabilization of wild-type p53 by hypoxia-inducible factor 1alpha." *Nature.* 392, no. 6674 (1998): 405-8.

Appelhoff, RJ, et al. "Differential function of the prolyl hydroxylases PHD1, PHD2, and PHD3 in the regulation of hypoxia-inducible factor." *J Biol Chem 279*, 2004: 38458–38465.

Ashall, L, et al. "Pulsatile Stimulation Determines Timing and Specificity of NF-kappa B-Dependent Transcription." *Science 324*, 2009: 242-246.

Bagnall, J, et al. "Tight control of Hypoxia Inducible Factor (HIF)-alpha transient dynamics is essential for cell survival in hypoxia." *J. Biol. Chem.(SUBMITTED)*, 2013.

Berra, E, E Benizri, A Ginouvès, V Volmat, D Roux, and J Pouysségur. "HIF prolyl hydroxylase 2 is the key oxygen sensor setting low steady-state levels of HIF-1alpha in normoxia." *EMBO Journal 22*, 2003: 4082-4090.

Box, A H, and D J Demetrick. "Cell cycle kinase inhibitor expression and hypoxia-induced cell cycle arrest in human cancer cell lines." *Carcinogenesis* 25 (2004): 2325-35.

Britton, N F. *Essential Mathematical Biology.* Springer, 2003.

Bruning, U, L Cerone, Z Neufeld, S Fitzpatrick, and A Cheong. "MicroRNA-155 promotes resolution of hypoxia-inducible factor 1alpha activity during prolonged hypoxia." *Mol Cell Biol* 31 (2011): 4087–4096.

Carmeliet, P, et al. "Role of HIF-1alpha in hypoxia-mediated apoptosis, cell proliferation and tumour angiogenesis." *Nature* 394 (1998): 485-90.

Chávez, J C, F Agani, P Pichiule, and J C LaManna. "Expression of hypoxia-inducible factor-1alpha in the brain of rats during chronic hypoxia." *J Appl Physiol.* 89 (2000): 1937-42.

Chaplain, M A J. “Avascular growth, angiogenesis and vascular growth in solid tumours: The mathematical modelling of the stages of tumour development.” *Mathematical and Computer Modelling* 23 (1996): 47-87.

Chen, D, M Li, J Luo, and W Gu. “Direct interactions between HIF-1 alpha and Mdm2 modulate p53 function.” *J Biol Chem.* 278, no. 16 (2003): 13595-8.

Cherry, J L, and F R Adler. “How to make a biological switch.” *J Theor Biol.* 203, no. 2 (2000): 117-33.

Dayan, F, M Monticelli, J Pouyssegur, and E Pecou. “Gene regulation in response to graded hypoxia: The non-redundant roles of the oxygen sensors PHD and FIH in the HIF pathway.” *Journal of Theoretical Biology 259*, 2009: 304-316.

Edelstein-Keshet, L. *Mathematical Models in Biology.* Philadelphia: Society for Industrial and Applied Mathematics, 2005.

Edwards, L M, and I Thiele. “Applying systems biology methods to the study of human physiology in extreme environments.” *Extrem Physiol Med. Mar 22;():8. doi: 10.1186/2046-7648-2-8.* 2, no. 1 (2013).

Epstein, A C, et al. “C. elegans EGL-9 and mammalian homologs define a family of dioxygenases that regulate HIF by prolyl hydroxylation.” *Cell.* 107, no. 1 (2001): 43-54.

Fercher, A, G V Ponomarev, D Yashunski, and D Papkovsky. “Evaluation of the derivates of phosphorescent Pt-coproporphyrin as intracellular oxygen-sensitive probes.” *Anal Bioanal Chem* 396 (2010a): 1793–1803.

Fercher, A, S M Borisov, A V Zhdanov, I Klimant, and D B Papkovsky. “Intracellular O2 sensing probe based on cell-penetrating phosphorescent nanoparticles.” *ACS Nano.* 5, no. 7 (2011): 5499-508.

Fercher, A, T C O'Riordan, A V Zhdanov, R I Dmitriev, and D B Papkovsky. *Imaging of cellular oxygen and analysis of metabolic responses of mammalian cells.* Vol. 591, in *Live Cell Imaging*, edited by D B Papkovsky, 257-73. Humana Press, 2010b.

Folkman, J, and M Hochberg. “Self-regulation of growth in three dimensions.” *J Exp Med.* 138 (1973): 745-53.

Gardner, L B, Q Li, M S Park, W M Flanagan, G L Semenza, and C V Dang. “Hypoxia inhibits G-1/S transition through regulation of p27 expression.” *J Biol Chem 276*, 2001: 7919-7926.

Gérard, C, and A Goldbeter. “Temporal self-organization of the cyclin/Cdk network driving the mammalian cell cycle.” *Proc Natl Acad Sci U S A.* 106, no. 51 (2009): 21643-8.

Geva-Zatorsky, N, et al. “Oscillations and variability in the p53 system.” *Molecular Systems Biology 2*, 2006.

Goda, N, H E Ryan, B Khadivi, W McNulty, R C Rickert, and R S Johnson. “Hypoxia-inducible factor 1alpha is essential for cell cycle arrest during hypoxia.” *Mol Cell Biol.* 23 (2003): 359–69.

Goda, N, S J Dozier, and R S Johnson. “HIF-1 in cell cycle regulation, apoptosis, and tumor progression.” *Antioxid Redox Signal.* 5, no. 4 (2003): 467-73.

Goldbeter, A. “Zero-order switches and developmental thresholds.” *Mol Syst Biol.*, 2005.

Goodwin, B C. “Oscillatory behavior in enzymatic control processes.” *Adv Enzyme Regul.* 3 (1965): 425-38.

Graeber, T G, J F Peterson, M Tsai, K Monica, A J Fornace Jr, and A J Giaccia. “Hypoxia induces accumulation of p53 protein, but activation of a G1-phase checkpoint by low-oxygen conditions is independent of p53 status.” *Mol Cell Biol.* 14, no. 9 (1994): 6264-77.

Greijer, A E, and E van der Wall. “The role of hypoxia inducible factor 1 (HIF-1) in hypoxia induced apoptosis.” *J Clin Pathol.* 57, no. 10 (2004): 1009-14.

Hammond, E M, and A J Giaccia. “The role of p53 in hypoxia-induced apoptosis.” *Biochem Biophys Res Commun.* 331, no. 3 (2005): 718-25.

Hammond, E M, M J Dorie, and A J Giaccia. “ATR/ATM targets are phosphorylated by ATR in response to hypoxia and ATM in response to reoxygenation.” *J Biol Chem.* 278, no. 14 (2003): 12207-13.

Hansson, L O, A Friedler, S Freund, S Rüdiger, and A R Fersht. “Two sequence motifs from HIF-1α bind to the DNA-binding site of p53.” *Proc Natl Acad Sci U S A.* 99, no. 16 (2002): 10305–10309.

Haupt, S, M Berger, Z Goldberg, and Y Haupt. “Apoptosis - the p53 network.” *J Cell Sci.* 116 (2003): 4077-85.

Henze, A T, et al. “Prolyl hydroxylases 2 and 3 act in gliomas as protective negative feedback regulators of hypoxia-inducible factors.” *Cancer Res.* 70, no. 1 (2010): 357-66.

Horrée, N, E H Gort, P van der Groep, A P Heintz, M Vooijs, and P J van Diest. “Hypoxia-inducible factor 1 alpha is essential for hypoxic p27 induction in endometrioid endometrial carcinoma.” *J Pathol.* 214 (2008): 38-45.

Hsieh, M M, et al. “HIF prolyl hydroxylase inhibition results in endogenous erythropoietin induction, erythrocytosis, and modest fetal hemoglobin expression in rhesus macaques.” *Blood* 110 (2007): 2140-2147.

Huang, J, Q Zhao, S M Mooney, and F S Lee. “Sequence determinants in hypoxia-inducible factor-1alpha for hydroxylation by the prolyl hydroxylases PHD1, PHD2, and PHD3.” *J Biol Chem* 277 (2002): 39792–39800.

Hunziker, A, M H Jensen, and S Krishna. “Stress-specific response of the p53-Mdm2 feedback loop.” *BMC Syst Biol.* 4, no. 94 (2010).

Jiang, B H, G L Semenza, C Bauer, and H H Marti. “Hypoxia-inducible factor 1 levels vary exponentially over a physiologically relevant range of O2 tension.” *Am J Physiol* 271 (1996): 1172-80.

Ke, Q, and M Costa. “Hypoxia-inducible factor-1 (HIF-1).” *Mol Pharmacol.* 70 (2006): 1469-80.

Kitano, H. “Systems biology: a brief overview.” *Science.* 295, no. 5560 (2002): 1662-4.

Koch, C J, J Kruuv, H E Frey, and R A Snyder. “Plateau phase in growth induced by hypoxia.” *Int J Radiat Biol Relat Stud Phys Chem Med.* 23 (1973): 67-74.

Kohn, K W, J Riss, O Aprelikova, J N Weinstein, Y Pommier, and J C Barrett. “Properties of switch-like bioregulatory networks studied by simulation of the hypoxia response control system.” *Molecular Biology of the Cell* 15 (2004): 3042-3052.

Konopka, A K. *Systems Biology: Principles, Methods, and Concepts.* Boca Raton, FL: CRC Press, 2007.

Koumenis, C, et al. “Regulation of p53 by hypoxia: dissociation of transcriptional repression and apoptosis from p53-dependent transactivation.” *Mol Cell Biol.* 21, no. 4 (2001): 1297-310.

Krishna, S, M H Jensen, and K Sneppen. “Minimal model of spiky oscillations in NF-kappaB signaling.” *Proc Natl Acad Sci U S A.* 103, no. 29 (2006): 10840-5.

Kunze, R, W Zhou, R Veltkamp, B Wielockx, G Breier, and H H Marti. “Neuron-specific prolyl-4-hydroxylase domain 2 knockout reduces brain injury after transient cerebral ischemia.” *Stroke* 43 (2012): 2748-56.

Löffler, M, S Postius, and F Schneider. “Anaerobiosis and oxygen recovery: Changes in cell cycle distribution of ehrlich ascites tumor cells grown in vitro.” *Virchows Archiv B* 26 (1978): 359-368.

Lagarias, J C, J A Reeds, M H Wright, and P E Wright. “Convergence Properties of the Nelder-Mead Simplex Method in Low Dimensions.” *SIAM J. Optim.* 9 (1998): 112-147.

Lahav, G, et al. “Dynamics of the p53-Mdm2 feedback loop in individual cells.” *Nat Genet.* , 2004: 147-50.

Latchman, D S. “Transcription-factor mutations and disease.” *N. Engl. J. Med* 334 (1996): 28–33.

Lee, J W, S H Bae, J W Jeong, S H Kim, and K W Kim. “Hypoxia-inducible factor (HIF-1)alpha: its protein stability and biological functions.” *Experimental and Molecular Medicine* 36 (2004): 1-12.

Leek, R D, I Stratford, and A L Harris. “The role of hypoxia-inducible factor-1 in three-dimensional tumor growth, apoptosis, and regulation by the insulin-signaling pathway.” *Cancer Res.* 65, no. 10 (2005): 4147-52.

Leshem, Y, and O Halevy. “Phosphorylation of pRb is required for HGF-induced muscle cell proliferation and is p27kip1-dependent.” *J Cell Physiol.* 191 (2002): 173-82.

Levine, A J. “p53, the cellular gatekeeper for growth and division.” *Cell.* 88, no. 3 (1997): 323-31.

Liu, W, S M Shen, X Y Zhao, and G Q Chen. “Targeted genes and interacting proteins of hypoxia inducible factor-1.” *Int J Biochem Mol Biol.* 3, no. 2 (2012): 165–178.

Ma, L, J Wagner, J J Rice, W Hu, A J Levine, and G A Stolovitzky. “A plausible model for the digital response of p53 to DNA damage.” *Proc Natl Acad Sci U S A.* 102, no. 40 (2005): 14266–14271.

Mahaffy, J M, and C V Pao. “Models of genetic control by repression with time delays and spatial effects.” *J Math Biol.* 20, no. 1 (1984): 39-57.

Martins, M L, S C Ferreira Jr., and M J Vilela. “Multiscale models for the growth of avascular tumors.” *Phys. Life Rev.* 4, no. 2 (2007): 128-156.

Metzen, E, D P Stiehl, K Doege, J H Marxsen, T Hellwig-Burgel, and W Jelkmann. “Regulation of the prolyl hydroxylase domain protein 2 (phd2/egln-1) gene: identification of a functional hypoxia-responsive element.” *Biochemical Journal* 387 (2005): 7.

Minamishima, Y A, J Moslehi, R F Padera, R T Bronson, R Liao, and W G Kaelin Jr. “A feedback loop involving the Phd3 prolyl hydroxylase tunes the mammalian hypoxic response in vivo.” *Mol Cell Biol.* 29, no. 21 (2009): 5729-41.

Mitchison, J M. *The Biology of the Cell Cycle.* London: Cambridge University Press, 1971.

Murray, J D. *Mathematical Biology: I. An Introduction (Interdisciplinary Applied Mathematics) (Pt. 1).* 3rd. Springer, 2001.

Nelder, J A, and R Mead. “A Simplex Method for Function Minimization.” *The Computer Journal* 7 (1965): 308–313.

Nelson, D E, V Sée, G Nelson, and M R White. “Oscillations in transcription factor dynamics: a new way to control gene expression.” *Biochem Soc Trans. Dec;( ):.* 32, no. Pt 6 (2004): 1090-2.

Nieminen, A L, S Qanungo, E A Schneider, B H Jiang, and F H Agani. “Mdm2 and HIF-1alpha interaction in tumor cells during hypoxia.” *J Cell Physiol.* 204, no. 2 (2005): 364-9.

Novák, B, and J J Tyson. “A model for restriction point control of the mammalian cell cycle.” *J Theor Biol.* 230, no. 4 (2004): 563-79.

Owen, M R, T Alarcón, P K Maini, and H M Byrne. “Angiogenesis and vascular remodelling in normal and cancerous tissues.” *J Math Biol.* 58 (2009): 689-721.

Palsson, B O. *Systems biology: properties of reconstructed networks.* New York: Cambridge University Press, 2006.

Paszek, P, et al. “Population robustness arising from cellular heterogeneity.” *Proc Natl Acad Sci U S A* 107 (2010): 11644-9.

Pellegrin, P, A Fernandez, N J Lamb, and R Bennes. “Macromolecular uptake is a spontaneous event during mitosis in cultured fibroblasts: implications for vector-dependent plasmid transfection.” *Mol Biol Cell* 13 (2002): 570-578.

Polking, J C. *dfield and pplane.* 2002. http://math.rice.edu/~dfield/dfpp.html (accessed June 28, 2013).

Powis, G, and L Kirkpatrick. “Hypoxia inducible factor-1alpha as a cancer drug target.” *Mol Cancer Ther.* 3 (2004): 647-54.

Powis, G, and L Kirkpatrick. “Hypoxia inducible factor-1alpha as a cancer drug target.” *Mol Cancer Ther.* 3 (2004): 647-54.

Qu, Z, J N Weiss, and W R MacLellan. “Regulation of the mammalian cell cycle: a model of the G1-to-S transition.” *Am J Physiol Cell Physiol.* 284, no. 2 (2003): 349-64.

Qutub, A A, and A S Popel. “A computational model of intracellular oxygen sensing by hypoxia-inducible factor HIF1 alpha.” *J Cell Sci.* 119 (2006): 3467-80.

Ravi, R, et al. “Regulation of tumor angiogenesis by p53-induced degradation of hypoxia-inducible factor 1alpha.” *Genes Dev.* 14, no. 1 (2000): 34-44.

Reynolds, T Y, S Rockwell, and P M Glazer. “Genetic instability induced by the tumor microenvironment.” *Cancer Res.* 56, no. 24 (1996): 5754-7.

Rieger, T R, R I Morimoto, and V Hatzimanikatis. “Bistability explains threshold phenomena in protein aggregation both in vitro and in vivo.” *Biophys J* 90 (2006): 886–895.

Rigoutsos, I, and G Stephanopoulos. *Systems Biology: Volume II: Networks, Models, and Applications.* New York: Oxford University Press, 2007.

Roose, T, S J Chapman, and P K Maini. “Mathematical models of avascular tumor growth.” *SIAM Review* 49, no. 2 (2007): 179–208.

Saraste, A, and K Pulkki. “Morphologic and biochemical hallmarks of apoptosis.” *Cardiovasc Res.* 45, no. 3 (2000): 528-37.

Schmidt-Nielsen, Knut. *Animal physiology: adaptation and environment.* Cambridge University Press, 1997.

Schmierer, B, B Novák, and C J Schofield. “Hypoxia-dependent sequestration of an oxygen sensor by a widespread structural motif can shape the hypoxic response--a predictive kinetic model.” *BMC Syst Biol.* 4, no. 139 (2010).

Semenza, G L. “HIF-1 and human disease: one highly involved factor.” *Genes & Development* 14 (2000): 1983-1991.

Semenza, G L. “HIF-1 and mechanisms of hypoxia sensing.” *Current Opinion in Cell Biology* 13 (2001): 167-171.

Semenza, G L. “Hydroxylation of HIF-1: oxygen sensing at the molecular level.” *Physiology (Bethesda)* 19 (2004): 176-82.

Smith, T G, P A Robbins, and P J Ratcliffe. “The human side of hypoxia-inducible factor.” *Br J Haematol* 141, no. 3 (2008): 325–334.

Stiehl, D.P., R. Wirthner, J. Koditz, P. Spielmann, G. Camenisch, and R.H. Wenger. “Increased prolyl 4-hydroxylase domain proteins compensate for decreased oxygen levels - Evidence for an autoregulatory oxygen-sensing system.” *Journal of Biological Chemistry* 281 (2006): 23482-23491.

Swat, M, A Kel, and H Herzel. “Bifurcation analysis of the regulatory modules of the mammalian G1/S transition.” *Bioinformatics.* 20, no. 10 (2004): 1506-11.

Tuckerman, J R, et al. “Determination and comparison of specific activity of the HIF-prolyl hydroxylases.” *FEBS Lett.* 576 (2004): 145–150.

Tyson, J J, and B Novak. “Regulation of the eukariotic cell-cyclemolecular antagonism, hysteresis, and irreversible transitions.” *J. Theor. Biol.* 210 (2001): 249–263.

van Uden, P, NS Kenneth, and S Rocha. “Regulation of hypoxia-inducible factor-1alpha by NF-kappaB.” *Biochem J 412*, 2008: 477–484.

Wang, G, R Reisdorph, R E Jr. Clark, R Miskimins, R Lindahl, and W K Miskimins. “Cyclin dependent kinase inhibitor p27(Kip1) is upregulated by hypoxia via an ARNT dependent pathway.” *J Cell Biochem.* 90, no. 3 (2003): 548-60.

Wang, Y V, M Wade, E Wong, Y C Li, L W Rodewald, and G M Wahl. “Quantitative analyses reveal the importance of regulated Hdmx degradation for p53 activation.” *Proc Natl Acad Sci U S A.* 104, no. 30 (2007): 12365-70.

Wykoff, C C, C W Pugh, P H Maxwell, A L Harris, and P J Ratcliffe. “Identification of novel hypoxia dependent and independent target genes of the von Hippel-Lindau (VHL) tumour suppressor by mRNA differential expression profiling.” *Oncogene* 19 (2000): 6297-305.

Zimmermann, K C, and D R Green. “How cells die: apoptosis pathways.” *J Allergy Clin Immunol.* 108 (2001): S99-103.

Chapter 7

Appendix

7.1 'fminsearch': a MATLAB function based upon the Nelder-Mead Simplex Algorithm

'*fminsearch'* is a minimisation function found in the numerical computing programme, MATLAB. *fminsearch* attempts to find a minimum of an unconstrained multivariable function using function evaluations starting at an initial estimate. To do this, *fminsearch* uses the Nelder-Mead simplex algorithm, a direct search method (no derivative information), for multidimensional unconstrained minimisation (Nelder and Mead 1965, Lagarias, et al. 1998). This algorithm uses a simplex: a geometrical figure consisting of a convex hull of $n+1$ points in n-dimensions (representing the n independent variables of the function) and all their interconnecting edges, faces etc. A simplex is represented as a triangle in two dimensions and a tetrahedron in three dimensions. At each step of the method, a non-degenerate simplex is maintained, i.e. simplexes that enclose a finite n-dimensional volume. If one point is defined as the origin, the other n points define vectors that span the *n*-dimensional space.

The algorithm starts by first making a simplex around the initial estimate (of length n), x_{init}, by adding 5% of each component, $x_{init}(i)$, to the point x_{init} , making n more points. These n vectors and x_{init} make up the initial simplex. If $x_{init}(i) = 0$, then 0.00025 is used as the i-th component. The simplex is then repeatedly modified according to the following series of steps in order to converge on a minimum of the function of interest. The steps are repeated until the simplex has a diameter less than the specified tolerance.

7.1.1 The Algorithm (one iteration)

- Let x_i denote the list of points in the current simplex with $i = 1, \ldots, n+1$.
- ORDER the points of the simplex according to the value of the function, $f_i = f(x_i)$ say, at that point from lowest to highest, i.e. for $f_1 \leq f_2 \leq \ldots \leq f_n \leq f_{n+1}$, the points are ordered $x_1, x_2, \ldots, x_n, x_{n+1}$.

  In each iteration either:

  (1) A new vertex replaces the current worst point x_{n+1}, or

  (2) n new points form a new simplex along with the current best point x_1.
- Calculate the REFLECTED point, $r = 2m - x_{n+1}$, where $m = \Sigma x_i/n\,, i = 1, \ldots, n$ (the centroid of the remaining points $x_1, \ldots, x_n$). Then calculate $f(r)$.
- If $f_1 \leq f(r) < f_n$, accept r and terminate the iteration. REFLECT
- If $f(r) < f_1$, calculate the EXPANSION point, $s = m + 2(m - x_{n+1})$, and calculate $f(s)$.

  (a) If $f(s) < f(r)$, accept s and terminate the iteration. EXPAND

(b) Otherwise, accept r and terminate the iteration. REFLECT

- If $f(r) \geq f_n$, perform a CONTRACTION between the better of x_{n+1} and r:
  (a) If $f(r) < f_{n+1}$, calculate $c = m + (r - m)/2$ and calculate $f(c)$. If $(c) < f(r)$, accept c and terminate the iteration. CONTRACT OUTSIDE Otherwise; continue with the next step (bullet point).
  (b) If $f(r) \geq f_{n+1}$, calculate $cc = m + (x_{n+1} - m)/2$ and calculate $f(cc)$. If $(cc) < f(r)$, accept cc and terminate the iteration. CONTRACT INSIDE Otherwise; continue with the next step (bullet point).
- Calculate the n points, $v_i = x_1 + (x_i - x_1)/2$, and calculate $f(v_i)$ for $i = 2, \ldots, n + 1$. The simplex at the next iteration is then made up of the points $x_1, v_2, \ldots, v_{n+1}$. SHRINK

Iterations stop after a termination criterion has been met. These can be specified by a vector difference tolerance, in x, or a function value difference tolerance, in f, between iterations. (The *fminsearch* default magnitude for both is 1×10^{-4}).

7.2 The Error Envelope

In Chapter 2 we categorised fits found using both the free-optimisation method for the bell-shaped data and the constrained-optimisation method for the entire data by developing a systematic formula that defines an '*Error Envelope*' (see Figure 7-1). The *Error Envelope* is made up of an upper and lower bound defined by:

$$\mathrm{EXP}(t) \pm \beta\big(\max\big(\mathrm{EXP}(t)\big) - \min\big(\mathrm{EXP}(t)\big)\big) \tag{7.1}$$

Where $\mathrm{EXP}(t)$ represents the time-series vector of experimental data and β defines the width of the envelope. This was implemented in order to compare more usefully the effect of constraining the parameter optimisation process during data-fitting. A solution curve that fits within the bounds of the envelope is classified as a '*Good Fit*' and those that lie without are '*Bad Fits'*. The constraint was relaxed slightly so that if the curve is classified as a *Bad Fit*, but less than $\lceil 0.01\times\mathrm{length}(\mathrm{EXP}(t))\rceil$ points of the ODE solution lie outside the envelope, it is re-classified as a *Good Fit*. This relaxed constraint was introduced after scrutinising the error envelope results visually. The original formula seemed too strict for some cases when only one or two points lay outside the envelope (the resolution of the data is of the order of a hundred points so the correction term only amounts to the admission of one or two points). It was felt that a combination of a narrow envelope with 1% points allowed outside was preferable to a wider envelope.

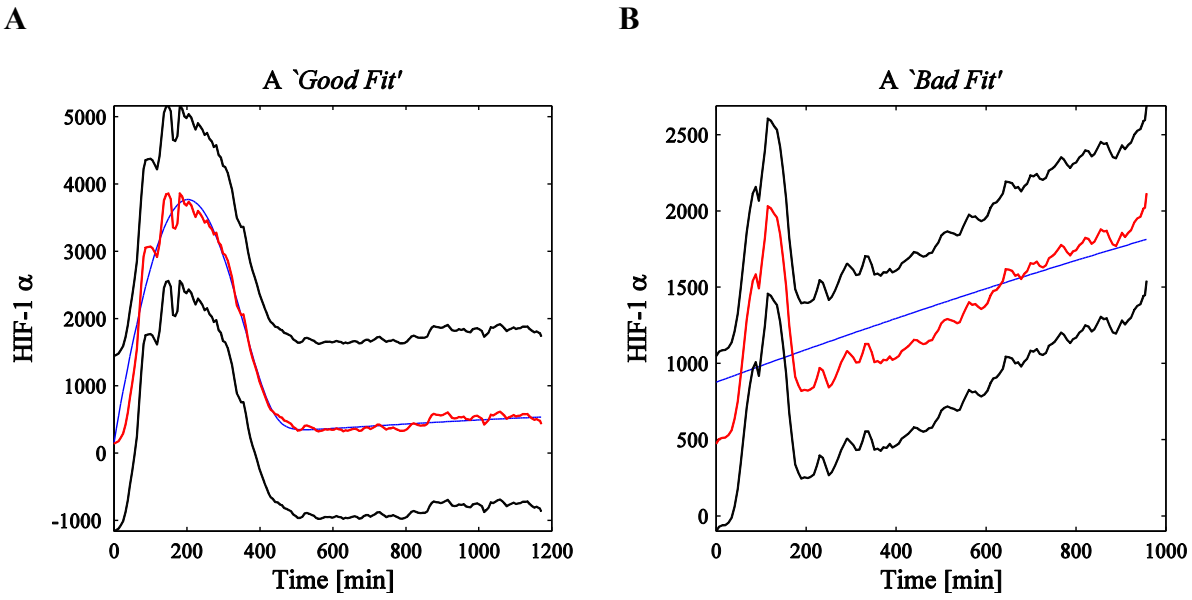

Figure 7-1: An example of a *Good Fit* (A) and a *Bad Fit* (B) as defined by the *Error Envelope* formula (7.1). The figure visually represents the envelope, a measure of error allowed to the best-fit given by our HIF-1α model such that we still classify it as a 'good/successful' representation of the dynamics observed experimentally. Plots show the optimised ODE solution-curve x representing HIF-1α (blue); the experimental single-cell HIF-1α data (red); and the upper and lower bounds of the *Error Envelope* (black). The width used in the envelope is $\beta = 0.35$ from the formula.

7.3 Linear Stability Analysis of the 4-component Model

In Chapter 3 we developed the following 4-component model of the HIF-1α signalling pathway:

$$\begin{aligned}
\frac{dx}{dt} &= S - \left(\frac{x}{x+\gamma}\right)(h_1 y_1 + h_2 y_2 + h_3 y_3) \\
\frac{dy_1}{dt} &= S_1 - d_1 y_1 \\
\frac{dy_2}{dt} &= S_2 + kx - d_2 y_2 \\
\frac{dy_3}{dt} &= S_3 + kx - d_3 y_3.
\end{aligned} \tag{7.2}$$

The equilibrium values of system (7.2) are given by,

$$\frac{dx}{dt} = \frac{dy_1}{dt} = \frac{dy_2}{dt} = \frac{dy_3}{dt} = 0.$$

This occurs when,

$$y_1 = \frac{S_1}{d_1} = y_1^{EQ}, \qquad y_2 = \frac{S_2 + kx^{EQ}}{d_2} = y_2^{EQ}, \qquad y_3 = \frac{S_3 + kx^{EQ}}{d_3} = y_3^{EQ},$$

where $x = x^{EQ}$ represents the value of x which yields $dx/dt = 0$. This value occurs when

$$S = \left(\frac{x}{x+\gamma}\right)\left(\frac{h_1 S_1}{d_1} + \frac{h_2 S_2}{d_2} + \frac{h_3 S_3}{d_3} + kx^{EQ}\left(\frac{h_2}{d_2} + \frac{h_3}{d_3}\right)\right)$$

$$\Rightarrow k\left(\frac{h_2}{d_2} + \frac{h_3}{d_3}\right)(x^{EQ})^2 + \left(\sum_{i=1}^{3}\frac{h_i S_i}{d_i} - S\right)x^{EQ} - S\gamma = 0$$

$$\Rightarrow x^{EQ} = \frac{\left(S - \sum_{i=1}^{3}\frac{h_i S_i}{d_i}\right) \pm \sqrt{\left(\sum_{i=1}^{3}\frac{h_i S_i}{d_i} - S\right)^2 + 4kS\gamma\left(\frac{h_2}{d_2} + \frac{h_3}{d_3}\right)}}{2k\left(\frac{h_2}{d_2} + \frac{h_3}{d_3}\right)}.$$

Considering that x must be positive for feasibility (representing the amount of HIF-1α protein) we have

$$x^{EQ} = \frac{\left(S - \sum_{i=1}^{3}\frac{h_i S_i}{d_i}\right) + \sqrt{\left(\sum_{i=1}^{3}\frac{h_i S_i}{d_i} - S\right)^2 + 4kS\gamma\left(\frac{h_2}{d_2} + \frac{h_3}{d_3}\right)}}{2k\left(\frac{h_2}{d_2} + \frac{h_3}{d_3}\right)},$$

$$y_1^{EQ} = \frac{S_1}{d_1}, \qquad y_2^{EQ} = \frac{S_2 + kx^{EQ}}{d_2}, y_3^{EQ} = \frac{S_3 + kx^{EQ}}{d_3},$$

as the unique equilibrium point of the system.

We can non-dimensionalise system (7.2) to make the stability analysis easier. The system contains the following dimensional quantities:

Variable	Dimension	Parameter	Dimension
x	C	S, S_1, S_2, S_3	CT^{-1}
y_1	C	γ	C
y_2	C	h_1, h_2, h_3	T^{-1}
y_3	C	k	T^{-1}
t	T	d_1, d_2, d_3	T^{-1}

Table 7-1: A table of variables and model parameters of system (7.2) and their respective dimensions.

By defining the following dimensionless quantities we can re-write the ODEs of the system. We scale time and protein values with the PHD induction rate and basal synthesis rates:

$$t^* = kt, \qquad x^* = \frac{k}{S}x, \qquad y_1^* = \frac{k}{S_1}y_1, \qquad y_2^* = \frac{k}{S}y_2, \qquad y_3^* = \frac{k}{S}y_3.$$

Now we can write

$$\frac{dx^*}{dt^*} = \frac{k}{S}\frac{1}{k}\frac{dx}{dt} = 1 - \left(\frac{x^*}{x^* + \frac{k}{S}\gamma}\right)\left(\frac{h_1}{S}\frac{S_1}{k}y_1^* + \frac{h_2}{S}\frac{S_2}{k}y_2^* + \frac{h_3}{S}\frac{S_3}{k}y_3^*\right)$$

$$= 1 - \left(\frac{x^*}{x^* + \gamma^*}\right)(h_1^* y_1^* + h_2^* y_2^* + h_3^* y_3^*),$$

$$\frac{dy_1^*}{dt^*} = \frac{k}{S_1}\frac{1}{k}\frac{dy_1}{dt} = 1 - \frac{d_1}{S_1}\frac{S_1}{k}y_1^* = 1 - d_1^* y_1^*,$$

$$\frac{dy_2^*}{dt^*} = \frac{k}{S}\frac{1}{k}\frac{dy_2}{dt} = \frac{S_2}{S} + \frac{k}{S}\frac{S}{k}x^* - \frac{d_2}{S}\frac{S}{k}y_2^* = S_2^* + x - d_2^* y_2^*,$$

$$\frac{dy_3^*}{dt^*} = \frac{k}{S}\frac{1}{k}\frac{dy_3}{dt} = \frac{S_3}{S} + \frac{k}{S}\frac{S}{k}x^* - \frac{d_3}{S}\frac{S}{k}y_3^* = S_3^* + x - d_3^* y_3^*,$$

where we have the following non-dimensional quantities:

$$\gamma^* = \frac{k}{S}\gamma, \qquad h_i^* = \frac{S_i}{Sk}h_i, \qquad d_i^* = \frac{1}{k}d_i \text{ for } i = 1,2,3 \text{ and } S_i = \frac{1}{S}S_i \text{ for } i = 2,3.$$

We drop the $*$ for notational simplicity and acquire the following system:

$$\frac{dx}{dt} = 1 - \left(\frac{x}{x + \gamma}\right)(h_1 y_1 + h_2 y_2 + h_3 y_3)$$

$$\frac{dy_1}{dt} = 1 - d_1 y_1$$

$$\frac{dy_2}{dt} = S_2 + x - d_2 y_2$$

$$\frac{dy_3}{dt} = S_3 + x - d_3 y_3.$$

For the linear stability analysis we will use the notation:

$$\dot{x} = f(x, y_1, y_2, y_3), \qquad \dot{y_1} = g(x, y_1, y_2, y_3), \qquad \dot{y_2} = m(x, y_1, y_2, y_3), \qquad \dot{y_3} = n(x, y_1, y_2, y_3)$$

such that we can write the following Jacobian matrix equation,

$$\frac{d\boldsymbol{\epsilon}}{dt} = \begin{pmatrix} f_x & f_{y_1} & f_{y_2} & f_{y_3} \\ g_x & g_{y_1} & g_{y_2} & g_{y_3} \\ m_x & m_{y_1} & m_{y_2} & m_{y_3} \\ n_x & n_{y_1} & n_{y_2} & n_{y_3} \end{pmatrix}\Bigg|_{\mathbf{z}^{EQ}} \begin{pmatrix} \epsilon_x \\ \epsilon_1 \\ \epsilon_2 \\ \epsilon_3 \end{pmatrix}$$

$$= \mathbf{A}\boldsymbol{\epsilon}$$

$$\Rightarrow \boldsymbol{\epsilon} = \mathbf{v}e^{\lambda t} \Rightarrow \lambda\mathbf{v} = \mathbf{A}\mathbf{v}.$$

From our Jacobian matrix $\mathbf{A}$, we find the eigenvalues by solving the corresponding characteristic equation, $|\mathbf{A} - \lambda\mathbf{I}| = 0$.

$$|\mathbf{A} - \lambda\mathbf{I}|$$

$$= \begin{vmatrix} -\left(\frac{\gamma}{(x^{EQ}+\gamma)^2}\right)\left(h_1 y_1^{EQ} + h_2 y_2^{EQ} + h_3 y_3^{EQ}\right) - \lambda & -h_1\left(\frac{x}{x^{EQ}+\gamma}\right) & -h_2\left(\frac{x}{x^{EQ}+\gamma}\right) & -h_3\left(\frac{x}{x^{EQ}+\gamma}\right) \\ 0 & -d_1 - \lambda & 0 & 0 \\ 1 & 0 & -d_2 - \lambda & 0 \\ 1 & 0 & 0 & -d_3 - \lambda \end{vmatrix}$$

$$= \lambda^4 + \left(d_1 + d_2 + d_3 - \mathbf{A}_{1,1}\right)\lambda^3 + \left(d_1 d_2 + d_2 d_3 + d_1 d_3 - \mathbf{A}_{1,1}(d_1 + d_2 + d_3) - \mathbf{A}_{1,3} - \mathbf{A}_{1,4}\right)\lambda^2$$
$$+ \left(d_1 d_2 d_3 - \mathbf{A}_{1,1}(d_1 d_2 + d_2 d_3 + d_1 d_3) - \mathbf{A}_{1,3}(d_1 + d_3) - \mathbf{A}_{1,4}(d_1 + d_2)\right)\lambda$$
$$- d_1 d_2 d_3 \mathbf{A}_{1,1} - d_1 d_3 \mathbf{A}_{1,3} - d_1 d_2 \mathbf{A}_{1,4}$$
$$= \lambda^4 + a_1\lambda^3 + a_2\lambda^2 + a_3\lambda + a_4$$

By using the Routh-Hurwitz criteria (Chapter 2, section 2.2.2.1 and equation (2.10)) we can see that we have a stable equilibrium if $a_1 > 0$, $a_3 > 0$, $a_4 > 0$ and $a_1 a_2 a_3 > a_3^2 + a_1^2 a_4$. Since $\mathbf{A}_{1,1} < 0$, $\mathbf{A}_{1,3} < 0$ and $\mathbf{A}_{1,4} < 0$ it is clear that $a_1 > 0$, $a_3 > 0$ and $a_4 > 0$. It can also be shown that as long as all parameters and variables are positive (which they are by feasibility and definition) that $a_1 a_2 a_3 > a_3^2 + a_1^2 a_4$. Therefore we have a unique, stable equilibrium for system (7.2).

7.4 Limitations of FLIM Imaging Data with pO_2 Calibration

In Chapter 4 we converted lifetime data from FLIM experiments into oxygen concentration data. A result of using the calibration curve defined in Figure 4-3 to convert FLIM images into oxygen concentration units was that only certain data was feasible for further use in the parameterisation of our model of spatial oxygen dynamics. These limitations suggest the need for more accurate lifetime (μs) to pO_2 (μM) unit conversions. We attempted to prevent any unrealistic extrapolation of the calibration curve by omitting data with very short lifetime values (<35 μs) as described in section 4.4.1 but this was not enough to prevent erroneous data fitting.

Preliminary fitting showed that despite the cutting of data relating to short lifetime values (i.e. normoxia); these normoxic data still exhibited oxygen concentration values that were unfeasibly high by our calculations. This occurred in the case where the external oxygen concentration was 17% (e.g. *Sphere 1*). pO_2 values were found inside the sphere which were greater than the external oxygen condition, C_∞, the theoretical maximum (see Figure 7-2). For these reason further data-cutting was carried out to remove this anomalous data from the fitting process.

A

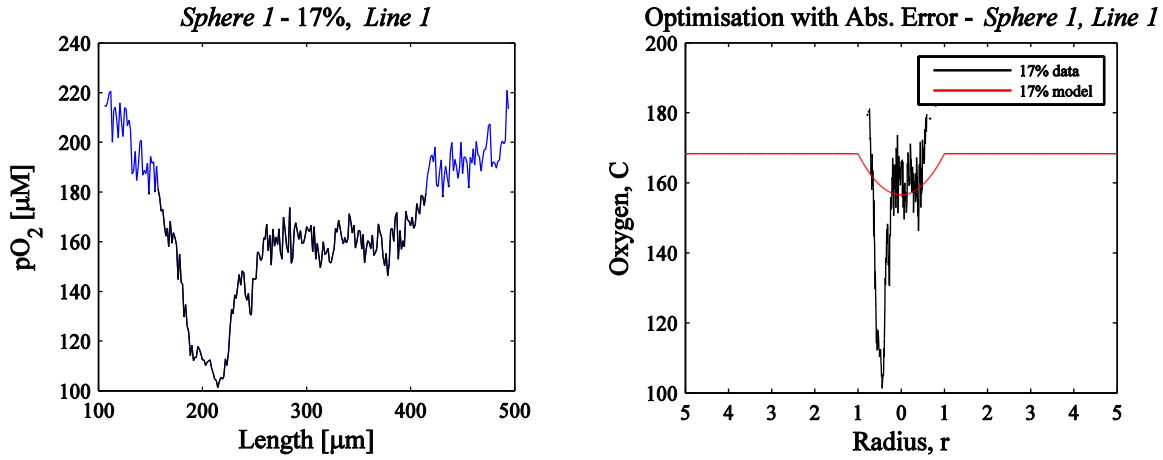

B

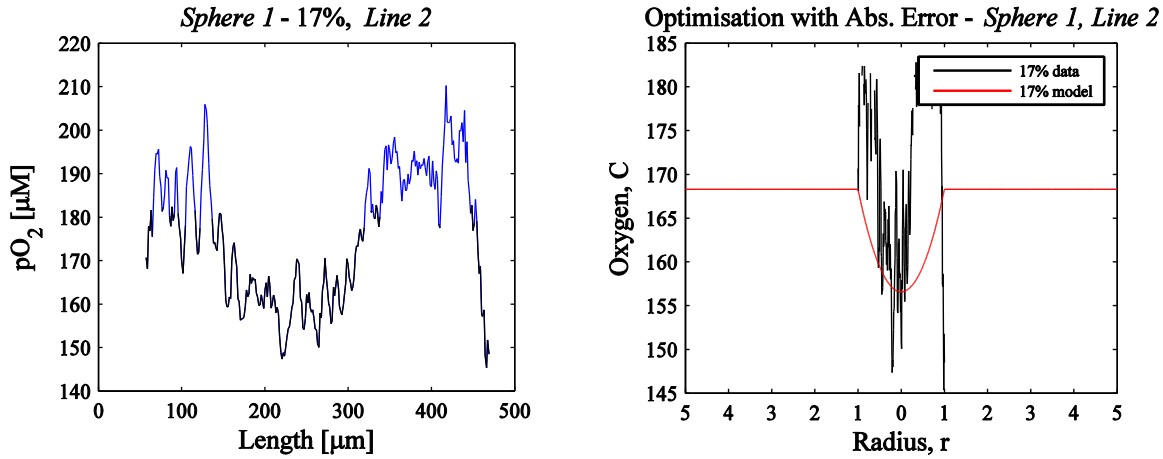

Figure 7-2: Data-fitting results for the oxygen concentration distribution across *Sphere 1* (17% external O_2 conditions) taken from two different cross-section sites as described in Figure 4-5: *Line 1* (A) and *Line 2* (B). Blue experimental data in the left-hand plots indicates data omitted from fitting due to the data lying outside of the calibration curve in Figure 4-3. Right-hand plots show the attempted data-fitting with the model (red curve). Preliminary fitting of the black data showed that the data was still unfeasibly high when assuming a theoretical maximum of 17% at the source of oxygen.

As part of a preliminary fitting process, parameter optimisation was carried out individually for all spheres. In total 13 different cross sections were fitted to representing data from 3 neurospheres: *Sphere 1*; *Sphere2*; and *Sphere 3*. *Sphere 3* data was fit to but there was only one external oxygen condition for this data and we were interested in the change in oxygen distribution within the same sphere across different oxygen conditions. *Sphere 3* data was also not particularly well suited to unit calibration as most data points were calibrated to be 0µM. *Sphere 1* data was suitable in 8% conditions but in 17% conditions the pO_2 values were too unrealistic to fit to given the constraint of the boundary conditions (i.e. 17% is the maximum and occurs at C_∞). Only *Sphere 2* data was recorded at 8% and 3% conditions and the pO_2 values generated for these lifetime values fell within the feasible range of fitting. We proceeded with *Sphere 2* data for further model development.